Progress in Materials Science 89 (2017) 92–193

Contents lists available at ScienceDirect

Progress in Materials Science

journal homepage: www.elsevier.com/locate/pmatsci

# Fundamentals and advances in magnesium alloy corrosion

M. Esmaily [a,*], J.E. Svensson [a], S. Fajardo [b,c], N. Birbilis [d], G.S. Frankel [b], S. Virtanen [f], R. Arrabal [e], S. Thomas [d], L.G. Johansson [a]

[a] Department of Chemistry and Chemical Engineering, Chalmers University of Technology, Gothenburg 412 96, Sweden
[b] Fontana Corrosion Center, Department of Materials Science and Engineering, The Ohio State University, Columbus, OH 43210, USA
[c] Department of Surface Engineering, Corrosion and Durability, National Center for Metallurgical Research (CENIM-CSIC), Madrid 28040, Spain
[d] Department of Materials Science and Engineering, Monash University, Victoria 3800, Australia
[e] Departamento de Ciencia de Materiales, Universidad Complutense, Madrid 28040, Spain
[f] Department of Materials Science (LKO, WW-4), University of Erlangen-Nuremberg, 91058 Erlangen, Germany

## ARTICLE INFO

*Article history:*
Received 26 November 2016
Received in revised form 30 March 2017
Accepted 22 April 2017
Available online 15 May 2017

*Keywords:*
Mg
Electrochemistry
Atmospheric corrosion
Alloying
Composites
Biodegradable alloys

## ABSTRACT

There remains growing interest in magnesium (Mg) and its alloys, as they are the lightest structural metallic materials. Mg alloys have the potential to enable design of lighter engineered systems, including positive implications for reduced energy consumption. Furthermore, Mg alloys are also emerging as viable biodegradable materials and battery electrodes. In spite of the greatest historical Mg usage at present, the wider use of Mg alloys remains restricted by a number of inherent limitations, including vulnerability to corrosion, poor formability and low creep resistance. This review covers recent research that has led to advances in Mg-alloy corrosion; including the application of contemporary methods for understanding Mg corrosion, the establishment of an electrochemical framework for Mg corrosion, illumination of alloying effects, and attempts at corrosion resistant Mg alloys. A discussion drawing from many sources provides an unbiased focus on new achievements, as well as some contentious issues in the field. The electrochemistry of Mg is reviewed in detail, including so-called anodic hydrogen evolution and cathodic activation. This review also covers atmospheric corrosion, and biodegradable Mg alloys. Finally, past and present trends in the field of Mg corrosion are reviewed, identifying knowledge gaps, whilst attempting to also identify future developments and directions.

## Contents

1. Introduction . . . 94
   1.1. The need for "light weighting" . . . 94
   1.2. A unique metal . . . 95
   1.3. An historical background of Mg corrosion . . . 95
   1.4. Alloying systems . . . 96
   1.5. Review synopsis . . . 98
2. Methods of analysis for Mg corrosion research . . . 98
   2.1. Corrosion testing in aqueous media . . . 99
      2.1.1. Electrochemical techniques . . . 99

---

* Corresponding author at: Department of Chemistry and Chemical Engineering, Chalmers University of Technology, SE-412 96 Gothenburg, Sweden.
*E-mail address:* mohsen.esmaily@chalmers.se (M. Esmaily).

http://dx.doi.org/10.1016/j.pmatsci.2017.04.011
0079-6425/

- 2.1.2. Localized electrochemical techniques . . . . . 101
- 2.1.3. Non-electrochemical techniques . . . . . 102
- 2.2. Corrosion testing in atmospheric conditions . . . . . 103
  - 2.2.1. Field exposures (outdoor environments) . . . . . 104
  - 2.2.2. Accelerated corrosion testing (ACT) . . . . . 105
  - 2.2.3. Laboratory exposures at constant RH . . . . . 106
  - 2.2.4. Field exposures, corrosion testing and corrosion experiments in the lab . . . . . 106
- 2.3. Analytical tools for Mg corrosion research . . . . . 108
  - 2.3.1. Statistics in Mg alloy corrosion . . . . . 108
  - 2.3.2. Electron backscatter diffraction (EBSD) . . . . . 109
  - 2.3.3. Scanning Kelvin probe (SKP) and SKP-force microscopy (SKPFM) . . . . . 110
  - 2.3.4. X-ray diffraction (XRD) . . . . . 110
  - 2.3.5. Interference microscope (IM) (profilometry) . . . . . 111
  - 2.3.6. Cross sectional analysis . . . . . 111
  - 2.3.7. Transmission electron microscope (TEM) . . . . . 113
  - 2.3.8. Three-dimensional (3D)-imaging/EDX/EBSD . . . . . 113
  - 2.3.9. X-ray photoelectron spectroscopy (XPS) . . . . . 113
  - 2.3.10. Auger electron spectroscopy (AES) . . . . . 113
  - 2.3.11. Secondary ion mass spectrometry (SIMS) . . . . . 114
  - 2.3.12. Fourier Transform InfraRed (FTIR) spectroscopy . . . . . 114
  - 2.3.13. Raman spectroscopy . . . . . 114
  - 2.3.14. Ion Chromatography (IC) . . . . . 115
  - 2.3.15. Environmental scanning electron microscopy (ESEM) . . . . . 115
  - 2.3.16. X-ray computed tomography (CT) . . . . . 115
  - 2.3.17. High-resolution methods for future studies . . . . . 115
  - 2.3.18. A comparison between analytical methods . . . . . 116
- 3. Aqueous corrosion of Mg . . . . . 117
  - 3.1. Generalities of Mg corrosion . . . . . 117
  - 3.2. Mg corrosion mechanism . . . . . 119
    - 3.2.1. Anomalous HE on anodically polarized Mg surfaces . . . . . 119
    - 3.2.2. Univalent Mg ($Mg^+$) theory . . . . . 120
    - 3.2.3. Effects of corrosion film and surface enrichment of impurities . . . . . 121
    - 3.2.4. Increased catalytic activity . . . . . 125
  - 3.3. Composition effects on the corrosion of Mg alloys . . . . . 128
    - 3.3.1. Solubility of metals in Mg . . . . . 129
    - 3.3.2. Tolerance limits of metals in Mg . . . . . 130
    - 3.3.3. Synopsis of alloy chemistry upon Mg alloy corrosion . . . . . 132
    - 3.3.4. A kinetic framework for compositional effect upon Mg corrosion . . . . . 134
  - 3.4. Role of reinforcing phases/particles . . . . . 137
    - 3.4.1. Reinforcements for Mg-MMCs . . . . . 138
    - 3.4.2. Manufacturing routes and interfacial reactions . . . . . 138
    - 3.4.3. Corrosion behavior of Mg-MMCs . . . . . 147
  - 3.5. Biodegradation of Mg alloys . . . . . 148
    - 3.5.1. Crucial aspects of Mg corrosion in view of the biomedical applications . . . . . 149
    - 3.5.2. Mg corrosion in (simulated) body environments . . . . . 150
    - 3.5.3. Role of simulated body fluids . . . . . 150
    - 3.5.4. Static vs. Dynamic conditions . . . . . 151
    - 3.5.5. Role of proteins . . . . . 151
    - 3.5.6. Role of cells . . . . . 152
    - 3.5.7. In vitro vs. in vivo corrosion . . . . . 153
    - 3.5.8. Influence of Mg corrosion products on the biocompatibility . . . . . 153
    - 3.5.9. Approaches to control Mg corrosion for biomedical applications . . . . . 154
    - 3.5.10. Tailored alloys and microstructures . . . . . 154
    - 3.5.11. Surface modification and coatings . . . . . 155
    - 3.5.12. Conclusions: Understanding biocorrosion of Mg alloys? . . . . . 156
- 4. Atmospheric corrosion . . . . . 157
  - 4.1. Atmospheric corrosion versus corrosion during immersion . . . . . 157
  - 4.2. Factors influencing atmospheric corrosion . . . . . 159
    - 4.2.1. Rain and mist . . . . . 159
    - 4.2.2. Relative humidity and condensation . . . . . 159
    - 4.2.3. Substances influencing atmospheric corrosion . . . . . 160
    - 4.2.4. Inorganic salts . . . . . 160
    - 4.2.5. Gases . . . . . 160
    - 4.2.6. Temperature . . . . . 162
    - 4.2.7. Ultraviolet (UV) radiation . . . . . 162
  - 4.3. Atmospheric corrosion of Mg and Mg alloys . . . . . 162

4.3.1. The role of chloride . . . 163
4.3.2. The role of carbon dioxide ($CO_2$) . . . 163
4.3.3. The role of sulfur dioxide ($SO_2$) . . . 166
4.3.4. The role of nitrogen dioxide ($NO_2$) and ozone ($O_3$) . . . 166
4.3.5. The role of temperature . . . 167
4.3.6. Mg (alloy) atmospheric corrosion at the nanoscale . . . 167
4.3.7. Novel concepts in atmospheric corrosion of Mg alloys . . . 170
4.4. Protection against atmospheric corrosion . . . 174
4.4.1. Protection strategies: Chemistry and microstructure . . . 175
4.4.2. Protection strategies: Surface modification . . . 176
5. Outlook . . . 177
5.1. Corrosion mechanism . . . 177
5.2. Effect of alloying . . . 178
5.3. Mg-based MMCs . . . 179
5.4. Mg biocorrosion . . . 180
5.5. Atmospheric corrosion . . . 180
5.6. Protection against atmospheric corrosion . . . 180
Acknowledgement . . . 181
References . . . 181

# 1. Introduction

## 1.1. The need for "light weighting"

Climate change is now a major concern. The polar ice caps are reported to be melting and sea levels are rising due to an increase in the average temperature of the Earth's atmosphere and oceans [1]. Global warming is driven by increasing levels of tropospheric gases that contribute to the so-called greenhouse effect. Carbon dioxide ($CO_2$) is the most important "greenhouse gas" and the continuous increase of $CO_2$ concentrations is known to be chiefly responsible for global warming (Fig. 1) [2]. Hence, reducing emissions of $CO_2$ is an urgent matter. Burning fossil fuels for ground, air, and marine transportation accounts for 15–25% of total greenhouse gas emissions in regions such as Europe and North America [3]. As the largest source of $CO_2$, the road transportation sector is bound to shift towards low-emission vehicles without delay. This need is clearly stated in emission standards such as the EC No 443/2009 and 510/2011 in Europe, specifying that the fleet average to be achieved by all new cars is 95 g (g) of $CO_2$ per kilometer (km), *i.e.*, 40% of the 2007 fleet average of 158.7 g/km [4,5], which requires considerable efforts from the automotive industry. The use of lighter components is an effective way to reduce demands on fuel resources, increase energy efficiency, and decrease $CO_2$ emissions. For example, in a typical passenger car, an overall weight saving of ~10% yield fuel savings on the order of 20–30%, without drastic changes in design [6].

Furthermore, the economic benefits of lightweight materials are tempting. It has been estimated that a one kg weight reduction in an aircraft results in fuel savings of ~1150 USD during its lifetime [9,10]. If the effects of air pollution are also

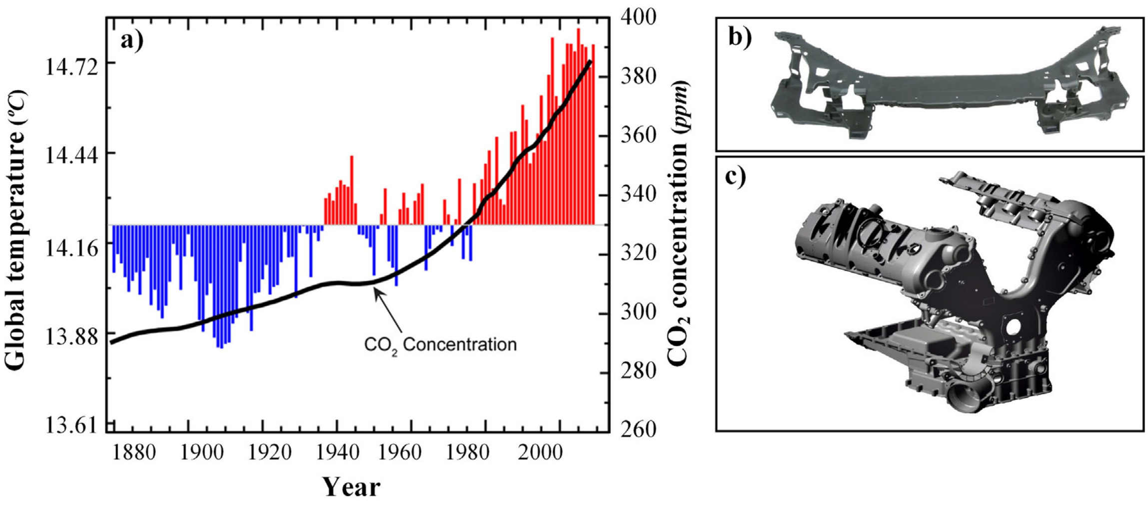

**Fig. 1.** The urgent issue of climate change and lightweight automotive solutions. (a) Increase in atmospheric carbon dioxide levels and the global temperature anomaly [7]. (b and c) Examples of die-cast Mg alloys for (b) engine cover and oil housing (powertrain application; Porsche), and (c) instrument panel beam (structural application; Volvo) [8]. Reproduced with permission from NACE International, Houston, TX.

taken into account, it becomes apparent that fuel-saving weight reductions can be highly cost effective. These factors, along with emissions targets in various nations, are drivers for lightweight products. Thus, in today's automobiles, many components, such as the crank case, camshaft sprocket, gearbox housing, several covers, and the arm of the electric generator, can be replaced with light alloys to meet the demand for decreasing vehicle weight [6,10].

The use of magnesium (Mg) alloys in the automotive sector (see *e.g.,* the two die-cast Mg alloy parts in Fig. 1b and c) has been steadily growing in the past 15 years [8], however as covered in this review, issues such as corrosion severely restrict the wider insertion of Mg alloys – making this review both timely and important.

### *1.2. A unique metal*

Magnesium is the lightest engineering metal with a density of ~1.7 g/cm$^3$, which is significantly lower than aluminum (Al, 2.7 g/cm$^3$), titanium (Ti, 4.5 g/cm$^3$), and iron (Fe, 7.9 g/cm$^3$), respectively [6]. Mg is the 8th most abundant element in the earth's crust and there are, thus, ample resources to cover the use of its alloys in various engineering sectors. Mg alloys have been shown to be capable of the highest strength-to-weight ratio of structural alloys, however their balance of properties (other than strength) remains under intense research; including corrosion, ductility and creep. Other advantages of Mg include; exceptional dampening capacity, its non-toxicity towards the environment and the human body (Mg alloys are considered ideal options for biodegradable implants), ease of machining by high speed milling and turning (*e.g.,* 5–10 times longer tool life than Al), and versatility (*e.g.,* processable by rolling, extrusion) [11]. Mg alloys have excellent castability, allowing the fabrication of complex shapes by high productivity methods such as high pressure die casting. Depending on geometry, Mg parts can be die cast up to 50% faster than the same parts in Al [11,12]. Finally, compared to polymers, Mg alloys show superior mechanical properties and higher thermal conductivity. In addition, Mg is 100% recyclable, which is usually not the case for polymers [13].

Considering the advantages and modest cost of Mg (particularly the cost per unit volume) [8,12], the use of Mg alloys remains notably limited. The corrosion resistance of Mg, being the subject of this paper, is one of the key "Achilles heels" of the metal that restricts the usefulness of Mg alloys. Even in cases when one property of Mg-alloys can be enhanced, such as creep resistance with heavy rare earth element loadings, this further aggravates corrosion [14]. Similarly in cases when strength increases are sought in Mg-alloys, it is nominally at the detriment of corrosion performance, such that corrosion is the lowest common denominator that requires critical attention. Further, the ability of Mg to burn in air and the rapid oxidation of molten Mg in air together with the pyrophoric nature of Mg powders, are additional issues that somewhat restrict the use and complicate the fabrication of Mg alloys – to foundries with appropriate environmental control.

### *1.3. An historical background of Mg corrosion*

The first to propose that Mg is an element was Scottish physician Joseph Black in 1755 [15]. Metallic Mg was isolated by Davy in 1808 and prepared in coherent form by Bussey in 1831. Today, the two main methods for producing Mg involve high temperature reduction of MgO by Si and the electrolysis of molten $MgCl_2$, respectively [16]. The vulnerability of Mg to corrosion was documented from early on. In 1831, Bussey carried out the first corrosion experiment on Mg in an outdoor environment and reported that "*Mg becomes covered with the hydroxide after exposure to moist air, but remains un-attacked in dry air*" [17]. In 1866, the corrosion behavior of Mg in aqueous solution was studied by Beetz [18] who noted that Mg exhibits hydrogen evolution (HE) during anodic polarization, the first mention of the so-called negative difference effect (NDE), which is also known as anodic HE (see Section 3.1).

The exploitation of Mg corrosion with regards to bio-degradable properties of Mg were first noted in 1878 by Huse, who used Mg wires as a ligature to stop bleeding vessels in human patients [19]. However, the rapid corrosion and the associated hydrogen release was noted by many surgeons and the biocompatibility of Mg was questioned [20] (see Section 3.5).

The first Mg alloy that was introduced in 1908 by Pistor and Moschel [16] had a composition of Mg 90%, Al 9%, and other 1% (by weight). From very early on, it was noted that Mg-alloys corrode "*badly*" [21]. To this end, in the 1920s, some of the most important (still relevant to this day) work on Mg-alloy corrosion was conducted by Boyer [21]. The work of Boyer highlighted the relevance of impurities upon Mg corrosion, and the need to sequester impurities. The work was extended in the 1940s by Hanawalt and McNulty [22] (see Section 3.3).

In 1954 Petty made the contentious suggestion that the unipositive $Mg^+$ ion plays an important role in the aqueous corrosion of Mg [23]. It merits comment that to date, no spectroscopic isolation of this ion has ever occurred (see Section 3.2). Several decades later, the emergence of analytical tools with higher resolution and spectroscopic ability has allowed further understanding to evolve regarding Mg corrosion. In 1993, Splinter et al. [24] studied the composition of films formed on Mg, for the first time. The work was continued by Nordlien et al. [25–27] who used high-resolution microscopy to analyze the composition of surface films formed on Mg and Mg alloys.

The key developments in regards to corrosion of Mg alloys are summarized pictorially in Fig. 2. It is noted that a recent surge in activity in the last decade has indicated that there is significant problems that the issues typically associated with Mg alloys are capable of being resolved. For example, 2015 witnessed the demonstration of an ultra-light corrosion resistant Mg alloy (Mg-Li), offering both corrosion resistance (from a "protective" surface film) as well as cold workability (owing to a body centered cubic (bcc) matrix) (see Section 3.3). Another example is that certain Mg alloys have lately passed extensive

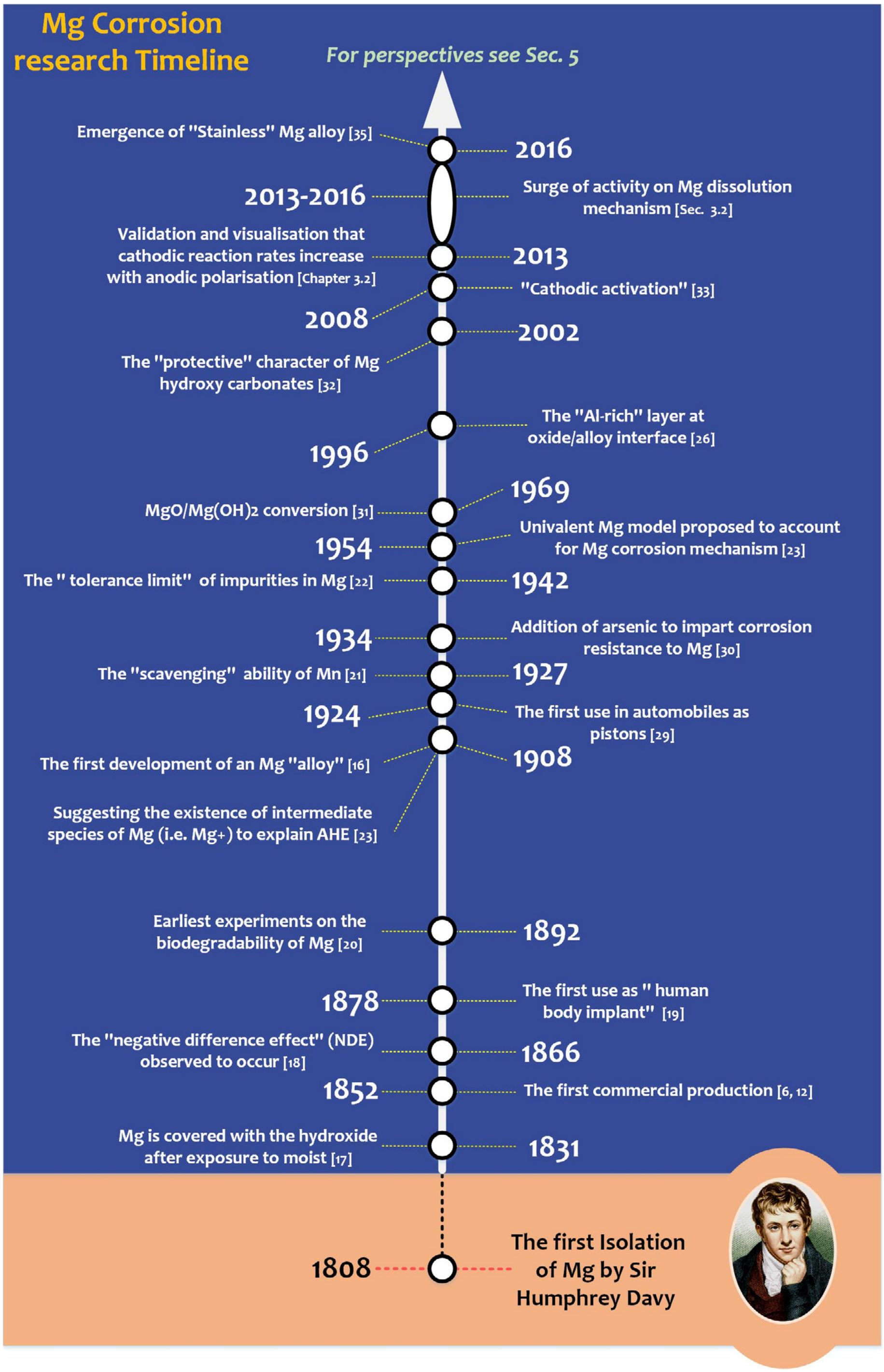

**Fig. 2.** Timeline of scientific and technological developments of Mg corrosion research, indicating "landmarks" since the isolation of Mg metal in 1808.

flammability tests and now possible to use as seat structures in commercial aircraft [28], promising an important role for the future of Mg alloys (see prospective in Section 5).

## *1.4. Alloying systems*

Pure Mg is soft and mechanically weak, with a tensile strength of ~20 MPa [11]. Thus, there have been significant efforts on developing Mg alloys for different applications (see Fig. 3). Mg alloys are typically multiphase materials, consisting of a

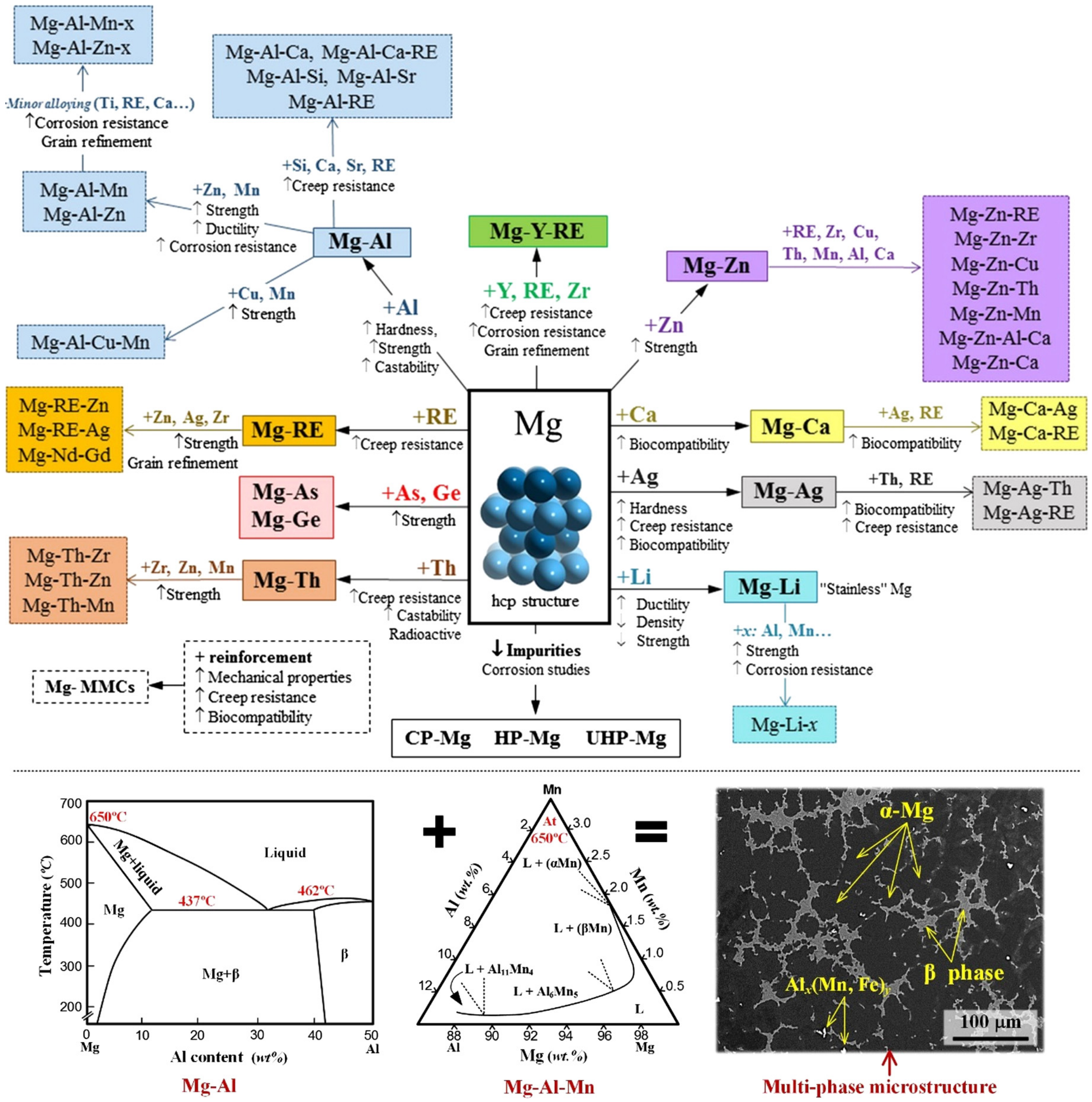

**Fig. 3.** (a) Summary of Mg alloy development, and (below) phase diagram for the Mg-Al binary system (extreme left) and Mg-Al-Mn isothermal section (in the middle) as well as a micrograph showing a typical microstructure of an Mg-Al alloy AZ91. Phase diagrams are reproduced based on [38,39]. The Mg-Al diagram is reproduced with permission from Elsevier. The Mg-Al-Mn diagram is reproduced with permission from the journal IJRM, ©Carl Hanser Verlag GmbH & Co. KG, Muenchen.

dispersion of intermetallic particles in the α-Mg matrix. The multiphase nature of the alloys is mainly due to the non-equilibrium character of solidification and provides mechanical strength to the materials. The commonest Mg alloys belong to the Al-containing families and include alloys AZ91, AM60, AM50 and AZ31 [6,29]. In view of the importance of Mg-Al alloys, the corresponding phase diagram is also included in Fig. 3, as an example. A typical solidification microstructure of cast Mg-Al alloys consists of primary α-Mg grains (hexagonal, space group P6$_3$/mmc, $a = 0.32$ nm and $c = 0.521$ nm), and may include casting porosity and "secondary" α-Mg or inter-dendritic regions [36].

The latter regions are decorated with intermetallic β phase particles ($Mg_{17}Al_{12}$) with a cubic crystal structure (space group 1$\bar{4}$3 m, $a = 1.056$ nm). The common Mg-Al alloys also contains about 0.4% (mass) manganese (Mn), and thus, particles with the chemical composition $Al_x(Mn,Fe)_y$ including $Al_8Mn_5$ are formed in inter-dendritic regions. Additional intermetallic particles entities reported include, $Al_6Mn$, $Al_4Mn$, and AlMn depending on the solidification or processing route [12,36–39].

### *1.5. Review synopsis*

This review aims to present a comprehensive state-of-the-art overview of key concepts in Mg-alloy corrosion. The review takes a holistic approach to the relevant topics, at times being concise and critical, with timely focus on key developments, including challenges and opportunities in Mg corrosion research. This review should allow both new and experienced researchers entering the field to be informed of the various critical aspects of the field and its relevance to materials science more generally, in a single narrative. The review is organized with Section 2 devoted to experimental approaches, covering corrosion experiments and analytical tools that may be used in Mg corrosion research. Important issues associated with the different experimental approaches are identified, describing advantages and limitations, whilst giving recommendations for use in Mg corrosion research. Section 3 is a systematic summary and review of various aspects of Mg corrosion in "aqueous" media. This section covers recent advances in the understanding of the mechanism of Mg corrosion, the effect of alloying, biodegradable properties of Mg alloys - ending with a summary on the corrosion of Mg-alloys reinforced with ceramics. Section 4 reviews the role of various atmospheric gases and substances in the atmospheric corrosion of Mg and Mg-Al alloys and protection strategies used to make Mg alloys less vulnerable to atmospheric corrosion. This section focuses on the corrosion behavior of Mg-Al alloys, being the most commonly used alloying systems, *i.e.,* Mg-Al alloys. In Section 5 (outlook), we capture opportunities for new research that is enabled by recent advances in experimental methodology and recent scientific advances.

Despite the growing interest in Mg alloys, a comprehensive treatment of Mg alloy corrosion, from experimental methodologies to fundamentals and corrosion behavior in service environments, is lacking. There are review papers on different aspects of Mg corrosion, including the mechanism of dissolution [40,41], the effect of composition [42], and bio-corrosion [43,44]. However, there are no reviews inclusive of, for example; the environmental degradation of Mg alloys (*i.e.,* atmospheric corrosion) or the corrosion behavior of Mg-based metal matrix composites (Mg-MMCs). Furthermore, few reviews take a comprehensive un-biased approach, in addition to the timely nature of capturing the surge of research activity in the past three years.

The key concept behind presenting a comprehensive review of the subject is to also enable workers in the field to have a platform for which new research ideas may stem, based on recent advances and from translation of recent work in other fields. Indeed, past and present trends in the field of Mg corrosion are reviewed, identifying apparent knowledge gaps, whilst attempting to also identify future developments and research directions in the field. To this end, the review has been focused in size, and as such, the subjects including stress corrosion cracking (SCC) are deliberately not covered. However, such issues have been previously reviewed [45,46].

## 2. Methods of analysis for Mg corrosion research

In many cases, corrosion experiments are designed to elucidate certain aspects of the process in order to help provide models for the prediction and control of corrosion in an engineering context. To this end, it is often essential to determine corrosion rate and other relevant corrosion parameters and to relate corrosion behavior to the composition, microstructure, and surface chemistry of the system studied. Also, it is typically important to determine the composition of corrosion products, or any surface films. In the case of multiphase materials such as most Mg alloys, it may also be important to determine the phases present and their phase fraction, composition and distribution – allowing a relationship to be determined between corrosion and microstructure. To achieve this, it is common practice to make use of a set of conventional methods, including visual inspection, optical and electron microscopy and electrochemical measurements. Uniquely for Mg corrosion, since the relative rates of corrosion are higher than other engineering alloys, and since the cathodic reaction is water reduction (producing $H_2$), it is also common to employ gravimetric methods and hydrogen gas collection as a means of corrosion assessment.

During the last decade, corrosion research has benefited from the rapid development of many analytical techniques. For example, modern electron microscopes not only provide much better sensitivity and higher resolution than previously, but also offer many new capabilities. New methods for preparing samples for microscopy have also contributed greatly to the study of corrosion morphology and surface films. Indeed, many other analytical methods, including scanning Kelvin probe force microscopy (SKPFM), electron backscatter diffraction (EBSD), Nano-secondary ion mass spectrometry (NanoSIMS), and interference microscope (IM), in combination with statistical treatment, have become available, enabling researchers to break new ground in Mg alloy corrosion.

To make the best possible use of the rapid development of analytical tools, a basic understanding of the techniques is needed. This includes both capabilities and limitations and issues related to cleanliness, sample preparation, accuracy and precision. It is often a challenge to find the "right" combination of analytical methods for an investigation. In general, the use of methods that are highly "local" in character such as transmission electron microscopy (TEM), should always be complemented by methods such as scanning electron microscopy/energy-dispersive X-ray (SEM/EDX) that provide information on the μm scale and by methods (*e.g.,* X-ray diffraction (XRD) and Fourier transform infrared spectroscopy (FTIR)) that work on the cm scale. Only then can it be ascertained whether the nm scale measurements are relevant *and* representative.

Analytical methods that employ "harsh conditions", including electron microscopy but also other high vacuum techniques, cause some corrosion products, *e.g.,* Mg hydroxy carbonates (see Section 4.3.2), to decompose. They should therefore be complemented by non-destructive methods such as XRD and FTIR. In order to study transient processes such as the initiation of corrosion, *in situ* studies may be necessary. These and other analytical techniques used in Mg corrosion research are shortly reviewed below. In addition, this section also provides information about how to perform atmospheric corrosion experiments on Mg.

There are recent reviews covering methods used in certain areas of Mg corrosion research. Kirkland et al. [43] reviewed the methodologies used to study the corrosion of biodegradable Mg implant materials. Dauphin-Ducharme et al. [47] reported on the fundamentals of some scanning probe techniques in Mg corrosion research. In this section, we comprehensively review the most important corrosion testing methods, experimental approaches as well as analytical tools that have been used, or have a potential to be used, in the field of aqueous and atmospheric research of Mg and Mg alloys.

### *2.1. Corrosion testing in aqueous media*

The most widely used techniques for exploring the corrosion behavior of metallic materials in general, including Mg (alloys), involve immersing the samples in a corrosive solution. A simple search in *Web of Science* indicates that more than 88% of all Mg corrosion studies are related to immersion in aqueous solutions. As a rule of thumb, immersion testing is much faster and in many cases more aggressive than atmospheric corrosion testing, due to reasons explained in Section 4.1. In this section we summarize common "electrochemical" and "non-electrochemical" methods used in Mg corrosion research.

### *2.1.1. Electrochemical techniques*

There are numerous available techniques for measuring the corrosion rate of Mg alloys in aqueous solutions, which can be used independently or simultaneously. These typically include weight loss (mass loss), hydrogen collection, electrochemical and non-electrochemical methods as well as chemical analysis of the solution. Given the electrochemical nature of the corrosion process, it is not surprising that electrochemical methods are frequently used. It may also be noted that even though weight loss measurements are well established and stand out by their simplicity, they only provide an average corrosion rate, require comparatively long times (relative to electrochemical testing) and rely on the use of appropriate pickling/cleaning procedures. Hydrogen collection methods, despite some limitations, can be readily used for monitoring the instantaneous corrosion rate of Mg alloys even in real-time, by using both volumetric and gravimetric methods as demonstrated by Lebouil et al. [48], Curioni [49] and later Fajardo et al. [50]. Electrochemical methods are important and rapid tools for assessing the corrosion of metals, but aspects of their interpretation have been shown to be non-trivial in the case of Mg alloys, since their behavior is more complex than most other metals [51,52]. As an example, Kirkland et al. [43] provide an overview of the primary advantages and limitations of different corrosion rate measurement methods. This section will cover a number of electrochemical techniques used for determining the corrosion resistance or corrosion rate of Mg and its alloys.

*2.1.1.1. Potentiodynamic polarization (PDP).* PDP employs a potentiostat, reference electrode, and counter electrode to scan the potential of an electrode over a fixed interval at a fixed rate [53]. The requirement of a potentiostat for PDP means that this method gained popularity in the past few decades. Fig. 4a shows a set of representative PDP curves of commercially pure (CP) Mg in solutions with different NaCl concentration [51], noting that the potentials have been corrected for ohmic resistance. The PDP response provides information about the relative rates of the anodic and cathodic kinetics. It is clear from this

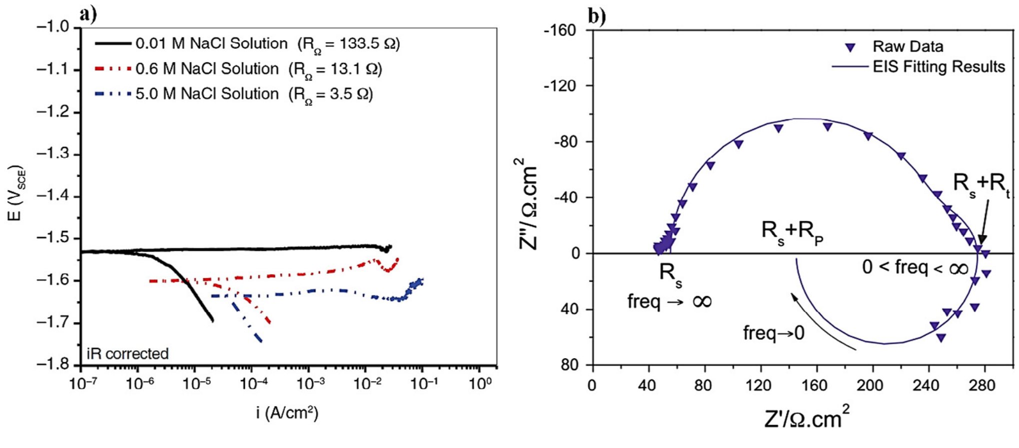

**Fig. 4.** Typical potentiodynamic polarization and EIS results of Mg and Mg alloys. (a) Potentiodynamic polarization curves showing the effect of NaCl concentration in commercially pure Mg [51]. Potential scan rate was 1 mV $s^{-1}$ (current density is presented as absolute value), and (b) Nyquist plot of a high purity Mg after 24 h of immersion at open circuit conditions in 0.1 M NaCl solution exhibiting an inductive-type behavior at low frequency values [54]. Reproduced with permission from NACE International, Houston, TX. All rights reserved. Reprinted with permission from Elsevier.

figure that the PDP method can provide information on e.g., the effect of chloride concentration on both the anodic and cathodic reactions. It is also clear that the anodic Tafel slop for Mg is very low, concomitant with Mg being non-polarizable (*i.e.,* difficult to increase the potential of the Mg electrode without reaching excessive anodic current densities). The PDP measurements also allow for the determination of the instantaneous corrosion rate ($i_{corr}$) at $E_{corr}$. Assuming activation controlled kinetics of both the anodic and cathodic half reactions, Tafel extrapolation from potentials far enough from the $E_{corr}$ should intersect at ($i_{corr}$, $E_{corr}$) [53]. Alternatively a computer can fit an idealized form of the curve to the experimental data to extract these values and the Tafel slopes.

Instantaneous corrosion rate can also be determined by potentiodynamic polarization measurements over a smaller range of potential around $E_{corr}$ using the linear polarization resistance (LPR) method [53]. The slope of a linear plot of current vs. potential when the current changes polarity (dE/dI), defined as the polarization resistance ($R_p$), is inversely proportional to corrosion rate, as described by the Stern - Geary equation with the proportionality constant, B [55]. A recent tabulation of B values has been conveniently presented by Bland et al. [51], which was benchmarked using gravimetric and chemical (inductively coupled plasma optical emission spectrometry (ICP-OES) methods. This recent presentation of information by Bland et al. [51] has significantly contributed to the understanding of the Tafel slopes associated with Mg and Mg-alloys, inclusive of tabulation of data from the pertinent works to date. Such work reveals that the typical proportionality constant, B, values for Mg are ~36 mV (in 0.6 M NaCl). The LPR method is relatively non-destructive because the external perturbation applied to the electrode is small compared, for example, to the large range of potentials applied during potentiodynamic polarization.

Even though the LPR method and Tafel fitting of potentiodynamic polarization data is generally reliable and a reproducible method for corrosion rate determination, their use for Mg is complicated by several factors. Accurate analysis by these methods requires that both half reactions be controlled by activation polarization, that is, by charge transfer across the electrode/electrolyte interface. Copious HE during both anodic and cathodic polarization curves creates ohmic potential drops that are difficult to compensate for [50], as exemplified in the distorted shapes at high current values in the anodic branch of the polarization curves shown in Fig. 4a. Corrosion films affect the exposed area, and reaction rates even near $E_{corr}$ can be coverage dependent [45]. For these reasons, instant corrosion rate determinations using PDP should be used with caution and their combination with other electrochemical and non-electrochemical techniques, *e.g.,* EIS and hydrogen collection, is usually recommended.

Finally, dissolution of Mg (alloys) under anodic polarization is accompanied by persistent HE that increases with the amount of anodic polarization [56]. This phenomenon, which will be described in detail below, contradicts standard electrochemical kinetics for activation-controlled reactions. As a result of these factors, polarization curves presented in a semi-logarithmic plot (depicting E *vs.* log i) often do not exhibit linear regions expected of activation controlled kinetics, and analysis by Tafel fitting or extrapolation is too simplistic to account for the several processes occurring upon the electrode [52]. The $i_{corr}$ values inferred from potentiodynamic polarization curves for pure Mg/Mg alloys may not reflect the actual rate of corrosion of the metal, since other parasitic chemical/electrochemical reactions may simultaneously occur at the Mg surface. Nonetheless, the polarization curves are useful for assessing approximate corrosion rates and the influence of various parameters such as alloying content. In fact, the most useful aspect of potentiodynamic polarization results collected for Mg alloys is not the determination of corrosion rate itself, but the relative changes in the branches that represent anodic and cathodic kinetics. Such changes are independent of the issues associated with correct corrosion rate determination, but critical for understanding alloying effects. Furthermore, it must be noted that potentiodynamic polarization is the only method by which the mechanistic effect (in an electrochemical sense) of alloying can be determined in a manner that provides discrimination between anodic and cathodic kinetics.

*2.1.1.2. Potentiostatic polarization.* This method is based on the same principles as potentiodynamic measurements, but only a single fixed potential is applied and the current is measured. Potentiostatic polarization measurements can be useful when specific processes are sought to be investigated. Some examples of the use of these type of measurements include electrodeposition of different species to form protective coatings on Mg surfaces [57,58] and the study of HE during anodic polarization [59,60].

*2.1.1.3. Galvanostatic and Galvanodynamic polarization.* In electrochemical reactions, the potential and current are mutually dependent; it is possible to control either one and measure the other. With the advent of potentiostats, most methods involve the application of a controlled potential and measurement of the current. The main reason for this is that conditions exist for which multiple potentials result in the same current, so current control does not provide a single valued function, whereas potential control does. As also well known, current control methods do not allow any passivity (should passivity occur) to be detected [61]. However, under some circumstances galvanostatic tests (in which a constant applied current is maintained) can be useful (as galvanostatic test allow charge control, and are the basis for coulostatic measurements). Also, potentiostats are not required, so that less sophisticated (and less expensive) equipment can be used for a galvanostatic polarization test.

Galvanostatic polarization measurements have been widely used for Mg based alloys, in the study of Mg dissolution mechanisms. More specifically, this method is of common practice when investigating the enhanced rates of HE during anodic polarization [34,50,56,60–63]. This phenomenon, commonly referred to as the NDE and briefly introduced previously, will be further developed in the following sections. Galvanostatic tests allow for easy comparison of the rate of HE with the applied current; including comparison of any simultaneous mass loss (via Faradays law).

In galvanodynamic polarization measurements the current is scanned or stepped analogously to potentiodynamic polarization tests. This approach has not been widely used in the study of Mg corrosion since galvanostatic measurements traditionally provided more accurate values of the HE rate (necessary to determine the real amount of Mg dissolved). However, recent experimental developments showed that galvanodynamic testing coupled with real-time gravimetric HE collection revealed comparable values to those determined by galvanostatic experiments, thus providing complete information of the HE rate over a range of applied current density values of interest [50].

*2.1.1.4. Electrochemical impedance spectroscopy (EIS).* The EIS method consists of measuring the response of an electrode to a small amplitude (typically 5–25 mV) sinusoidal potential perturbation at different frequencies. A complete presentation of the EIS technique is beyond the scope of this review, but fitting of the results to an equivalent circuit provides another means to determine $R_p$ as well as information about the capacitive and inductive responses of the interface [64]. As described for the Linear Polarization method, $R_p$ determined by EIS can be used to assess the corrosion rate using the Stern - Geary relationship if the Tafel slopes are known or can be approximated [55]. With the aim of overcoming the issues of accurate determination of Tafel slopes, King et al. [54] performed direct measurement of the corrosion current by hydrogen collection and mass loss, coupled with simultaneous EIS measurement. From that investigation “apparent” Stern-Geary coefficients were obtained that can be used to evaluate the corrosion current from EIS data.

This approach was extended by Bland et al. [51] for a number of Mg alloys, along with a review of the Stern-Geary coefficients from the literature. The rationalization of the inductive response of Mg when studied using EIS was elegantly studied recently in real time, whereby EIS was coupled with on-line spectroelectrochemistry [65]. That study unequivocally showed that the low frequency impedance limit is the parameter of interest with respect to determination of the “real” corrosion rate (which is definitively determined from on-line spectroelectrochemistry) – putting to rest decades of controversy regarding the impedance response of Mg.

At this point, it is necessary to further comment on the apparent inductive behavior (characterized by data in the second quadrant of a Nyquist plot), characteristic of Mg alloys, exhibited at low frequencies (see Fig. 4b). As pointed out by King et al. [54], even though many papers on Mg present EIS data with inductive response, the behavior is most often disregarded, and the point where the spectrum first crosses the real axis at intermediate frequencies, the charge transfer resistance, $R_t$, is used to determine corrosion rate with the Stern-Geary equation rather that the low frequency impedance limit. It is evident that $R_p \ll R_t$ (see Fig. 4b) and ignoring the low frequency portion of the spectrum leads to underestimation of the corrosion rate as has been proven by comparing to non-electrochemical methods such as mass loss [54], and has been one of the main sources of erroneous theories regarding Mg corrosion mechanisms [60]. Therefore, an accurate analysis of the EIS spectra, including the determination of $R_p$, requires the inclusion of an inductor in the equivalent circuit.

### 2.1.2. Localized electrochemical techniques

*2.1.2.1. Scanning vibrating electrode technique (SVET).* The SVET is an electrochemical method that detects and quantifies localized electrochemical activity on metallic substrates using a vibrating microprobe to measure the local voltage drop in solution. This voltage drop results from, and is a measurement of, local cells on the surface of a sample. By scanning the vibrating probe along the electrode surface at a fixed height (~100 μm), it is possible to produce maps of the spatially resolved net current associated with the local corrosion cells on a surface [66,67]. The SVET is an *in situ* technique that allows for mapping in a 1–5 $mm^2$ area either potential or current (by using previously calibrated data) in a small volume of solution. The SVET method has been used in the study of different topics in the field of Mg corrosion. For instance, Williams et al. [33] studied the localized corrosion behavior of freely corroding Mg in NaCl solution and identified intense local anodic activity at the front of an expanding corrosion ring and strong cathodic activity in the center of the ring. In another study, the propagation of localized corrosion was found to be under cathodic control, since the number and intensity of the local anodic regions increased in proportion to the area of the exposed local cathode [68]. Furthermore, the SVET has shown to be a powerful technique in the study of HE on anodically polarized Mg [34,61].

*2.1.2.2. Scanning electrochemical microscopy (SECM).* The SECM uses an ultra-microelectrode (UME) to scan the substrate surface at a fixed height (with a distance of 2–4 times that of the probe diameter), detecting the electrochemical activity on the electrode surface as a consequence of the electrochemical response that the probe experiences when in close proximity with the substrate surface. More precisely the SECM signal is based on measuring the diffusion-limited current of a redox-active couple (*e.g.,* $Fe^{2+}/Fe^{3+}$). With a spatial resolution in the micrometer scale or below, SECM has found application in corrosion studies. Similar to the SVET, SECM provides a map of the electrochemical activity of the surface [69]. However, while the SVET measures net currents flowing to distant cathodes (after proper conversion of the local voltage drop in solution), the SECM allows for the discrimination between the activity of different electroactive species by polarizing the UME at a potential of interest [69]. Indeed, the UME, which acts as the sensing probe, behaves as an independently-controlled working electrode and measures the current generated by the oxidation or reduction of the species of interest. Under diffusion control, this provides a measure of the flux of oxidized/reduced species in solution to the UME. By using a bipotentiostat, both the tip and the substrate can be polarized, allowing for (in the case of Mg) the amount of dissolved metal or the $H_2$ evolved away from the open circuit conditions to be explored. Full description of the SECM method and modes of operation for the study of Mg corrosion can be found elsewhere [69]. The SECM has shown to be a powerful technique in the study of Mg alloys in simulated biological fluids [70] and the localized corrosion of Mg alloys in NaCl solutions [71].

The SECM has been also used to study the phenomenon of anomalous HE (or NDE, see Section 3.2). Even though the hydrogen evolution reaction (HER) is not a diffusion-controlled reaction, $H_2$ oxidation mapping using the SECM provides qualitative results [72]. For instance, Tefashe et al. [73] investigated the local flux of HE on a corroding Mg alloy surface using the substrate-generation/tip-collection (SG/TC) mode of SECM and showed that, through careful control of the corroding media and immersion time, quantitative SECM approach curves could be obtained. Dauphin-Ducharme et al. [74] correlated local HE with micron scale resolution with the morphology and chemical composition of microstructural components on the surface of a sand-cast AM50 during corrosion using SECM and SEM. The role of Fe impurity concentration and the role of the corrosion film on the anomalous HE of pure Mg have also been investigated [72,75], as will be discussed in more detail below.

*2.1.2.3. Atomic emission spectroelectrochemistry (AESEC).* The AESEC method was first introduced by Ogle at al. [76] in 2000 and is based on the use of an ICP-OES placed downstream from an electrochemical flow cell. The method is a unique electrochemical analytical tool that permits a direct measurement of the partial elemental dissolution rates ''live'' during a corrosion process in the presence of a corrosive media – and most critically, in the absence of an applied polarization.

In fact, it is the AESEC method that arguably altered contemporary Mg corrosion research, providing two unique observations: (i) the "real" corrosion rate at open circuit, which was significantly higher than ever previously assumed or measured and (ii) an unequivocal determination of the valence of Mg [75]. The latter ended debate and allowed the field to progress towards studying the dissolution mechanism in an unbiased manner, which is a critical advance that allows mechanistic interpretations to be founded on a definitive platform of understanding regarding Mg valence. AESEC has been employed to analyze the anodic dissolution of metals including steel [77–79], Zn [80], and Mg [75,81]. An example of the use of AESEC is the work done by Thomas et al. [75] who recently utilized the technique for measurement of $Mg^{2+}(aq)$ dissolved during and following anodic polarization.

### 2.1.3. Non-electrochemical techniques

Even though electrochemical methods are of general use in the study of Mg corrosion, other methods are also of significant merit. This section will present two different non-electrochemical methods of common use in Mg corrosion research.

*2.1.3.1. Weight loss (mass loss) measurements.* The most common method for the study of metal corrosion, and considered by some to be the benchmark standard, is the weight loss method. In weight loss testing, the specimen mass and specimen geometry is measured before and after exposure to a corrosive environment for a period of time. The exposure conditions can include immersion in an aggressive solution or exposure to atmospheric conditions - such as real field environments or an accelerated atmospheric corrosion chamber. Prior to measuring the specimen mass after exposure, it is necessary to clean the sample to remove the corrosion products from the surface. This is a critical step as it can lead to inaccuracies including overestimation or underestimation of the corrosion rate as a consequence of an insufficient or excessive cleaning after immersion, respectively. In the case of Mg, it is recommended to use a dilute chromic acid solution that may contain silver and barium nitrate [82] (Note that a great care must be taken when working with the chromic acid solution as this electrolyte can be very dangerous). Weight loss measurements are limited by the resolution of the gravimetric device. For this reason, an accurate microbalance and multiple replicates to provide confidence in weight results result are required. Even though weight loss measurements are simple and well established, they only provide an average corrosion rate over the exposure period and this rate will often change with time. Nonetheless, weight loss tests can also provide an exposed surface from which assessment of corrosion morphology (*i.e.,* general, localized, etc.) can be ascertained.

*2.1.3.2. Hydrogen collection.* Since the primary cathodic reaction accompanying the dissolution of Mg and its alloys in aqueous electrolytes is water reduction that results in the evolution of hydrogen gas, the collection of hydrogen as an index to the rate of the cathodic reaction is logical. In the absence of an external perturbation, charge neutrality requires that the rate of the anodic reaction equals the rate of the cathodic reaction ($i_{anod} = |i_{cath}|$). Consequently, under open circuit conditions, it is possible to determine the instantaneous corrosion rate from the rate at which HE occurs on the electrode surface [50]. The HE collection method has been widely used for corrosion current density determination in the absence of an external polarization. Furthermore, it has also been used to study the HE exhibited by Mg alloys subjected to anodic or cathodic polarization.

Different experimental approaches have been used to perform HE collection measurements. The volumetric method is extremely simple and widely used. The corroding sample is covered with a funnel inserted into an inverted burette [83]. The hydrogen gas produced as the result of the corrosion reaction accumulates as bubbles that eventually detach from the surface and are collected in the top of the burette by displacing the solution contained in it. The volume of the $H_2$ evolved is then assessed by noting the level of the electrolyte inside the burette at various times during the experiment. Fig. 5a shows a schematic of the volumetric HE collection method. Even though it is a very simple method, there are issues associated with it. For example, some $H_2$ bubbles often remain attached to the walls of the funnel and the burette so they do not add to the gas volume at the top of the burette, leading an underestimation of the HE rate. Furthermore, as pointed out by Kirkland et al.

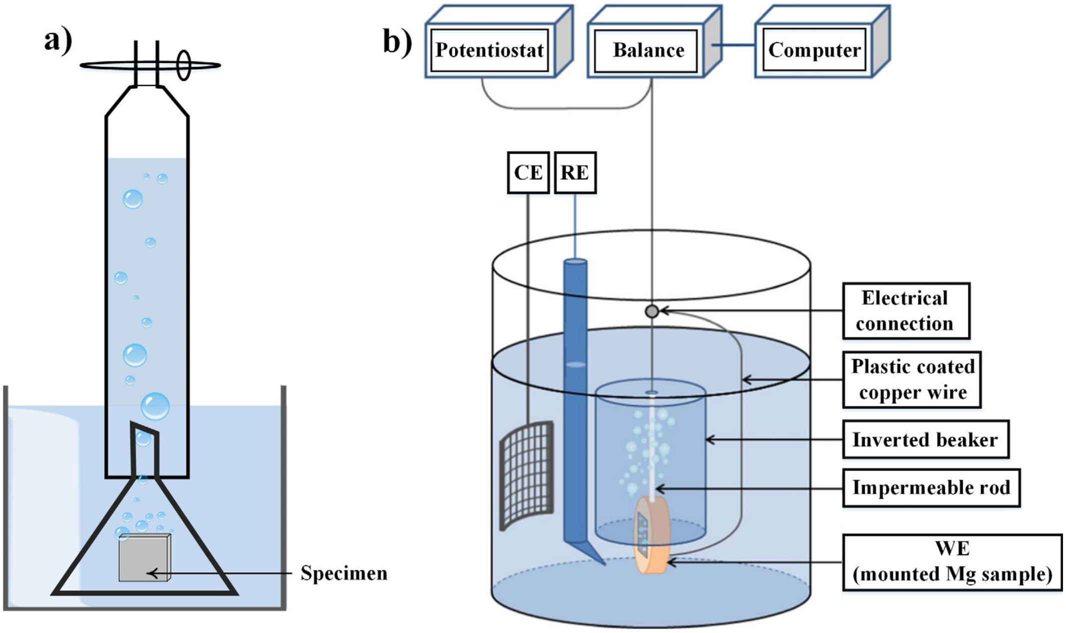

**Fig. 5.** Schematic of the experimental setups for hydrogen gas collection: (a) volumetric method, and (b) gravimetric method. Reproduced based on [50,83] with permission from The Electrochemical Society, licensed under CC-BY 4.0.

[43], the volumetric method is not suitable for the study of alloys with high corrosion resistance or short experimental times because insufficient $H_2$ is produced for reliable measurements of the amount of gas collected.

Recently, Curioni presented a gravimetric method for real-time HE collection based on the measurement of the buoyancy force resulting from the accumulation of hydrogen in a submerged container [49]. This gravimetric measurement was further developed by Fajardo et al. [50] and its suitability for corrosion rate determination of Mg was assessed. Fig. 5b shows a schematic of the gravimetric HE collection method in which the Mg specimen is hung below an inverted beaker that is completely immersed into the test solution and connected to a precision balance by a fiber. The $H_2$ gas produced on the electrode surface accumulates inside the inverted beaker, decreasing its apparent weight by a buoyant force. Even bubbles still attached to the corroding sample generate buoyancy that alters the apparent weight. The evolution of the weight with time can be recorded automatically by a computer connected to the balance.

The main advantage of the gravimetric method is that it exhibits much higher sensitivity in HE detection than the volumetric method, which allows for hydrogen volume collection during polarization measurements with high temporal resolution. The method was evaluated using galvanostatic polarization of a high purity Mg specimen and recording the time evolution of the weight. More interestingly, it was also shown that the complete HE response over a range of applied current densities could be assessed in a single experiment using galvanodynamic polarization [50].

*2.1.3.3. pH measurements.* It is also possible to assess the corrosion rate of dissolving Mg by chemical titration. In this method, the pH of the electrolyte is maintained to a fixed value throughout the time of experimentation by titrating with an appropriate solution. The rationale behind this method is that, as the corrosion reaction proceeds, the pH will increase as a result of the cathodic half-reaction, *i.e.*, HE, and the volume of titrant needed to maintain the pH constant allows for the amount of charge consumed to be determined [84].

Even if this method may be suitable for the study of Mg alloy dissolution under open circuit conditions, its use is not so straightforward when an anodic polarization is applied. In this particular scenario, the net current flowing through the electrochemical cell should also be recorded. Note that metal hydrolysis may also influence the solution pH, thus introducing a source of error in the measurement, although this is relatively small for Mg. Furthermore, real-time measurements would also be limited by the experimental time required to carry out the titration as the experiment progresses, limiting the cathodic reaction kinetics evaluation.

### *2.2. Corrosion testing in atmospheric conditions*

The atmospheric corrosion of metals is studied both through exposures in real atmospheric environments, *i.e.*, field exposures, and by exposing samples to a carefully controlled and simplified atmospheric environment in the laboratory. Field exposures are performed both outdoors (*e.g.*, for building material and automotive applications) and in indoor environments,

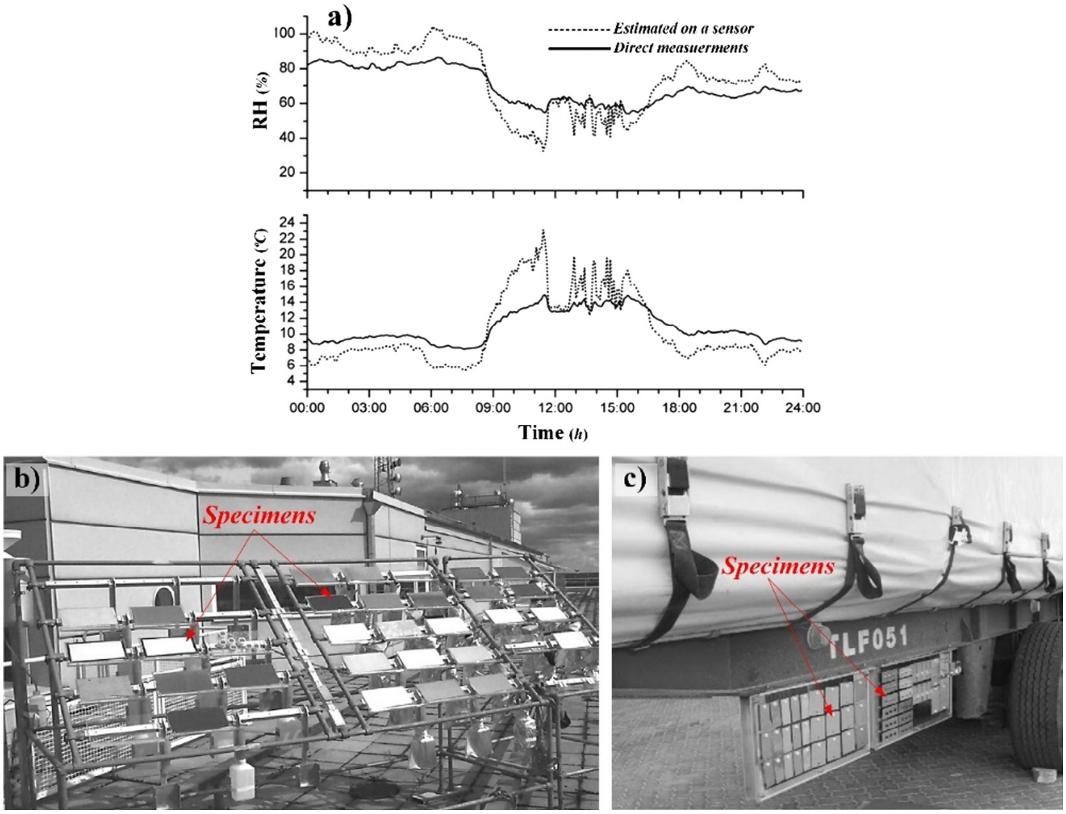

**Fig. 6.** The use of field exposures in atmospheric corrosion research. (a) RH (top) and temperature (bottom) variations during an atmospheric corrosion exposure in Australia, see [99] for details, (b) a typical "unsheltered" rack used for outdoor exposures of materials [101], and (c) a matrix of mounted specimens under a mobile truck [102]. Reproduced with permission from Elsevier.

**Table 1**
Corrosivity classification of outdoor atmospheric environments [85–87].

| Atmosphere | General characteristic | Rank of aggressiveness |
|---|---|---|
| Rural | Low levels of corrosive trace gases. Low levels of water soluble particulates. | 1 (Least corrosive) |
| Tropical rural | Low levels of industrial pollutants, *e.g.*, $SO_2$, but high levels of organic acids. High RH (>80%) | 2 |
| Urban industrial | Corrosive pollutant gases, *e.g.*, $SO_2$, and corrosive particulates from combustion | 3 |
| Marine, coastal | High level of sea salt particulates | 4 (Most corrosive) |

*e.g.*, electronics, equipment storage, and cultural artifacts. In this section, we shall briefly discuss some methods commonly used in Mg (alloys) atmospheric corrosion research.

### 2.2.1. Field exposures (outdoor environments)

Field exposures come with a high level of complexity. They are characterized by daily (*e.g.*, Fig. 6a)/seasonal variations in *e.g.*, temperature, rain, relative humidity (RH), and solar radiation as well as the presence of various contaminants, including trace gases, compounds dissolved in rain and particulates (refer Section 4.2). Because of differences in climate and in the occurrence of corrosive substances, the atmospheric corrosion behavior of metals varies a lot according to geographic location. The corrosivity of outdoor environments is often classified according to the occurrence of certain corrosive substances and to humidity. Thus, rural atmospheres are classified as mildly corrosive because of the low levels of corrosive substances while marine environments are considered more aggressive because of the high exposure to sea salt.

Heavily industrialized regions tend to be corrosive because of the presence of a range of reactive pollutants [85,86]. These classifications supposedly apply to all kinds of metals. However, it is cautioned that their usefulness is rather limited because of the very considerable differences in corrosion chemistry between metals (see *e.g.*, Table 1) [87,88]. Note that many environments such as volcanic and (frozen) desert are not mentioned in this table, see *e.g.*, [89]. During the last two decades, investigations of the corrosion of Mg (alloys) in outdoor environments are relatively scarce. However, some field exposures

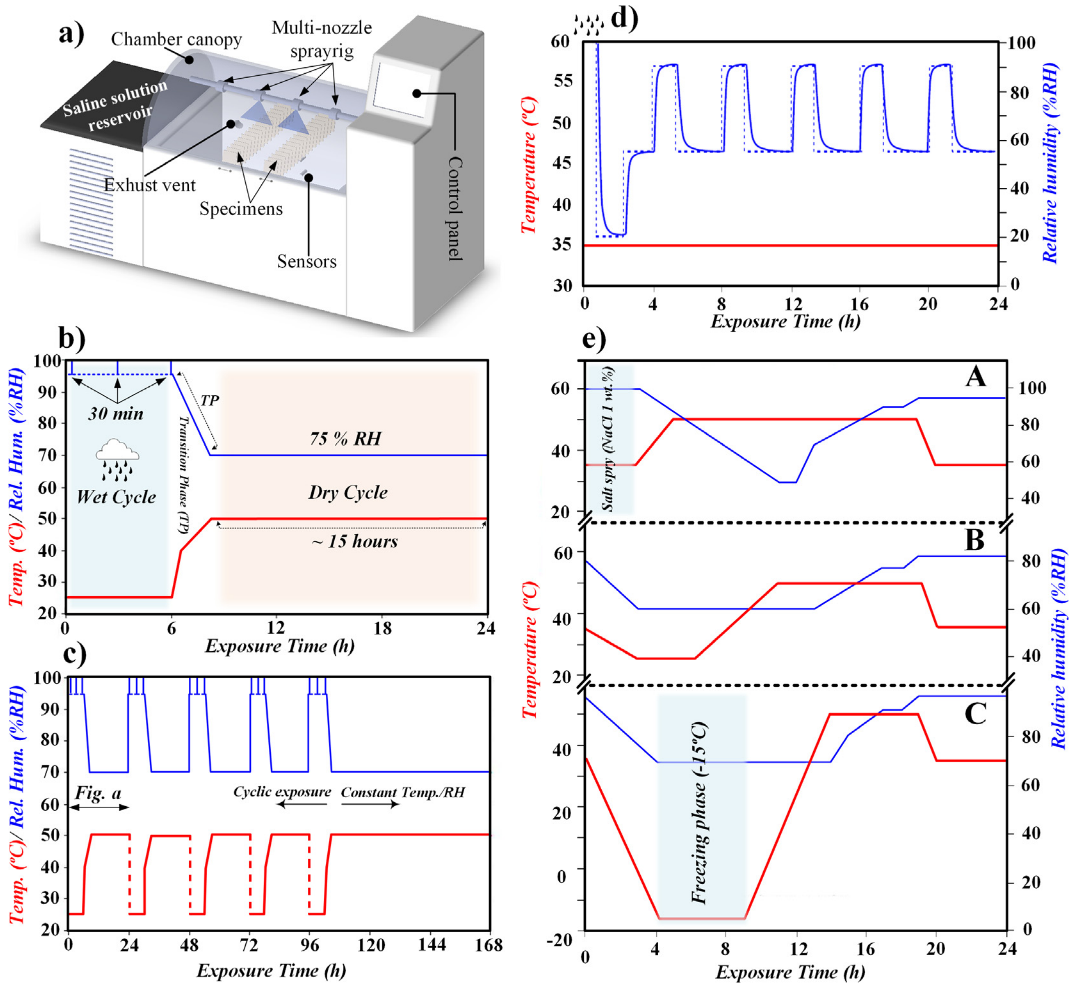

**Fig. 7.** CCT in atmospheric corrosion research. (a) Schematic diagram showing the components of a CCT chamber used in the automotive industry. Temperature and relative humidity (RH) cycles in the (b and c) Volvo ACT II (24- and 672 (week)-schemes), (d) Renault ECC1 (24 h-scheme shown), and (e) Volvo VDA 233-102 (Sequence of cycles A-B-A-C-A-B). Reproduced based on [107].

have been reported presenting data from polluted and unpolluted sites in China [90–93], Japan [94–96], France [97], and Sweden [97,98].

Field exposures are usually performed by mounting the specimens on racks in order to maintain the specimens in well-defined positions as well as isolated from each other, see a typical rack in Fig. 6b). Many details, including specimen dimensions and cleanness, need to be taken into account (*e.g.*, ISO 8565) [99]. Specimens could be mounted vertically or horizontally. Also, exposures can be performed both in sheltered and unsheltered conditions to monitor the effect of sheltering from surface rinsing and UV irradiation, *e.g.*, Sanders et al. [89]. Evaluating the atmospheric corrosion behavior of materials for specific applications may require exposures that are specially designed. For example, the atmospheric corrosion performance of components for *e.g.*, exterior parts of automobiles, should ideally be subjected to "mobile" exposures. In a project called "*Assessment of Corrosivity of Global Vehicle Environment*" the relative corrosivity of the vehicle environment towards several metallic materials, including AZ91D was measured [100]. The exposures were carried out by attaching coupons to trailers operating in six parts of the world (Fig. 6c and Section 4.3).

### 2.2.2. Accelerated corrosion testing (ACT)

Field testing in the automotive industry is costly and time consuming. An alternative is to accelerate real-world corrosion failures under "controlled" conditions (Fig. 7a). Continuous salt spray testing, *e.g.*, ASTM B117, initially designed to approximate the deposition of aerosols in marine environments, has been used for over seventy years to evaluate the corrosion performance of, *e.g.*, painted body panels. This procedure, although useful for comparative assessments of materials, leads to high corrosion rate values (*e.g.*, 0.1 mm/year ($5 \times 10^{-2}$ mg/cm$^2$/day) to 15 mm/year (7 mg/cm$^2$/day) for Mg alloys [103]) and corrosion mechanisms not observed in real service conditions, where other parameters need to be considered (*i.e.*, $CO_2$, $SO_2$, dry/wet periods, etc.). A more realistic approach is based on cyclic corrosion testing (CCT), typically involving alternating exposure to salt spray, dry and wet climate (Fig. 7b–d). The salt spray or salt fog is typically produced by air atomization of a sodium chloride solution with a concentration in the range between 0.5 and 5 wt.%, whereas temperature and RH variations during the dry and wet cycles are adjusted to reproduce the natural wetting and drying seen in atmospheric exposure.

Although, corrosion rates under cyclic testing mainly depend on the NaCl load, the dry/wet cycling has huge impact on the corrosion mechanism. For instance, the dry cycles may consolidate a layer of corrosion products, thus reducing the overall corrosion rate, but also create a concentrated aqueous solution promoting localized corrosion. Despite the large number of existing standards, there is a need for developing new and improved testing procedures [104]. Examples of recently introduced standards, providing more realistic results, are the ACT II [105] and VDA 233-102 procedures [106], the latter including a freezing phase at −15 °C to address the corrosion behavior of metallic component during winter in cold climes, see Fig. 7e. To conclude, it is cautioned that a testing procedure which is able to mimic the corrosion behavior of a material in a certain application often does a poor job at simulating the corrosion of other materials.

### *2.2.3. Laboratory exposures at constant RH*

In order to understand the sequence of events that causes a material to corrode in the atmosphere and to identify the critical factors that determine the rate of corrosion, it is necessary to perform systematic experiments in the laboratory, using simplified environments and a minimum of variable parameters. In combination with careful analysis of the chemistry and morphology of the corroding surface and its interplay with different environmental factors can yield mechanistic insights into the atmospheric corrosion of materials. In 1920s, Vernon, the father of atmospheric corrosion, performed the first laboratory atmospheric corrosion experiment [108] (see Section 4.2). During the last two decades, there have been significant experimental developments to perform well-controlled exposures [109–117]. The pioneering developments have resulted in significant advances in the understanding of how the atmospheric corrosion of different materials is influenced by individual atmospheric parameters, including temperature, RH and the presence of a variety of substances. For example, laboratory exposures have made it possible to understand the "synergetic" effect of the environmental factors on Mg corrosion (see Section 4.3).

Laboratory exposures are performed in a chamber where a specimen is exposed to a well-controlled flowing atmosphere consisting of filtered purified air and/or different atmospheric gases. The experimental set-up includes humidifier, flow controllers equipment for adding trace gases and equipment for measuring the gas composition [118]. Below, we present some examples of such experimental set-ups (Fig. 8), with a focus on systems that have been used in Mg corrosion research.

Fig. 8a and b shows an experimental set-up that has been developed over several years for investigating the corrosion behavior of materials, including Mg (alloys) [32,122]. In many cases, corrosive agents such as salt particles are added to the samples before exposure (Fig. 8a and b). The specimens are suspended using a nylon string. The gas flow, which is sequentially distributed through the eight parallel chambers, is typically 1000 mL/min, corresponding to an average flow velocity of about 1 mm/s. Only one sample is exposed in each chamber to avoid interaction between samples. The experiments are conducted at a constant RH that can regulated to any desired value to within ±0.3% by mixing measured amounts of dry air and air saturated with water vapor at the exposure temperature. To provide accurate control of RH, the humidifier and the exposure chambers are situated in the same thermostated water tank and care is taken to avoid condensation. $CO_2$ is added from a cylinder. A wide range of corrosive trace gases such as $SO_2$, $O_3$, $H_2S$, $Cl_2$, HCl, $O_3$, $NO_2$, and $HNO_2$ can be added at $10^{-9}$–$10^{-6}$ atm levels, using dry $N_2$ as a carrier. With minor modification, the set-up can be used in a wide range of temperatures from −20 to 60 °C. For exposures <0 °C, ethylene glycol is added to the water in the thermostated tank.

Fig. 8c is a schematic representation of a set-up used to examine the atmospheric corrosion behavior of Mg (alloys) in $CO_2$-free air. Corrosion often occurs in $CO_2$ depleted conditions, for instance in crevices or underneath organic coatings. The set-up (Fig. 8c) features a hermetically sealed desiccator. Humidity control is achieved by placing a beaker containing KOH(*aq*) solution in the desiccator. In addition to regulating RH to the desired value, the KOH solution functions as an efficient $CO_2$ absorbent, see [122,123] for more details.

Fig. 8d is a schematic of a chamber that provides a continuous and constant rate of NaCl deposition in the presence and absence of $CO_2$ and ultraviolet (UV) illumination [114]. A saturated NaCl solution is bubbled with air to generate an aerosol and the aerosol particles impinge on the samples. Hence, NaCl is continuously deposited, the samples being covered by a thin continuous NaCl(*aq*) layer after some time. Two inlets are used to maintain the RH around 100%. This exposure chamber has been used to study the atmospheric corrosion of metals like Cu, but not yet Mg (alloys).

Finally, the $SO_2$-induced atmospheric corrosion of several metals, including Mg (alloys) have been studied in laboratory using the two experimental set-ups shown in Fig. 8e and f. Time-resolved trace gas analysis can be used to determine the deposition rate of trace gases such as $SO_2$, $NO_x$, and $O_3$ at $10^{-9}$–$10^{-6}$ atm levels on metals. RH is regulated as described for the eight-chamber system (see above). Trace gases such as $SO_2$, $O_3$, and $NO_2$ are added to the dry air stream using permeation tubes. Ozone can be added using an ozone generator and a flow of dry purified air as a carrier [120].

### *2.2.4. Field exposures, corrosion testing and corrosion experiments in the lab*

While corrosion exposures in the field are in a certain sense the "gold standard" of atmospheric corrosion, revealing the "real" corrosion behavior in a certain environment, they also suffer from obvious limitations. From an "industrial" perspective, they are usually much to slow to be of practical use in the development of *e.g.,* corrosion protection. On the other hand, the multitude of pollutants and climatic factors, including many parameters that may be decisive for corrosion, and their variability, makes it is very difficult to understand the factors that are critical for corrosion.

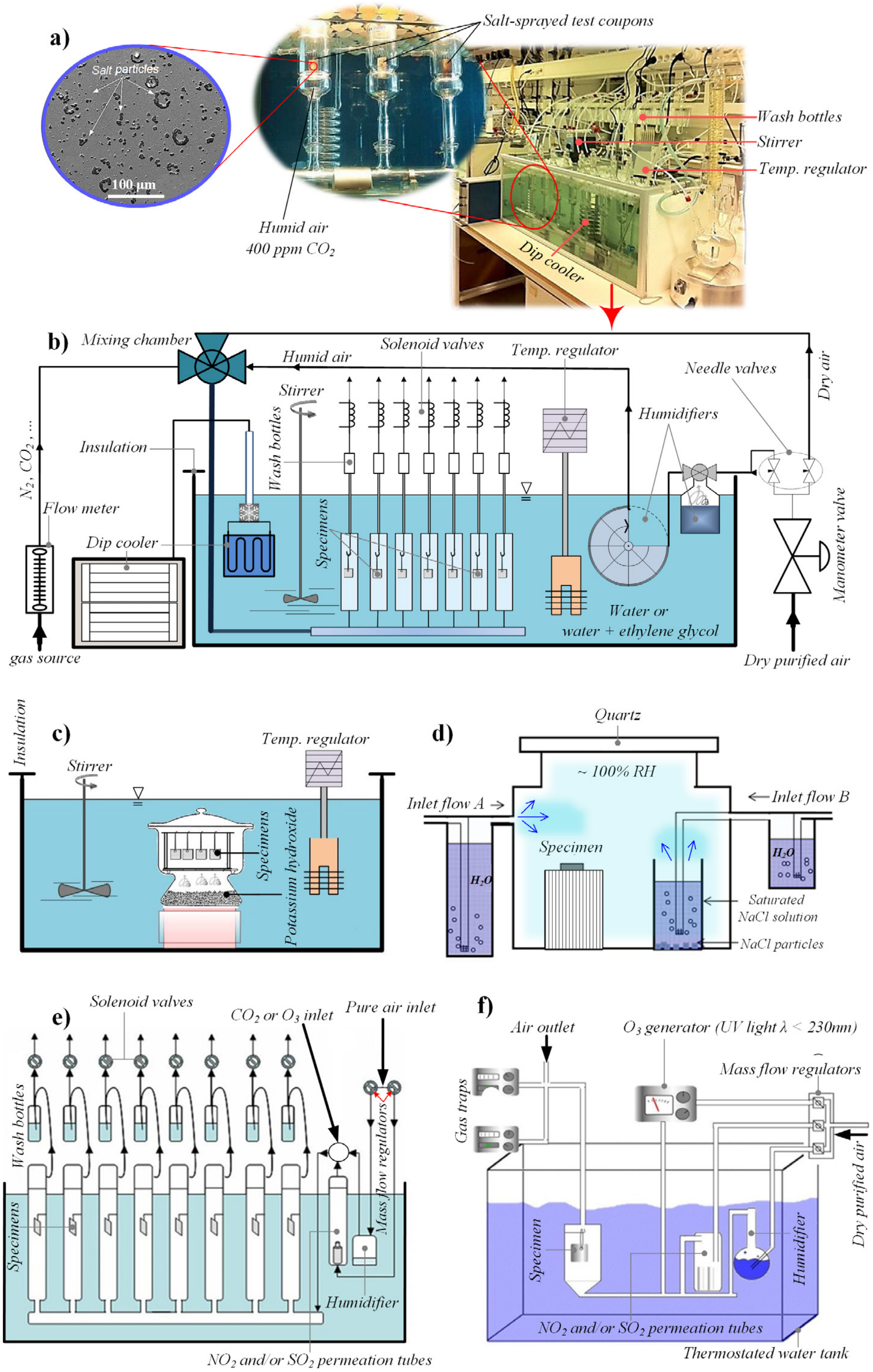

**Fig. 8.** Examples of well-controlled laboratory set-ups used to study atmospheric corrosion. (a and b) An exposure set-up in the presence of $CO_2$ and chloride-containing salt particles at different temperatures ((a) is adapted from [113,119]), (c) an exposure set-up in the absence of $CO_2$, (d) a schematic drawing of a chamber with constant deposition of NaCl [114], (e and f) Set-ups for $SO_2$-containing exposures [120,121]. Reproduced based on the cited studies. Figures copyright licensed under CC-BY 4.0.

The industry's need for relatively rapid and reliable ranking of materials and material systems is the driver behind the development of modern corrosion testing procedures, *e.g.*, involving a combination of salt spraying dry/wet cycling. However, they are only reliable and relevant to the extent that they can mimic the "real" corrosion processes that occur in the field. To understand the mechanism of corrosion, *i.e.,* the sequence of events and reactions that together make up the corrosion process for a material in a certain environment, well controlled, simplified laboratory exposures featuring a minimum of variables are absolutely necessary. On the other hand, in order to be technologically significant, the lab investigations must retain certain factors which are crucially important for atmospheric corrosion. Thus, in order to be relevant to a certain atmospheric corrosion situation, the laboratory exposure should be able to mimic both the corrosion morphology and the corrosion product composition found in the field. Also, the lab exposures should not accelerate corrosion overly much, compared to corrosion in the "field".

*2.2.4.1. Corrosion performance.* The rate of corrosion of several alloys exposed in laboratory can be close to those of field-based studies. When performing a laboratory exposure, it is important to employ the "right" set of parameters, *e.g.,* $CO_2$ concentration affects the pH of electrolyte, and thus, strongly affect the corrosion process (see Section 4.3.2). The ambient levels of $CO_2$ in the outdoor environment is $\sim$ 400 ppm [122]. Therefore, the exposure set-up (see Section 2.2.3, above) must maintain a constant $CO_2$ concentration of 400 ppm during the entire exposure period. Another crucial variable, affecting the NaCl-induced atmospheric corrosion performance (*i.e.,* the rate of corrosion) of metallic materials in general, and Mg alloys in particular, is the amount of NaCl added to the specimen's surface. For instance, deposition of 70 and 200 $\mu g/cm^2$ NaCl, equating to 550 and 1570 $\mu g/cm^2 y$ of chloride ions, respectively, correspond to the concentrations of chloride ions in urban areas and marine environments, but not in the immediate vicinity of the coastline [121,124,125].

*2.2.4.2. Composition of corrosion products.* Studies have shown that the composition of corrosion products of specimens exposed to laboratory exposures are in an excellent agreement with those reported to form in the corresponding outdoor environments for many metallic materials, including Mg (alloys) and Nickel (Ni) [126]. Thus, Mg sulfate hexahydrate, which is the dominant corrosion products in polluted or urban industrial environments [92], has been detected as the principal corrosion product in laboratory exposures with trace level of $SO_2$ [120]. Likewise, Mg hydroxy carbonates that are formed on Mg and its alloys during field exposures, in *e.g.,* rural and urban areas, are also shown to formed in substantial amounts under well-controlled laboratory exposures with ambient levels of $CO_2$ (see Section 4.3.2).

In summary, specimens exposed during well-controlled laboratory exposures (see above; Section 2.2.2) show substantial similarities to those exposed in the real-world environments. In fact, emergence of lab-based studies has made considerable advances in understanding the effect of individual atmospheric parameters on Mg corrosion, as summarized in Section 4.3.

## *2.3. Analytical tools for Mg corrosion research*

### *2.3.1. Statistics in Mg alloy corrosion*

When dealing with the properties of multiphase material such as Mg-Al alloys, it is highly beneficial to analyze the characteristics of the different phases mathematically. This can be seen even in the earliest Mg corrosion studies (*e.g.,* [127,128]), where micrographs were used to describe, *e.g.,* the size distribution of intermetallic particles.

Quantitative characterization can be performed over relatively large areas of interest (*e.g.,* 0.5–5 $mm^2$), providing an overall picture of the microstructure. This is especially applicable for the cast Mg alloys as they rarely exhibit a homogenous microstructure. An example is determining the volume fraction of β particles in Mg-Al alloys, wherein a single scanning electron microscopy (SEM) image is often not sufficient to decide whether the fraction of the phase is higher in one alloy than in another. This is also true for the size and distribution of other micro-constituents, for the area/volume fraction of casting pores and to some extent, for the size of grains in the alloys' microstructure. Quantitative/statistical assessments involve a few core tasks; (i) preparing the specimen free of any artifacts (careful sectioning, automated polishing and selective etching often produce the best results), (ii) acquiring several high quality SEM images with adequate magnification/contrast in an unbiased manner, and (iii) evaluating the micrographs using appropriate software (*e.g.,* Adobe Photoshop, ImageJ, and Image Pro-Plus) that can distinguish the phases' gray scales in the microstructural images (More information related to microstructural quantification, *e.g.,* ASTM standards, can be found in [129–132]). While the software mentioned can determine the area/volume fraction of the phases, more systematic steps can be taken to quantify the distribution of the phases. For example, the *quadrant method* and *nearest neighbor distance (NND) method* are well suited for a quantitative analysis of the distribution of phases.

The quadrant technique is particularly handy for quantifying the distribution of *e.g.,* casting pores, and intermetallic particles. It can explain the probability distribution of specific events occurring at specific intervals. Here, SEM micrographs are divided into square cells and the number of a specific feature in each quadrant is counted. An ordered/uniform distribution is expected to generate a large number of quadrants containing approximately the same number of the feature. In contrast, a clustered distribution would be expected to produce a combination of empty quadrants, quadrants with a small number of particles, and quadrants that are rich in particles. A random distribution would be expected to produce results somewhere in between these two extremes. The Poisson distribution and the negative binominal distribution are the probability functions used in the quadrant method (more details can be found in [133–136]).

The NND is a probability density function such that $P_{(r)}\,dr$ is the probability of finding the nearest neighbor of a particle with the same characteristics in the distance range $r$ to $(r + dr)$ [137]. First, the coordinates (X, Y) of events in the examined microstructural region are defined. The coordinates are $(X_1, Y_1), (X_2, Y_2), \ldots, (X_n, Y_n)$, where n is the total number of events.

The event-event distances are calculated in one, two, . . . , six directions. In each direction, the distance between the events is then calculated using the equations provided in [36,135,137,138].

Another statistical method that has been employed in analyzing the corrosion performance of Mg alloys is artificial neural networks (ANN). Development of Mg alloys with several alloying additions (ternary, quaternary and so on) and the prediction of their corrosion rate is challenging since it requires handling large data sets and ≥3 variables. The ANN is a recent approach, which is based on statistics, the key factors that affect a property (*e.g.*, corrosion rate, hardness, and yield strength) can be evaluated by using processing elements known as nodes or neurons. Satisfactory results on predicting the degradation rate of Mg alloys by using this approach have been reported in recent literature [139–143].

### *2.3.2. Electron backscatter diffraction (EBSD)*

EBSD is a well-established SEM-based method that provides information on *e.g.*, crystallographic orientation/texture, grain size, phase identification, and much more, with a typical spatial resolution down to ~100 nm [144], see *e.g.*, Fig. 9a.

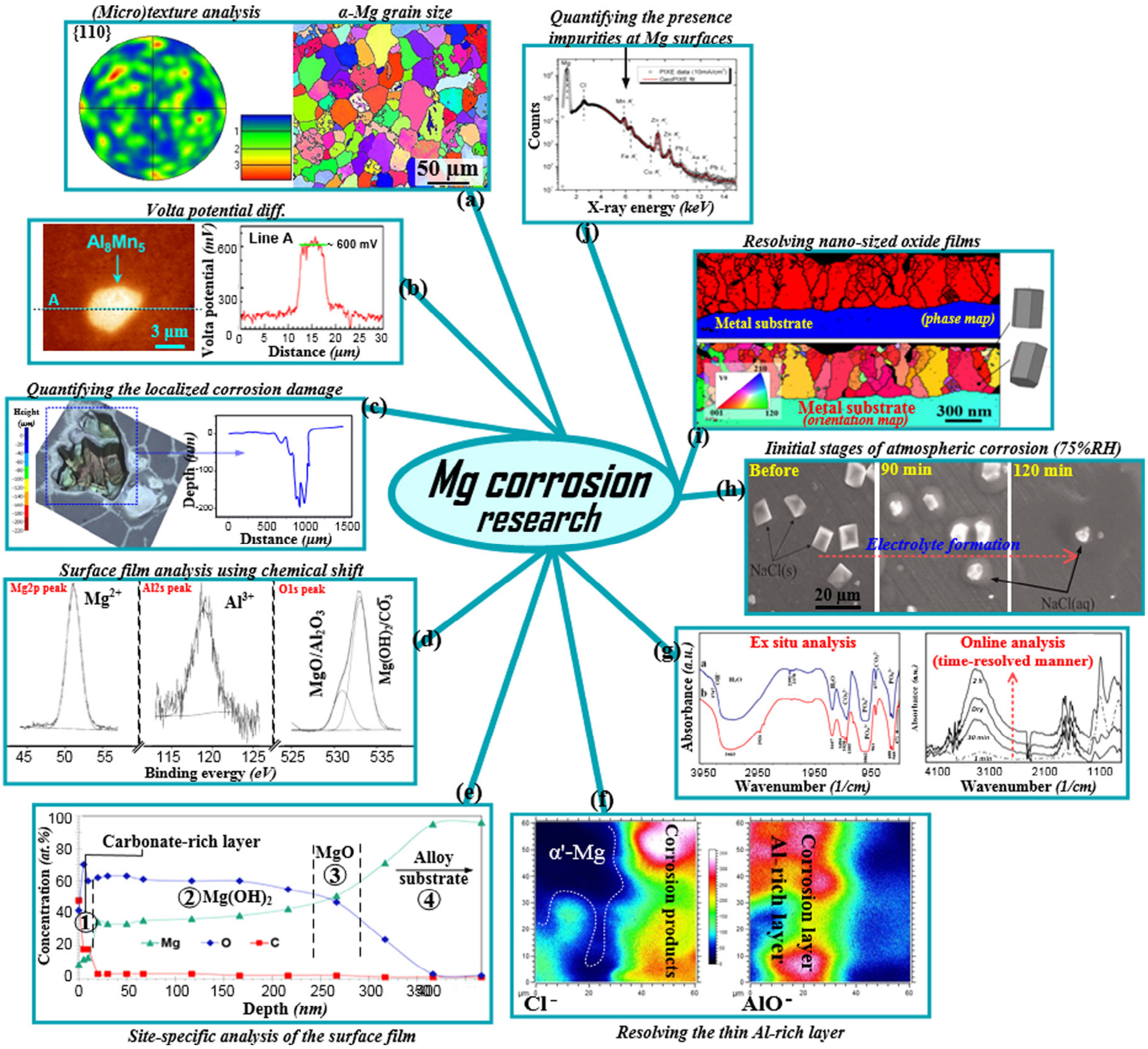

**Fig. 9.** Examples of the use of analytical tools in Mg corrosion research. (a) EBSD texture analysis and inverse pole figure (IPF) orientation map of AM50 [36], (b) a SKPFM image and corresponding Volta potential profile along line A on AZ61 [163], (c) 3D optical image of the corroded areas and surface profile of a corroded AZ91RC [164], (d) XPS spectra of AZ61 detecting different corrosion layers [165], (e) an AES depth profile (site-specific analysis on an area of $5 \times 5\ \mu m^2$) from α-Mg grains in AZ91D upon an atmospheric corrosion exposure [166], (f) a ToF-SIMS surface profile visualizing the Al-rich layer on corroded AM50 [167], (g) left: FTIR spectra from the surface of an exposed biodegradable Mg-Ca-Zn alloy [168], right: time-resolved IR spectra obtained from AZ91D after an atmospheric corrosion exposure [120], (h) *in situ* ESEM images, corresponding to "live" monitoring of the corrosion of Mg in a humid environment [123], (i) TKD phase (top) and IPF maps with schematic drawings of some crystals taken from a stainless steel exposed at 1100 °C [144], and (j) PIXE data representing the signals detected as a function of X-ray energy [169]. Reproduced based on the cited studies. Reprinted with permission from Elsevier and The Electrochemical Society.

Thus, EBSD can elucidate the relation between the microstructure and corrosion behavior of both cast and wrought Mg alloys and has resulted in significant advances in the field. The EBSD method has greatly contributed to understanding the behavior of processed and welded alloys, promoting applications in critical sectors such as aerospace and defense. The EBSD has been used to understand some crucial corrosion-related metallurgical aspects such as (dynamic and static) recovery and re-crystallization, crystallographic texture, and the anisotropy caused by the strong texture. Recent studies in this subject have demonstrated that the corrosion performance of Mg alloys can be improved by controlling texture [145–147]. An example is the work performed by Orlov et al. [145], who demonstrated that an integrated process of extrusion and equal-channel angular pressing, and noted that such an integrated process gives rise to an improvement in both corrosion resistance and strength of ZK60. The authors [145] suggested that the improvements in alloy properties were linked to grain refinement and the redistribution of zinc (Zn) and zirconium (Zr) solutes within the alloy microstructure. Another useful application of EBSD in Mg corrosion research is the investigation of the corrosion behavior of Mg alloy welds. One example is the recent study by Bland et al. [148], who studied the corrosion behavior of a heat treated alloy (AZ31 BH24) subjected to tungsten inert gas (TIG) welding. They report on the effects of grain growth and crystallographic orientation on corrosion of various isolated weld zones.

In regards to cast alloys (*e.g.,* AZ91, and AM50), EBSD has been used to determine the average size of α-Mg grains. It may be noted that EBSD is inherently more reliable/precise than metallographic techniques using image processing when analyzing the grain size in the matrix. Thus, a recent study [36] showed that the average size of α-Mg grains determined by EBSD was ~5 μm larger than that obtained using image processing of SEM images of the alloy. This is because image processing is done on the etched surface, which visualizes differences in Al content in each individual grain. This yields a smaller grain size because the inter-dendritic regions, corresponding to the α grain periphery which is low in Al, is not counted as part of the α-Mg grains. In contrast, EBSD imaging visualizes the α-Mg grains irrespective of Al gradients. We would like to add that a sample preparation procedure, which can result is data-rich EBSD maps, can be challenging, due to the soft and sensitive nature of Mg. An efficient method to prepare the surface for EBSD has been reported to be the use cold-stage argon (Ar)-ion-beam milling [149].

### *2.3.3. Scanning Kelvin probe (SKP) and SKP-force microscopy (SKPFM)*

In the late 1890s, a British physicist, Sir William Thompson, also known as Lord Kelvin, proposed a method to determine the "contact electricity" between two metal electrodes [150]. Nearly a century later, Stratmann et al. [151,152] developed SKP to the study of atmospheric corrosion of metals. SKP, with a lateral resolution of 10-100 s μm, was later evolved to SKP-force microscopy (SKPFM) to improve the lateral resolution (nm range). Moreover, SKPFM comes with the option to couple the measurements to surface topography maps. However, SKPFM is more susceptible to artifacts (*e.g.,* preparation induced-residual stresses) and more sensitive to experimental environment (*e.g.,* temperature and humidity) than SKP, making the interpretation of the acquired data difficult [153]. The methods generates Volta potential (also termed as the Volta potential difference, Δψ) maps of the surface, see *e.g.,* Fig. 9b. The Volta potential is the electrostatic potential difference between two constituents that are in contact and in thermodynamic equilibrium with each other [153,154].

These two techniques, *i.e.,* SKP and SKPFM, have shown great potential in corrosion studies. As mentioned above (Fig. 3 in Section 1.4), cast Mg alloys are multi-phase. Also, the micro-constituent particles are nobler than the α-Mg matrix, the difference being reflected in a Volta potential difference. When exposed to an electrolyte, the differences in nobility between second phase particles and α-Mg result in the formation of micro-galvanic cells (see Section 3). SKPFM has been used to investigate localized corrosion of Al alloys [155,156], and steels [157,158]. The method has also been widely utilized in Mg corrosion research [120,154,159–161]. Jönsson et al. [159] used SKPFM to determine the Volta potential difference between the α-Mg grains and the surrounding inter-dendritic regions and with intermetallic particles in alloy AZ91. Investigating the influence of neodymium (Nd) on the atmospheric corrosion performance of AZ91, Arrabal et al. [161] employed SKFPM to determine the Volta potentials of $Al_8Mn_4Nd$, α-$Al_{11}Nd_3$, $Al_3Nd$ and $Al_2Nd$ relative to the α-Mg matrix. They noted that the Nd-containing particles exhibited lower Volta potentials than Al-Mn, suggesting that Nd alloying would result in less intense micro-galvanic corrosion (see Section 4.4). In a comprehensive study, Hurley et al. [154] evaluated the micro-galvanic coupling of numerous intermetallic particles in the microstructure of several Mg alloys using AFM imaging in conjunction with SKPFM as well as SEM/EDX analyses. The study highlights the sensitivity of the SKPFM measurements to the composition of the intermetallic particles and the surrounding matrix and demonstrates the usefulness of SKPFM as a screening method to evaluate candidate Mg alloys with respect to micro-galvanic corrosion behavior. SKP has also been employed in Mg corrosion study, but to a much lesser extent than SKPFM, see [159,162]. An example is the study performed by Williams and Grace [162], who successfully analyzed the corrosion of organic-coated CP Mg specimens under high RH conditions.

### *2.3.4. X-ray diffraction (XRD)*

The use of XRD in Mg corrosion research dates back to 1933, when Whitby tried to examine the composition of the corrosion products formed on Mg during an exposure to an outdoor environment [170]. Since then, XRD has been, continuously and widely, employed in Mg corrosion research [92–97,110,119,122]. XRD is based on the inelastic scattering of monochromatic X-rays by atoms. Because the wavelength (λ) is of the same order as the nearest neighbor atomic distances in a condensed phase (about 1 Å), scattering by a solid leads to interference phenomena. Thus, the radiation scattered from a single crystal results in a three-dimensional (3D) array of diffracted beams [171]. In addition, by measuring the intensity and angle of the scattered radiation we can determine the arrangement of atoms within the crystal (= the crystal structure). In corrosion we are mostly concerned with metals and corrosion products that tend to consist of a large number of more or less randomly oriented crystallites. In that case, we are dealing with X-ray powder diffraction (properly XRPD, XRD is used here for convenience) and the scattered radiation instead forms cones in space. An X-ray powder diffractometer measures the scattered intensity and the angle θ between the primary X-ray beam and the scattered radiation. The resulting diffraction peaks fulfil Bragg's law: $n\lambda = 2d\sin\theta$ (where d is the distance between atom planes in a crystal) [171].

Because every crystalline compound gives rise to a unique array of d values and intensities, XRD is very powerful for identifying crystalline compounds in, *e.g.,* corrosion products. XRD easily distinguishes between corrosion products having similar or identical chemical composition. XRD has also the utility for analyzing corrosion product mixtures. A practical lower limit for identifying a compound in a powder mixture is about 5% and up to six phases can be routinely identified in a mixture. Peak intensities are used to estimate the relative amount of phases. The information depth in an X-ray powder diffraction experiment critically depends on the angle of incidence of the primary beam and on absorption by the sample. The latter scales as $z^2$, meaning that the information depth is relatively large for typical corrosion products on Mg [171].

XRD analysis can be done with many different measurement geometries. In corrosion studies, the two useful ones are the Bragg-Brentano (BB-XRD) and grazing incidence (GI-XRD) geometries. The latter is much more surface-sensitive due to the small angle of incidence (0.5–5°), on the order of 100 nm, as opposed to the BB-XRD, which offers the information depth of ∼>10 μm [171,172].

Due to experiments being carried out under ambient conditions and because radiation damage is not an issue, XRD is very useful for analyzing corrosion products that decompose under more severe conditions, *e.g.,* under high energy radiation or under (Ultra-) high vacuum conditions. For example, the identification of layered double hydroxides (see Section 4.3.7) on Mg-Al alloys, which has been recently done by XRD [95], could not have been achieved by *e.g.,* SEM/EBSD or XPS, because of decomposition. This is also the case for the Mg hydroxy carbonates (Section 4.3.2). XRD inherently has low lateral resolution (typically, the analyzed area is several mm in size) [171,172]. Hence, XRD is often combined with other "global" measurements such as gravimetry and chemical analysis to provide a very detailed description of the overall corrosion product composition. It should be added that the main advantages of XRD are accurate and rapid measurements, minimal sample preparation, and relatively straightforward data interpretation. Limitations include the inability to identify amorphous constituents, very poor lateral resolution and a high detection limit.

### *2.3.5. Interference microscope (IM) (profilometry)*

IM employs light interference phenomena to generate superimposed images of a non-flat object, making possible the visualization of (localized) corrosion damage in metallic materials [173]. Thus, the IM is highly relevant to Mg corrosion research; with modern IMs delivering a measurement range of several millimeters (or higher) and a spatial resolution down to 1 nm.

The data from an IM can be converted to 3D surface topography images, and then, to statistical information on the damage depth and damage density, and thus, the method offers qualitative/quantitative information regarding the population and average depth of localized corrosion damage with various sizes. In addition, IM can be used, to some extent, to monitor the progress of corrosion front, deep in the alloy substrate, see [161,174]. The IM analysis is conducted on corroded surfaces after having removed the corrosion product *via* leaching and pickling procedures, if the material is exposed under atmospheric conditions. A difficulty associated with the technique is visualization of the lateral growth of the localized corrosion damage deep in the bulk (*i.e.,* it is almost impossible to determine whether the damages are connected or not using the profilometry). It may be noted that similar technologies such as confocal microscopy and focus variation microscopy provide similar information. An example of 3D topography is given in Fig. 9c.

### *2.3.6. Cross sectional analysis*

Ideally, plan-view SEM images and/or the data acquired from the IM method should be complemented by cross-sectional analysis, especially to obtain information on lower strata in the corrosion product, on the corrosion product/metal interface and concerning localized corrosion. Cross sections can be produced mechanically (comprising cutting, grinding and polishing) [175] or be means of focused ($Ga^+$) ion beam (FIB) milling [175] or broad ($Ar^+$) ion beam (BIB) milling [149,175].

FIB milling tools, such as dual beam FIB/SEM [176], are utilized in microstructural investigations, offering a combination of high-resolution imaging and flexible nano/micro-machining capabilities that provide site-specific cross sections in a region of interest (in the range 5–200 μm width and 20–100 μm depth). It should be added here that newer instruments, *e.g.,* the plasma focused ($Xe^+$) ion beam (PFIB) microscope, which incorporates plasma ion source technology, have the capability to produce site-specific cross-sectioning > 20 times faster than conventional FIB microscopes. The PFIB is also able to mill much larger area (∼0.5 μm) with a better precision and high-resolution imaging at low beam currents, compared to present dual beam FIB/SEM microscopes, see [176].

During the last decade, FIB technology has contributed significantly to the understanding of Mg alloy corrosion. Research groups at Macmaster University (Canada), and Oak Ridge National Laboratory (USA) have pioneered the use of FIB, in combination with high resolution microscopy, to study surface films on *e.g.,* Mg alloys [177–185]. Fig. 10, which will be treated in detail in following sections, shows a few examples, where FIB has been used to produce cross sections through oxide scales/corrosion products and the metal substrate. It may be noted that FIB-prepared cross sections feature a much lower amount of artifacts than mechanically prepared cross sections. Furthermore, the cross sections made by, *e.g.,* lift-out procedure, in FIB

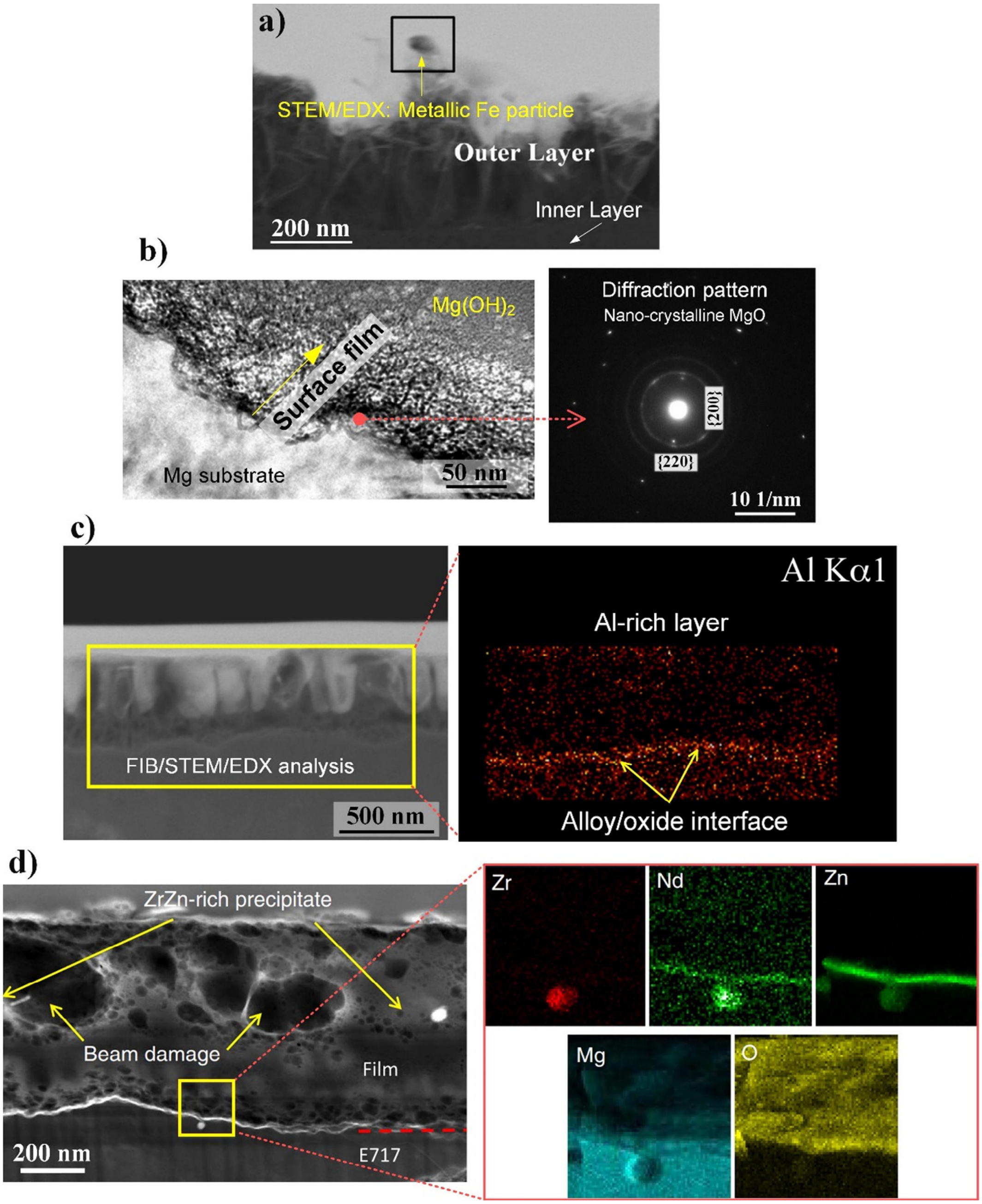

**Fig. 10.** FIB/(S)TEM analysis of the surface films formed on Mg and Mg alloys. (a) FIB/STEM analysis showing a strong evidence for the presence of Fe-rich particle in the corrosion layer formed on Mg after applying potentiostatic anodic polarization at −1.0 $V_{SCE}$ for 30 min [177], (b) a TEM micrograph and a diffraction pattern detecting nanocrystalline MgO at the interface region, after exposure to pure water for 48 h [178], (c) the formation of Al-rich layer at the interface region, after exposure to NaCl solution for 96 h [179], and (d) a FIB/STEM/EDX analysis showing a Zn-rich layer at the interface region as well as nanosized precipitates in the underlying alloy and near the interface region on E717 alloy, after immersion in water for 24 h [180]. Reproduced with permission from Elsevier and The Electrochemical Society (licensed under CC-BY 4.0).

are smooth and damage-free thin foils, making it possible to examine the chemistry/composition of the corrosion products at very high resolution. It is worth noting that it is currently possible to produce high quality lamellae (thickness of 50–100 nm) using a fast lift-out procedure in ~2 h, more information can be found by reaching authors of [144].

The BIB produces wide (~1.5 mm in width and several hundred microns deep), and accurate cross sections through the corrosion products and metal substrate with a minimal amount of artifacts as compared to mechanical grinding/polishing [144,176]. Considering the large surface area of the BIB-prepared cross sections, the method can in principle replace mechanical cross sectioning, being very well suited to study localized corrosion on heavily corroded samples or when statistic treatment of the data is crucial. An example of BIB-prepared cross sections and the corresponding sample preparation procedure for a corroded Mg alloy can be found in [149].

### 2.3.7. Transmission electron microscope (TEM)

TEM is used to characterize the microstructure and chemistry of materials at the nanoscale. In TEM, a fast-moving electron, with a wavelength of much less than 1 Å (where 1 Å = $10^{-10}$ m), is transmitted through a thin sample [186]. TEM has far better resolution than conventional SEM imaging and is extremely useful for determining the crystal structure, crystallographic orientation, and chemical composition of microstructural features and corrosion layers. During the last decade, researchers have taken advantage of several different TEM operational modes in studying the microstructure and corrosion morphology of Mg alloys [25–27,177–185], including TEM/EDX [177], scanning TEM (STEM) [178], high resolution TEM (HRTEM) [187,188], energy filtered TEM (EFTEM) (has not been used in Mg corrosion research), convergent-beam electron diffraction (CBED) [178], and, most recently, vibrational EELS [189]. TEM analysis of FIB-prepared thin foils allows researchers to investigate the surface film locally and with a minimum amount of artifacts. Due to its capabilities and increased availability, the use of TEM in Mg corrosion studies has grown rapidly since 1992 when Warner et al. [190] used a TEM, for the first time, to view the oxide/hydroxide films formed on an Mg (alloy) substrate. TEM(STEM)/EDX results have provided much useful information in Mg corrosion research such as: (i) the surface film formed on Mg exposed to water is composed of an inner compact MgO layer and a top $Mg(OH)_2$ layer (see Fig. 10a and b and Section 3.1), (ii) the MgO layer formed upon exposure of Mg to water is nano-crystalline (see Fig. 10b), (iii) noble impurity elements (*e.g.*, Fe) can be entrapped in the $Mg(OH)_2$ layer (see Fig. 10a and Section 3.2), and (iv) in the case of Mg-Al alloys, an Al-rich layer forms at the oxide/alloy substrate. Note that while surface sensitive methods (see Section 2.3.9–2.3.11) can provide some of the mentioned information (*e.g.*, the thickness and chemical composition of corrosion layers as well enrichments of alloying elements like Al and Zn at the metal/oxide interface), the presence of noble impurity elements in the surface film and the nano-crystalline nature of the MgO layer are aspects of Mg corrosion that can only be studied using FIB/(S)TEM/EDX.

It is cautioned that TEM analysis (*e.g.*, STEM/EDX, and CBED) of corroded Mg samples can cause significant "beam damage", see (Fig. 10d) [174], including "dehydration" of corrosion films, complicating the interpretation of results. To avoid beam damage cooling the sample to $N_2(l)$ temperature during analysis in the TEM (using cooling stage) is recommended.

### 2.3.8. Three-dimensional (3D)-imaging/EDX/EBSD

The interplay between corrosion and the Mg alloy microstructure often produces a complex corrosion microstructure, the surface of the remaining metal being strongly convoluted, sometimes featuring corrosion pits that penetrate deep into the substrate. To investigate and characterize this type of corrosion attack, it is highly desirable to complement "conventional" 2D techniques by 3D methods. Advanced SEM/FIB microscopes (Dual-beam systems) equipped with EDX and EBSD detectors have been utilized to perform 3D microstructural studies on the corrosion of, *e.g.*, Al alloys [191], steels [192]. However, very few papers deal with Mg alloys. Krebs et al. [193] used a combination 3D imaging and correlative imaging to study the corrosion of alloy AZ31 in salt water, providing information on the relation between the distribution of Al-Mn particles and the development of the corrosion front. Recently, Shahabi-Navid et al. [194] elegantly used a FIB dual workstation to perform 3D imaging of AM50 and AZ91D that had suffered localized corrosion in the atmosphere. The investigation revealed very deep and meandering corrosion pits that tended to be interconnected deep within the bulk. To summarize, the systematic use of 3D imaging to investigate the complex relation between alloy microstructure and corrosion is still in its infancy. However, we are convinced that 3D methods have great potential in corrosion research, especially for Mg alloys.

### 2.3.9. X-ray photoelectron spectroscopy (XPS)

The basis of the XPS method is the ejection of photoelectrons from a solid caused by absorption of soft X-rays [195]. It is a high-vacuum technique and the information is dominated by the topmost atomic layers. The energy spectrum of the emitted electrons is used to extract detailed information on both the elemental and chemical composition of the surface [195,196]. Thus, the chemical shifts of the characteristic electron energies in XPS enables determining whether, *e.g.*, Mg is metallic or oxidized, and indeed, to conclude what type of compound Mg has formed (see *e.g.*, Fig. 9d) [167,197]. Furthermore, the composition/thickness of the corrosion products/layers can be studied using depth profiling by Ar ion etching. However, it should be noted that the combination of ion sputtering, high energy radiation and high vacuum sometimes cause decomposition of the very compounds you intended to analyze. The XPS is much used to investigate, *e.g.*, oxide layers on Mg and its alloys. Thus, in the early 1990s, Splinter et al. [24] used XPS to study the chemical composition and the thickness of the oxide film formed on pure Mg in water. In relation to corrosion, the inherently poor lateral resolution (on the order of 100 μm) is a main drawback of XPS. Hence, the method is not very well suited for investigating localized corrosion or multi-phase alloys such as Mg alloys. Still, Feliu et al. [198] used XPS to correlate the chemistry of the surface film on Mg-Al alloys to alloy composition. Indeed, Ballerini et al. [199] employed XPS to examine the films formed on alloy AZ91 in a salt spray corrosion test, reporting that the composition of the surface film depended on the alloy microstructure. Other examples of the use of XPS in Mg corrosion research can be found in [167,200–206].

### 2.3.10. Auger electron spectroscopy (AES)

Like XPS, AES provides both elemental and chemical information from thin surface layers on metals. However, AES is inherently more useful than XPS in corrosion work because of the high lateral resolution. While both AES and XPS are electron spectroscopy methods, AES uses electrons as the exciting radiation instead of X-rays. Moreover, while the photoelectrons emitted are core electrons in XPS, Auger electrons are ejected as a result of de-exitation of the ionized atom to its ground state [196]. With a lateral resolution in the range 10–100 nm, AES is very suitable for high resolution surface chemistry analysis which is often required in corrosion. Still, AES exhibits a depth resolution (a few nanometers) and a sensitivity (0.1 at.%) similar to XPS [197]. Similar to XPS, AES is often combined with ion sputtering to provide depth profiles. AES has been widely employed for investigating the composition of surface films on Mg [203–206] and Al alloys [207–209]. Splinter et al. [24] were the first to use AES for studying the surface films formed on Mg. Zheng et al. [210] employed AES to characterize the surface of the biodegradable Mg alloy ZK60 modified by Fe ion implantation. Recently, the composition/thickness of the surface films formed on alloy AZ91D (see Fig. 9e) was studied using a high resolution AES (HR-AES) instrument [166]. The relation between surface film composition and alloy microstructure was investigated in a site specific manner using nano-indentation prior to corrosion.

### *2.3.11. Secondary ion mass spectrometry (SIMS)*

SIMS features a unique combination of extremely high sensitivity for all elements from hydrogen to uranium, high lateral resolution imaging ($\sim$40 nm), and a very low background, which permits a high dynamic range (>5 decades) [211]. One important drawback is that the information on composition is not quantitative. Time-of-flight SIMS (TOF-SIMS) is a high vacuum technique which focuses a pulsed beam of ions (often Cs or Ga) onto a specimen surface, thus creating secondary ions in a sputtering process. The ions generated from the sample surface are then accelerated into a "flight tube" and their mass is calculated by measuring the time to reach the detector (= time-of-flight) [212]. The analysis of a single compound in SIMS generates an assortment of atomic and molecular ions which is characteristic of that compound. Hence SIMS inherently can provide chemical information from the surface [167,213–216]. The analyzed surface is abraded during SIMS analysis and by increasing the ion current the technique can provide depth profiles. Despite its several attractive capabilities, ToF-SIMS has been little used in Mg corrosion. Seyeux et al. [216] employed ToF-SIMS to carry out depth profiling of the surface film formed on pure Mg, $Al_3Mg_2$ and $Mg_{17}Al_{12}$ in water. They claimed that they detected Mg-hydride on the corroded surfaces by ToF-SIMS. Unocic et al. [180] conducted a SIMS hydrogen depth profile on pure Mg exposed in $^{18}O$ water and $D_2O$ and reported the presence of H at the surfaces of all their specimens. Recently, ToF-SIMS was used to examine enrichments of Cl and Al in corrosion product films formed on alloy AM50 exposed to atmospheric corrosion in the presence of NaCl (see Fig. 9f) [167].

### *2.3.12. Fourier Transform InfraRed (FTIR) spectroscopy*

In IR spectroscopy, infrared radiation is passed through a sample and the absorption spectrum is recorded. The interaction with a vibrating molecule or solid causes certain wavelengths of the radiation to be absorbed. For absorption to happen, the vibration must involve a change in dipole moment. In corrosion, FTIR spectroscopy is often used in specular reflectance mode or in diffuse reflectance mode. FTIR is very surface sensitive, being able to detect much less than a monolayer of a compound on a surface. Importantly, the measurements are done under ambient conditions, meaning that it is ideal for, e.g. *in situ* atmospheric corrosion experiments [217,218]. IR spectra can be recorded from surfaces with a lateral resolution which depends on the wavelength, being on the order of 10 μm (FTIR microscopy) [217]. With Mg corrosion, FTIR it is a valuable complementary technique that allows detection of small amounts of corrosion products that are liable to decompose when subjected to vacuum and exposed to e.g. an electron beam. It may be noted that FTIR is especially useful for detecting brucite ($Mg(OH)_2$), because of the absence of hydrogen bonding in that compound. Thus, the OH stretching vibrations in brucite generate a very sharp peak at high wavelength (3600 $cm^{-1}$) which is ideal for identification. Also, the conversion of brucite to other compounds, *e.g.*, Mg hydroxy carbonates results in the disappearance of that peak because the hydroxide ions in these compounds are hydrogen bonded [120]. Examples of the use of FTIR in Mg and Al corrosion research can be found in [119,120,203,219] (see the right hand plot in Fig. 9g).

FTI reflection absorption spectroscopy (FT-IRAS), is a modification of FTIR, which enables *in situ* monitoring of the corrosion product formation during corrosion. In an FT-IRAS microscope, the spectrometer is connected to an exposure cell, providing a stable gaseous environment where corrosion can proceed. The use of FT-IRAS in studying the atmospheric corrosion of Mg and its alloys is limited [120]. An example of a time-resolved FT-IRAS spectra is shown in Fig. 9g).

### *2.3.13. Raman spectroscopy*

Raman spectroscopy is a spectroscopic technique that can fingerprint molecules through the sensing of vibrational modes of molecular bonds [220]. As such, Raman spectroscopy is an appropriate technique to study metal surfaces, and in particular coating layers and corrosion products. As an example, this technique has been used in the field of Mg alloy corrosion to characterize the chemical composition of different coating systems such as Zn based conversion coatings on AM60 Mg alloy [221], calcium phosphate/chitosan composite coatings on micro-arc oxidized AZ91D Mg alloy [222], and cerium conversion coatings on Mg [223].

An important advantage of Raman spectroscopy is that it is a non-destructive technique that allows for *in situ* identification of corrosion products. An example is the work of Samaniego et al. [224] who used *in situ* Raman spectroscopy to analyze the chemical composition of the corrosion products formed on pure Mg during potentiodynamic polarization. This investigation, as will be discussed below, attempted to determine the existence of unipositive Mg and its influence on the mechanism of Mg dissolution by using modern spectroscopic techniques while reproducing the experiments performed by an earlier paper. [23].

### 2.3.14. Ion Chromatography (IC)

IC is used to study water chemistry, measuring the concentration of ions including anions (*e.g.*, $Cl^-$) as well as cations (*e.g.*, $Mg^{2+}$) with sensitivity in the ppb range. The IC method separates ionic species according to their interactions with an ion exchanger resin, enabling separation of based on the affinity to the ion exchanger and subsequent quantitative analysis of individual ions [225]. The IC analysis is done on water-soluble corrosion products removed by leaching in Milli-q water (pH 7) [225], determining the amount of water soluble anions removed by leaching. Considering the stability of the Mg corrosion products formed under atmospheric environments (see Section 4.3), the use of IC has been limited to atmospheric corrosion studies. Applications of the IC method in corrosion studies were investigated by Nash and Kelly [226] in the early 1990s. In Mg corrosion research, Jönsson et al. [227] examined water-soluble $Cl^-$ on AZ91 after exposure to atmospheric corrosion in the presence of NaCl. The method was also used by Lindström et al. [32] and Esmaily et al. [120], who studied the corrosion products formed on several Mg alloys after exposures to the ambient atmospheric in the presence of NaCl.

### 2.3.15. Environmental scanning electron microscopy (ESEM)

The environmental SEM (ESEM) provides almost the same sort of information as the SEM does, however, it offers several advantages over conventional SEMs. Firstly, difficult specimens including wet and insulating ones, can be investigated in an ESEM. The ESEM does this by enabling a gaseous environment, *e.g.*, water vapor, to be present in the instrument chamber while retaining rather high resolution. Moreover, ESEM investigations can be done under a variety of conditions; (i) temperatures in the range −30 to 1500 °C, (ii) pressures up to 10 Torr or ∼6700 Pa, and (iii) humidity up to 99% RH [228]. These capabilities offer an exceptional opportunity to view dynamic processes occurring on material surfaces "live" and in a time-resolved manner (Fig. 9h). Viewing the initial stages of the interactions between surfaces and their surrounding environmental contaminations *e.g.*, gaseous species and alkali salts is one of the practical applications of an ESEM *in situ* experiment [229,230]. In spite of these benefits, it is only lately that the technique has started to make an impact in corrosion science [123,231,232]. In regards to Mg corrosion, Chen et al. [231] investigated the corrosion behavior of Mg alloys by changing the RH of the ESEM chamber. They examined the corrosion of the alloy AZ91 in wet and dry cycles to study the effect of process parameters on corrosion product formation. Esmaily et al. [123] examined the feasibility of using ESEM in studying the atmospheric corrosion behavior of high-purity (HP) Mg. After arriving at a reliable route for preparing the sample and arranging the experiment, it was shown that the corrosion morphology and the corrosion product composition generated *in situ* in the ESEM were in agreement with those of the samples exposed in a conventional way, *ex situ*.

### 2.3.16. X-ray computed tomography (CT)

CT is a useful and non-destructive characterization technique for imaging of medical, biological and materials science specimens at the millimeter to micron scale [233]. Currently, there are very few studies dealing with corrosion phenomena using CT imaging [233–235]. For instance, Burnett et al. [233] examined the proliferation and growth of pitting corrosion sites in sensitized austenitic stainless steel immersed in chloride-containing aqueous solution by this method. As explained above, a more in-depth insight into the materials properties requires 3D characterization to explore the interconnectivity of networks in localized/pitting corrosion. Considering that localized corrosion is a vital degradation-type in Mg and Mg alloys [233,235], the use of the X-ray CT imaging in the future studies is expected.

### 2.3.17. High-resolution methods for future studies

Recent advances in analytical tools enable the characterization of properties-microstructure relationships in metallic materials in a more localized manner and with a much higher resolutions than those listed above. Despite the list of analytical tools given above, there are techniques that are still under-appreciated and/or vastly under-explored in corrosion science. Below, some such methods which are potentially important analytical tools in the Mg corrosion field are provided.

i. *Transition Kikuchi diffraction (TKD)* is a new modification of EBSD. TKD analysis is performed on FIB-prepared thin foils as opposed to the conventional EBSD which is conducted on bulk samples. The use of a thin foil (thickness in the range 50–150 nm) provides a very high spatial resolution to ∼5 nm (Fig. 9i) (note: the resolution of conventional EBSD (100 nm) [144]. It provides the same type of information as EBSD does. Therefore, the TKD method has great potential for corrosion studies. It has the capability to map the fine-grained matter, *e.g.*, nanostructured metallic materials and oxides. The method has not yet been applied to the oxide films formed on Mg and Mg alloys. However, it was successfully employed to map grains in the size range 10–100 nm in oxide layers formed on high temperature materials at elevated temperatures [144,236,237]. In the near future, TKD might be considered as a very versatile tool for corrosion characterization which is faster and cheaper than TEM analyses. It is expected that the TKD method will soon shed more light onto the oxide layers formed on Mg (alloys).

ii. *NanoSIMS* features even higher resolution and chemical sensitivity than ToF-SIMS instruments. NanoSIMS has reached the spatial/lateral resolution required to extract information on the oxide layer thickness, oxide type, or oxygen/hydrogen penetration depth. Notably, NanoSIMS adds the possibility of mapping elements present at ppm levels. The method has been used to map oxide chemistry in intergranular cracks in stainless steels, enabling to discern the different oxide layers and clarify the role of minor segregants [238,239]. Similar to the TKD method, NanoSIMS has not been used in Mg corrosion studies. Presently, the method is rarely available due to the very high cost of the instrument.

iii. *Ion beam analysis (IBA)* employs MeV ion beams to determine the elemental composition of a material surface in a non-destructive manner. IMA has found widespread application in various research fields such materials science, geology, biology, and medicine. IBA is indeed collection of powerful analytical tools such as Rutherford backscattering spectroscopy (RBS), particle induced X-ray emission (PIXE), elastic recoil detection analysis (ERDA), and proton induced gamma-ray emission (PIGME) [240,241]. Of these, RBS and PIXE have been effectively employed in Mg corrosion research. The work performed by Cain et al. [59], is the single study using RBS, which provided strong evidence of Fe enrichment on the surface of a Mg anode. Regarding PIXE, the only available study, is a paper by Birbilis et al. [169], who also conducted trace analysis, and investigated surface enrichment of impurities such as Fe, copper (Cu), and Zn on pure Mg after 2 min exposure in a corrosive media (Fig. 9j). Certainly, the capabilities of IBA techniques for addressing Mg (alloy) alloy corrosion phenomena are largely unexplored.

### 2.3.18. A comparison between analytical methods

The corrosion process occurs on widely different length scales, from angstroms, corresponding to individual atoms and the breaking and making of chemical bonds, up to centimeters, such as in large corrosion cells (galvanic or macro-cell), or the grain structure of metallic materials. It is necessary to use a combination of analytical tools in order to bridge this range of scales for example in studying corrosion-microstructure relationships or the dissolution mechanism of Mg and its alloys. Above, we have touched on some of the methods in relation to Mg corrosion research. The sphere in Fig. 11a compares the capabilities and characteristics of a number of analytical tools and techniques that can provide information in relation to Mg corrosion research, elucidating *e.g.,* the structure/microstructure and the chemistry of the corroding surface.

While some are site-specific (*e.g.,* SEM/EDX, TEM, SKPFM, AES, SVET, and FIB), others are capable of providing a more general picture from the specimen surfaces (*e.g.,* IC, FTIR, XPS, and BIB). While some offer useful information from the outermost layers, *i.e.,* the surface film of a material (*e.g.,* AES, TKD, ToF-SIMS/NanoSIMS, and FIB/TEM), others deliver information from areas deep in the specimen (*e.g.,* SEM, BB-XRD, CT tomography, and statistical techniques). And finally, while some techniques are useful for characterizing the distribution of major elements like Mg, Al, and Zn (*e.g.,* SEM/EDX, and XRD), others provide information regarding trace elements like nickel (Ni), Fe, and Cu (*e.g.,* RBS, PIXE, AECES, ToF-SIMS, and FIB/TEM/EDX).

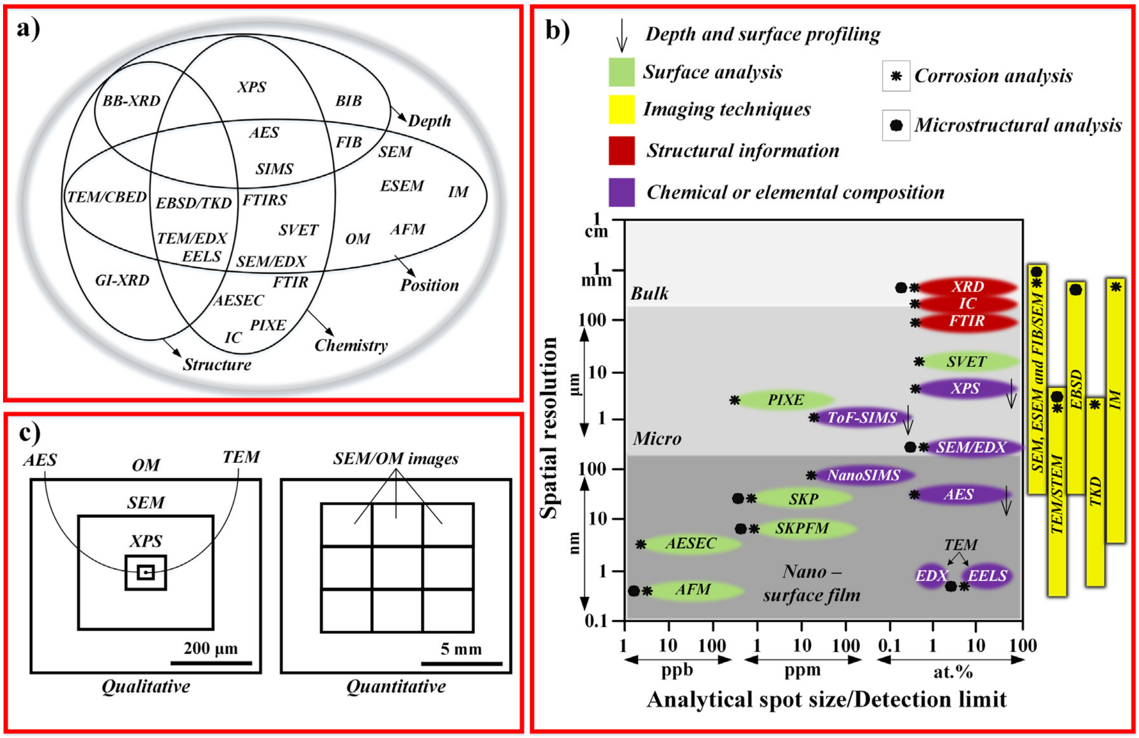

**Fig. 11.** A comparison between various analytical tools in Mg corrosion. (a) An overview of applications (structure/chemistry) and capabilities (depth/position) of the several analytical techniques that can be applied to Mg corrosion research, (b) detection limit versus spatial (lateral) resolution of the described methods, and (c) qualitative versus quantitative assessments of microstructure-corrosion relationships in Mg alloys.

It may be noted that some of the analytical techniques listed above can be employed both *ex situ and in situ* (*e.g.*, AESEC, XRD, FTIRS, and ESEM). *In situ* analysis implies the investigation of corrosion in real time and on the exact location where it occurs. The interest in *in situ* analysis in Mg corrosion research is currently increasing. This is because such investigations can be of great help in understanding the dynamics of a corrosion process because corrosion-related changes can be observed as they are occurring, rather than after the conclusion of the experiment as is usually the case (*i.e., ex situ* or post analysis). Thus, *in situ* methods can be used to detect the formation of initial corrosion products that are converted into more stable compounds as the corrosion process proceeds. Also, *in situ* methods allow observation of the corrosion process without disturbing it.

To summarize, the functional difference of these methods stems from parameters such as detection limit, spatial resolution (see Fig. 11b), and also the nature of the information that each individual method can provide (Fig. 11a and b). The use of quantitative information, *i.e.*, statistical information obtained from large areas (Section 2.3.1) for understanding the microstructure-corrosion relationships in Mg alloys is emphasized (Fig. 11c). Note that we have not covered all the analytical tools that are used or have the potential to be used in the field (the surface characterization tools such as photocurrent spectroscopy (PCS) and small-angle neutron scattering analysis (SANA)).

## 3. Aqueous corrosion of Mg

### *3.1. Generalities of Mg corrosion*

The comparatively poor corrosion resistance of Mg and its alloys can be mainly attributed to two key factors. These include: (i) the highly electronegative potential of Mg which allows corrosion to proceed even in the absence of oxygen, whereby the cathodic water reduction reaction predominates at such negative potentials and (ii) the poorly protective properties of any surface film formed upon Mg. This implies that any oxide or hydroxide layer that forms upon Mg is soluble in most aqueous environments or in the presence of humidity. Furthermore, Mg surface layers incompletely cover the underlying Mg metal surface and are highly defective (the Pilling-Bedworth ratio; see below) [42].

Prior to entering the details of aqueous corrosion of Mg, it is appropriate to start by describing film formation and the properties of the surface film formed on Mg.

In the absence of water, Mg reacts instantaneously in air at room temperature to form Mg oxide:

$$\mathrm{Mg(s)} + \frac{1}{2}\mathrm{O_2(g)} \rightarrow \mathrm{MgO(s)} \tag{1}$$

The reaction is highly exothermic so that fine Mg powders are pyrophoric. However, on Mg in bulk form the reaction only generates a surface film with a thickness of a few nm. Oxide film formation on metals in dry air at ambient temperature is often described by the Cabrera-Mott field-assisted cation transport mechanism, fitting film growth to a logarithmic relation [242]. Accordingly, it has been shown that the growth of MgO films on Mg in dry and humid air (and in water vapor) can be described by logarithmic kinetics. MgO has the cubic halite structure with an *a* value of 0.42 nm [243], see Fig. 12. It is important to note that MgO is a large band-gap insulator. The extremely poor electronic conductivity of MgO implies that it is unlikely to act as a cathode, except when it forms a film thin enough to allow electron tunneling. Indeed, the corrosion products commonly reported to form on Mg (*e.g.*, brucite and the Mg hydroxy carbonates, see Section 4.3.2) are also insulators.

The MgO/Mg Pilling-Bedworth ratio (the oxide/metal volume ratio) is 0.81. In the case of inward oxide growth (oxygen ion transport) this would give rise to tensile stresses and a discontinuous MgO layer. However, if the oxide grows outward (by $Mg^{2+}$ diffusion) the new oxide forms at oxide/gas interface and tensile stresses do not develop due to volume contraction [244,245]. Hence, the nature of the MgO layer formed at room temperature is predictable.

The details of the formation and growth of MgO films on Mg in water vapor were investigated by [246], describing it as a three-stage process. The first and second stages consisted of dissociative water adsorption and nucleation/growth of MgO islands, respectively. In the third stage the surface is completely covered by a 4 nm crystalline MgO layer of which grows extremely slowly in thickness, with inverse logarithmic kinetics.

Mg shows good corrosion resistance in dry air at ambient temperature owing to the MgO film. Indeed, most metals have exceptional corrosion resistance in the absence of water. The chemisorption of water on MgO was studied by Refson et al. [250] who showed that the process is especially favored on the MgO (1 1 1) surface. The adsorbed water molecules dissociate (*i.e.*, undergo protolysis) forming $OH^-$ and $H^+$ resulting in hydroxylation of the MgO surface:

$$\mathrm{O^{2-}(surface)} + \mathrm{H_2O(g)} \rightarrow \mathrm{2OH^-(surface)} \tag{2}$$

Equivalently:

$$\mathrm{MgO(surface)} + \mathrm{H_2O(g)} \rightarrow \mathrm{Mg(OH)_2(surface)} \tag{3}$$

The hydroxylation of the MgO film is illustrated in (Fig. 12), which is important to represent, as it is this bilayer structure that predominates Mg in the presence of moisture or aqueous immersion (*i.e.*, the most relevant surface for the scenario of Mg corrosion). It may be noted that the reaction of solid MgO with water to form solid $Mg(OH)_2$ (brucite) is favored by equilib-

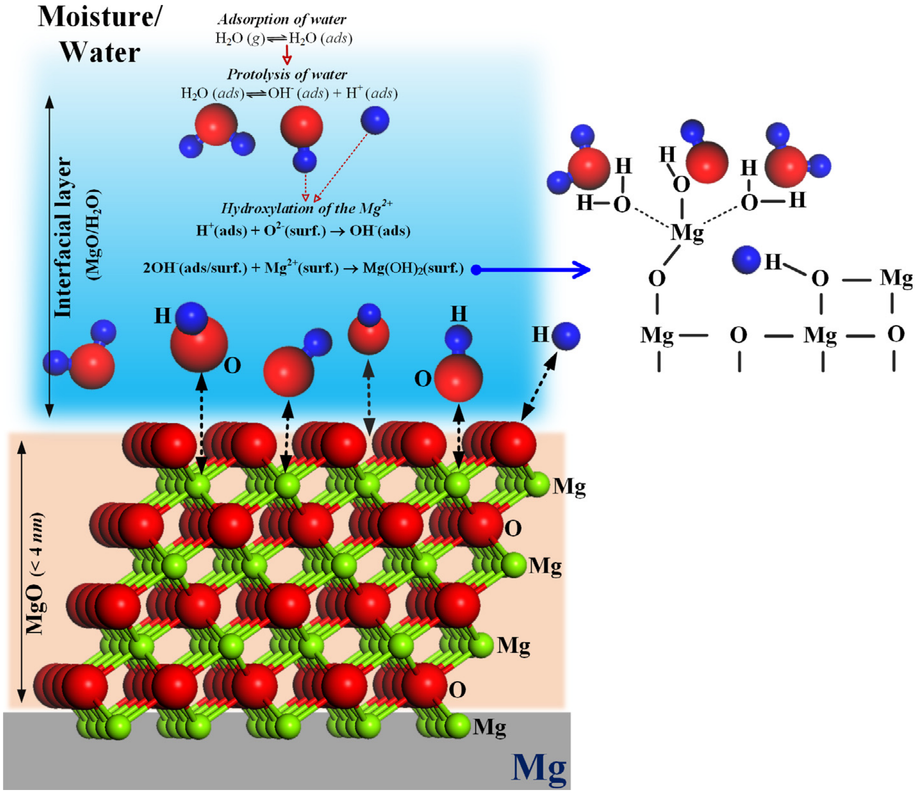

**Fig. 12.** Schematic illustration of the hydroxylation of MgO (111) surface. The atomic structures were visualized using the software BIOVIA Materials Studio 6.0. The illustration is drawn based on information provided in [194,247–249].

rium thermodynamics even at low concentrations of water vapor (>1 ppm $H_2O$). The corresponding reaction with liquid water:

$$MgO(s) + H_2O(l) \leftrightharpoons Mg(OH)_2(s) \tag{4}$$

Accordingly, the reaction of MgO with water vapor results in layered surface film consisting of a $Mg(OH)_2$ cap layer and a bottom MgO layer, see Fig. 10b.

MgO and $Mg(OH)_2$ are both relatively soluble in water. Thus, the film formed on Mg is non-protective in neutral and acidic aqueous solutions. The dissolution of the hydroxide film (according to Eq. (5)) results in an increase in the pH value of the electrolyte [251]:

$$Mg(OH)_2(s) \leftrightharpoons Mg^{2+}(aq) + 2(OH)^-(aq) \quad K_{sp} \sim 10^{-11} \tag{5}$$

It may be noted that MgO is significantly more soluble than brucite [25,251]:

$$MgO(s) + H_2O(l) \leftrightharpoons Mg^{2+}(aq) + 2(OH)^-(aq) \quad K_{sp} \sim 10^{-6} \tag{6}$$

The greater solubility of MgO compared to brucite implies that a surface water film easily becomes supersaturated with respect to $Mg(OH)_2$, allowing brucite to precipitate. Accordingly, in 1969 Vermilyea et al. [31] suggested the "dissolution-precipitation" mechanism for Mg corrosion, describing how the MgO film is dissolved and converted into macroscopic brucite precipitates. The resulting MgO film thinning is expected to cause oxidation (MgO formation) to be resumed or to trigger direct reaction between the metal and liquid water. Note that the surface films formed on Mg (alloys) is further discussed in Section 4.3.6.

Immersion in water thus tends to cause dissolution of the "quasi-passive" MgO/$Mg(OH)_2$ film, exposing the metal to the solution. Furthermore, impurities, second phases, or "noble" inclusions are not covered by the abovementioned double-layered film, in addition to such second phases being locally polarized at the potential of any Mg-alloy that they populate, such that localized corrosion is readily triggered.

Metallic corrosion is an electrochemical process in which the metal undergoes a change in its oxidation state due to its interaction with the environment, *i.e.*, an aqueous electrolyte. This process occurs by electron transfer at the interface of the electrode and involves the oxidation of metal atoms to form ionic species, which is accompanied by the liberation of electrons. For Mg, the oxidation half reaction is:

$$Mg \rightarrow Mg^{2+} + 2e^{-} \tag{7}$$

The electrons generated must be consumed by other species to maintain electroneutrality. Therefore, this oxidation or anodic half reaction must be accompanied by a reduction or cathodic reaction in which a molecule, atom, or ion gains electrons thus decreasing its oxidation state.

Depending on the environment, a number of different oxidizing species can act as electron acceptors. However, the primary reduction reactions in corrosion are the HER and the oxygen reduction reaction (ORR), each of which takes a different form in acids or bases:

$$2H^{+} + 2e^{-} \rightarrow H_2 \quad E^{\circ} = 0\ V_{SHE} \tag{8}$$

$$2H_2O + 2e^{-} \rightarrow H_2 + 2OH^{-} \quad E^{\circ} = -0.83\ V_{SHE} \tag{9}$$

$$O_2 + 4H^{+} + 4e^{-} \rightarrow 2H_2O \quad E^{\circ} = 1.23\ V_{SHE} \tag{10}$$

$$O_2 + 2H_2O + 4e^{-} \rightarrow 4OH^{-} \quad E^{\circ} = 0.4\ V_{SHE} \tag{11}$$

Reactions (8) and (9) occur in acidic environments, reactions (10) and (11) occur in neutral and alkaline environments. The above reactions are not influence by dissolved oxygen concentration (which plays a critical role in the corrosion process of all other engineering metals) as the corrosion potential ($E_{corr}$) of Mg-alloys is confined to the regime where water reduction is the dominant cathodic reaction (*i.e.*, $\ll 1\ V_{SHE}$) [252]. It is observed from the above reactions that in the case of atmospherically exposed Mg, the cathodic reaction will be water reduction, often also simply termed as HE. Consequently, the overall corrosion reaction for Mg is:

$$Mg + 2H_2O \rightarrow Mg(OH)_2 + H_2 \quad E^{\circ} = -2.37\ V_{SHE} \tag{12}$$

## 3.2. Mg corrosion mechanism

### 3.2.1. Anomalous HE on anodically polarized Mg surfaces

To have a full understanding of the Mg corrosion mechanism, it is necessary to account for the superfluous HE that occurs on anodically polarized Mg surfaces. This phenomenon as will be described herein, is a key feature of Mg (and Mg alloy) electrochemistry that merits specific attention. The HER is the primary cathodic reaction in Mg corrosion and it takes places spontaneously on Mg under open circuit (unpolarized) conditions. However, when Mg and its alloys are polarized anodically, causing higher rates of dissolution, increased rates of HE are also observed. Although this phenomenon has been commonly referred to by the name NDE, this is a historical term that provides a limited and sometimes inaccurate description of the phenomenon. NDE is defined as the difference between the HE rate under open circuit conditions and the rate associated with the HER during anodic polarization [253]. As defined, the NDE on anodically polarized Mg is often large. However, in some cases, the rate of HE decreases slowly over a wide range of potential above the open circuit potential (OCP). This behavior is part of the same phenomenon even though the difference would be positive and not negative. For these reasons, the authors believe that the use of NDE is not recommended and propose the more accurate term "anomalous HE", which will be used herein. It also merits qualification that the term "anomalous HE" refers to HE occurring as a result of anodic polarization, and not HE arising from an anodic reaction. The observation of anomalous HE is in contradiction with the well-accepted expression for activation-controlled kinetics, the Butler-Volmer equation (see Eq. (13)).

$$i_{HER} = i_{0,H,Mg}\left[\exp\left(\frac{(E - E_{rev,H})}{b_a}\right) - \exp\left(\frac{-(E - E_{rev,H})}{|b_c|}\right)\right] \tag{13}$$

where $i_{HER}$ is the current density associated with the HER (A/cm$^2$), $i_{0,H,Mg}$ is the exchange current density for the evolution of $H_2$ on Mg (A/cm$^2$), $E$ is the electrode potential (V), $E_{rev,H}$ is the reversible potential for the HER (V), $b_a$ is the value of the anodic Tafel slope and $|b_c|$ is the absolute value of the cathodic Tafel slope (V/dec). According to Eq. (13), the rate of a cathodic reaction such as the HER should decrease exponentially with increased anodic polarization and not increase. A graphical description of the anomalous HE phenomenon is shown in Fig. 13, where the calculated current densities for the HE obtained during galvanostatic experiments at different cathodic and anodic current densities of two different Mg purities are plotted against the measured potential. Dashed lines show the expected behavior for the HER according to Eq. (13) whereas empty circles above the open circuit potential, show the actual behavior.

It is worth noting that, as a consequence of the existence of anomalous HE, Mg and its alloys do not follow Faraday's law. In other words, it is not possible to estimate the amount of Mg dissolved under anodic polarization using just electrochemical methods due to the fact that, during the anodic perturbation, a certain amount of the electrons generated by the Mg oxidation reaction (Eq. (7)) do not flow through the potentiostat to the counter electrode but rather are consumed by the HER on the Mg electrode surface, thereby remaining undetected by the potentiostat. This was elegantly shown (and described below) from recent experiments employing the SVET [34].

Mg is the most active (*i.e.*, has the most negative electrochemical potential) of any structural metal, and will be polarized anodically when used in a structure that promotes galvanic interactions with other components. Consequently, elucidation

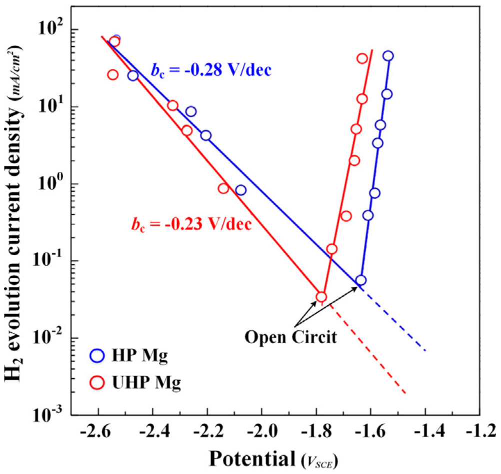

**Fig. 13.** Current density associated with HE for two different Mg purities (HP and UHP) in 0.1 M NaCl solution as a function of potential. Current density values were calculated from the HE rates during galvanostatic polarization measurements [56]. Reprinted with permission from Elsevier.

of the mechanism by which anomalous HE occurs is of critical scientific and technological interest and is fundamental in designing effective protection strategies against corrosion in the future. This section will cover the main mechanistic explanations that have been proposed to explain the phenomenon of anomalous HE since it was first reported by Beetz in 1866 [18].

### 3.2.2. Univalent Mg ($Mg^+$) theory

The univalent Mg theory, which is based on the hypothetical existence of $Mg^+$ as an intermediate in the anodic dissolution of Mg, has been the most widely discussed theory for anomalous HE on Mg over the last decades. In this theory, Mg and its alloys experience a two-step dissolution mechanism: (i) an electrochemical reaction in which a fraction of Mg dissolves into solution as $Mg^+$ (Eq. (14)) and (ii) $Mg^+$ undergoes a homogeneous chemical reaction with water to form $Mg^{2+}$ and $H_2$ (Eq. (15)). According to this mechanism, more $Mg^+$ is produced as the rate of Mg dissolution increases thus increasing the rate of HE.

$$Mg_{(s)} \rightarrow Mg^{+}_{(aq)} + e^{-} \tag{14}$$

$$Mg^{+}_{(aq)} + H_2O_{(l)} \rightarrow Mg^{2+}_{(aq)} + \frac{1}{2}H_{2(g)} + OH^{-}_{(aq)} \tag{15}$$

The existence of an intermediate species of Mg with lower valence than n = 2 was initially invoked by Turrentine in 1907 [254] but it was not until 1954 that Petty et al. [23] reported indirect experimental evidence of what they described as “unipositive Mg”. To reach that conclusion, Petty and coworkers carried out several experiments in which a solution was flowed past a dissolving Mg anode into a separate cell that contained an oxidizing agent. Since reduction of the oxidizing species was detected in the second cell and no other reducing species was present, they concluded that and intermediate species of Mg with n < 2 should be the source of electrons.

On the basis of Petty’s finding, Song and Atrens [41,255–259] have promoted the mechanism of univalent Mg as the explanation of anomalous HE. With the assumption of the production of $Mg^+$, it is possible to explain many observations such as the increase in HE rate with increasing applied current or potential. However, there are several aspects of this theory that remain unsolved and have raised criticism. The most evident is that there is no direct evidence of the existence of aqueous $Mg^+$ and this species has never been detected by any experimental technique. On the other hand, if $Mg^+$ indeed could exist in solution, it would be extremely reactive and would thus have an extremely short lifetime, less than microseconds [41]. However, according to Petty’s work, univalent Mg must be stable in aqueous solution for a considerable time without being oxidized by water. Furthermore, it should be noted that the Petty experiment was recently reproduced with coupling to *in situ* Raman spectroscopy [224]. Other reducing species never considered by Petty et al. [23], such as $SO_2$, formed during the experiment, thus showing that the most referenced evidence for the existence of $Mg^+$ can be rationalized by alternate explanations. Therefore, direct experimental evidence for $Mg^+$ is still lacking.

Atrens et al. recently reported an average oxidation number of Mg under open circuit conditions of less than 1 (n < 1), and even as low as 0.06 [260]. To rationalize this observation, the presence of crevice corrosion caused by $H_2$ bubbles sealing pits or defective regions in the Mg oxide film was hypothesized. However, gas bubbles adsorbed on the surface could only obstruct circular-shaped cavities that were widely separated. This situation does not resemble the roughness observed on dissolving Mg surfaces. Furthermore, if such a mechanism did occur, it could explain any observation of n < 2 and therefore

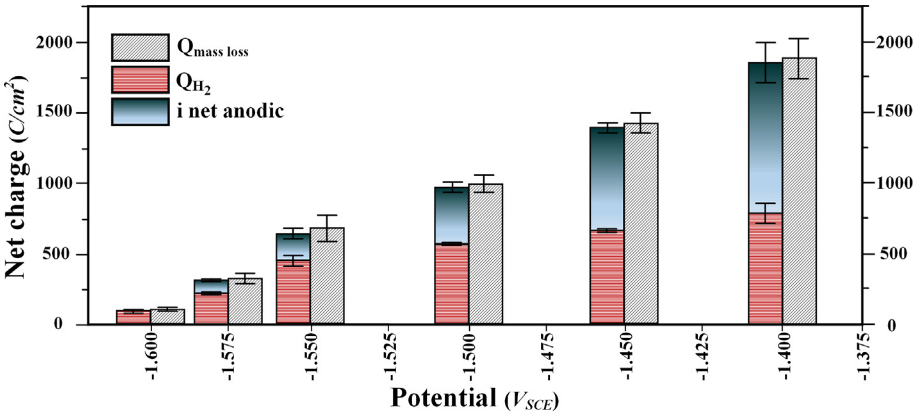

**Fig. 14.** Net charge associated with HE plus to the net charge measured by the potentiostat during potentiostatic polarization compared to mass loss as a function of potential for a HP Mg in 0.6 M NaCl solution [59]. Reproduced with permission from The Electrochemical Society, licensed under CC-BY 4.0.

obviates the need to invoke the univalent Mg mechanism under any conditions. The observation of apparent values of n < 2 is an indication of the difficulties in the accurate determination of n, which is complicated by several factors such as the formation of a partially protective corrosion film during Mg dissolution.

The accurate assessment of n during Mg dissolution has been the focus of several recent observations. Kirkland et al. [261] studied the dissolution of pure Mg under galvanostatic polarization using real-time video recordings on a triangular electrode design that allowed uniform dissolution and determined n to be around 2 in a range of applied currents from 0.5 to 20 mA. Cain et al. [59] studied the enrichment of transitions metals on dissolving Mg using RBS for which they carried out potentiostatic polarization measurements at different applied potentials while simultaneously collected the $H_2$ that evolved from the Mg surface. Following testing, the samples were cleaned with chromic acid and weight loss was measured. The results, which are shown in Fig. 14, provide strong evidence for n = 2. The same conclusion was reported in a previous work by Bender et al. [262]. It is worth noting that these studies used 2 equivalents per mol of dissolved Mg to assess the charge balance. Rossrucker et al. [263,264] investigated the real-time dissolution of Mg in NaCl and buffered solution under galvanostatic polarization by means of a flowing cell coupled with an ICP-MS. These authors also found that Mg dissolution stoichiometry proceeds via $Mg^{2+}$. Finally, Lebouil et al. [265] and Światowska et al. [81] studied the anodic dissolution of Mg using atomic emission spectroelectrochemistry finding direct evidence that n = 2. Consequently, the univalent Mg theory should be considered as purely hypothetical until direct evidence on the existence of $Mg^+$ is provided.

### 3.2.3. Effects of corrosion film and surface enrichment of impurities

On a freshly prepared Mg surface exposed to an aqueous solution (such as dilute chloride solutions), corrosion proceeds at the edges of growing patches that leave corrosion product in their wake. The Mg corrosion product has been shown to exhibit enhanced catalytic activity towards the HER [34,49,52,56,72]. In other words, the dark corrosion film formed during Mg corrosion at the OCP promotes the evolution of $H_2$ at a faster rate than uncorroded areas on the sample. This behavior is not expected at first glance because a thick film of oxide or hydroxide corrosion products might be relatively resistive. In fact, the corrosion film formed on Mg consists of an outer columnar mixed Mg oxide-hydroxide layer on top of a Mg oxide rich inner layer [166,177], see Sections 2.3.7 and 4.3.6. A number of papers have covered the catalytic properties of the corrosion film towards the HER at the OCP based on the results of Williams et al. [266] which will be discussed in detail below. Birbilis et al. [60] provided strong evidence of the enhanced catalytic nature of previously dissolved Mg surfaces towards the HER by performing a series of electrochemical tests on pure Mg in 0.1 M NaCl solution. Potentiostatic cathodic polarization tests at −1.9 $V_{SCE}$ carried out immediately after anodic galvanostatic polarization showed enhanced cathodic current density over a range of different applied anodic currents. It is worth noting that these set of experiments were performed consecutively, thus the amount of charge passed was cumulative and the surface was progressively more covered with corrosion film [60]. Salleh et al. [72] used SECM to show that the rate of HE on Mg surfaces artificially covered with $Mg(OH)_2$ is about 2–3 times faster at the OCP than on the pristine Mg surface (Fig. 15). They also showed that the current associated with HER during cathodic potentiostatic polarization at −1.9 $V_{SCE}$ was about 4–6 times faster on the $Mg(OH)_2$ coated surface than on the non-coated pristine Mg surface. Curioni [49] studied the corrosion behavior of Mg at the OCP and during potentiodynamic polarization in NaCl solution by means of hydrogen collection coupled with optical imaging and found that the dark regions that progressively propagate across the surface due to the corrosion reaction of Mg support substantially higher cathodic activity compared to the unattacked regions. There is substantial evidence that the dark film is the primary site of cathodic reaction for Mg dissolving at its OCP.

Curioni [49] hypothesized that these corroded regions could be the reason for the increased cathodic activity exhibited by Mg during anodic dissolution if they propagated across the surface at a faster rate as anodic polarization propagation increased. However, to attribute the anomalous HE phenomenon to the increased coverage of corroded regions requires that

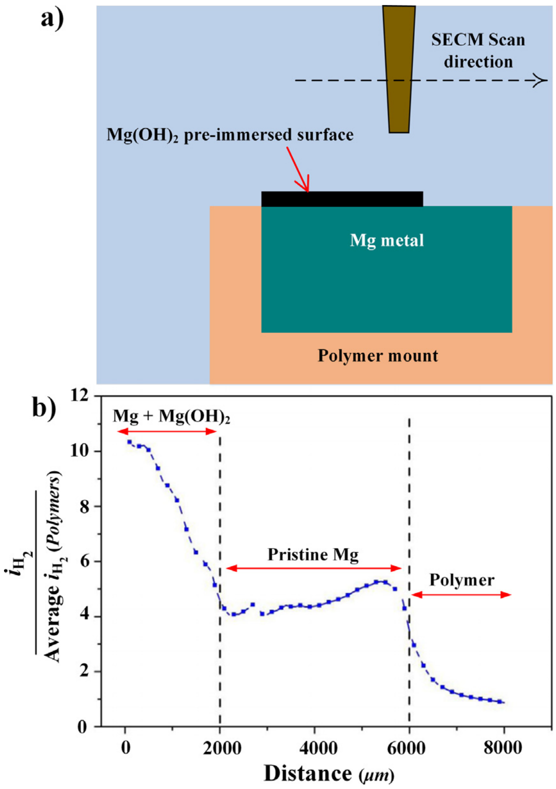

**Fig. 15.** Catalytic activity towards the HER associated with the film determined by SECM. (a) Schematic representation of the setup used for the SECM experiments, and (b) normalized $H_2$ oxidation currents measured during a line scan from the $Mg(OH)_2$ coated Mg surface, through the pristine Mg surface, and to the polymer surface [72]. Reprinted with permission from Elsevier.

these products will maintain (or even increase) their ability to support the HER, and Tafel kinetics would suggest the reverse. It is also worth noting that the rate of HE increases several orders of magnitude with increasing anodic polarization, which is considerably more than the increase of 2–3× on $Mg(OH)_2$ coated Mg reported by Salleh et al. [72].

Williams et al. [33] studied the HE on pure Mg during anodic polarization using the SVET. They found that $H_2$ evolved at or very close to the dark filiform tracks of corrosion product. Furthermore, it was reported that the filiform-like tracks coupled with intense local anodes at their leading edges that left behind regions of sustained cathodic activity. Following the breakdown of the native oxide film, the local current distributions from SVET (see Fig. 16a) indicate that the total net anodic and net cathodic currents increase linearly at comparable rates and that the growth of the net cathodic currents corresponds with a greater fraction of corroded surface. Based on these observations, the mechanism depicted in Fig. 16b was proposed where a fraction of the electrons generated by the Mg dissolution reaction is consumed by HE at the regions covered with dark corrosion product. The observation of net cathodes on an anodically polarized surface is remarkable and has been used to explain the phenomenon of anomalous HE on the basis of the corrosion product film. On the basis of this finding, the SVET was used to study the propagation of the dark corrosion product through the metal surface under open circuit conditions. It was observed that the morphology of the attack is directly dependent on the concentration of NaCl in the electrolyte and the amount of Fe present in the material [266]. At a fixed Fe concentration, radial disc-like propagation is exhibited in highly concentrated NaCl solutions whereas lower concentrated NaCl environments lead to a filiform-like attack. This behavior was attributed to an ohmic effect that influences the current flow in the electrolyte between the net anodes (leading edges) and the net cathodes (dark regions), which are galvanically coupled. A solution with higher NaCl concentration, and thus higher conductivity, allows for more distant galvanic coupling and leads to a radial disk-like attack. On the other hand, solutions with lower conductivity constrain the current flux between net anodes and cathodes, leading to filiform-like tracks that maintain the distance between the galvanically coupled regions at a minimum [266].

Even though the dark corrosion film exhibits enhanced catalytic activity towards the HER and the corroded area increases with time, which generates progressively more corrosion film, the rate of HE measured using $H_2$ collection methods is often constant with time, rather than increasing with time. Instead, the HE rate depends on the anodic current density applied or the rate of corroded area production, not the amount of corroded area. These observations are not consistent with the notion that the dark corrosion regions are the primary source of anomalous HE.

It should also be considered that the aforementioned dark corrosion product could consist of more than just $Mg(OH)_2$. Since Mg is the most active of the structural metals (and the most active of the majority of alloying elements in

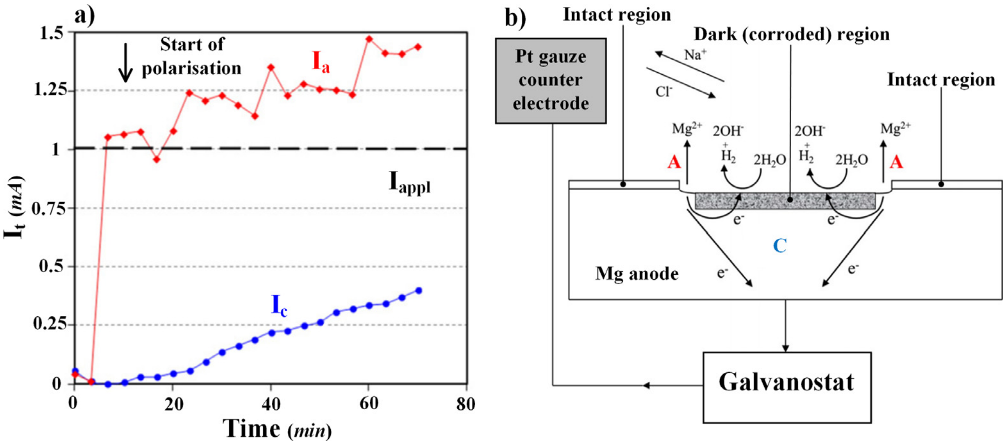

**Fig. 16.** Electrochemical activity of an anodically polarized Mg surface determined by SVET. (a) SVET-derived integrated current density values emerging from a HP Mg surface under anodic galvanostatic polarization at 1 mA/cm$^2$. (b) Schematic model for the anomalous HE [34]. Reprinted with permission from Elsevier.

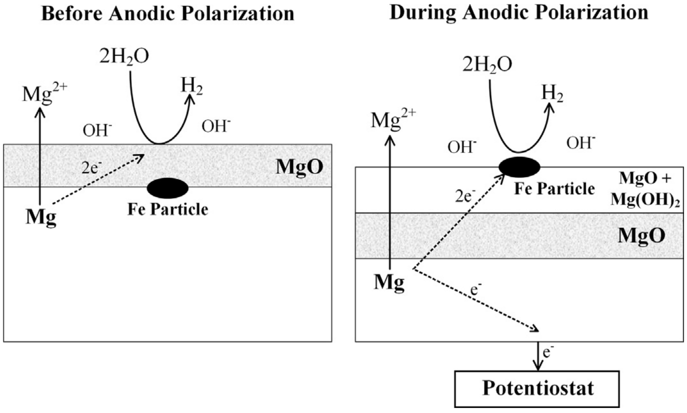

**Fig. 17.** Effect of surface enrichment of impurities on the anomalous HE | Schematic model based on the effect of impurity enrichment on a Mg surface for the anomalous HE [177]. Reprinted with permission from Elsevier.

Mg-alloys), almost any metallic impurity or alloying element will be more noble. The effect of impurities more noble than Mg (which includes essentially all transition metals) on its corrosion behavior has been known for a long time [22]. As the result of preferential dissolution of Mg during open circuit corrosion or anodic polarization, impurities present in the bulk material, such as Fe, may accumulate in or under the dark corrosion film formed on the surface. As a result, the concentration of impurities at the surface could become substantially higher than the concentration in the bulk metal. Sites of enriched noble elements with higher exchange current density for the HER ($i_{0,H}$) than that of Mg would lead to enhanced rates of HE even at potentials for which Mg is anodically polarized. Taheri et al. [177] identified small Fe-rich particles embedded in the outer layer of the corrosion film of a HP Mg electrode after anodic polarization (see Fig. 10a) which lead these authors to propose the mechanisms shown in Fig. 17. However, as mentioned by Cain et al. [53] it is not yet clear how noble impurities embedded in what is assumed to be poorly conductive film would lead to the high HE rates exhibited under anodic polarization. Lysne et al. [252] developed a model for Fe enrichment on a Mg surface subjected to anodic dissolution and concluded that the Fe enrichment efficiency is actually very poor, and that enrichment, whilst having some definitive role, is not however principally responsible for the enhanced HE rates on anodically polarized Mg. Cain et al. [59] studied the enrichment of transition metals on dissolving Mg using RBS and revealed direct evidence of Fe enrichment in the corrosion oxide/hydroxide film but, more importantly, under the film on the metal surface of a Mg anode.

Enrichment of impurities under the corrosion film and in electrical contact with the metal is a more reasonable scenario for the enhancement of HE by accumulated noble impurities. However, as reported also by Lysne et al. [267], the enrichment efficiency was low. Along the same lines were the results reported by Birbilis et al. [169], who studied surface impurity enrichment during Mg dissolution by means of PIXE measurements. Even though the concentration of surface impurities was shown to appreciably increase after anodic dissolution, enrichment efficiency was less than 1%. $H_2$ collection measurements on an ultra-high purity (UHP) Mg specimen with a nominal impurity concentration in the bulk metal of ~1 ppmw in

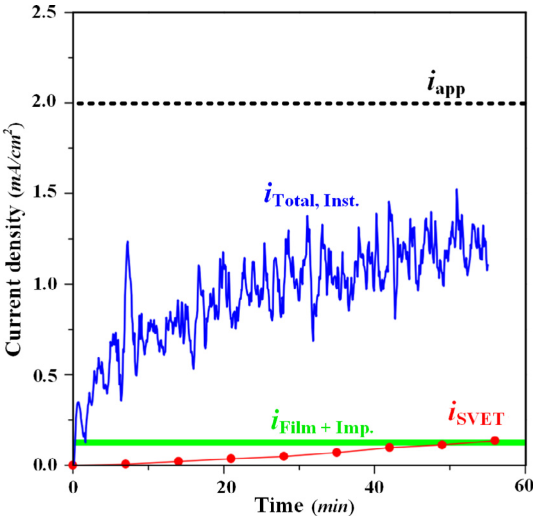

**Fig. 18.** Compilation of the absolute value of the different cathodic current densities measured in a UHP Mg electrode in 2 M NaCl solution. Red circles are the SVET-derived integrated cathodic current density ($i_{SVET}$). Dashed line is the net anodic current density applied ($i_{app}$). Solid blue line is the instantaneous current density associated with HE ($i_{Total,Inst.}$) obtained using the gravimetric method. Solid green is the hydrogen evolution current density associated with the corrosion product and accumulation of noble impurities ($i_{Film+Imp.}$) [61]. Reprinted with permission from Elsevier.

NaCl solution, where the accumulation of impurities can be reasonably neglected, showed that the rate of HE increased remarkably with anodic polarization [59,61]. Finally, the enrichment of impurities should, like formation of corrosion product, increase with time during corrosion at open circuit or polarization at anodic potentials, which is not consistent with the observation of a steady state HE rate under both conditions. Consequently, even if the accumulation of noble impurities on the electrode surface occurs and contributes to some part of the anomalous HE, this mechanism is not wholly, or even substantially, responsible for the enhanced rates of HE in Mg during anodic polarization.

Even though the dark corrosion film promotes HE at a faster rate than the uncorroded surface at the OCP, it was recently shown that its contribution to the total HE rate during anodic polarization is small [60]. To study the role of the corrosion film, these authors used *in situ* SVET during galvanostatic polarization, gravimetric $H_2$ collection and potentiodynamic polarization measurements on UHP Mg (99.9999% Mg) in NaCl solution. Fig. 18 summarizes the total cathodic current densities calculated by these separate techniques. The $i_{SVET}$ data represent the cathodic current densities calculated by numerical integration of the SVET maps and the green bands represent the range of contribution to the HE expected from the dark film and impurities ($i_{Film+Imp}$). The quantity ($i_{Film+Imp}$) was calculated from the extrapolation of the Tafel line associated with cathodic polarization curves measured immediately after the anodic galvanostatic experiments were finished. The primary assumptions were that the corrosion film formed during Mg dissolution and the accumulated impurities formed during anodic polarization do not change significantly during subsequent cathodic polarization, so that the surface during cathodic polarization represented the condition at the end of the anodic polarization [56]. The excellent agreement between $i_{Film+Imp}$ and $i_{SVET}$ suggests that both approaches accurately measure the HER associated with the dark product and impurities. As mentioned before, the extremely high purity of the UHP Mg material (~1 ppm total impurity concentration) indicates that it is unlikely that the accumulation of noble impurities play an important role here. Furthermore, Fig. 18 also shows that the total rate of HE as determined gravimetrically ($i_{Total}$) was one order of magnitude higher than $i_{Film+Imp}$, indicating that the dark corrosion film plays a minor role in anomalous HE. Furthermore, the evolution of anomalous $H_2$ was recently studied by Fajardo et al. [268] on HP Mg in an acidic citric acid buffer solution where the typical dark corrosion product exhibited in neutral and alkaline solutions was not found. These authors observed anomalous HE even in the absence of a dark corrosion product, providing strong evidence that the occurrence of anomalous HE is independent of the presence this corrosion product. This finding is in contradiction with that reported by Lebouil et al. [265], where Mg dissolution was studied in a phosphate buffer solution (pH = 6.7) under potential control, exhibiting decreased HE rates with increasing applied anodic potentials.

Höche et al. [269] proposed a different explanation for anomalous HE in which the Fe impurities present in the Mg specimen would leave the surface by non-Faradaic release associated with the dissolution of the surrounding Mg matrix, and then redeposit on the Mg surface after dissolution at their own open circuit potential in the electrolyte, as shown in Fig. 19. This mechanism has been proven for the redistribution of Cu from $Al_2CuMg$ intermetallic particles in Al alloys [270]. In addition to Fe redeposition, Höche and coworkers hypothesized that the enhanced rates of HE at anodic polarization may be favored by the Heyrovsky mechanism for the HER that could take place on these freshly created Fe-rich patches [269]. The effect of Fe redeposition was further investigated by Lamaka et al. [271] who carried out immersion tests on

**Fig. 19.** Schematic model based on the effect of Fe re-deposition on a Mg surface for the anomalous HE [269]. Published by the PCCP Owner Societies.

HP Mg (99.95% Mg) with 220 ppm by weight of Fe in NaCl solution in the absence and presence of several different Fe-complexing agents.

The presence of complexing agents in solution should tie up Fe ions, thereby preventing Fe reposition and enhanced HE. Indeed, HE collection measurements at the OCP showed that all of the Fe complexing agents efficiently lowered the corrosion rate of Mg, which is strong support for the role of noble impurity elements in the corrosion process. It also suggests that the enhanced rates of HE under anodic polarization can be explained by replating of previously dissolved Fe impurities. In a very recent study, Yuwono et al. [272] studied the electrochemical stability of Mg surfaces in an aqueous environment using first principles density functional theory (DFT) simulations. In this study, based on previous work by Williams et al. [273] where water dissociation was studied on Mg(0001) surfaces, the DFT results indicate that at the OCP, the Volmer-Heyrovsky pathway for the HER is favored. Simulations of Mg(0001) Fe-doped surfaces showed that Fe impurities, either in the first or second layer, support the cathodic reaction at Mg(0001) surface by lowering the energy required to transfer the electron used in the HER [272]. Even though this mechanism of Fe release and replating can explain the enhanced rates of HE exhibited during Mg dissolution under open circuit conditions, it is also not consistent with the constant rates of HE observed on Mg surfaces during anodic polarization. It is also expected that Fe replating could be affected by the convection in the electrolyte near the dissolving Mg surface generated as a consequence of the intense HE during anodic dissolution, particularly at large polarizations. For these reasons, more research is needed to validate this mechanism for anomalous HE.

Rossrucker et al. [263] studied the effect of pH on the HE during anodic polarization Mg and showed the important influence of pH alteration in the near surface region of dissolving Mg. Experiments used a flowing cell coupled with an ICP-MS unit and parallel HE collection measurements in different buffered and unbuffered solutions (pH range from 3 to 10.5). Flow cell measurements showed that anomalous HE was absent for low applied anodic currents in a neutral buffered solution, whereas it was promoted at high anodic polarization currents and unbuffered electrolytes. Anomalous HE was observed using HE collection measurements in the high pH buffer solution (as well as in unbuffered 0.1 M NaCl). Modification of the surface film on Mg caused by local changes in the surface pH plays a role in phenomenon of anomalous HE [263].

### *3.2.4. Increased catalytic activity*

When the potential is far above the reversible potential, the Butler-Volmer equation shown in Eq. (13) describing HER under activation-controlled kinetics can be simplified to the Tafel equation:

$$i_{HER} = i_{0,H,Mg} \exp\left(\frac{-(E - E_{rev,H})}{|b_c|}\right) \tag{16}$$

where $i_{HER}$ is the current density associated with the HE reaction (A/cm$^2$) and the rest of the parameters have the same meaning previously described. It is clear from Eq. (16) that changes in one or more values of the parameters in the equation, such as $E_{rev,H}$, $i_{0,H,Mg}$ and $b_c$, could cause the increased rates of HE for Mg at potentials more positive than its OCP. Changes in $E_{rev,H}$ and $b_c$ have been shown to have a small effect [62], but the catalytic activity of a surface is known to have a huge impact on the rate of HE. For example, the exchange current densities for the HER on different metals vary by a factor of $10^{10}$ [274]. It is possible to describe the ability of anodically polarized Mg surfaces to support HE at increasing rates as being the result of an increase in the exchange current density for the HER ($i_{0,H,Mg}$) [62]. The exchange current density reflects the kinetic properties of a particular interfacial system, including redox half reaction and electrode surface, under pure activation-control at equilibrium, and is generally assumed to be constant for that system. However, a dissolving Mg surface is far from equilibrium, and it is not unreasonable to assume that the surface is altered by the dissolution process. The schematic in Fig. 20 shows how an Evans diagram of the Mg dissolution and HER half reactions could be affected if $i_{0,H,Mg}$ increases due to anodic polarization [62]. In this analysis, $E_{rev,H}$ and $b_c$ remain constant, which might not be accurate but their variation should be small. In the cathodic region of the curve (below the OCP), $i_{0,H,Mg}$ is assumed to be relatively invariant. However, as the anodic current increases from $i_1$ to $i_4$, it is proposed that $i_{0,H,Mg}$ is enhanced from $i_{0,H,Mg,1}$ to $i_{0,H,Mg,4}$. The bold line in Fig. 20 represents the resulting HE rate, which takes the form typically observed in an $i_{HER}$ vs. potential plot for Mg like that shown in Fig. 13. It is possible to express the effects of an increase in catalytically active corrosion product film or continual enrichment or re-deposition of more-noble impurity elements by an increase in $i_{0,H,Mg}$.

However, as described above, experiments have shown that the impact of the corrosion film and impurities is small relative to the large increase in HE rate with increasing anodic current or potential. Consequently, in this view the source of anomalous HE is suggested to occur at the actively dissolving anodic regions, which have a surface that is catalytic for the HER [242].

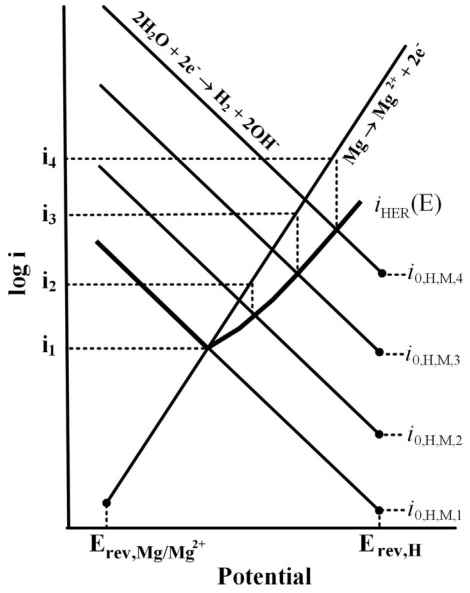

**Fig. 20.** Schematic Evans diagram explaining the increased rates of anomalous HE with increasing potential by the effects of exchange current density for HER [62]. Reprinted with permission from Elsevier.

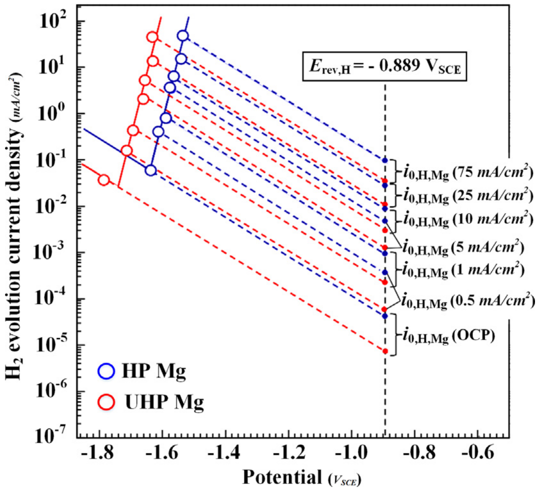

**Fig. 21.** Exchange current density for HER determination on the HP and UHP Mg electrodes in 0.1 M NaCl solution [56]. Reprinted with permission from Elsevier.

Using this framework to describe anomalous HE, Fajardo et al. [56] calculated $i_{0,H,Mg}$ for HP (99.98%) and UHP (99.9999%) Mg as a function of the applied galvanostatic current density (see Fig. 21). To carry out this calculation, the cathodic Tafel line for HER was first determined by semi-logarithmic fitting of $i_{HER}$ values obtained volumetrically during cathodic polarization (Tafel slope of −0.23 V/dec, for both materials). Then a series of cathodic lines with the same slope of −0.23 V/dec and intersecting each of the current density points associated with HE during anodic polarization were extrapolated to $E_{rev,H} = -0.889\ V_{SCE}$ (pH = 11). By this analysis, $i_{0,H,Mg}$ was shown to increase remarkably in both materials, by as much as 4 orders of magnitude at the highest anodic current density applied. In these experiments, even the UHP Mg with 1 ppm by weight of impurity concentration exhibited extremely high rates of anomalous HE, suggesting that impurities, either enriched or re-deposited, do not play a significant role in the anomalous HE mechanism.

Fig. 22a shows the values for the HE rates associated with the corrosion film and the accumulated impurities during anodic polarization as predicted by the extrapolation of the cathodic polarization curves (according to the protocol described in the previous section). Even though the rates of anomalous HE showed a clear effect of the initial impurity content, their relative independence on the anodic current density applied, thus with the amount of corrosion film deposited and the concen-

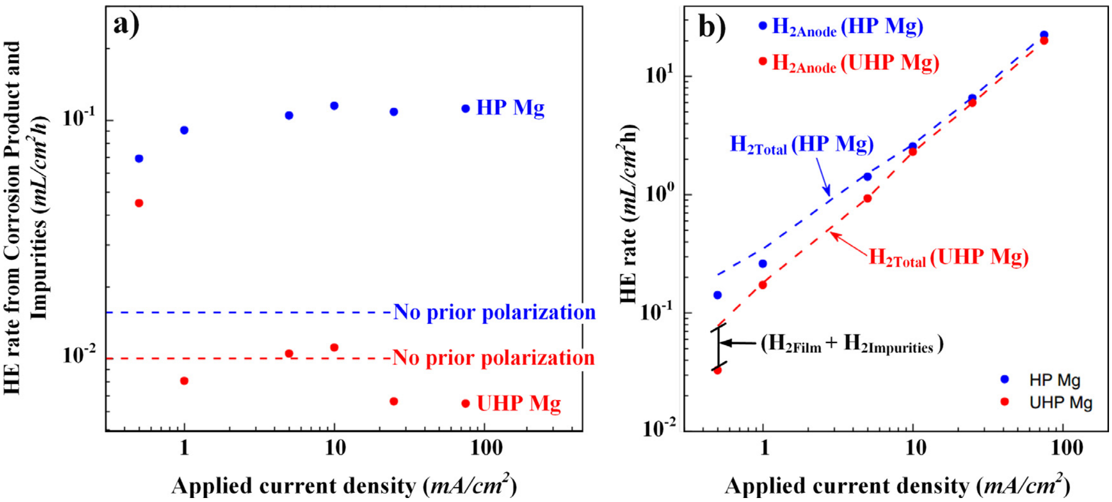

**Fig. 22.** Contribution of the film, accumulated impurities, and anodic regions to the total anomalous HE. Hydrogen evolution rate associated with (a) the corrosion product and accumulation of noble impurities, and (b) the dissolving anodic regions for the HP and UHP Mg electrodes in 0.1 M NaCl solution. [56]. Reprinted with permission from Elsevier.

tration of accumulated impurities, is further evidence that neither surface enriched impurity elements nor the Mg corrosion product is responsible for the anomalous HE phenomenon.

Fig. 22b shows the HE rate associated with the regions dominated by the anodic dissolution reaction as determined from the difference between the total HE rates (measured volumetrically during anodic polarization) and the HE rates associated with the accumulated noble impurities and the corrosion film presented shown in Fig. 22a, according to Eq. (17) [275].

$$H_{2,Total} = H_{2,Anode} + H_{2,Film} + H_{2,Impurities} \tag{17}$$

Even though a contribution of the corrosion film and accumulated impurities was found at the lowest applied anodic current densities, $H_{2,\mathrm{Anode}}$ was essentially equal to $H_{2,\mathrm{Total}}$ for the rest of the current densities applied, suggesting that anomalous HE is associated with the regions dominated by the anodic dissolution reaction.

With the aim of confirming these results and providing direct evidence of the source of anomalous HE, *in situ* SVET during galvanostatic polarization, gravimetric $H_2$ collection and potentiodynamic polarization measurements were used on the same UHP Mg material in NaCl solution [61], as was mentioned above. Fig. 23 shows a compilation of all the different

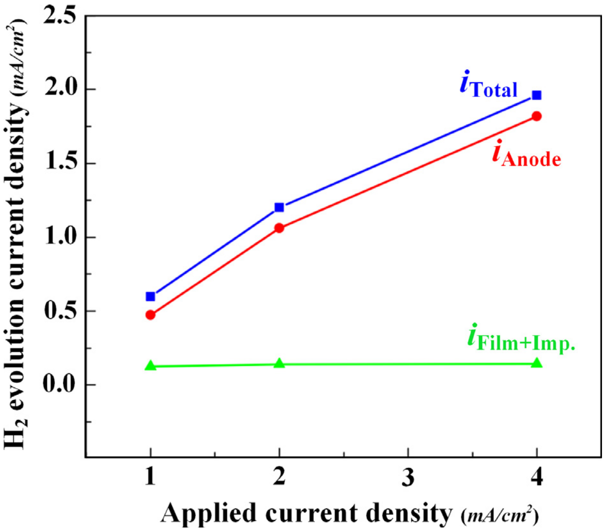

**Fig. 23.** Compilation of the absolute value of the different cathodic current densities measured in a UHP Mg electrode in 2 M NaCl solution as a function of the applied current density. $i_{Total}$ is the HE current density calculated from the steady state HE rate using the gravimetric method. $i_{Anod.}$ is the HE current density associated with the regions dominated by the anodic Mg dissolution reaction. $i_{Film+Imp.}$ is the HE current density values associated with the corrosion product and accumulation of noble impurities [61]. Reprinted with permission from Elsevier.

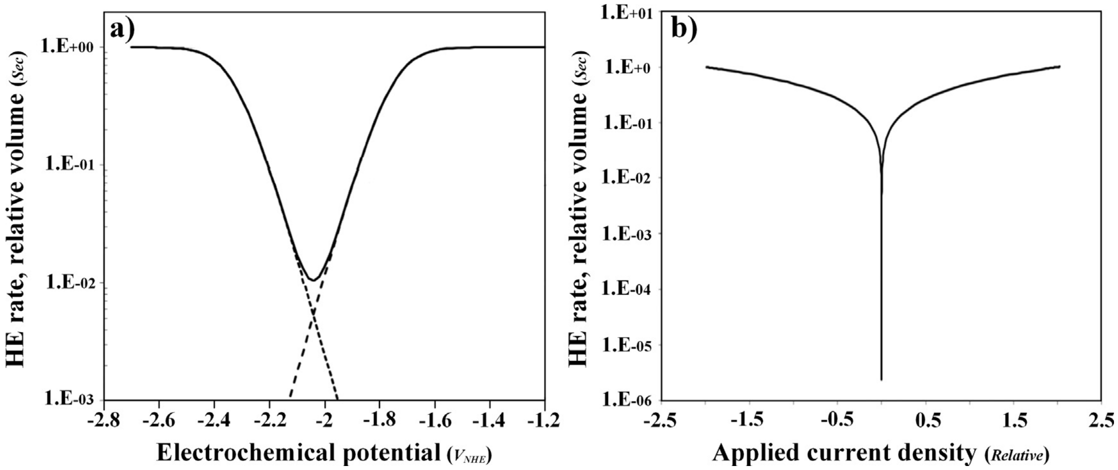

**Fig. 24.** DFT simulation of the anomalous HE on dissolving Mg surfaces. Model predicted HE rate as a function of (a) the applied potential, and (b) the applied current density [276]. Reproduced by permission of The Electrochemical Society.

components to the total HE current density according to Eq. (17). The values of $i_{Anod}$ were slightly lower than $i_{Total}$ and increased with the applied current density (as embodied by increased values of $i_{0,H,Mg}$). The values of $i_{Film+Imp}$ were much smaller, providing solid and direct evidence that primary source of anomalous HE are the regions dominated by the anodic dissolution reaction of Mg.

In a recent paper, Taylor [276] proposed a first-principles surface reaction kinetic model for HE on Mg. This model simulates the electrochemical response of an Mg surface under both cathodic and anodic polarization, and reaction rates were calculated using DFT simulation. The proposed mechanism is based on the following reactions:

$$2Mg^* + H_2O_{(l)} \rightarrow Mg^*OH + Mg^*H \tag{18}$$

$$2Mg^*H \rightarrow H_2 + 2Mg^* \tag{19}$$

$$Mg^*OH + e^- \rightarrow Mg^* + OH^- \tag{20}$$

$$4Mg^* + 2H_2O + 2e^- \rightarrow H_2 + 2OH^- + 4Mg^* \tag{21}$$

$$Mg^*OH + Mg_{(metal)} \rightarrow Mg^{2+} + OH^- + Mg^* + e^- \tag{22}$$

Eq. (18) describes how a molecule of water adsorbs on the Mg metal surface and dissociates to produce adsorbed atomic hydrogen and adsorbed hydroxy radical, consuming two metal sites ($Mg^*$). The adsorbed atomic hydrogen ($Mg^*H$) could recombine to produce $H_2$ that would leave the surface in the form of gas and restore two fresh metal sites (Eq. (19)).

Eq. (20) considers the electrochemical reduction of $Mg^*OH$, which makes new metal sites available, allowing for more water molecules to adsorb and dissociate (these being the source of atomic H). The sum of these equations just represents the water reduction reaction, Eq. (21). Dissolution of the Mg through the oxidation of the $Mg^*OH$ site by Eq. (21) would clear the surface of adsorbed OH under anodic polarization conditions. Estimation of some parameters was required, but the resultant prediction of the rate of HE as a function of potential mimicked that observed during $H_2$ collection experiments (see Fig. 24). This initial model assumes that water molecules adsorb and dissociate onto metallic Mg surface, and incorporation of an oxidized surface should be considered.

In this section, it has been shown that the dissolution mechanism of Mg is a complex process where different parameters such as the anodic regions, corrosion product formation and noble impurities present on the electrode surface (whether embedded in the corrosion film or electrochemically re-deposited after self-corrosion in the bulk solution) can play a role. It has also been shown that, among these several factors, experimental evidence suggests that the evolution of hydrogen at anodic potentials is dominated by the regions where the net anodic reaction occurs. However, more investigation is still needed to fully understand the influence of all the parameters involved in the process and to further elucidate the corrosion mechanism of Mg and anomalous HE.

### *3.3. Composition effects on the corrosion of Mg alloys*

The utility of Mg as an engineering or structural material necessitates alloying in order to achieve the required physical properties. Pure Mg alone, does not provide sufficient strength [16], and it has thus been alloyed from its early use in all but the applications where it was needed to serve as a sacrificial anode. From the very early usage of Mg alloys, it was noted that Mg-alloys were "*seriously handicapped by the uncertainties surrounding their resistance to corrosion*" [21]. It was further noted that whilst considerable efforts were being focused on alloying Mg for the purposes of developing strong alloys, considerably less effort had been focused on corrosion. Somewhat ironically, the situation remains to date, whereby whilst there has been much work studying the corrosion of Mg-alloys since the pioneering work of Boyer [21] and Hanawalt [277]; a focus on the development of corrosion resistant Mg-alloys has not been widespread. However, it can be stated that with some confidence that the role of a large number of alloying additions upon the corrosion of Mg has been elucidated in the recent decade by numerous works from around the world. To this end, such works are summarized herein in a concise manner where the key outcomes are emphasized, along with new advances and remaining challenges highlighted.

### *3.3.1. Solubility of metals in Mg*

When considering the influence of alloying upon the corrosion of Mg, it is important to take a metallurgical viewpoint in order to understand the nature of Mg as an alloy system. Compared to other engineering alloys, Mg is rather unique on the basis that a large number of elements have either very limited or no solubility in Mg. The solubilities of a large number of elements are <0.05 wt.% in pure Mg and such elements can be generalized as being insoluble in Mg [42]. This was recently highlighted in a review by Gusieva [42], who also noted that when alloying Mg, several forms of insolubility tends to occur. These forms of insolubility were summarized as: (i) complete and full insolubility (*i.e.,* Mg-Ge, Mg-Fe, and Mg-Nb), (ii) no solubility and the immediate formation of an intermetallic Mg-X compound (*i.e.,* Mg-Si), and (iii) some minor solid solubility followed by complete insolubility (*i.e.,* Mg-Zr). These three scenarios (i–iii) are unique, on the basis that classical alloying involves some solid solubility, followed by the formation of an intermetallic (which occurs in the Mg-Al or Mg-RE systems). The insolubility of elements in Mg presents a problematic scenario from a corrosion perspective for a number of reasons. Firstly, it means that Mg cannot be readily alloyed for the purposes of improving resistance to corrosion (such as the case of Cr additions for Fe forming so-called "stainless steels"), as outlined in [278,279].

Secondly, most elements are comparatively "more noble", given the electrochemically active nature of Mg, meaning that the electrochemistry of Mg-alloy surfaces is heterogeneous and localization of cathodes (and anodes) is established, leading to rapid corrosion rates. Such aspects are rationalized below. An abridged summary of the solubility of elements in Mg is presented herein in Fig. 25.

It is evident from Fig. 25 that only finite number of elements have appreciable solubility (*i.e.,* >1 wt.%) in Mg. Of the elements with some solid solubility in Mg, the vast majority have a high density (*i.e.,* they are comparatively heavy), and if alloyed with Mg, would render the use of Mg redundant on the basis that overall alloy density would be greater than alternate (*i.e.,* Al-based) alloys. As such, elements with appreciable solubility in Mg are not considered logical (for structural alloys), and therefore the overwhelming majority of all commercial Mg-alloys have compositions that typically have the following characteristics, (i) they contain second phase particles, (ii) the total alloy loading is <10 wt.%, (iii) they rely on alloying with Al in order to maintain a low density, and (iv), in Al-free systems, they rely on alloying with rare earth elements for strengthening. Examples of contemporary use of Mg-alloys were recently provided by Abbott [8]. An example of the evolution of corrosion rate (expressed as $i_{corr}$, the corrosion current density) with alloy loading is given in Fig. 26 for the Mg-Ce system.

It is evident from Fig. 26 that increased alloy loading dramatically increases the volume fraction of intermetallic phase present in the alloy microstructure (in spite of some solid solubility of Ce in Mg), with the loading of 4.76 wt.% Ce leading to ~20% volume fraction $Mg_{12}Ce$. In the case of Ce additions, it is revealed that alloying results in a near monotonic increase of corrosion potential ($E_{corr}$) and corrosion rate ($i_{corr}$) with alloying above the solubility limit ($C_s$) of 0.74 wt.% Ce. This relationship between $E_{corr}$ and $i_{corr}$ indicates that Ce alloying increases the cathode reaction kinetics upon Mg, resulting in

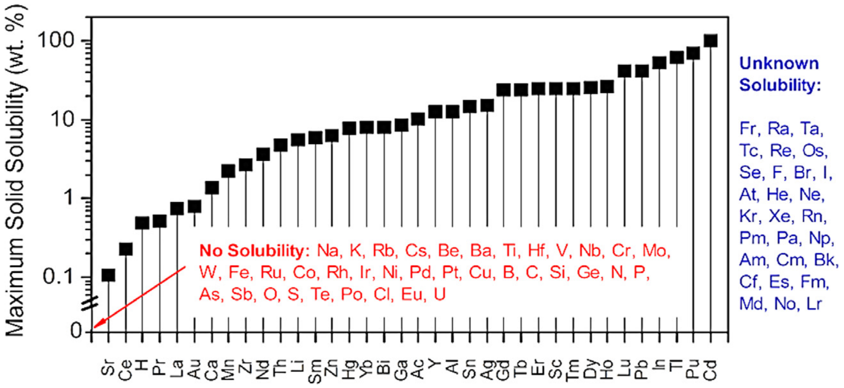

**Fig. 25.** Maximum solid solubility (at any temperature) of elements in Mg. All elements are listed, indicating that a large proportion of elements either have no solubility in Mg, or remain unexplored. Prepared from data in [26,39,280,281].

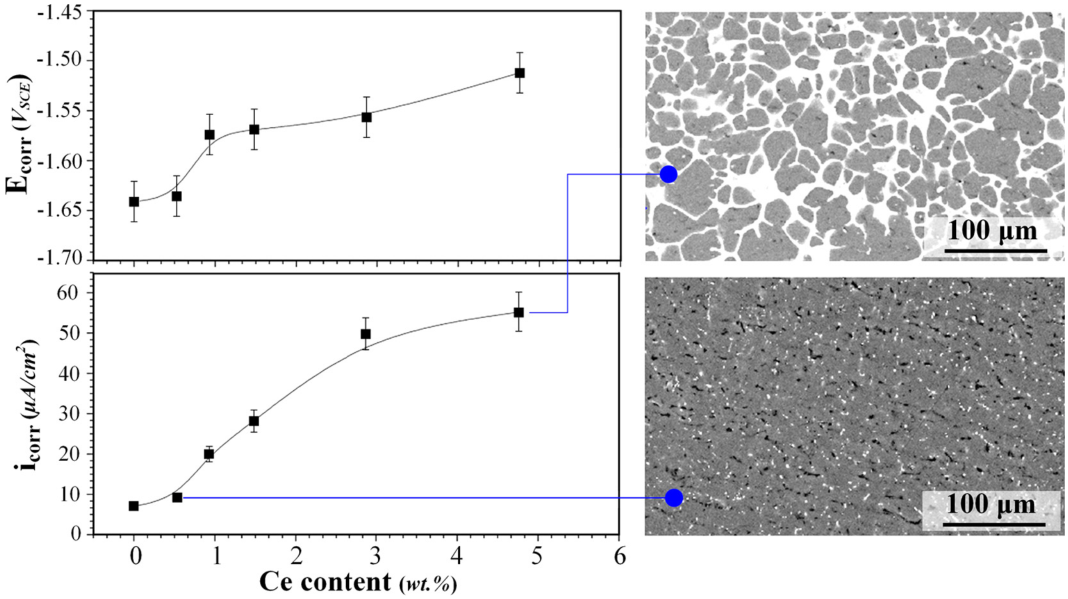

**Fig. 26.** Evolution of the corrosion potential ($E_{corr}$) and corrosion rate ($i_{corr}$) in 0.1 M NaCl as a function of Ce alloying in Mg. Corresponding backscattered electron micrographs shown, indicate the increase in volume fraction $Mg_{12}Ce$ intermetallic phase. Reproduced based on [14]. Reprinted with permission from Elsevier.

enhanced corrosion [14]. The same result in regards to microstructural evolution and trends in increased $E_{corr}$ and $i_{corr}$ has also been revealed for Mg alloyed with La, Nd, and Y [14,141,284,285].

### *3.3.2. Tolerance limits of metals in Mg*

From the earliest of classical works on the corrosion of Mg [21], the notion that Mg of "inferior quality" was "corroded badly" has been noted. The notion of tolerance limits for impurities in Mg has since become well recognized, and perhaps the most focus has been regarding the tolerance limit of Fe in Mg [278,282,283,286–288]. A focus on Fe is natural, given that ferrous metals can be found in cast houses, crucibles, tooling and even machining operations. Over the course of some decades, it has been empirically determined that a Fe tolerance limit of ~170 ppmw Fe in Mg is a limit beyond which corrosion rapidly accelerates [283]. However, tolerance limits equally stringent, if not more stringent, are also relevant to a number of transition metals, such as Cu, Co, Ni, Mo, and Cr. Hanawalt et al. [278] elucidated the effects of a number of different impurities in Mg, including Fe, Cu, and Ni – establishing tolerance limits, above which the corrosion rate of Mg increased dramatically. The values were ~170 ppm for Fe, 1000 ppm for Cu, and 5 ppm for Ni. McNulty and Hanawalt [22] also studied the corrosion of high purity of Mg in 3 wt.% NaCl using hydrogen collection and an early utility of anodic polarization, revealing that tolerance limits of metals in Mg is a critical aspect to assuring appropriate (and predictable) corrosion performance. The tolerance limits of impurities in Mg alloys and also the influence of alloy processing methods on the tolerance limits can be found in [289,290].

An abridged summary has been compiled, including the most recent literature, to present to so-called tolerance limits and the role of key alloying elements on the resultant corrosion rate of Mg (Fig. 27). The data in Fig. 27 is the most comprehensive synopsis to date, and has been carefully compiled in order to present the results in normalized units of mg/cm$^2$/day. This was done intentionally, as representations of Mg-alloy corrosion rates in the units of mm/year make the assumption of general corrosion, which has been shown to be an incorrect assumption [139,291]. It is however now well recognized that corrosion of Mg alloys proceeds with dynamic anodes and cathodes evolving upon the corroding surface [33,174,292].

The presentation of Fig. 27 provides important insights in its own right, as the deleterious effect of transition metals is evident. It seen that a large number of elements have the ability to dramatically increase the corrosion rate of Mg with increased loadings, including Sr [291], Ca [296], and rare earths [14,285,291]. Zr at low concentrations is also detrimental to corrosion [297]. It is also revealed that Al, Zn, and Mn have a moderate effect on the corrosion of Mg. Of the binary additions that were shown to unequivocally reduce the rate of Mg corrosion, only As and Ge have revealed an ability to impart corrosion resistance to Mg, as recently, and importantly, reported [294,295].

It is noted that the representation of data such as in Fig. 27, whilst important, is unable to provide a mechanistic insight into the response observed. To this end, the mechanistic influence of alloying is reported in the subsequent sections. Prior describing the mechanistic effects of alloying however, it merits comment to complete the description of impurity effects on the basis of revisiting the Fe effect. As reported by Simanjuntak et al. [288], arguably the single biggest contribution to corrosion protection of Mg and its alloys to date is the notion of intentionally adding Mn to the family of Mg-Al alloys

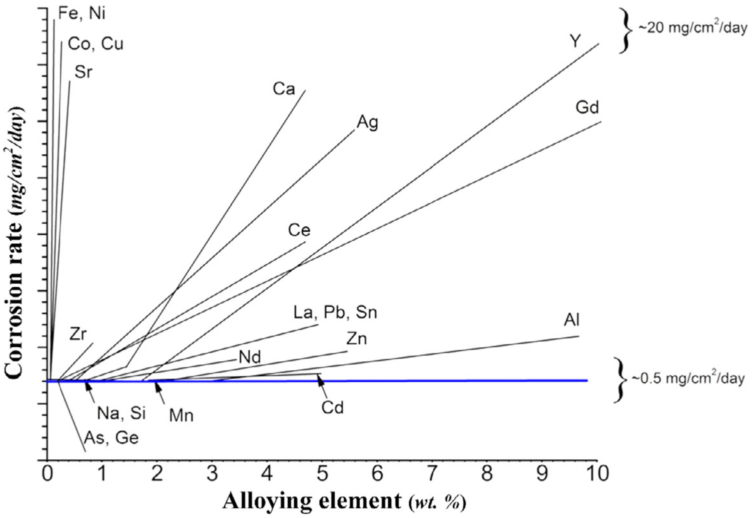

**Fig. 27.** Effect of alloying in the case of binary Mg-alloys in NaCl electrolytes, presented in the form of the original plot by McNulty et al. [278] and later Makar et al. [283]. The present representation has been inclusive of modern works, including those in [14,42,141,283–287,293,297]. Herein, the corrosion rate has been normalized to mg/cm$^2$/day to not make any assumptions regarding the morphology of corrosion. Indicative ranges of corrosion rates are also provided, whilst the trends in the role of alloying elements are the prime feature being presented.

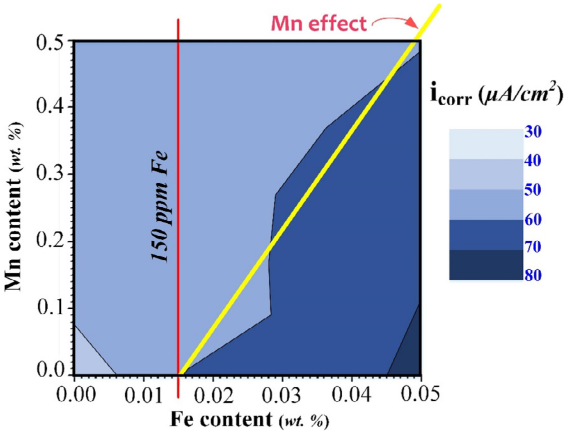

**Fig. 28.** Contour plot derived from empirical data indicating the variation in corrosion current density in 0.1 M NaCl over a finite range of Fe and Mn content, whereby the Fe content on the x-axis represents 0–500 ppmw. Reproduced based on [288]. Reproduced with permission from NACE International, Houston, TX.

[278]. To date, the Mg-Al alloys present the vast majority of commercial Mg-alloys. When Mn is added to Mg alloys containing Al, the impurity Fe is sequestered by the formation of an intermetallic compound with Al and Mn - in the general form of an $Al_xMn_yFe_z$ compound where the stoichiometry is composition dependent - decreasing corrosion rates dramatically. This effect is seen graphically in Fig. 28, indicating the so-called "Mn-effect" (or the "scavenging" ability of Mn) on a range of custom produced Mg-Mn-Fe alloys.

The so-called Mn effect, in spite of having been reported for nearly a century from empirical evidence, was recently revisited by Gandel and co-workers in the context of revealing Fe sequestration methods in not only Mg-Al alloys, but also in Al-free Mg alloys (such as the Mg-RE system) and Mg alloys that contain Zr for grain refinement. It was shown from such work that a hitherto unreported mechanism of Fe "encapsulation" from Mn was revealed (Fig. 29). This notion of Fe encapsulation has not previously been reported, but was definitively revealed and rationalized on the basis of solute rejection (of Mn from Fe) during melt solidification and cooling [287].

Such a finding indicates that the impurities in Mg alloys, and their potential interactions are both more complex than previously thought, but also very difficult to predict from CALPHAD analysis (*i.e.*, calculated phase diagrams from equilibrium thermodynamics). As such, there remains significant important work in regards to unambiguously characterizing the so-called Mn-effect in order to engineer its deployment in new Mg-alloy systems including those that may include diverse alloying elements.

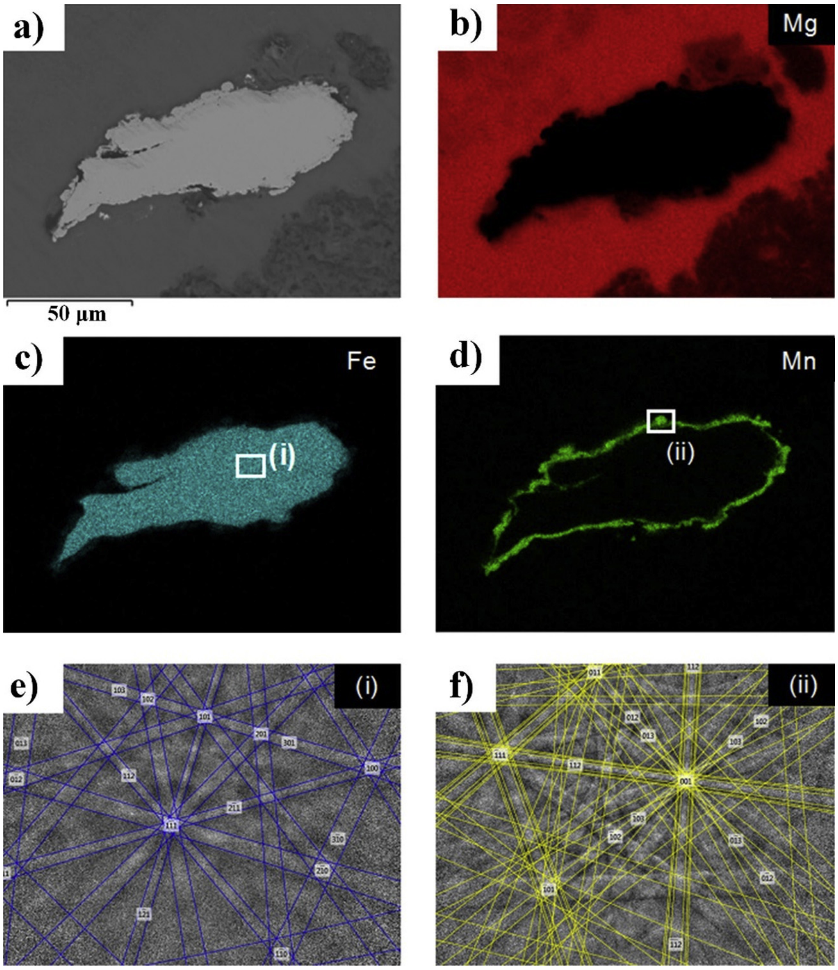

**Fig. 29.** (a) BSE-SEM image of Mn-Fe particle in Mg alloy Mn-Zr-Fe. (b) Corresponding EDX map of Mg content. (c) Corresponding EDX map of Fe content. (d) Corresponding EDX map of Mn content. (e) EBSD Kikuchi pattern of internal structure of Mn-Fe particle (region denoted as (i). (f) EBSD Kikuchi pattern of outside layer of Mn-Fe particle (region denoted as (ii)) [287]. Reprinted with permission from Elsevier.

### *3.3.3. Synopsis of alloy chemistry upon Mg alloy corrosion*

One of the most defining features of Mg-alloys in regards to their electrochemical characteristics is that due to the limited solubility of most elements in crystalline Mg, only rather minimal changes to the corrosion potential ($E_{corr}$) of Mg-alloys are realized. This was summarized recently in a compilation by Cain and co-workers, and abridged in Fig. 30.

From Fig. 30 it is apparent that the relative confinement of the corrosion potential is inclusive of a number of commercial and experimental alloys. This however, may be anticipated on the basis that in the preceding section it was revealed that Mg is weakly polarizable [54]. Due to the very low Tafel slope of the anodic reaction (see Eq. (7) in Section 3.1), great variations in chemistry have only a minimal effect on $E_{corr}$. Fig. 30 also reveals the range of potentials that are realized for Mg containing intermetallic particles, and Mg-based glasses. The latter, non-crystalline forms of Mg will not be extensively reviewed herein, however it merits comment that Mg-glasses have the following characteristics. They include compositions that include appreciable alloying additions [298–300]; compositions that have glass-forming ability (nominally based on the Mg-Ca-Zn system, or the Mg-Cu-Y system [301,302]); and have been shown to suffer incongruent dissolution, with corrosion rates not superior to crystalline Mg alloys [303]. Claims of superior corrosion resistance of Mg-based metallic glasses are generally unable to be confirmed by detailed studies, whilst the notion that Mg is selectively dissolved (*i.e.,* by dealloying at potentials where Mg oxidation is favored) means that Mg-glasses are predisposed to incongruent dissolution.

Of the intermetallic phases that nominally form in Mg-alloys, the electrochemical response of such intermetallic particles in isolation is presented in Fig. 31. The study by Sudholz et al. [304] regarding the electrochemical response of Mg-based intermetallics remains the most comprehensive to date, revealing that all intermetallics surveyed – with the notable exception of $Mg_2Ca$ – possess a corrosion potential more noble than pure Mg. As such, intermetallic particles in Mg-alloys will nominally serve as local cathodes (as at the potential of the Mg-alloy they populate, they will be polarized cathodically).

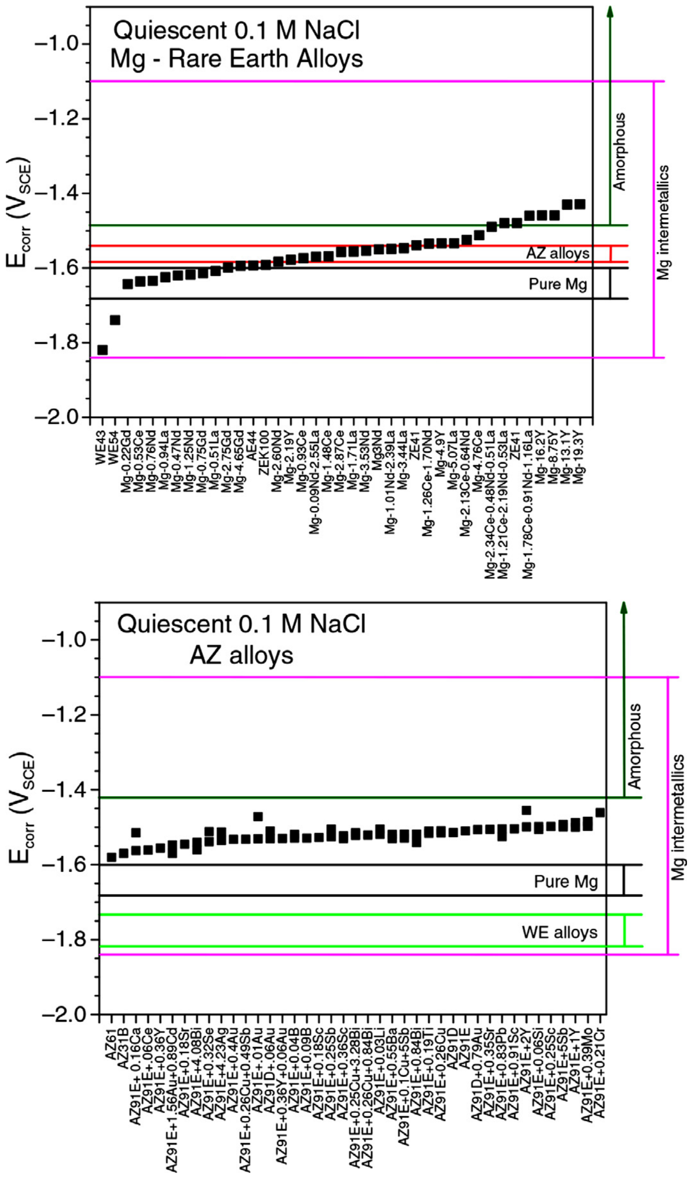

**Fig. 30.** (Top) Summary of AZ alloy corrosion potentials ($E_{corr}$) measured in quiescent 0.1 M NaCl, (bottom) Summary of corrosion potentials ($E_{corr}$) in quiescent 0.1 M NaCl for rare earth containing to Mg-alloys. Note: Alloying additions to Mg are in wt.%. [252]. Reproduced with permission from NACE International, Houston, TX.

The ability of each intermetallic to sustain the cathodic reaction (which for the potentials of interest is the reduction of water), varies according to their composition.

In regards to the corrosion rates measured upon Mg-alloys, the compilation of data empirically collected to date reveals a unique feature distinct to Mg-alloys. This feature was noted by Kirkland et al. [305] who surveyed a range of Mg-alloys in simulated body fluid. That study revealed that depending on the alloy composition, the resultant corrosion rate could vary over several orders of magnitude. Furthermore, based on the preceding discussion, such wide variations in the resultant corrosion rate arise as a result of minimal change in corrosion potential, and based on the limited solubility of metals in Mg, with limited alloy loading. Such wide variations in corrosion are not observed in other alloy systems, meaning that the range of corrosion rates realized on Mg cover a spectrum from moderate to extremely rapid. For example, an Mg-5Ca was reported to corrode at an equivalent penetration rate of >50 mm/year (>24 mg/cm$^2$/day) [305].

Compiling the available data on the corrosion of Mg-alloys in a standard electrolyte, namely quiescent 0.1 M NaCl (pH 6), Gusieva presented a compilation of corrosion rates for Mg-alloys in units that are independent of any assumptions of cor-

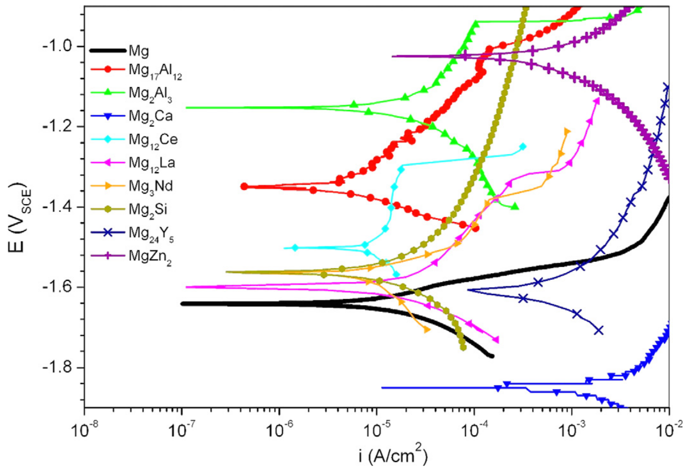

**Fig. 31.** Potentiodynamic polarization curves for intermetallic phase present in, and common to, the Mg-alloys systems. The data was collected using the microelectrochemical capillary cell method, and is presented along with pure Mg for comparison (40 ppm by wt. Fe), in 0.1 M NaCl [304]. Reproduced with permission from NACE International, Houston, TX.

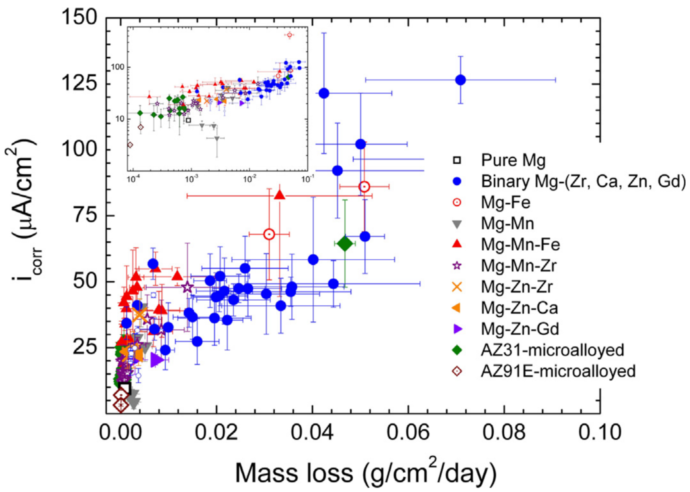

**Fig. 32.** Corrosion rate expressed as corrosion current density ($i_{corr}$) versus mass loss rate (mass loss determined from 1 day exposure in 0.1 M NaCl). Inset shows same data, with logarithmic axes [283]. Reproduced with permission from NACE International, Houston, TX.

rosion morphology. This compilation is shown below in Fig. 32, revealing a spread of corrosion rates of 3 orders of magnitude.

### *3.3.4. A kinetic framework for compositional effect upon Mg corrosion*

The wide range of corrosion rates realized for Mg-alloys (as revealed in Fig. 32) is a useful compilation in an engineering sense, however similar to the reportage of impurity tolerance limits, such representations do not reveal the mechanistic aspects responsible for corrosion rates. In order to determine the mechanistic aspects that dictate the corrosion rates realized upon Mg-alloys, potentiodynamic polarization testing is the most convenient method to employ – as it provides information regarding anodic and cathodic reaction rates sustained by a given alloy. There are obvious caveats such as the destructive nature of potentiodynamic polarization tests, and such tests being an instantaneous (*i.e.,* not long term) test, however for the purposes of inspection and comparison of anodic and cathodic reaction rates, no alternate method is more appropriate. An example of potentiodynamic polarization data is given in Fig. 33, which reveals typical polarization curves realized on pure Mg and a number of Mg-binary alloys. The binary alloys reported in Fig. 33 were all carefully prepared and homogenized in order to consist of a microstructure that was a uniform single-phase solid solution [291].

Inspection of Fig. 33 alone reveals that in all cases, the alloying additions (which are considered to be relatively minor, <1 wt.%, and confined to solid solution) resulted in an increased $E_{corr}$, and a movement of the cathodic branch of the polarization curve to the right - concomitant with enhanced cathodic kinetics. As a consequence of the inspections such as those

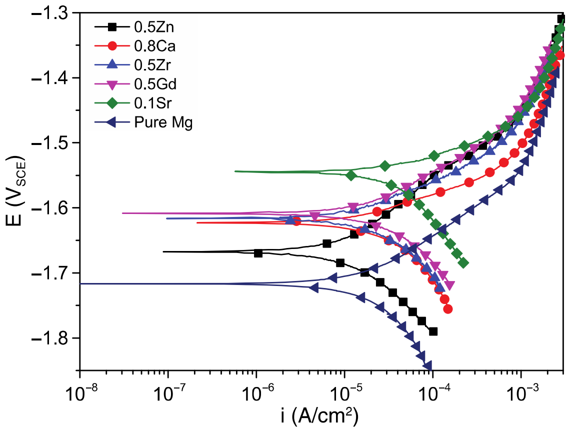

**Fig. 33.** Typical potentiodynamic polarization curves for homogenized (i.e., solution heat treated and quenched) binary Mg-alloys tested in 0.1 M NaCl at 25 °C. The data presented is uncorrected for ohmic drop. Compositions are given in wt.%. [291]. Reproduced with permission from NACE International, Houston, TX.

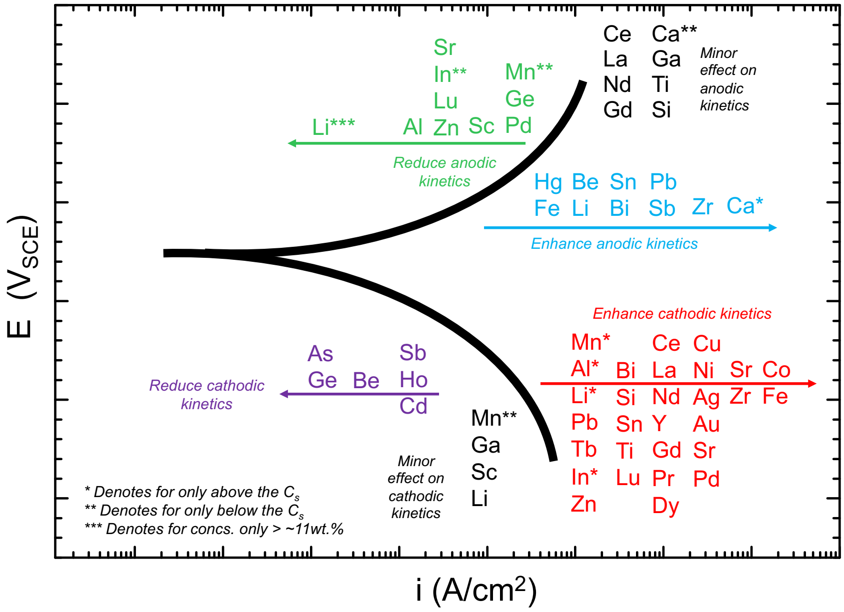

**Fig. 34.** Schematic representation of the electrochemical impact of alloying elements in Mg (data was derived from that reported in [35,42,291,294,306]). The schematic depicts the ability of alloying additions to modify either anodic or cathodic kinetics (or both). $C_S$ represents solid solubility.

made here for the data in Fig. 33, it is possible to assess the reported polarization curves for Mg-alloys in the literature to date; to determine the phenomenological effect of alloying on reaction kinetics. To this end, a schematic of alloying effects was reported initially by Gusieva, and such a form of representation has been adopted herein whilst being modified to incorporate the most recent literature reports (Fig. 34). The result is a unified presentation that provides a holistic overview of the influence of alloying upon either the anodic or cathodic reaction rates sustained by Mg.

The information provided in Fig. 34 is an abridged consolidation of over 1000 unique tests, and unequivocally represents the state of the art in regards to understanding the influence of alloying on Mg corrosion. The understanding comes from the ability to interpret the effect of alloying on either the anodic or cathodic partial reaction; and the extent (indicated by the distance along the respective arrow) to which the partial reaction is influenced. Direct observation of Fig. 34 reveals that a large number of alloying additions enhance cathodic kinetics. Under open circuit conditions, this results in enhanced corrosion. This mechanism of corrosion rate enhancement (*i.e.*, cathodic activation) in Mg alloys, is now considered a hallmark of Mg corrosion. It is recalled that such cathodic activation has been shown to occur even in the case of pure Mg following Mg

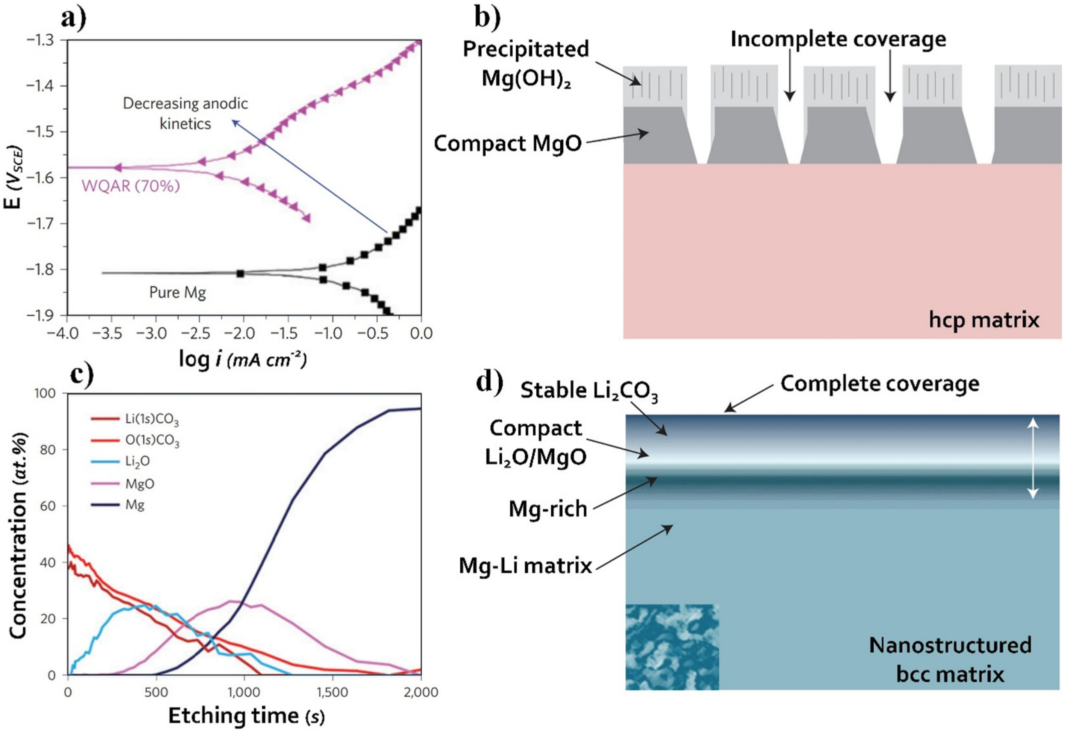

**Fig. 35.** The superior corrosion resistance of an Mg-Li alloy. (a) Potentiodynamic polarization curve for pure Mg and a water quenched and cold-rolled (WQAR (70%)) Mg–Li alloy after immersion in 0.1 M NaCl, (b) XPS depth profile of the Mg-Li alloy, showing the various surface layers present, (c) schematic of the incomplete coverage of the surface film developed on conventional hcp Mg, and (d) complete coverage of a thicker surface film on the solute nanostructured bcc Mg–Li alloy. The inset in d denotes the solute nanostructure [35]. Reprinted by permission from Macmillan Publishers Ltd: Nature Materials, copyright 2015.

dissolution [34,266], however, the notion of cathodic activation in the case of Mg alloys in undoubtedly also enhanced by surface enrichment of noble alloying elements [169,179,180,184], also see Fig. 10a in Section 2.3.7. Such surface enrichment of noble alloying elements was depicted rather elegantly in several recent works, whereby the apparent surface enrichment of noble elements is attributed to the selective dissolution of Mg from the surface during polarization or corrosion [169,179,180,184].

Fig. 34 also reveals that a large number of elements can activate the anodic reaction. This has been attributed to several mechanisms (focusing on only those with the greatest effect) including the high reactivity of Ca; the disruption of any partially protective surface film by low melting point metals such as Sn or Pb; or the anodic activation imparted by Zr [307]. In cases where the alloying element is capable of suppressing the anodic kinetics, then this is nominally offset or superseded by a concomitant increase in cathodic kinetics, such that corrosion rates are either similar or slightly enhanced with alloying. Examples in this category include Al, Zn, and Mn. One notable, recent exception is the addition of >11 wt.% Li was recently revealed to offer significant restriction of anodic dissolution kinetics [35]; shown in Fig. 35a. In the case of heavy Li loadings, the crystal structure of the Mg matrix is bcc (as opposed to hcp for conventional Mg alloys). This change in substrate crystal structure, together with a microstructure free from coarse particles, and the heavy Li loading, were all posited to contribute to superior corrosion resistance. The restriction of anodic kinetics was principally attributed to the dynamic development of a carbonate rich surface film, which was carefully characterized by photoelectron spectroscopy (Fig. 35b) [287]. The enhanced corrosion resistance of the bcc Mg-Li system (which was noted to be enhanced by thermomechanical processing [35]) was subsequently validated using on-line ICP-MS [308], supporting the phenomenological surface structure and chemistry presented in Fig. 35c and d. Other than the unique Mg-Li based system recently reported, no other reports of restriction of anodic kinetics for Mg are prevalent.

Once again, from inspection of Fig. 34, it is possible to explore which elements have some ability to restrict the cathodic reaction rate upon Mg. It has been recently revealed that arsenic (As) is rather potent at the retardation of cathodic kinetics upon Mg [294,309]. This can also be seen pictorially from Fig. 36. Such an inhibiting effect on the cathodic reaction was able to reduce the rate of corrosion of Mg by a large extent, reducing the hydrogen evolved (from water reduction) by about an order of magnitude (with a 0.37 wt.% addition of As to Mg). More recent work has focused on reproducing the cathodic inhibition effect imparted by As, and has also identified Ge as a suitable corrosion inhibiting element [295]. The notion of such functional alloying additions, and the notion of imparting suppression of cathodic kinetics (so again, kinetically restricting corrosion) is not an area that had previously been adequately tackled. Detailed analysis using the SVET has provided some

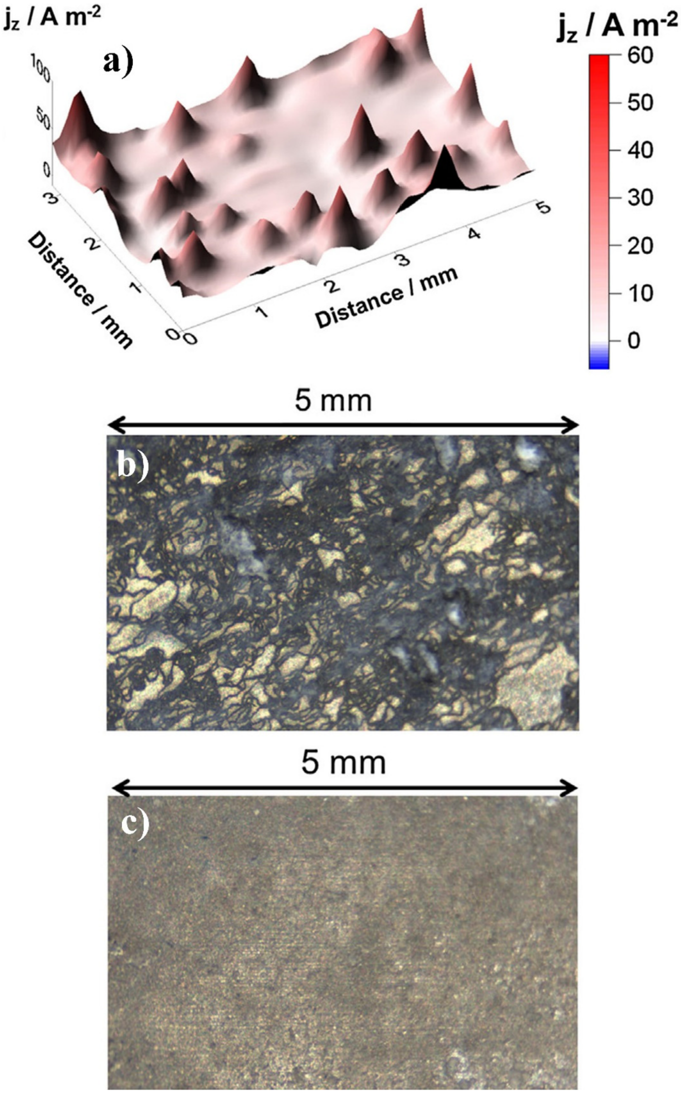

**Fig. 36.** Surface plot showing SVET determined current ($j_z$) distribution above an Mg-0.37 wt.% As specimen (a) recorded after 2 h of galvanostatic polarization at 1 mA cm$^{-2}$ in 0.1 mol dm$^{-3}$ NaCl(aq) at pH 7. Images comparing the appearance of pure Mg and Mg-As after 6 h anodic polarization are shown in (b) and (c) respectively [309]. Reprinted with permission from Elsevier.

insight into the mechanistic aspects of protection, however there is considerable future work to be done in order to understand (let alone mimic and optimize) the ability to restrict cathodic kinetics.

Prior to concluding this section, a comment regarding alloy processing is also warranted. For example, there are numerous studies that report the performance of a single Mg alloy, which has been prepared or processed utilizing a number of methods to achieve a specific grain size, texture, or simply, severe deformation. Such aspects were review briefly by Gusieva [41], however it can be stated that processing will have at least some influence on Mg corrosion. This is because alloy processing (such as extrusion, and rolling) can impact the distribution of solute, revolutionize intermetallic particles, or alter texture [36,140,145,149,310]. However, as can be observed from Fig. 36, the corrosion rates realized from a variety of Mg alloys span over many orders of magnitude. On the influence of alloy processing upon corrosion, whilst alloy processing may alter the rate of corrosion by some degree, the overall change of corrosion rates arising from a change in alloy chemistry is much more dominant. This was shown recently by Xia et al. [306], who concluded that chemistry effects dominate processing effects on the issue of corrosion.

### 3.4. Role of reinforcing phases/particles

Mg-MMCs combine the specific strength and castability of Mg alloys with the unique properties of the reinforcement, and thus, could be promising candidates for many lightweight applications in the automotive and aerospace industries. The rein-

**Table 2**
List of typically studied reinforcements in Mg-MMCs [318,319].

| Type | Reinforcement |
|---|---|
| Carbon-based | SiC, C (fiber, CNT, MWCNTs), TiC, $B_4C$ |
| Oxides | $Al_2O_3$, $SiO_2$, $ZrO_2$, MgO, $Y_2O_3$, $TiO_2$ |
| Bioapplications | Tri-calcium phosphate, Hydroxyapatite, Fluorapatite, Bredigite, etc. |
| Borides | $TiB_2$, $ZrB_2$ |
| Nitrides | $Si_3N_4$, AlN |
| Other | $Ti_2Al$, $Mg_2Si$, metallic (Cu, Ni, Al, Cu, Mo, Fe) |

forcement is typically – although not exclusively – a ceramic with a high melting point [311], wear resistance and high stiffness. The main rationale behind developing Mg-MMCs is related to the fact that Mg alloys on their own are more prone to wear, creep and thermal shock restricting their implementation in several applications. In fact, the strength increase that has been reported to arise in the case of Mg-MMCs is not significant [312], and aforementioned wear, creep, and thermal expansion properties are sought to be improved by appropriate reinforcing phases or particles.

The corrosion behavior of Mg-MMCs has received relatively little attention, with the research similar to those of Al-MMCs [313], focused mainly on mechanical properties. The earliest corrosion research upon Mg-MMCs indicated that they have a strong tendency for corrosion [314–316]. Generally speaking, the Mg-MMCs are prone to galvanic corrosion both during immersion in aqueous solutions and also by exposure to moisture in the atmosphere [311,317–320]. The galvanic corrosion cells form in Mg-MMCs between; (*i*) the metal matrix and the cathodic reinforcements (*e.g.*, carbon fibers [318]), and (*ii*) the metal matrix and other electronically conducting compounds that form during processing, including reaction products and intermetallic phases (*e.g.*, $Mg_2Si$ [321]). Also, commercially available reinforcing particles which have been used in most studies (see Table 2) contain comparatively "noble" impurities such as Fe, Ni, Ti, and Mo (as detailed in Section 3.3) which could cause corrosion of the Mg-MMC [322]. Herein, a concise review is provided regarding; (i) the effect of processing on the formation of the most important interfacial reactions, (ii) the relationship between the microstructure and corrosion of Mg-MMCs, and (iii) recent developments and future challenges in the context of corrosion of Mg-MMCs.

### 3.4.1. Reinforcements for Mg-MMCs

Some important parameters used to evaluate a reinforcement from the perspective of both mechanical properties and corrosion resistance include, morphology, volume fraction, size, distribution, orientation and reactivity of the reinforcement. The MMCs are often classified according to the aspect ratio (length : diameter) of the reinforcement, as this indicates whether the reinforcement is particles, whiskers or short fibers, continuous fibers, laminates or sheets [319,323]. The particle-reinforced materials which are the focus of this section, exhibit attractive characteristics such as isotropic behavior and also can be easily processed by conventional methods. Ceramic reinforcements such as carbides, borides and oxides are commonly used in Mg-MMCs (Table 2) [323]. In fact, the SiC particulates have been widely investigated reinforcements due to their easy availability, stability in many molten Mg alloys and relatively good wettability with Mg [323]. Recently, reinforcing particles such as fluorapatite [320], tri-calcium phosphate [324], poly(lactic-co-glycolic acid) [325] or hydroxyapatite [326] have been used to develop bio-degradable Mg-MMCs. These reinforcements serve to alter the corrosion rate of the Mg alloy and could also promote the formation of apatite-layers on the MMC surface, during the bone-healing process.

### 3.4.2. Manufacturing routes and interfacial reactions

The mixing of the Mg/Mg alloy matrix and reinforcements can be performed *via* liquid-state, solid-state, semi-solid and also by deposition processes [318,323,327–329] (details are given in Table 3). The processed Mg-MMCs (with pure Mg, Mg-Al-Zn, Mg-Al-Mn and Mg-Zn alloys as the dominant matrices) exhibit compositions and microstructures close to that of un-reinforced alloys. However, one important difference between the reinforced and un-reinforced systems is the formation of interfacial reaction products. Several interfacial reactions could occur at the reinforcement/molten Mg interfaces [318,323]. Some probable reactions that could occur at the interface of ceramic reinforcements and molten Mg are presented in Eqs. (23)–(33). The nature/type of the reaction depends on the manufacturing method and governs the physical properties of the MMCs [328–331]. When the processing is performed at higher temperatures, liquid-state processes may occur (see Table 2), which could promote the formation of interfacial products between the matrix and reinforcements [135,318,319,332,333].

$$Al_2O_3 + 3Mg \rightarrow 3MgO + 2Al \tag{23}$$

$$4Al_2O_3 + 3Mg \rightarrow 3MgAl_2O_4 + 2Al \tag{24}$$

$$Al_2O_3 + MgO \rightarrow MgAl_2O_4 \tag{25}$$

$$SiC + 2Mg \rightarrow Mg_2Si + C \tag{26}$$

**Table 3**
Summary of characteristics of common processing techniques used for Mg-based MMCs. Note: Characteristics are summarized based on [318,323,327–329].

| Process | Characteristics |
|---|---|
| Liquid-state | ✓ Low cost<br>✓ Ability to produce complex and thin walled components<br>✓ More common than solid-state processes |
| Stir-casting | ✓ Reinforcement added into the melt followed by casting or conventional forming<br>✓ Simplest and most cost effective method for discontinuous reinforcement<br>✓ Mixing by mechanical stirring or by other means<br>✓ For particle-reinforced MMCs with <30% volume fraction<br>× Difficult control of melt viscosity<br>× Reinforcement segregation (sinking or floating depending on the density)<br>× Undesirable intermetallics formed by reaction between melt and reinforcement |
| Gas pressure infiltration | ✓ Pre-form is infiltrated with a molten alloy through an applied inert gas<br>✓ Capable of producing particle-reinforced MMCs with >30% volume fraction (including fiber-reinforced)<br>✓ Short processing time reduces interfacial reactions<br>✓ Production of partially reinforced components is possible<br>× Reinforcement can be damaged<br>× Lower pressures and higher processing times than squeeze casting<br>× Coarsened microstructures |
| Squeeze casting | ✓ Pre-form is infiltrated with a molten alloy under pressure<br>✓ Widely used for Mg-MMCs (including fiber-reinforced)<br>✓ Up to 40–50% volume fraction<br>✓ Short processing time reduces interfacial reactions<br>✓ Low porosity and fine-grained microstructures suitable for heat treatment<br>✓ Production of partially reinforced components is possible<br>× High pressures may promote gas entrapment and Mg oxidation<br>× Not useful for large scale production |
| Semisolid processing (compo-casting when referred to MMCs) | ✓ Reinforcement added into semisolid slurries followed by casting or conventional forming<br>✓ Mixing by mechanical stirring or by other means<br>✓ Enables better mixing than stir-casting due to larger shearing forces<br>× Reinforcement tends to form clusters<br>× Undesirable intermetallics formed by reaction between matrix and reinforcement<br>× Gas absorption has to be avoided during mixing |
| Solid-state | ✓ Lower processing temperatures than liquid-state processes (avoids undesirable reactions)<br>✓ Capable of producing high volume fraction composites<br>× More costly and time consuming than liquid-state processes |
| Powder metallurgy | ✓ Matrix powder and reinforcement with a certain size relationship are blended and subsequently consolidated by processes such as extrusion or forging<br>✓ Even distribution of reinforcement (discontinuous is preferred) |
| Diffusion bonding | ✓ Matrix and reinforcement in good contact at elevated temperature and pressure<br>✓ Wide variety of matrixes<br>✓ Control of volume fraction<br>× Long processing times<br>× High temperature and pressure<br>× Complex shapes are difficult to obtain |
| Deposition | ✓ Capable of producing a wide range of composites<br>× Less common than liquid- and solid-state processes |
| Spray | ✓ Liquid, semisolid and/or solid particles (matrix and discontinuous reinforcement) are deposited at high speed on a substrate for manufacture of semifinished products (ingots, tubes, and strips)<br>✓ Low matrix segregation and uniform distribution of reinforcement<br>✓ Suitable for alloys of poor castability<br>× 95% of theoretical density is common<br>× A subsequent consolidation step is needed<br>× Some limitations due to explosive nature of Mg powder |

$$3\mathrm{SiC} + 4\mathrm{Al} \rightarrow \mathrm{Al_4C_3} + 3\mathrm{Si} \tag{27}$$

$$3\mathrm{SiC} + 4\mathrm{Al} + 6\mathrm{Mg} \rightarrow 3\mathrm{Mg_2Si} + \mathrm{Al_4C_3} \tag{28}$$

$$2\mathrm{SiC} + \mathrm{Al} + 4\mathrm{Mg} \rightarrow 2\mathrm{Mg_2Si} + \mathrm{AlC_2} \tag{29}$$

$$2\mathrm{SiC} + \mathrm{Al} + 5\mathrm{Mg} \rightarrow 2\mathrm{Mg_2Si} + \mathrm{Al_2MgC_2} \tag{30}$$

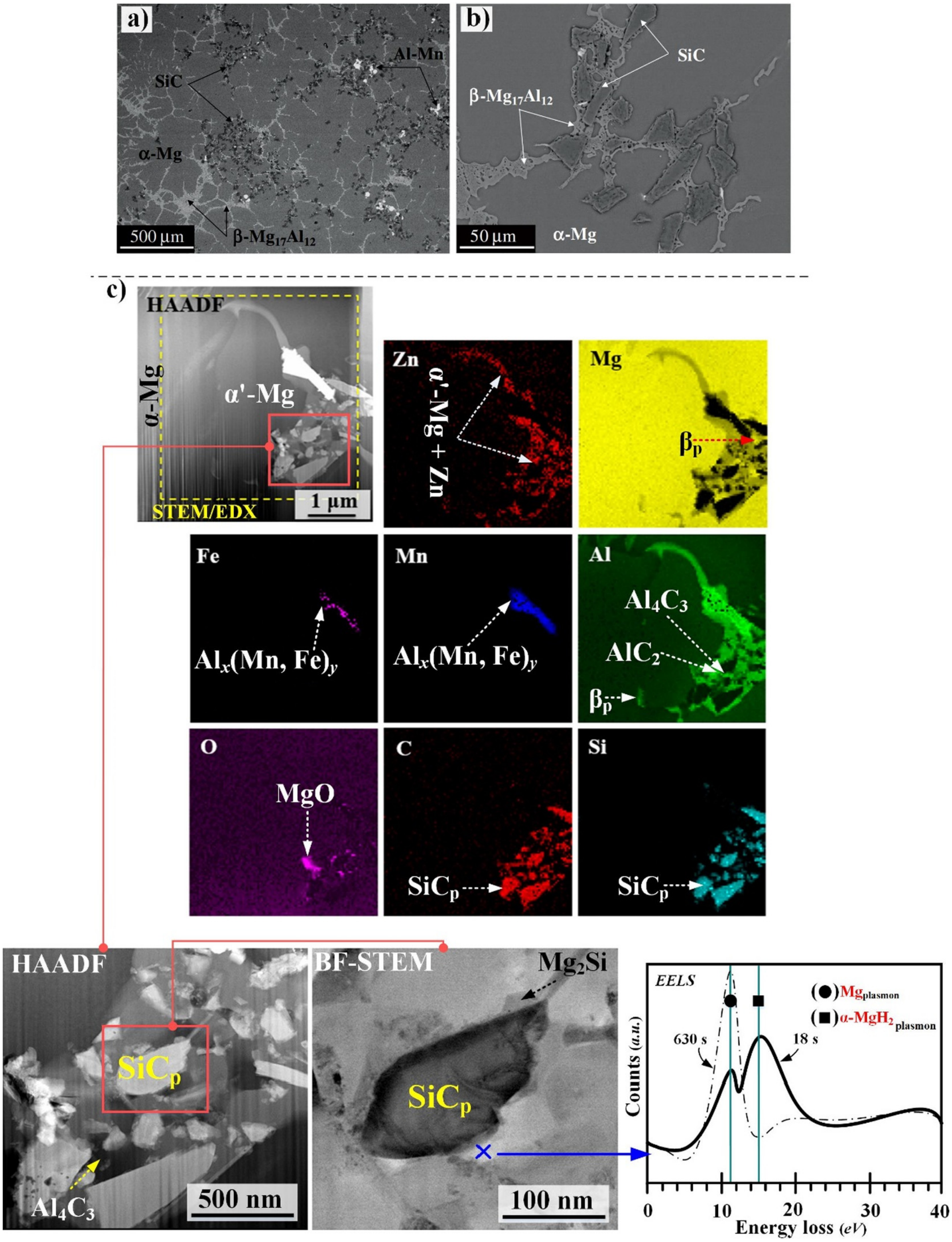

**Fig. 37.** The Microstructure and interfacial reactions in SiC reinforced Mg-based MMCs. The microstructure of SiC-reinforced MMCs (a and b) Scanning electron micrographs of AZ91/SiC composite obtained via semisolid processing [322,337], and (c) STEM micrographs (taken at different magnifications) and STEM/EDX maps of AZ91D/SiC as well as a time-resolved (low-loss) EELS spectra providing evidence for the formation of Mg hydride (reproduced based on reproduced based on [135]). Reproduced with permission from Elsevier.

$$2C + Mg \rightarrow MgC_2 \tag{31}$$

$$2C + 3Mg \rightarrow Mg_3C_2 \tag{32}$$

$$3C + 4Al \rightarrow Al_4C_3 \tag{33}$$

**Table 4**
Summary of corrosion data for Mg-based MMCs. Note that fraction of reinforcement is in vol.% unless otherwise specified. Note (1): Corrosion rates were converted into mg/cm$^2$/day by the authors using the original available data. Note (2) (p) Particle, (mf) monofilament, (f) fiber, (sf) short fiber, and (w) whisker.

| Ref. | Matrix and reinforcement | | Processing and reinforcement specs | Environment | Corrosion rate (mg/cm$^2$/day $^1$) | Current density (mA/cm$^2$) | Comments |
|---|---|---|---|---|---|---|---|
| 1986 [314] | AZ31B | 26.5% C | Hot pressing<br>C(f) 100 µm length<br>$TiB_2$ + AZ91C coating | N NaCl<br>pH 8.4 | 1.8 (for 10% surface area of exposed graphite) | – | – Galvanic corrosion between matrix and reinforcement |
| 1987 [315] | Mg-1% Al | 30% C | Squeeze casting<br>C(f) T300 PAN-based | Ambient conditions | $0.05^*$ | – | – Galvanic corrosion between matrix and reinforcement<br>– Interfacial reaction $Al_4C_3$ |
| 1993 [316] | ZE41 | 0% SiC<br>50% SiC | Not specified processing<br>SiC(mf) | 0.5 M $NaNO_3$ oxygenated (30 °C) | $\sim 3.5^*$<br>$\sim 18^*$ | – | – Galvanic corrosion at matrix/reinforcement<br>– Carbon-rich surface on reinforcement |
| | | | | 0.5 M $NaNO_3$ de-aerated (30 °C) | $\sim 4.3^*$<br>$\sim 7^*$ | – | |
| 1994 [338] | ZE41 | 0% SiC<br>50%SiC | Not specified processing<br>SiC(mf)<br>140 µm diameter | 3.15 wt.% NaCl<br>0.5 M $Na_2SO_4$<br>0.5 M $NaNO_3$<br>de-aerated and oxygenated | $3.5–5^*$<br>$4–40^*$ | – | – Results of Mg/SiC are also presented<br>– Galvanic corrosion between matrix and reinforcement<br>– Carbon-rich surface on reinforcement |
| 1995 [339] | ZC71 | 0% SiC<br>12% SiC | Stir-casting and extrusion<br>SiC(p) < 20 µm | Salt spray | $<2^*$<br>$<40^*$ | Electrochemical data in 3.5 wt.% NaCl is presented graphically | – Less protective surface film due to reinforcement<br>– No evidence of galvanic corrosion between matrix and reinforcement |
| 1996 [340] | Mg | SiC | Magnetron sputtering<br>Model MMC<br>SiC(p) 3 µm | 3.5 wt.% NaCl | – | 0.010 | – No evidence of galvanic corrosion between matrix and reinforcement |
| 1998 [341] | AZ91C | 0% $Al_2O_3$<br>20% $Al_2O_3$ | Cast ingot<br>$Al_2O_3$(sf)<br>5 µm diameter<br>50 µm length | 3.5 wt.% NaCl<br>pH 10.5 | 0.4<br>3.0 | Graphically presented | – Less protective surface film due to reinforcement |
| 1998-2004 [342–346] | ZK60 | 17% SiC | Powder metallurgy<br>SiC(p) 3 µm | 3.5 wt.% NaCl | $\sim 10^*$ | 0.960–1.56 | |
| 2004 [347] | AZ80A | 20% SiC | Powder metallurgy<br>SiC(p) 3 µm | 0.1 N NaCl | 36 | 529 (1 h)<br>884 (24 h) | – Less protective surface film due to reinforcement |
| | | 20% SiC | | 1 N NaCl | 57 | 3920 (1 h)<br>5676 (24 h) | |
| | | 20% SiC | | 0.1 N $Na_2SO_4$ | 0.22 | 84 (1 h)<br>109 (24 h) | |
| | | 20% SiC | | 1 N $Na_2SO_4$ | 1.8 | 148 (1 h)<br>252 (24 h) | |
| | ZK60A | 20% SiC | | 0.1 N NaCl | 27 | 407 (1 h)<br>460 (24 h) | |
| | | 20% SiC | | 1 N NaCl | 72 | 1365 (1 h) | |

(*continued on next page*)

**Table 4** (*continued*)

| Ref. | Matrix and reinforcement | | Processing and reinforcement specs | Environment | Corrosion rate (mg/cm$^2$/day $^1$) | Current density (mA/cm$^2$) | Comments |
|---|---|---|---|---|---|---|---|
| | | | | | | 1466 (24 h) | |
| | | 20% SiC | | 0.1 N $Na_2SO_4$ | 0.19 | 107 (1 h)<br>64 (24 h) | |
| | | 20% SiC | | 1 N $Na_2SO_4$ | 1.62 | 147 (1 h)<br>117 (24 h) | |
| 2005 [348] | AZ91D | 0% TiC<br>5% TiC | Stir-casting<br>TiC(p) 1–2 μm | 3.5 wt.% NaCl | ∼5$^*$<br>∼60$^*$ | Graphically presented | – Galvanic corrosion between matrix and reinforcement |
| 2005 [349] | AZ91 | 20% SiC | Squeeze casting<br>β-SiC(w)<br>0.1–1.0 μm diameter<br>30–100 μm length | 3.5 wt.% NaCl | 4$^*$ | 0.010 | – |
| 2007 [350] | Mg (99.99%) | 0% SiC<br>6% SiC<br>16% SiC | Mechanical disintegration deposition<br>α-SiC(p) 25 μm | 1 M NaCl | 6.4$^*$<br>8.6$^*$<br>21.7$^*$ | 0.590<br>0.794<br>1.905 | – No significant galvanic corrosion between matrix and reinforcement<br>– Defective nature of surface film due to reinforcement |
| 2007 [351] | AS41 | 0% $Al_2O_3$<br>20% $Al_2O_3$ | Squeeze casting<br>$Al_2O_3$(f) Saffil | pH 12 | – | 1.075 × $10^{-3}$<br>0.903–0.966 × $10^{-3}$ | – Comparable corrosion behavior with and without reinforcement<br>– No evidence of galvanic corrosion between matrix and reinforcement<br>– Al-rich areas, surrounding the fibers formed by interfacial reaction, act as cathodes |
| | | 0% $Al_2O_3$<br>20% $Al_2O_3$ | | 100 ppm NaCl pH 12 | - | 0.957 × $10^{-3}$<br>1.286–1.376 × $10^{-3}$ | |
| | | 0% $Al_2O_3$<br>20% $Al_2O_3$ | | 0.03 wt.% NaCl | - | 1.537 × $10^{-3}$<br>1.069–1.216 × $10^{-3}$ | |
| | | 0% $Al_2O_3$<br>20% $Al_2O_3$ | | 0.3 wt.% NaCl | - | 4.313 × $10^{-3}$<br>4.688–4.884 × $10^{-3}$ | |
| | | 0% $Al_2O_3$<br>20% $Al_2O_3$ | | 3 wt.% NaCl (pH 9.3) | 0.9$^*$<br>0.9$^*$ | – | |
| 2008 [352] | AZ91D | 0–5 wt.% CNT | Powder metallurgy<br>CNT: 5 μm length | 3 wt.% NaCl | Non clear data | Non clear data | – Improved anticorrosion properties by adding reinforcement<br>– Higher stability of the oxide film |
| 2008 [353] | Mg (99.9%) | 0% Cu<br>0.3% Cu<br>0.6% Cu<br>1% Cu<br>0.1% Mo<br>0.3% Mo | Disintegrated melt deposition<br>Cu(p) X μm<br>Mo(p) 44 μm | 3.5 wt.% NaCl | 7$^*$<br>124$^*$<br>237$^*$<br>241$^*$<br>139$^*$<br>258$^*$ | 0.065<br>1.500<br>3.500<br>2.750<br>3.500<br>5.650<br>6.600 | – Galvanic corrosion between matrix and reinforcement |
| 2009 [354] | AS41 | 0% C<br>25% C | Squeeze casting<br>C(sf) Sigrafil C-40 | 3 wt.% NaCl (pH 9.3) | 2.6$^*$<br>3.6$^*$ | Graphically presented | – Galvanic corrosion at matrix/reinforcement<br>– Interfacial reaction; $Al_4C_3$ and $Al_2MgC_2$ |
| | AS41 (0.5Ca) | 0% C<br>25% C | | | 1.0$^*$<br>3.4$^*$ | | |
| 2009 [355] | AZ31 | 6% SiC | Stir-casting<br>SiC(p) 10 μm | 3.5 wt.% NaCl | – | 0.1–0.5 | – |
| 2009 [356] | ZC71 | 12%SiC | Not-specified<br>SiC(p) 20 μm | 3.5 wt.% NaCl | 0.2$^*$ | – | – |
| 2009 [357] | AZ92 | 0% SiC | Powder metallurgy | 3.5 wt.% NaCl | 1.008$^*$ | – | |

Table 4 (*continued*)

| Ref. | Matrix and reinforcement | | Processing and reinforcement specs | Environment | Corrosion rate (mg/cm$^2$/day $^1$) | Current density (mA/cm$^2$) | Comments |
|---|---|---|---|---|---|---|---|
| | | 5% SiC<br>10% SiC | SiC(p) 5 µm | | 1.056$^*$<br>1.344$^*$ | | – Little corrosion at matrix/ reinforcement<br>– Reinforcement breaks continuity of Mg matrix<br>– Less protective corrosion products |
| | | 0–10% SiC | | 98%RH 50 °C | – | – | Negligible influence of the reinforcement |
| 2010 [358] | Mg (99.9%) | 0 wt.% CNT<br>0.3 wt.% CNT<br>1.3 wt.% CNT | Disintegrated melt deposition<br>CNT, 20 nm diameter<br><100 µm length | 3.5 wt.% NaCl | 10.5<br>17<br>120 | 0.027<br>0.056<br>0.572 | – Galvanic corrosion between matrix and reinforcement |
| 2010 [359] | AZ31B | 0% CNT<br>0.89% CNT<br>2.66% CNT | Powder metallurgy | 0.51 M NaCl | 1.92$^*$<br>234.72$^*$<br>1448.64$^*$ | – | – Galvanic corrosion between matrix and reinforcement |
| 2011 [360] | AZ91E | 0% TiC<br>56 wt.% TiC | Pressureless melt infiltration<br>TiC(p), 1.12 µm | 3.5 wt.% NaCl | – | 2.9<br>$8.8 \times 10^{-3}$ | – Some evidence of a galvanic corrosion between matrix and reinforcement |
| 2011 [361] | Mg | 0 wt.% CNT<br>0.1 wt.% CNT | Stir-Casting<br>CNT Baytubes C 150P | 3.5 wt.% NaCl | ~5<br>7.5–17.5 | 0.030<br>0.072–0.28 | – Galvanic corrosion at matrix/ reinforcement<br>– Dispersion of the reinforcement increases corrosion |
| 2011 [362] | AM50 | 0% $ZrO_2$<br>5% $ZrO_2$<br>10% $ZrO_2$ | Stir-casting<br>$ZrO_2$(p) 50–100 µm | 5 wt.% NaCl | 55$^*$<br>15$^*$<br>31$^*$ | 0.130<br>0.036<br>0.074 | |
| 2012 [363] | AZ91 | 0%<br>1 wt.% CNT<br>5 wt.% CNT | Stir-Casting<br>CNT Baytubes C 150P | 3.5 wt.% NaCl | 0.3<br>0.5–0.9<br>1.9–2.4 | | – Galvanic corrosion between matrix and reinforcement<br>– Dispersion of the reinforcement increases corrosion |
| 2013 [364] | AZ61B | 0%<br>0.73% CNT<br>2.10% CNT<br>0.71% C<br>1.37% C<br>1.56% C | Powder metallurgy<br>CNT: NC7000<br>9.5 nm diameter<br>1.5 µm length<br>C(f): VGCF<br>150 nm diameter<br>8 µm length | 3 wt.% NaCl | 2.69<br>18.61<br>75.18<br>14.24<br>19.28<br>29.84 | – | – Galvanic corrosion between matrix and reinforcement<br>– Al enrichment around reinforcement reducing surface potential difference |
| 2013 [365] | AM60 | 0% $Al_2O_3$<br>9% $Al_2O_3$ | Preform casting<br>4 µm diameter | 1 wt.% NaCl | – | 0.005<br>0.007 | – Reinforcement breaks continuity of Mg matrix<br>– Al-rich areas, surrounding the fibers<br>– No evidence of galvanic corrosion |
| | | | | 3.5 wt.% NaCl | | 0.001<br>0.006 | |
| 2014 [366] | Mg-6Al | 0 wt.% CNT<br>0.5 wt.% CNT | Powder metallurgy<br>CNT | 3.5 wt.% NaCl | 0.02$^*$<br>0.02$^*$ | – | |

(*continued on next page*)

**Table 4** (*continued*)

| Ref. | Matrix and reinforcement | | Processing and reinforcement specs | Environment | Corrosion rate (mg/cm$^2$/day $^1$) | Current density (mA/cm$^2$) | Comments |
|---|---|---|---|---|---|---|---|
| | | 1 wt.% CNT<br>2 wt.% CNT | 9.5 nm diameter<br>1.5 μm length | | $0.07^*$<br>$0.1^*$ | | |
| 2015 [367] | AZ91D | 0% TiC-$Ti_2$Al-$TiB_2$<br>X% TiC-$Ti_2$Al-$TiB_2$ | Infiltration | 3.5 wt.% NaCl | | 0.76<br>0.07 | – Composite material shows passivating behavior |
| 2015 [368] | AZ91 | 0% SiC<br>5% SiC<br>10% SiC<br>15% SiC | Semisolid<br>α-SiC(p) 10 μm | 3.5 wt.% NaCl | 1.1–1.2<br>1.9–2.7<br>3.9–7.5<br>6.2–9.6 | 0.0105–0.0443<br>0.0642–0.0779<br>0.1067–0.2703<br>0.0840–0.2498 | – Reinforcement promotes refinement and nucleation of β phase increasing galvanic corrosion |
| 2015 [369] | AE42 | 0%<br>20% $Al_2O_3$<br>15% $Al_2O_3$ + 5% SiC<br>10% $Al_2O_3$ + 10% SiC<br>10% $Al_2O_3$ + 15% SiC | Squeeze casting<br>$Al_2O_3$(f) Saffil<br>3–8 μm diameter<br>200 μm length<br>SiC(p) 5–20 μm | 5 wt.% NaCl<br>pH 11 | $\sim 0.5^*$<br>$\sim 1.5^*$<br>$\sim 2^*$<br>$\sim 1.6^*$ | Electrochemical data is presented graphically | – Defective nature of surface film due to reinforcement<br>– Reinforcement may introduce impurities |
| 2015 [370] | AM50 | 0 wt.% SiC<br>10 wt.% SiC<br>10 wt.% SiC purified | Stir-casting<br>~20 μm | 0.5 M NaCl saturated with $Mg(OH)_2$ | – | 0.025<br>0.25<br>0.15 | – Purified reinforcement improves corrosion resistance of MMC |
| 2016 [337] | AZ91D | 0% SiC<br>2% SiC<br>5% SiC<br>10% SiC | Semisolid<br>SiC(p) 15–25 μm | 3.5 wt.% NaCl | 0.07<br>2<br>11<br>12 | | – Detrimental effect of reinforcement on the continuity of β phase<br>– Galvanic corrosion at matrix/reinforcement<br>– Heterogeneous matrix/reinforcement interfaces |
| 2016 [322] | AZ91D | 0% SiC<br>10% SiC<br>10%SiC | Semisolid<br>SiC(p), 0.72 μm<br>Rheocasting<br>SiC(p): 13 μm | 95%RH 20 °C<br>50 μg/cm$^2$ NaCl<br>400 ppm $CO^2$ | $0.36^*$<br>$0.85^*$<br>$0.69^*$ | – | – Interfacial reaction when nano-sized and un-oxidized SiC used; $Al_4C_3$, $AlC_2$ and MgO<br>– Less protective character of β phase in MMCs<br>– Non-conclusive evidence of galvanic corrosion at matrix/reinforcement<br>– Casting defects in MMCs |

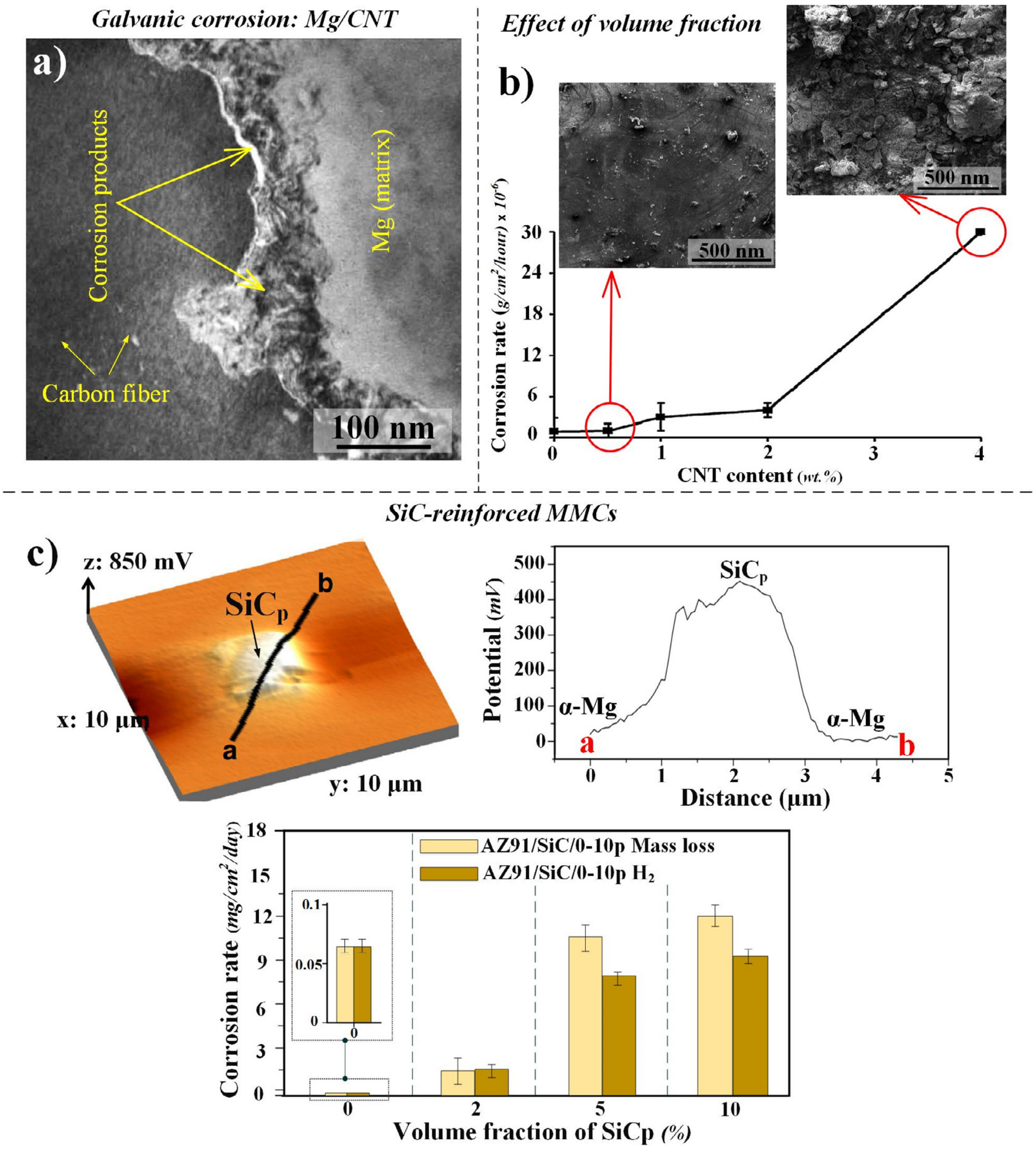

**Fig. 38.** Micro-galvanic corrosion in Mg-based MMCs. (a) Corrosion product layers formed between the fiber and the matrix in a carbon-reinforced MMC [316], (b) effect of CNT content on the corrosion rate of the composites after potentiodynamic polarization [366], and (c) a Volta potential map and the corresponding profile of a SiC particle as well as corrosion rate as a function of the volume fraction of reinforcement calculated from mass loss and hydrogen collection experiments [337]. Reproduced with permission from Elsevier.

It merits comment that the interfacial products which may form during the reactions as listed above, are not necessarily thermodynamically stable. For instance, $MgC_2$ and $Mg_3C$ are endothermic compounds decomposing at 500 °C and 650 °C respectively. Therefore, the presence of such reaction products seems to be unlikely when the processing is performed in the temperature range of 700–800 °C [334]. In case of Mg-Al/C, Mg-Al/CNT and Mg-Al/SiC composites, carbide precipitation could occur due to the high reactivity of Al with C. Plate-shaped $Al_4C_3$ and $Al_2MgC_2$ are the most commonly reported carbides in such composite systems, although other stoichiometries of the carbides have also been proposed (*e.g.*, $AlC_2$, and $Al_4Mg_2C_3$) [322,335]. Viala et al. [336] performed a detailed study analyzing the interfacial reaction products. It was observed that at 726 °C, $Al_2MgC_2$ forms in Mg-Al alloys containing 0.6–19 wt.% Al and $Al_4C_3$ forms when the Al content is >19 wt.%.Interfacial reactions also take place when the processes are operated at lower temperatures. The studies on the microstructure (Fig. 37a and b) of Mg-MMCs produced using semi-solid casting techniques (*e.g.*, rheocasting) have shown that many different types of interfacial products may form, including C- and O-containing compounds, carbides (*e.g.*, $Al_4C_3$, $Al_2MgC_2$, and $Mg_2C_3$), silicides (*e.g.*, $Mg_2Si$), and even MgO. Many of these compounds have been detected using SEM/EDX

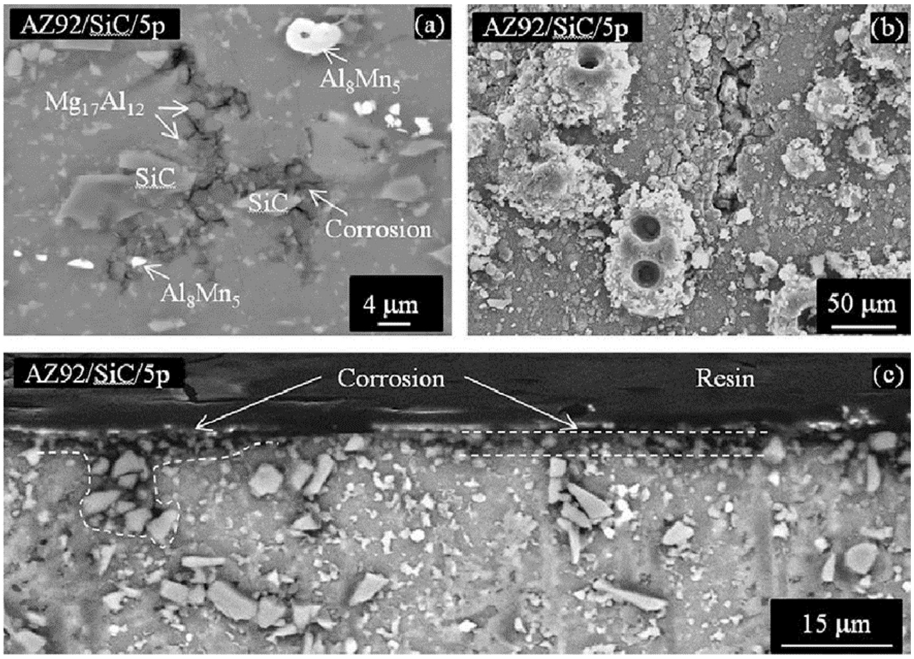

**Fig. 39.** SEM micrographs of the morphology of the corrosion attack in the AZ92/SiC/5p composite after exposure to (a) 3.5 wt.% NaCl for 1 h, (b) salt fog for 48 h, and (c) 98% RH for 28 days [357]. Reprinted with permission from Elsevier.

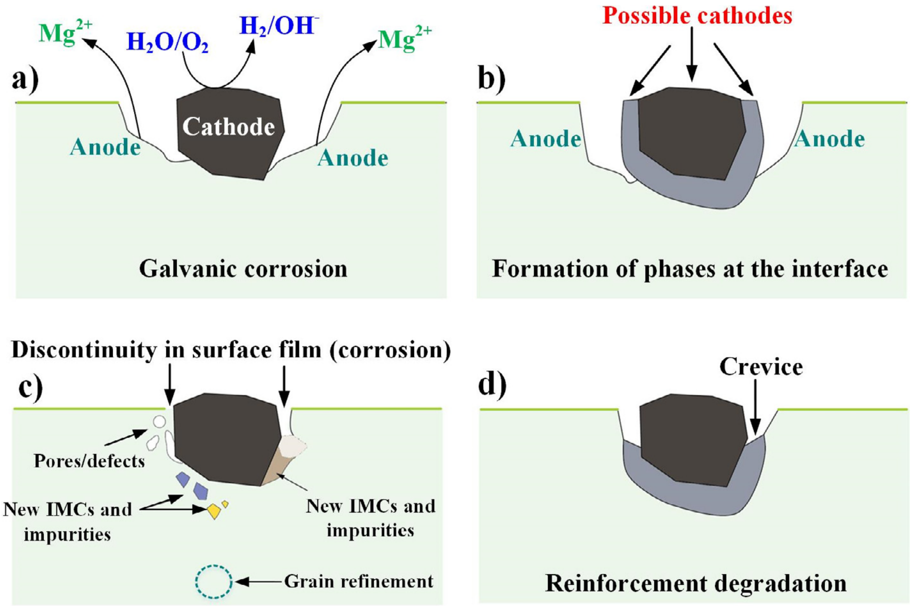

**Fig. 40.** Schematic illustration of corrosion processes in Mg-based MMCs. (a) Galvanic couple between matrix and reinforcement, (b and c) interfacial reaction between matrix and reinforcement and discontinuity in surface film and microstructural changes around the reinforcement, and (d) reinforcement degradation and crevice corrosion.

[135,332,333], XRD [135,322,333], and STEM/EDX (Fig. 37c) [322] typically interspersed in the microstructures of various Mg-alloy based MMCs. In addition to all those compounds, a recent study has demonstrated, using TEM/EDX/EELS, that $MgH_2$ (Mg hydride) could also be formed as an interfacial product (Fig. 37c) [135].

The presence of such compounds deteriorates both the mechanical properties and corrosion resistance of Mg-MMCs (see below). It was proposed that the formation of such reaction products is related to the poor wettability of the ceramic particles dispersed in molten Mg and therefore, various pre-processing techniques (*e.g.*, the pre-treatment of particles and coating/oxidization of the ceramic particles) are used to improve the wetting of ceramic particles.

It has been demonstrated that the formation of many types of interfacial products (*e.g.*, $Mg_2Si$ and MgO) is hindered when SiC particles are pre-oxidized [318,322,323]. Also, interfacial reactions at the matrix/reinforcement interface can minimized by keeping temperatures low and contact times short during processing, which is a feature of semisolid and solid processes (see Table 3).

### *3.4.3. Corrosion behavior of Mg-MMCs*

A comprehensive literature survey encompassing previous research on the corrosion characteristics of Mg-MMCs is provided in Table 4. The Mg-MMCs contain reinforcement/metal interfaces and also other reaction products dispersed in the metal matrix (as discussed in the preceding sections). Thus, the corrosion characteristics Mg-MMCs are much more complex than that of monolithic Mg alloys owing to the influence of the added reinforcement particles and also the reaction products formed during the melt/reinforcement particle interactions. In the following section, we review the possible reasons for the poor corrosion resistance of Mg-MMCs.

*3.4.3.1. Micro-galvanic corrosion between matrix and reinforcements.* The notion of micro-galvanic corrosion between the matrix and reinforcement has been documented (see *e.g.*, Fig. 38a and b) in some of the earliest classical works on the corrosion of Mg-MMCs by Trzaskoma [314], Hall [315], and Hihara et al. [316]. The SiC particles are common reinforcing ceramic materials used in Mg-MMCs and do not generally cause galvanic corrosion [322,368], however there have been some exceptional cases. Mingo et al. [337], Arrabal et al. [356], and Pardo et al. [357] highlighted a contradictory behavior of SiC particles, with respect to the galvanic corrosion in the Mg-MMC (Fig. 38c). Mingo et al. [337] observed a shift in the cathodic branch towards higher current densities for an Mg-MMC containing SiC particles, which may be attributed to the enhanced cathodic activity of SiC particles. However, this may not always be the case with respect to SiC particles in Mg-MMCs as there may be large variations in electrical resistivities of SiC particles (ranging from $10^{-5}$ to $10^{13}\ \Omega\,\text{cm}$) depending on the impurity levels [316]. The work done by Kamieniak and Malik [370] is an example on the effect of impure and purified SiC on the overall corrosion performance of an AM50/SiC composite. It should also be noted that a carbon-rich surface, which behaves more like graphite than SiC can also be formed during processing [316]. The presence of such carbon-rich surfaces on SiC particles have been reported in the very early works of Hihara and Kondepudi [316] on SiC filaments. In case of galvanic corrosion between matrix and SiC, it is also important to consider that the corrosion rate may significantly vary depending on the amount of dissolved oxygen in the solution, nature of aggressive species and reinforcement orientation [338].

Galvanic corrosion has not been observed when using $Al_2O_3$ or $ZrO_2$, as reinforcing particles in Mg-MMCs, possibly due to their insulating characteristics although compositional segregation in the vicinity of these reinforcements may result in galvanic corrosion, as noted by Bakkar et al. [351]. Several different reaction products (*e.g.*, Al carbide and the semiconducting $Mg_2Si$) may form between the SiC particles and the melt during fabrication of the MMCs (see Fig. 37 and Eq. (23)–(33)) and hence their cathodic activities need to be considered. Gupta et al. [321] identified that $Mg_2Si$ is cathodic towards the matrix of the Mg-Al alloy (AS31) and triggers its micro-galvanic corrosion, whereas other compounds such as MgO and $MgAl_2O_4$ may not play a prominent role in the electrochemical processes. They also proposed that the Al carbide-$Al_4C_3$, is a poor electronic conductor and may not participate in corrosion.

*3.4.3.2. Reinforcement-induced microstructural changes.* Several studies have revealed that incorporation of the reinforcement slightly affects the microstructure of Mg-MMCs, correspondingly influencing corrosion of the Mg-MMC (see Fig. 4b). The microstructural changes induced by the reinforcing materials include grain refinement, porosity and contamination. Zhang et al. [365,368] identified that SiC promoted the refinement and nucleation of $\beta$-$Mg_{17}Al_{12}$ in the Mg-Al alloy which consequently increased the galvanic corrosion. Similarly, Esmaily et al. [322] showed that a high fraction of porosity can deteriorate the corrosion performance of Mg-MMCs reinforced with SiC particles.

*3.4.3.3. Less protective surface films formed due to incorporation of reinforcement.* Several authors have attributed the poor corrosion performance of Mg-MMCs to the poor protection imparted by the surface films formed upon the MMC (see Table 4). This includes the surface films both formed by the reactions with oxygen in air and also the corrosion products precipitated from aqueous solutions. It was proposed that the reinforcement particles disrupt the continuity of the Mg matrix, thus creating preferential sites for corrosion initiation. The effect of such reinforcement particles in initiating preferential corrosion has been shown by Pardo et al. [357] (Fig. 39).

*3.4.3.4. Reinforcement degradation.* The reinforcements and the interfacial products may undergo degradation upon contact with moisture or aqueous solutions. This leads to the formation of micro-crevices at the matrix/reinforcement interfaces in a similar manner to certain Al-based MMCs [371]. However, in case of Mg-MMCs, crevice corrosion is not supposed to be too detrimental since the traditional crevice corrosion mechanism involving oxygen depletion and acidification does not take place. The deleterious effect is that interfacial degradation may lead to an increase in the effective area of the cathodic reinforcement, thus increasing galvanic corrosion. The examples of degradation processes include the hydrolysis of compounds such as $Al_4C_3$ and $Al_2MgC_2$ in composite materials containing C-based reinforcements (*e.g.*, SiC, CNT, C fibers, $B_4C$, and TiC). The hydrolysis reactions of the compounds are indicated in Eqs. (34) and (35) [372,373].

$$Al_4C_3 + 12H_2O \rightarrow 4Al(OH)_3 + 3CH_4 \tag{34}$$

$$2Al_2MgC_2 + 8H_2O \rightarrow 2MgAl_2O_4 + 4CH_4 \tag{35}$$

The liberation of methane ($CH_4$) has been confirmed in Al-MMCs [372] and is believed to be partly responsible for the presence of pores, cracks or crevices surrounding the reinforcement [373] (see the schematic illustration in Fig. 40). However, no visible degradation has been observed for materials such as SiC, TiC, $Al_2O_3$ and $ZrO_2$, see e.g., [374]. Carbon has a high chemical stability in aqueous solutions. However, it has been reported that graphite fibers can be oxidized to $CO_2$ under anodic polarization, leading to crevice formation in certain Mg-MMCs [356].

To conclude, the corrosion problems in Mg-MMCs are attributed to the presence of cathodically active reinforcements and also, interfacial products (or phases) formed during the extensive matrix/reinforcement reactions, which occur during the manufacture of Mg-MMCs. The corrosion behavior of Mg- MMCs can be improved by exercising control on interfacial reactions. For example, in the case of SiC reinforcements, a recent study has shown that the formation of an insulating silica ($SiO_2$) glass layer upon the SiC surface (by pre-oxidation of the particles) could decrease their cathodic activities. The $SiO_2$ surface also minimizes the formation of interfacial reaction products and improves wettability. This also results in the Mg-MMCs having a superior quality, with the presence of fewer casting pores which are beneficial from a corrosion standpoint. Another strategy for mitigating the corrosion issue seems to be use reinforcements that: (i) are electronically insulating so that they are not cathodically active and (ii) do not react with molten Mg at a significant rates. There are only few such compounds, *i.e.*, alumina, zirconia, yttria, and similar highly stable oxides, which have poor reactivity with Mg, thus posing a challenge to synthesize Mg-MMCs.

Mg-MMCs primarily experience galvanic corrosion due to galvanic coupling between the reinforcement and matrix, also, between the metal matrix and interfacial reaction products. Several different reaction products (Eqs. (23)–(35)) may form at the metal matrix/reinforcement interfaces and depending upon their electrical properties, they may or may not participate in the galvanic corrosion of Mg-MMCs. An interesting avenue for future work, will be to explore whether surface coatings found effective upon commercial Mg alloys [266] can effectively protect Mg-MMCs from corrosion.

### 3.5. Biodegradation of Mg alloys

In the classic applications of Mg alloys, namely their use as light structural materials, for instance in the transportation industry, their major advantage is their low density. However, their poor corrosion resistance is a limiting factor for a widespread use. On the other hand, this very characteristic is the basis for a strikingly different application of Mg alloys, *i.e.*, in biodegradable biomedical implants. Examples of such devices include cardiovascular (*e.g.*, stents) or temporary orthopaedic fixtures that are only required in the body for the time of healing [375–381]. Corrosion (or bioabsorption) in the body fluids would save a second operation for removal of the temporary device. Furthermore, negative effects are possible when an implant is left in the body for a long period after it is no longer needed for its medical purpose. The concept of exploiting the spontaneous and relatively fast dissolution of Mg based materials for temporary medical devices is not new, as described in a review on the history of biodegradable Mg based implants [382]: A very early clinical report on the use of Mg wires as ligature for bleeding vessels was given in 1878! The early attempts for the use of Mg alloys in biomedical applications had poor success, at least partially due to a limited understanding of Mg alloy corrosion. Since then, significant progress in Mg technology from the materials science point of view has been achieved. The renewed interest for biodegradable Mg based implants has grown tremendously in the last 10–15 years. The current state of the art on biodegradable metals has recently been reviewed by Witte et al. [383]. In principle, any metal that readily corrodes in aqueous solutions and is considered non-toxic has potential for these applications. However, a vast majority of work in the field has been carried out on Mg alloys, and significantly less attention has been given to Fe based materials (or even less for other metals).

For temporary orthopaedic devices, in addition to biodegradation, the elastic modulus of Mg alloys is another beneficial property, as it matches the modulus of bone better than most other metallic alloys, which decreases stress-shielding effects [384]. The concept of using a readily corroding metallic material for non-permanent implants is seemingly simple, as it is based on a spontaneous degradation process. However, in detail the corrosion processes are very complex. As already discussed in the earlier sections of this review article, the corrosion behavior of Mg and Mg alloys is quite intriguing, and the detailed dissolution mechanisms even in more simple exposures than the body environment are still under intensive research. The successful application of resorbable Mg biomedical devices is challenging because, even though Mg ions are non-toxic, the side effects of Mg dissolution such as $H_2$ gas evolution or alkalization are of concern [383,385]. In addition, many conventional Mg alloys seem to show too high corrosion rates in the biological environment (at least the initial corrosion rate), even though the desired corrosion rate (and hence the degradation time) very strongly depends on the targeted application. Therefore, novel alloys as well as for biocompatible coatings and surface modification are being sought. A mechanistic understanding of the complex interactions between corrosion Mg alloy surfaces and the biological environment also remains to be solved.

### *3.5.1. Crucial aspects of Mg corrosion in view of the biomedical applications*

The requisite that Mg and its alloys should corrode in the biological environment, which in principle is a NaCl based aqueous solution buffered to pH 7.4 (see next section for more details) is as such no challenge. As discussed in Section 3.1, due to the low thermodynamic stability ($E^\circ = -2.4$ V *vs.* SHE), Mg based materials readily oxidize in presence of water, thereby liberating $H_2$ gas from water. Moreover, formation of protective, stable Mg oxide/hydroxide layers [$MgO/Mg(OH_2)$] on the surface is only possible in alkaline environments and in the absence of aggressive anions such as chloride ions (which are present in body fluids).

Hence, kinetic barriers provided by highly protective passive films, such as found for instance on stainless steels or Ti alloys in many environments, are not a factor for Mg alloys in body fluids. In fact, whereas stable and spontaneous passivity is crucial for permanent implant materials, it is not desired for temporary implants, as it would hamper the biodegradation concept.

A serious concern in biomedical applications of Mg alloys is that the anodic Mg dissolution (oxidation) reaction is always coupled with cathodic water decomposition generating $H_2$ gas by a direct reduction of $H^+$ from $H_2O$, as has been described above. The dangers of $H_2$ gas generation in biomedical applications depend on the rate and spatial distribution of its production. If $H_2$ gas generation is sufficiently slow, the gas can be transported away from the site of its generation and local build-up of significant volumes of gas can be avoided. The rate of the $H_2$ gas evolution is influenced by all factors that influence the corrosion rate, and will therefore depend on the alloy, surface treatments, as well as on the surrounding environment. As discussed in earlier sections of this review article, cathodic activation of Mg (alloys) can take place upon active dissolution. Therefore, the HE rate is not expected to show a linear time dependence. However, in biologically relevant environments, the electrochemical behavior of Mg alloys is not identical to simple NaCl solutions, as the presence of, for instance, Ca and phosphate ions lead to formation of different type of corrosion product layers than in NaCl [386–388] (this is discussed in more detail below).

Another concern for biomedical applications is surface alkalization due to Mg dissolution. In non-buffered solutions Mg dissolution can lead to high alkalinity (pH 10–12) of the electrolyte because of the limited hydrolysis of the $Mg^{2+}$ ion. Even in buffered solutions (such as body fluids) a modest pH increase in the vicinity of corroding Mg alloy surfaces will take place [380]. The alloy composition and subsequently the amount of different cations released in the alloy corrosion influence the hydrolysis reactions, and as a consequence the alkaline pH shifts vary for different alloys.

It is interesting to note that, for many applications of Mg alloys, the alkaline pH shift on the surface can be beneficial, as it aids passivation of the Mg surface by formation of stable $Mg(OH)_2$ surface layers. For instance, in crevices or under deposits on the alloy surface strong alkalization could take place due to hindered exchange of the solution with the bulk environment, possibly leading to self-limiting propagation of Mg corrosion. This is in contrast to many other alloys, in which metal cation hydrolysis reactions lead to local surface acidification. The local anodic sites in crevices of such alloys become extremely aggressive, strongly accelerating the localized dissolution. Even though the alkaline pH shift renders the Mg surface more passive, such effects are expected to be harmful for the biological surroundings [389]. The pH increase, on the other hand, can further influence both the precipitation of various types of (Ca/Mg)-phosphate layers on the surface, as well as protein adsorption (which will be discussed in more detail below).

Regarding the mode of corrosion, Mg alloys seldom corrode in a uniform manner, as most alloys are heterogeneous, *i.e.,* multiphase alloys. Because almost all alloying elements (and impurities) are nobler than Mg, intermetallic phases rich in the alloying elements will typically act as local cathodes coupled with the Mg matrix anode. Coupling with more noble surface sites not only accelerates dissolution of the Mg matrix, but also leads to non-uniform corrosion morphology. A non-uniform corrosion process can result in local loss of the mechanical integrity of devices (for instance, breakage of single struts in stents). Moreover, lifetime prediction is significantly more difficult for non-uniform dissolution than for uniform layer-by-layer removal of material.

The methodologies for studying biodegradation of Mg alloys can impact their assessment. The corrosion of a metal in its environment is always a complex system, and all internal (material and surface) and external (environment) parameters can play a significant role. Research in the field of biodegradable metals has been carried out on a large variety of alloys, in different type of simulated body environments, using different experimental approaches to study the corrosion behavior. In many practical applications, the applicability of data generated in the laboratory to the behavior in the field is not straightforward, and certainly the case of materials in the human body is not the simplest system. Even for nominally simple *in vitro* testing, interpretation of findings is not always straightforward. For example, electrochemical data such as from impedance spectroscopy gives information on the kinetics of reactions, but it does not always provide direct information on the reaction mechanisms. For example, the final fate of cations formed in the anodic oxidation reaction can be either dissolution into solution (solvation) or binding in corrosion product layers. The growth of corrosion product layers on the surface may be reflected in the electrochemical data, for instance, by a change of the interfacial capacity. However, a mechanistic interpretation of the impedance data is often difficult without supporting independent information. Solution analysis, on the other hand, gives direct information on the concentration of dissolved metal cations. Therefore, to understand the degradation behavior in detail, information from many different types of experimental approaches should be collected. Regarding biodegradation, in addition to conventional laboratory based studies, *in vivo* corrosion behavior and biocompatibility need to be considered as well.

### 3.5.2. Mg corrosion in (simulated) body environments

The corrosive environment of the human body consists of a 0.14 M NaCl solution with small amounts of other inorganic species, such as $Ca^{2+}$, $PO_4^{3-}$, and $HCO_3^-$ [390]. The presence of chloride ions typically leads to accelerated corrosion, whereas phosphates and carbonates may promote the formation of protective or partially protective corrosion product layers. The body temperature of 37 °C can somewhat accelerate the corrosion reactions compared to the room temperature, but the temperature also has an influence on precipitation of various types of Ca-phosphates from the body fluids. For example, the solubility of Ca-phosphates is temperature dependent. The normal pH of blood is 7.4, buffered by the $CO_2/HCO_3^-$ system. However, local variations of the pH value can occur, as discussed in more detail below. In addition to the variety of inorganic components of body fluids, the presence of organic components such as biomolecules, proteins, cells, or bacteria, can further influence corrosion reactions. These different factors show a variety of interactions with the corroding Mg alloy surface and with each other, making the corrosion scenario highly complex. Some of these interactions are summarized in Fig. 41 and will be discussed in detail in the following sections.

The processes depicted in Fig. 41 can be summarized as the following:

1. Mg corrosion leads to release of $Mg^{2+}$, $H_2(g)$ generation and alkalization.
2. $OH^-$ ions produced by the cathodic reaction associate with Mg dissolution is detrimental to cells.
3. The pH increase promotes precipitation of Ca-phosphate on the alloy surface.
4. The increased alkalinity can kill bacteria.
5. Carbonates are incorporated in the growing surface layers.
6. Chloride ions attack the alloy surface, and $MgCl_2$ forms.
7. Cells and proteins adhere to the Mg surface. Cells on the surface produce lactic acid.
8. Proteins in solution can complex $Mg^{2+}$ cations.

### 3.5.3. Role of simulated body fluids

Various types of simulated body fluids have been used for the study of Mg alloy biodegradation in the laboratory. Unfortunately there is no clear agreement on what is the best type of environment to simulate the *in vivo* conditions. It has been frequently observed that the corrosion rate of Mg alloys varies significantly, depending on the type of simulated body fluid used for the study (see *e.g.,* [386–388,391]. In addition, even the type of buffer used can play a decisive role [388,392,393]. This strongly hampers a direct comparison of different data in the literature.

The exact roles of the different inorganic and organic species present in various simulated body solutions in the Mg dissolution mechanisms have not yet been unambiguously clarified. It is clear that more complex corrosion products, such as different types of (Ca/Mg) phosphates and carbonates, form in simulated body fluids than in simple saline solutions. These corrosion products not only influence the corrosion rate, but for sparingly soluble corrosion products, complete degradation

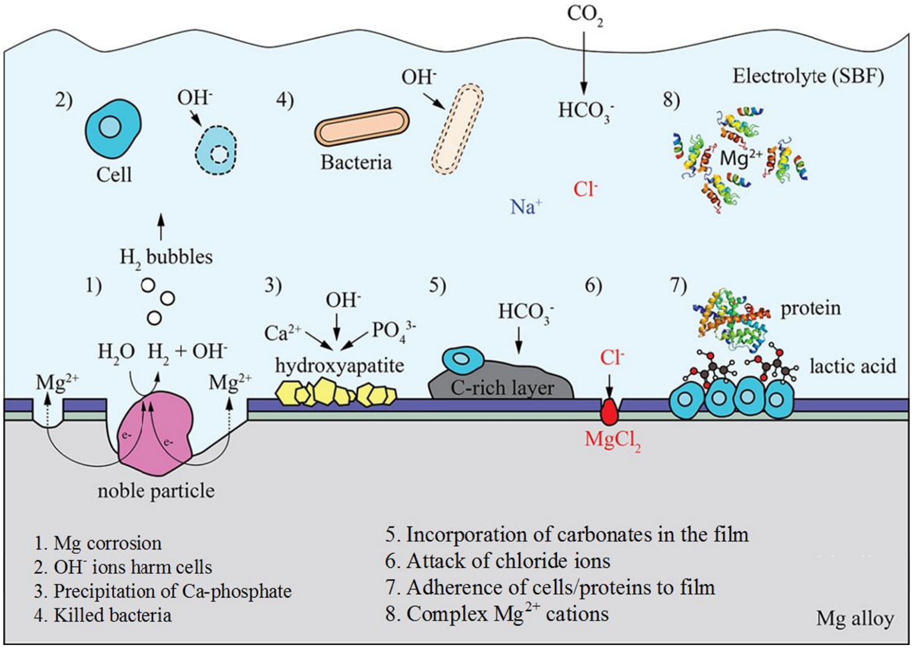

**Fig. 41.** Schematic representation of some possible interactions between a corroding Mg alloy surface and a biological environment. Note: Events 1–8 are explained in detail in the text.

of the implant will not take place. Instead, a gradual conversion of the metallic material into corrosion products occurs. Because the different simulated body fluids contain slightly different amounts of $Ca^{2+}$, carbonates/hydrocarbonates and phosphates, and the $Mg^{2+}$ concentration will depend on the dissolution rate and mass transport, the specific conditions at the surface such as the local pH value can vary and different stoichiometries of corrosion product layers can precipitate. Tese different types of precipitates can be expected to have different protection properties.

The different corrosion layers formed on Mg surface in SBF (simulating the inorganic components of body fluids) and in cell culture medium (D-MEM: inorganic components, amino acids, glucose) affect the subsequent corrosion protection behavior. Typically, significantly more protective layers are formed on Mg surface in D-MEM. In a recent study it was demonstrated that "passivation" of Mg in D-MEM solution is only observed when the measurements are carried out in solutions expose to air, *i.e.,* outside of an incubator [394]. In the best case (3 day immersion in D-MEM), corrosion rates determined by impedance spectroscopy and by potentiodynamic polarization measurements indicated up to 20 times higher corrosion resistance than for a freshly immersed sample. Cross-sectional characterization of the samples showed formation of a double-layered corrosion product layer on the surface, consisting of an inner porous layer and a compact outer layer. Soaking the Mg samples in D-MEM in incubator (37 °C, 5% $CO_2$) did not lead to formation of highly protective films on the surface; in this case the compact outer layer was absent. The origin of these different types of layers can be explained by measuring the pH in medium during immersion of Mg. The pH increase was stronger when the measurements were carried out outside of the incubator, as the presence of a sufficient amount of $CO_2$ is required for full buffering of the medium. A higher pH value slows down Mg dissolution, which slows the production of $H_2$ bubbles and aids the formation of a compact corrosion layer on the surface. In addition, characterization of the composition of the layers indicates a higher amount of carbonate on the surface for layers formed in the incubator. Also the Ca/P-ratio was found to vary depending on the exposure conditions.

This example clearly demonstrates that all experimental parameters during laboratory studies of Mg corrosion (composition of electrolyte, temperature, and gas atmosphere) can very strongly influence the results. This observation is not surprising, but it illustrates the need to define suitable *in vitro* testing conditions for Mg alloy corrosion for correct prediction of the biodegradation in the body, which is discussed in detail below.

As mentioned above, the D-MEM electrolyte also contains amino acids. Amino acids can influence corrosion of Mg (and other metals) by chelation reactions of metal cations [395]. In addition to the different stability of the chelate complexes between the different amino acids and $Mg^{2+}$, the isoelectric points also vary. Therefore, various scenarios of interactions between the surfaces charge of the Mg surface and positively or negatively charged amino acids could be expected. In addition, glucose present in D-MEM has been shown to influence the degradation behavior of pure Mg [396]. On the one hand, glucose can transform into gluconic acid, which attacks Mg because of the pH decrease. On the other hand, glucose was observed to influence the Mg corrosion layer formation by coordinating $Ca^{2+}$ ions in solution. The detailed role of the different amino acids, as well as other organic constituents of D-MEM, is still under exploration.

### *3.5.4. Static vs. Dynamic conditions*

The corrosion scenario in real biomedical applications is always more complex than in laboratory experiments. For instance, the hydrodynamic condition (*e.g.,* blood flow) around the implant surface influences mass transfer (*e.g.,* transport of Mg corrosion products, $Mg^{2+}$ cations, and $OH^-$ anions, away from the surface). Consequently, the local surface chemistry evolves with time and can be drastically different than under static conditions. This in turn would influence the biological and the corrosion reactions. Also, because the surface layers on corroding Mg alloys are formed by dissolution-precipitation processes, solution flow can be expected to significantly influence the growth of these layers. In spite of the general agreement that the dynamic conditions can play a significant role in degradation rates and modes, most laboratory experiments have been carried out under stagnant conditions. Only few reports have systematically studied the influence of flow on biodegradation of Mg [396–398]. Typically, higher corrosion rates were observed under dynamic conditions than under stagnant conditions. In addition to the average degradation rate, the corrosion morphology was also influenced by flow. These effects were attributed to mass transfer as well as flow-induced shear stress effects. It should be mentioned in this context that the hydrodynamic conditions on the implant surfaces depend on the type of implantation (*i.e.,* stents *vs.* bone-healing devices, blood flow, and tissue coverage) and may change upon time.

### *3.5.5. Role of proteins*

In addition to the inorganic species present in body fluids, the presence of biomolecules such as proteins can significantly influence the corrosion rate. However, studies on the influence of proteins on Mg alloy corrosion, have generated somewhat conflicting results. Proteins certainly influence the dissolution behavior, but the effects depend on the specific alloy and protein [397]. Also, the influence of proteins on Mg dissolution rate can change with time such that they might first inhibit and then later accelerate corrosion. Proteins can complex metal cations, which might accelerate dissolution, but they can also reduce corrosion by adsorbing on metal surfaces to form a protective layer [399–401]. Both of these effects depend on the nature of the metal surface and the protein in question. It is therefore hardly surprising that a comparison of different research results on different systems is not straightforward. As recently discussed in the literature [397], both acceleration and inhibition of Mg alloy corrosion by proteins in electrolyte has been observed. A direct comparison of the results of the different groups is not straightforward, as experiments have been carried out on different alloys and under different corrosion scenarios. For example, the different electrolytes used include SBF, Hank's solution, and D-MEM, and the effects of single protein such as albumin, or of serum have been studied. Protein adsorption on surfaces depends on the hydrophilic/

hydrophobic character of the surface, as well as on the surface charges of the metal and the protein. As described above in this section, the nature of the surface layers forming on Mg differs in different types of simulated body fluids, so protein adsorption can also be different. The presence of proteins in solution in turn also influences the formation of the Ca-phosphate conversion layers [394,397]. The pH changes in the electrolyte upon Mg dissolution depend on the immersion conditions and the pH will influence the charge of the metal surface and electrostatic interactions that may either enhance or diminish protein adsorption.

### 3.5.6. Role of cells

In addition to the presence of biomolecules in body fluids, the biological environment contains living cells. The Mg corrosion products ($Mg^{2+}$, $H_2$ gas, and pH increase) can influence the adhesion and proliferation of cells on Mg surface [389,402,403] so careful assessment of suitable protocols for an *in vitro* study of cell adhesion on corroding Mg surfaces is needed. For example, refreshing of the medium is required during long-term experiments. In addition to the effect of Mg dissolution products on cell attachment, cell adhesion layers on Mg surface can also influence the corrosion rate of Mg. Until now, relatively few studies have been dedicated to this topic, but there is growing evidence that cell adhesion layers can slow down Mg corrosion [404,405]. In a recent investigation, growth of endothelial and osteoblast-like cells on pure Mg surfaces was shown to significantly slow down corrosion, and a correlation between the confluency of cell layers and charge-transfer resistance values measured by impedance spectroscopy after 1 and 5 days of cell culturing was observed (see Fig. 42) [404]. Similar effects were reported earlier for the Mg alloy AZ91 by *in vitro* culturing of HeLa cells [405]. In these studies, the corrosion-inhibiting effect of cells was attributed to a blocking of the electrochemically active surface by the cell layers, including cell bodies and extracellular matrix. However, other effects of cells on corrosion should be considered as well. As discussed by Hiromoto et al. [406], pH changes can take place below cell layers on metal surfaces. Such pH changes could be related to cell metabolism products (lactic acid formation, pH decrease), infection reactions (pH decrease), and/or hydrolysis reactions of dissolving metal cations (typically pH decrease). The pH decrease measured on stainless steel and on titanium with fibroblast cells cultured directly on the metal surfaces was attributed to the "occluded cell" environment [406]. Because the pH increases strongly in the vicinity of Mg dissolution, a hindered exchange of the electrolyte on by the blocking cell layer might lead to a stronger alkalization than on an open Mg surface and might counterbalance the pH decrease

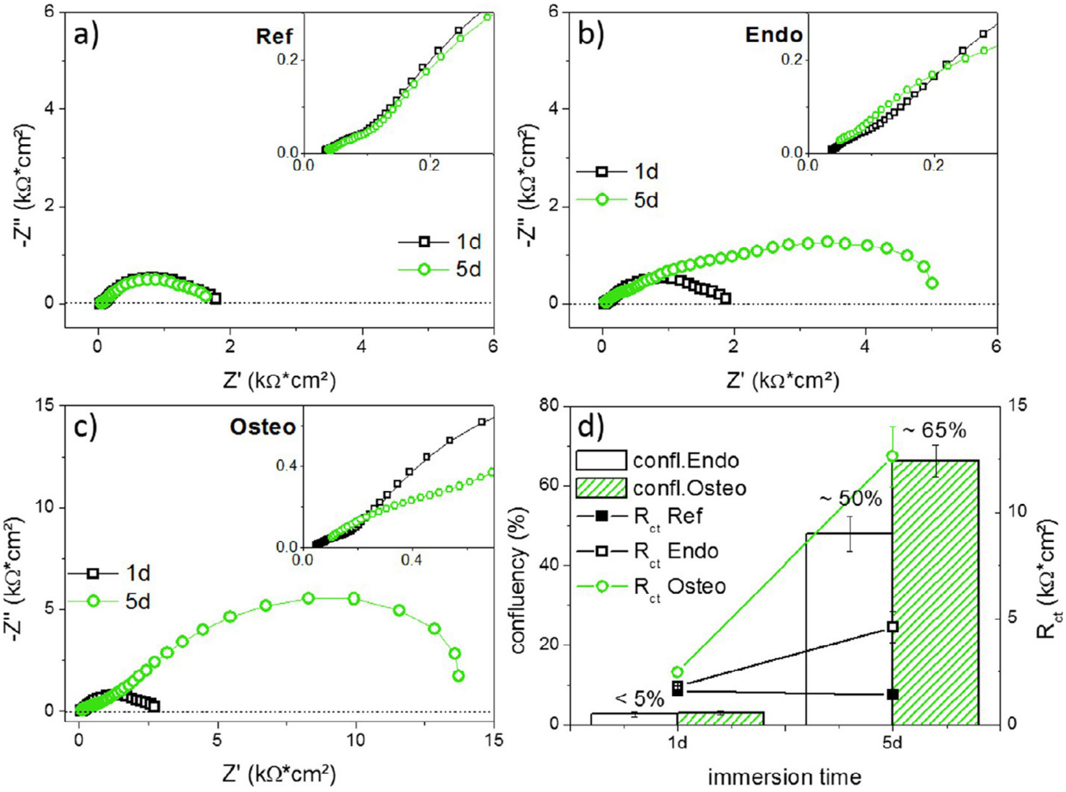

**Fig. 42.** Electrochemical impedance spectroscopy measurements after 1 and 5 days of *in vitro* cell culture: (a) Nyquist plots of Mg samples without cells immersed in cell culture medium, (b) samples incubated with endothelial cells (DH1+/+), (c) samples incubated with osteosarcoma cells (Mg63), and (d) comparison of calculated total charge transfer resistances and cell confluency as a function of immersion time [404]. Reprinted with permission from American Chemical Society.

expected by the production of lactic acid by cells. Therefore, pH regulation could be a factor contributing to the corrosion-inhibiting effect of cells. However, such a possible effect still needs to be experimentally validated.

In a recent study, the influence of human primary osteoblast cells cultured on Mg based alloys on the degradation process was studied in detail [407]. Osteoblasts were demonstrated to influence the degradation process both actively by their metabolic activity and by their role in mediating bone formation as well as passively by the cell layer formation. The detailed effects on the degradation interface were alloy dependent, but significant influences of the cells on the corrosion rate were observed.

The effect of growing cells on metal surfaces on corrosion can be different for different types of cells. It has been reported that activated macrophages accelerate corrosion of a Mg alloy, which was attributed to the release of reactive oxygen species by the cells [408]. To summarize the influence of living cells on the corrosion process of Mg alloys, it is clear that complex alloy- and cell-dependent interactions take place. There is some proof that cell layers can slow down corrosion by blocking the active surface, but cell metabolism products (*e.g.,* lactic acid and reactive oxygen species) can accelerate corrosion. The detailed mechanisms of the interactions between the corroding Mg alloy surfaces and living cells are still far from being understood at this point.

### *3.5.7. In vitro vs. in vivo corrosion*

As described above, corrosion of Mg alloys in simulated biological solutions is a complex process. Some of the parameters to be considered include temperature, pH, buffer type, surrounding gas atmosphere, a high number of inorganic ions, amino acids, proteins, cells, hydrodynamic conditions. Many studies have been carried out with the aim of exploring the influence of one of these parameters, but determination of the mechanisms is complicated by the fact that these parameters are not independent of each other. Moreover, many of the factors influencing Mg alloy corrosion may have multiple operative mechanisms. For example of proteins can both adsorb on the surface and/or complex metal cations. Depending on the system at hand, one of the operative mechanisms can be more dominant than the other.

The situation becomes even more complex when considering *in vivo* scenarios. At present, a limited amount of data is available on the *in vivo* behavior of Mg alloys, and especially systematic and direct comparisons of *in vitro* and *in vivo* degradation. An attempt was made to carefully analyze the existing literature in a recent review [409]. Interestingly, the *in vivo* corrosion rates showed a smaller range of values (between 0 and 1.5 mm/year (0.7 mg/cm$^2$/day)) than *in vitro* corrosion rates (between 0.1 and 2 mm/year ($5 \times 10^{-2}$–1 mg/cm$^2$/day)). In addition, for all alloys the corrosion rates were 1–5 times lower for *in vivo* than *in vitro*. The correlation between the *in vitro* and *in vivo* corrosion rates also strongly depends on the electrolyte chosen for the laboratory studies. While some possible reasons for the lower corrosion rates observed *in vivo* can be identified, such as a lower chloride concentration in blood plasma as compared to most synthetic media, or the presence of proteins and cells, many unknowns remain. The authors emphasized that the anatomical location of the implant as well as the surgical procedure can also influence the subsequent degradation behavior. Hence, there is lack of information about the detailed *in vivo* conditions that would enable understanding of the origin of the different corrosion rates observed.

A recent investigation reports on the long-term *in vitro* and *in vivo* degradation of a Mg alloy with different types of Ca-phosphate coatings [410]. A major difference was found in the morphology of the attack below the coatings. The attack was almost uniform *in vitro*, whereas *in vivo* a strong localization of the attack was observed. This difference was attributed to the implant/tissue interface, leading to a lower diffusivity for *in vivo* conditions.

### *3.5.8. Influence of Mg corrosion products on the biocompatibility*

The Mg corrosion products including released species ($Mg^{2+}$, alloying elements, $H_2$ gas, and $OH^-$) and solid corrosion products affect the material biocompatibility. As already previously mentioned, $Mg^{2+}$ cations are typically considered as non-toxic or even beneficial for many biological processes in the human body. For instance, $Mg^{2+}$ ions have been shown to improve proliferation and migration of endothelial cells [411]. However, a recent detailed study on the influence of Mg extracts on mesenchymal stem cell fate and osteoblastogenesis indicates quite complex, positive or negative influences on the cell differentiation via various pathways [412]. Further work is required to unambiguously understand the way Mg release may influence the biological surroundings. The release of the alloying elements from Mg alloys should also be considered. Due to a rather strong interest of rare earth containing Mg alloys, cytotoxicity limits of these elements have been studied [413,414]. Recently, the response of endothelial cells on a number of Mg alloying elements (Al, Ca, Zn, Y, Dy, Nd, and Gd) as a function of ion concentration was reported; here a dose-dependent inhibitory effect on cell viability and proliferation was observed for all tested elements [394].

Evolution of $H_2$ gas by Mg corrosion was a concern even during the early trials for use of Mg in medicine [382]. If the rate of hydrogen gas evolution from corrosion is too high, detrimental gas pockets can form around the implant, and any approach to control the Mg dissolution rate will also affect the rate of hydrogen gas evolution. In this context it may be of interest to note that the fact that the amount of Mg corrosion is directly correlated to the amount of hydrogen gas evolving enables a simple, non-invasive measurement of the Mg alloy *in vivo* degradation rate with the help of electrochemical $H_2$ gas sensors [415].

The well-known alkalization occurring in the vicinity of a corroding Mg alloy surface has been frequently discussed as possibly being deleterious for the surrounding biological environment. Indeed it is known that alkaline pH shift can lead to cell death [416]. A pH shift can also influence protein functions. In this context it is noteworthy that the pH changes in the vicinity of the corroding implant would strongly depend on the distance of measurement, and determination of the true surface pH is not possible. In addition, localization of anodic and cathodic reactions on a heterogeneous Mg alloy surface lead to local variations in the pH. Recently, the local pH distribution during *in vitro* dissolution of a binary MgCa alloy was studied by scanning electrochemical microscopy, enabling a high-resolution determination of the local pH changes [417]. Strong local variations in pH of more than 3 units between anodic and cathodic sites of the surface were observed. Such findings suggest that the biological species around Mg alloy implants could be exposed to high alkalinity with local and temporal variations. In contrast to the often mentioned negative effect of alkaline pH shifts on cells, the surface alkalization could bring Mg alloys an inherent antimicrobial property. In fact, Mg metal has been found to show significant *in vitro* antibacterial properties against *Escheria coli*, *Pseudomona aeruginosa,* and *Staphylococcus aureus* the effect being similar to fluoroquinone antibiotic. This antibacterial effect was clearly be ascribed to the alkaline pH as a result of Mg dissolution, not to the release of $Mg^{2+}$ ions [418].

Finally, Mg alloy degradation leads not only to the formation of soluble species, but also to the precipitation of insoluble corrosion products as surface layers (or also in the surroundings). These sparingly soluble compounds, such as Mg-hydroxide and different types of (Mg/Ca) phosphate or carbonate can also have an impact on biocompatibility. Insoluble degradation products formed from pure Mg and rare earth containing Mg alloy corrosion have been observed to show a highly detrimental effect on cells [419]. These surface layers formed will slow down degradation and influence protein adsorption and cell attachment to the Mg surface by changing the surface chemistry and morphology.

### *3.5.9. Approaches to control Mg corrosion for biomedical applications*

In addition to the challenges in understanding the corrosion mechanisms of Mg alloys in biological environments, there is the issue of controlling the corrosion rate and mode. The initial corrosion rate of Mg alloys is often too fast, and a highly reactive Mg alloy surface can be harmful for the biological environment. Strong hydrogen bubbling takes place when a bare Mg alloy sample is introduced to any type of simulated body fluid. Combined with this, local alkalization in the vicinity of the surface can be observed. So while the general corrosion rate needs to be tailored to match the desired lifetime of the device, it is even more desirable to have a controlled time-dependence of the corrosion rate. For instance, initial slow corrosion would allow a development of a stable bio-interface and would enable the mechanical integrity of the device to be maintained for the required period. This should be followed by faster dissolution and finally by a complete removal of the device by soluble corrosion products. Extremely intensive research efforts have been carried out for the control of biodegradation of Mg alloys, both in exploration of novel alloys as well as for developing new types of surface modification approaches. The challenge in both strategies is to combine optimization of the corrosion behavior with the tailored and desired biological performance for the specific targeted application.

### *3.5.10. Tailored alloys and microstructures*

Alloy development for biodegradable implants requires consideration of tailored corrosion behavior, suitable mechanical properties, excellent biocompatibility (this excluding many conventional alloying elements of Mg, *e.g.,* Al), and if possible even desired bioactivity. By meticulous control of alloy chemistry (alloying elements and impurities), processing, heat treatments and resulting microstructures, significant progress has been made in the development of novel alloys with promising *in vitro* and *in vivo* properties, as summarized in a recent review [420]. However, the perfect alloy with the optimized property profile seems not yet to exist. Part of the problem is confirmation of the properties because, as previously described, there is no agreement on the best way to test and rank the corrosion behavior of biodegradable metals, and to match the properties *in vivo*.

One alloy system of interest for biodegradable implants is Mg alloyed with Y, Zr, and rare earth elements, but Mg-Ca and Mg-Ca-Zn alloys have also been investigated. Other alloying elements explored are Ca, Mn, Zn, and Sr, which are expected to lead to additional beneficial biological effects [421]. A survey of the biocorrosion behavior of commercial and exploratory Mg alloys demonstrates that the dissolution rate of different alloys can vary by three orders of magnitude (see Fig. 43). This variation in dissolution rates by alloying is very high, especially considering that it is not based on passivation effects [305]. In addition to a variation of corrosion rates, the study discussed differences in observed corrosion morphologies between the different alloys. Moreover, for some alloy systems, namely Ca-rich alloys, formation of voluminous insoluble corrosion products was observed, which could raise concerns for applications in the human body.

In general, the important role of impurities for the corrosion behavior of Mg alloys is very well known, as described above. For biodegradable Mg alloys, degradation rates of ultra-high purity Mg ($\approx$ 2 ppm Fe, produced via a distillation process) have been shown to be very low both *in vitro* and *in vivo*, and good agreement was found between the laboratory tests and *in vivo* tests in the femur of rats [422].

As the microstructure of (Mg) alloys plays a major role both for the corrosion behavior and for mechanical properties, various approaches to influence the biodegradation behavior and at the same time to achieve beneficial mechanical properties for the alloys have been explored. For instance, a high-strength, low-alloy, high-purity Mg-Zn-Ca alloy has been developed that exhibits high strength and simultaneously high ductility due to grain size refinement, together with slow degradation rate [423]. The slow corrosion rate results from the tailored composition of the intermetallic particles, in particular the reduction of Zn content, which leads to formation of anodic intermetallic particles instead of cathodically active intermetallic particles. Another approach to influence both the mechanical properties and the corrosion behavior simultaneously is to decrease the grain size by severe plastic deformation (SPD) techniques, leading to formation of ultra-fine grained materials. While significant effects of grain refining on the corrosion behavior have been reported on Mg in standard NaCl

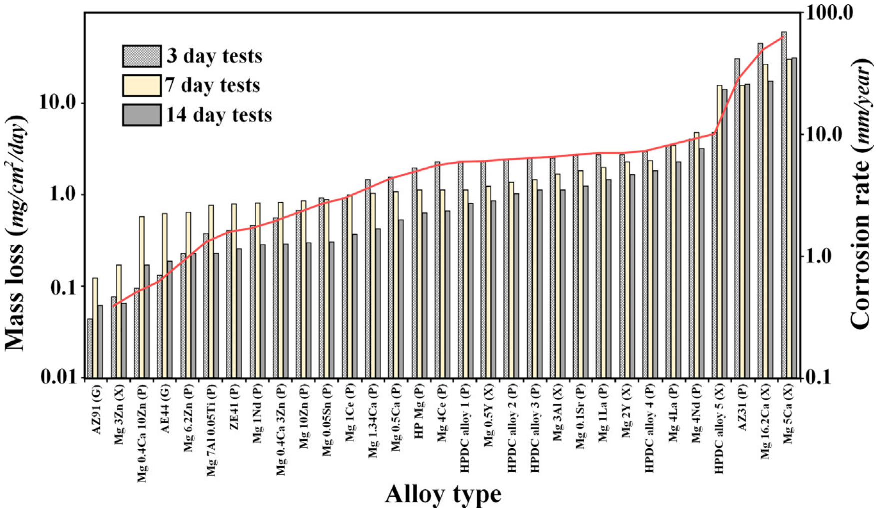

**Fig. 43.** Corrosion rates for selected Mg alloys measured at 37 °C in MEM. High purity Mg was <40 ppm Fe. All compositions given in wt.%. Note: The notation 'G' refers to alloys which suffered a general corrosion mode, 'P' refers to a pitting corrosion mode, and 'X' refers to extremely localized corrosion [305]. Reprinted with permission from Elsevier.

electrolytes [424], only few studies can be found on biomedical application of SPD-treated Mg alloys [425–427]. These studies indicate beneficial effects due to grain refinement achieved by equal channel angular pressing both on the mechanical properties as well as on the corrosion resistance of Mg alloys. Regarding the corrosion behavior, the decrease in the size of second phase particles and the resulting increase in microstructural homogeneity decreased localization of corrosion. Moreover, Mg-Zn-Ca bulk metallic glasses have been of interest as prospective materials for biodegradable implants [300,428]. Due to their homogeneous, single-phase amorphous nature, they exhibit good mechanical properties and are possibly be less prone to localized corrosion than conventional crystalline, multi-phase alloys of a similar composition.

### *3.5.11. Surface modification and coatings*

The different approaches studied for coatings and surface modification of biodegradable Mg alloys are so plentiful (*e.g.*, anodization, Ca-phosphate coatings, biodegradable polymers) that it is impossible to even mention all of them. Recent review articles [429–432] summarize some of the research carried out in the field. The highly reactive Mg alloy surface offers a challenge for coating approaches via aqueous chemistry. Pre-treatments are often required to minimize Mg corrosion during the coating process and to improve adhesion. The challenges for surface modification of biodegradable Mg alloys are complex, as the coatings should be biocompatible (and possibly biofunctional), should degrade in a controlled way, and also be compatible with the surgical procedure. However, many temporary implants are expected to degrade in a relatively short time (*e.g.*, some months to one year), so there is no need to develop perfect barrier coatings for these applications. In spite of the huge amount of literature to be found on various types of coating approaches to protect Mg alloys from too-fast biodegradation, many open challenges remain. In a large number of reports, the protective effect of the coatings is studied only for a short-term exposure [429]. However, knowledge of the time-dependence of the protective effects of coatings and of the degradation of the coatings themselves is required for successful application. A suitable coating for biodegradable Mg based implants should initially offer good protection to mitigate the negative effects related to fast burst of dissolution of a freshly implanted device, then degrade in a controllable manner, and finally enable complete dissolution of the coating and the underlying substrate. The required time-profile of degradation of course depends on the targeted application. One drawback in the design of coatings for tailored degradation is the unknowns between a test of degradation rate in the laboratory and true performance of the coating *in vivo*.

Another critical issue often ignored is adhesion of coatings on the Mg alloy surface. Poor adhesion leading to possible undermining of the coatings and delamination, or to filiform corrosion, is especially problematic with polymer coatings on Mg alloys. To improve adhesion and to optimize the time-dependent protection of coated Mg alloys, surface pretreatments and multi-layer coatings should be explored. Some coating approaches may be successful in protecting the Mg alloy surface against too-fast dissolution, but they eliminate the inherent beneficial biological properties of Mg alloys. An example is the bioactivity of Mg alloys associated with the formation of biomimetic Ca-phosphate, which may be desired for applications of Mg alloys in temporary orthopaedic devices. For instance, pure Mg is bioactive and induces Ca-phosphate precipitation in simulated body fluid [433]. Protecting Mg with biodegradable polymer coating, for instance polycaprolactone (PCL), can lead to very significant reduction in corrosion rates, but at the same time the bioactivity is strongly reduced [433]. To re-activate the Ca-phosphate formation, bioactive glass (BG) can be added to the PCL coating. However, the pro-

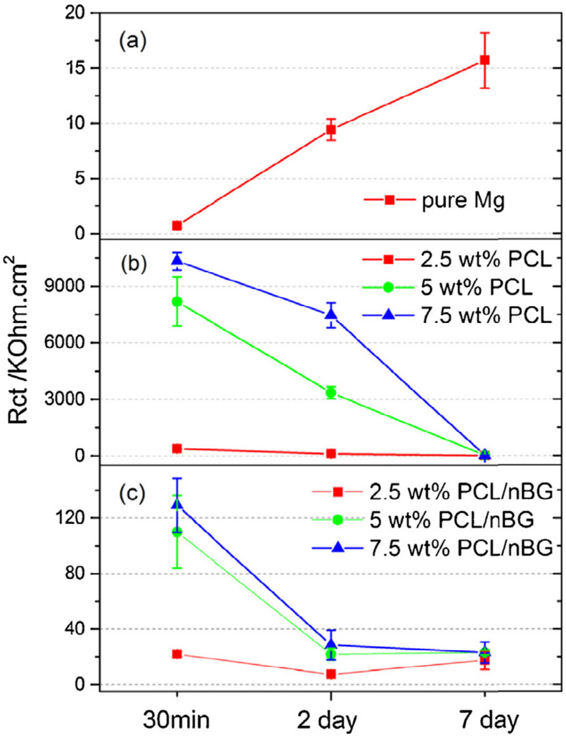

**Fig. 44.** Corrosion protection effect of coatings prepared by spin-coating on Mg. Charge transfer resistance ($R_{ct}$) for (a) pure Mg, (b) PCL, and (c) PCL/nBG coatings in DMEM solution for different immersion times at 37 °C. The wt.% in the legend indicates the concentration of PCL as dissolved in chloroform for spin-coating. The thickness of the coatings was ~1 µm for 2.5 % PCL, 2.4–2.6 µm for 5% PCL, and 6.7–6.8 µm for 7.5% PCL (independent of the addition of BG) [433]. Reprinted with permission from Elsevier.

tective effect of the PCL/BG composite coating was found to be drastically reduced and faster degradation of the coating took place compared with pure PCL coatings.

Nevertheless, even the PCL/BG composite coating showed a significant corrosion protection compared with the pure Mg surface. Results from electrochemical impedance spectroscopy characterization of these coatings are shown in Fig. 44. Hence, by tailoring the polymer/bioglass-ratio in such coatings, the corrosion behavior and the biological performance could be optimized for different possible bio-applications.

### *3.5.12. Conclusions: Understanding biocorrosion of Mg alloys?*

This section aims at illustrating the challenges in understanding and controlling the corrosion behavior of Mg alloys regarding their use as biodegradable implants. There has been tremendous research interest in the field in the last 10 years and the progress in determination of the critical factors of Mg alloy biocorrosion is impressive. Today, there is probably agreement on the necessity to carry out laboratory experiments in electrolytes that to the best of our current understanding mimic the *in vivo* environment. This in contrast to the early work, which often used far too simple laboratory conditions such as simple NaCl solutions for such studies. At the same time the elucidation of direct cause-effect relationships is more challenging as the systems studied become more complex. This result from both the complicated interactions between the corroding Mg alloy surface and a specific parameter, and the fact that the different species present in the biological environments (ions, biomolecules, and cells) are not independent of each other. Moreover, some of the corrosion-effecting parameters, such as proteins and cells, can have multiple possible operative modes on the corrosion process (for instance on the metal surface and in the electrolyte with metal cations). Therefore, even slightly changes in the experimental conditions can lead to varying chemical equilibria on the corroding interface, and, hence to a change in the observed degradation rate and mode. Due to the high complexity of the corroding system, a sophisticated set of research tools is required, including conventional techniques to study corrosion (electrochemistry, immersion testing, and $H_2$ gas collection), surface analysis, and solution analysis for metal release.

Nonetheless, the progress in general understanding of Mg alloy corrosion mechanisms and biodegradation is impressive, both in the exploration of Mg dissolution mechanisms as well as the correct use of experimental techniques and interpretation of results. Hopefully, the knowledge generated in the field of Mg alloy biocorrosion can in its turn be useful for elucidating complex reaction mechanisms of other metals and alloys under challenging environmental exposures. Moreover, the understanding on the influence of biomolecules and inorganic ions on Mg corrosion could lead to new insights in the development of novel inhibitors or conversion coatings for Mg alloys to be used in other applications.

## 4. Atmospheric corrosion

Metals exposed to the ambient atmosphere tend to suffer atmospheric corrosion, causing degradation of *e.g.,* infrastructure, cars, and buildings. In addition to the very substantial economic cost, atmospheric corrosion affects historical monuments and objects, resulting in irreparable damage to the world's cultural heritage [434–437]. In all, atmospheric corrosion accounts for more failures in terms of cost and tonnage than any other type of material degradation [88,434,438].

Atmospheric corrosion depends on the availability of water on the metal surface, as little or no corrosion occurs under "dry" atmospheric conditions. The role of water is connected to the thin oxide film that rapidly forms on the surface of most metals in air and that protects against further oxidation. Thus, the protective oxide film may be hydrolyzed by water and can dissolve in liquid water. The resulting thinning of the protective film allows metal oxidation to resume. In many cases oxide film dissolution in water triggers electrochemical corrosion, the anodic dissolution of metal coupled to cathodic reduction of an oxidant (usually $O_2$ or $H_2O$), via electronic conduction in the metal and ionic conduction in the aqueous electrolyte. Hence, rain, fog and dew can cause atmospheric corrosion. Indeed, a clean metal surface can suffer corrosion even in the absence of liquid water. Thus, when the RH approaches 100%, multilayer adsorption of water molecules gives rise to a surface layer with properties mimicking liquid water [88,99,118].

In addition to rain, dew, and RH, atmospheric corrosion is influenced by temperature and the presence of a whole range of atmospheric micro-constituents. They include gases such as $CO_2$, $SO_2$, $O_3$, $NO_x$, HCl, organic acids (*e.g.,* $CH_3COOH$), particulates including sea-salt, $(NH_4)_2SO_4$, soot, compounds dissolved in rain (including many of those just listed), as well as UV radiation (sunlight) [88,118,440]. $H_2SO_4$ and $HNO_3$ are mainly dissolved in raindrops, causing "acid rain". This assortment of compounds and substances influences corrosion in many ways. With some, the acid/base properties are crucial ($CO_2$, $H_2SO_4$, organic acids) while others play a role because of their oxidizing power ($O_3$) or because they can act as cathodes (soot). The role of sea-salt in atmospheric corrosion is connected both to its deliquescent nature (its ability to form an aqueous solution at RH < 100%) and to the corrosivity of its constituents (*i.e.,* NaCl) [88,441]. Importantly, the deposition of acids and soluble salts cause the conductivity of the water film present on the metal surface to increase a lot, resulting in higher corrosion currents. It may be noted that some gases (HCl, $SO_2$, and $HNO_3$) can react with the metal surface under dry conditions, forming small amounts of compounds (*e.g.,* chlorides), which later absorb water and form a surface electrolyte under conditions of higher RH, causing corrosion. Substances added on purpose to the environment can also impact atmospheric corrosion in a major way [118,438]. One example is the use of NaCl for deicing of roads, which causes corrosion of vehicles during winter.

In the following, we aim to supply a comprehensive summary, presenting the challenges and future prospects of the Mg atmospheric corrosion field. We first highlight the differences distinguishing atmospheric corrosion from aqueous corrosion. Next, general information on some important environmental factors and their influence on corrosion is introduced (Section 4.1). In addition, the atmospheric corrosion behavior of Mg and Mg-Al alloys is described in detail and the effect of environmental variables is discussed (Section 4.2). Furthermore, we provide some new insights into the field of Mg atmospheric corrosion *via* presenting two novel concepts surrounding atmospheric corrosion product composition and corrosion mechanism. Lastly, we illustrate the strategies that have researched and employed to protect Mg alloys against atmospheric corrosion.

### *4.1. Atmospheric corrosion versus corrosion during immersion*

Considering the dominant role played by the aqueous surface electrolyte, atmospheric corrosion can be regarded as a special case of aqueous corrosion. Still, a surface that is exposed to the atmosphere corrodes under conditions, which are rather different than those prevailing during immersion in an aqueous solution. Below, these differences and their consequences for Mg corrosion in the atmosphere and during immersion are discussed.

A number of investigations comparing the corrosion resistance of several Mg alloys under immersion conditions and in atmospheric corrosion are summarized in Tables 5 and 6. Due to the reasons explained in the Introduction, most studies concern the corrosion behavior of Mg-Al alloys. First, it may be noted that, while HP Mg (*i.e.,* impurity contents well below the respective tolerance limits, see Section 3.3) exhibits relatively slow corrosion during immersion in NaCl(*aq*) solution [104,441], it suffers rapid atmospheric corrosion in the presence of NaCl [166]. Second, Al additions increase the cathodic activity, and accordingly, the rate of corrosion of Mg-Al in aqueous media (*e.g.,* NaCl solution), after a certain "threshold" concentration (~3 wt.%), as discussed in Section 3.3. A closer look in the literature at the effect of Al (Table 5) shows that the immersion experiments have yielded rather contradictory results concerning the corrosion resistance of Mg-Al alloys in general and on the role of Al in particular. Thus, while some of the studies cited in Table 5 observed that the rate of corrosion decreases with increasing Al content (*e.g.,* Baril et al. [442] and Pardo et al. [443]), other workers report the opposite trend, *i.e.,* the rate of corrosion increases with Al content (*e.g.,* Zhao et al. [104] and Wang et al. [444]). In still other cases, HP Mg and Mg alloys with varying Al content (*e.g.,* AZ31 and AZ91) have been reported to exhibit very similar corrosion rates (see Inoue et al. [441]). Indeed, this inconsistency remains, even when the comparison is restricted to studies of relatively "long" exposure times and to the alloys that feature impurity levels below the so called "tolerance limit" (in Table 5).

**Table 5**
Literature rankings of the corrosion resistance of Mg alloys under immersion conditions.

| Corrosion rate | Environment/method/comments | Ref. |
|---|---|---|
| AM50 > AZ91 > AZ91Si (up to 80 h) | Sodium sulfate (EIS) | Baril et al. [442] |
| ZE41 > AM60 > AM30 > AZ91 > AZ31 ~ HP Mg (12 days) | Salt spray testing (WL) | Zhao et al. [104] |
| AZ31 ~ AZ91E ~ HP Mg (pH 9, >100 h) | Buffered chloride (EIS) | Inoue et al. [441] |
| AZ91 > AZ31 > AM60 > ZK60 (0.5 h) | NaCl solution (EIS) | Cheng et al. [445] |
| AZ91 > ZE41 > HP Mg ~ $Mg_2Zn_{0.2}Mn$ | Hank's solution (EIS) | Abidin et al. [446] |
| AZ91 > AZ21 > AZ501 | NaCl solution (EIS) | Song et al. [447] |
| AM50 > AZ91D > AM50 NdB > AZ91DNdB | NaCl solution (WL) | Arrabal et al. [448] |
| Mg5Al > Mg > Mg10Al ~ Mg15Al | NaCl solution (EIS) | Abady et al. [449] |
| Mg > AZ31 > AZ91 (20 h) | NaCl solution (EIS) | Wang et al. [444] |
| Mg > AP65 > AZ61 > AZ31 | $Mg(ClO_4)_2$ (EIS) | Udhayan et al. [450] |
| Mg < AZ91 < AZ31 | NaCl solution (EIS) | Singh et al. [451] |
| Mg > AZ91 > AS31 | $NaNO_3$ (Electrochem) | Shaye et al. [452] |
| Mg > AZ31 > AZ91 > AZ80 | NaCl solution | Pardo et al. [443] |
| Mg12Al > Mg9Al ~ Mg6Al ~ Mg2Al > Mg1Al | NaCl solution (EIS) | Liu et al. [103] |
| Mg10Al > Mg5Al > Mg22Al > Mg1Al > Mg41Al | NaCl solution (EIS) | Shi et al. [453] |

Note: WL: weight loss, EIS: Electrochemical Impedance Spectroscopy.

**Table 6**
Literature rankings of the corrosion resistance of the Mg alloys under atmospheric conditions.

| Corrosion rate | Environment/method | Ref. |
|---|---|---|
| AM20 > AM60 > AZ91D | $CO_2$, 95% RH, 22 °C (WL) | Lindström et al. [32] |
| AM50 > AZ91D | $CO_2$, 95% RH, 25 °C (WL) | Arrabal et al. [456] |
| HP Mg > AM20 > AZ31 > AM60 > AZ91D | $CO_2$, 95% RH, 22 °C (WL) | Esmaily et al. [166] |
| AZ31 > AM60 > AZ91D | Field exposure (in Japan) | Liao and Hotta [94] |

In contrast, the relatively few reports on the atmospheric corrosion performance of Mg-Al alloys are more consistent in this respect, *i.e.,* showing that Al alloying has a positive effect on the ability to resist corrosion. Thus, in study by Jönsson et al. [98] who exposed AZ91D and AM50 in a marine environment for 12 months, AM50 exhibited a metal loss of ~15 $g/m^2$, while the corresponding value for AZ91D was ~6.5 $g/m^2$. In another case, it has been reported that the measured corrosion rates of alloys AZ91 and AZ51 in a marine environment were 2.8 and 14.5 μm/year, respectively [454,455]. The same trend is apparent in investigations of the atmospheric corrosion behavior of Mg-Al alloys under controlled conditions in the laboratory, see Table 6. Thus, alloys with high Al content, *e.g.,* AZ91(D) are consistently reported to corrode slower than low Al content alloys, *e.g.,* AZ31, AM60, and AM50 [32,456,166,94].

The divergent results in Table 5 and lack of agreement with corrosion under atmospheric conditions imply that the corrosion behavior of Mg alloys under service conditions cannot be predicted by experiments performed under immersion. Indeed, this raises the question of how atmospheric corrosion differs from corrosion during immersion and how these differences affect the corrosion of Mg and Mg-Al alloys.

It is proposed that the single most important difference in conditions is the small amount of electrolyte in atmospheric corrosion. Thus, except in connection to rain and dew, the amount of liquid water during atmospheric corrosion is very limited. In many cases the corrosion processes occur in a water film that is less than 1 μm thick (see Section 4.2). Indeed, atmospheric corrosion is induced even by adsorbed water films that are only a few nm thick. Important consequences of the sparse electrolyte for corrosion can be summarized as follows:

- The thickness of the aqueous electrolyte affects both the anodic and cathodic processes. Already in 1972, Rozenfeld [88] noted that the passivity regions of Al and Mg were extended as the electrolyte film grew thinner. He attributed this behavior to easy access of oxygen to the surface, which facilitated the formation of passive and quasi-passive surface films.
- The relatively high resistance of the thin electrolyte present during atmospheric corrosion tends to diminish the size of the electrochemical corrosion cells. In contrast, the low resistance of the electrolyte under immersion in, e.g., NaCl(*aq*) solution, allows a large separation of anodic and cathodic sites, and thus, a stronger micro-galvanic corrosion.
- The thin aqueous film that is mostly present during atmospheric corrosion results in the absence of convection in the liquid, allowing build-up of large chemical gradients (*e.g.,* pH gradients) on the corroding surface, but do not easily develop during immersion.
- The aqueous surface layer is considered to be saturated with $O_2$, at least when corrosion products are absent. Also, atmospheric $CO_2$ has a major influence on the surface chemistry, affecting the pH in the aqueous layer, causing carbonization of the surface film and rapid reaction with the catholyte during electrochemical corrosion. Also, the aqueous film will tend to be saturated with respect to the corrosion products formed and the concentration of soluble salts (*e.g.,* NaCl) will tend to be quite high.

**Table 7**
Estimated number of water monolayers adsorbed on a metal surface at 25 °C [459].

| RH (%) | Number monolayers of adsorbed water |
|---|---|
| 20 | 1 |
| 40 | 1.5–2 |
| 60 | 2–5 |
| 80 | 5–10 |

- In contrast, in an immersion situation the dissolution of large amounts of corrosion products is required for the liquid to become saturated. Also, the influence of atmospheric gases (*e.g.*, $CO_2$) is less marked and much slower.
- As a consequence, the principal atmospheric corrosion products of Mg and its alloys (Section 4.3), *e.g.*, Mg hydroxy-carbonates, tend not to form under immersion conditions, being replaced by brucite ($Mg(OH)_2$), as the dominant corrosion product.

Taken together, these differences have important consequences for the corrosion behavior of Mg and its alloys. For example, the carbonated surface films formed during atmospheric corrosion appear to be protective in many cases. For Mg-Al alloys, the decrease in surface pH resulting from the influence of $CO_2$ appears to stabilize the alumina-containing surface film, which results in a pronounced and strong positive effect of Al content in the anodic dissolution of $\alpha$-Mg grains when exposed under atmospheric conditions. Furthermore, it is reasonable to assume that the buildup of the corrosion products can result in obstruction of anodic and, even, cathodic regions in the microstructure. The distinctive atmospheric corrosion behavior of Mg and Mg-Al alloys will be discussed further below.

## 4.2. Factors influencing atmospheric corrosion

### 4.2.1. Rain and mist

The dominant anions in rainwater are $Cl^-$, $NO_3^-$, and $SO_4^{2-}$. The crucial cations are $Na^+$, $K^+$, $Ca^{2+}$, $Mg^{2+}$, and $NH_4^+$ [457]. In the absence of pollutants, rainwater is slightly acidic (pH = 5.6) because of $CO_2$, which forms $H_2CO_3$ [458]. In "acid rain" pH may be <4 because of the uptake of compounds like $SO_2$, $H_2SO_4$, and $HNO_3$ [457,458]. The effect of rain on the corrosion is complex. Rain provides an electrolyte and maintains RH above the critical level at which corrosion commences. While rain can be acidic, rain can also remove corrosive dust and acidic deposits originating from gaseous atmospheric pollutants that have accumulated prior to rainfall. At a given location, surfaces exposed to rainfall are typically more resistant to corrosion than those that are seldom or never cleaned by rain [87,88]. In contrast to rain, fog does not clean the metal surface and is considered as more aggressive than rain [87].

### 4.2.2. Relative humidity and condensation

The electrolyte supporting the electrochemical corrosion process in ambient air is provided by water, which can be in the *liquid* or the *adsorbed* state. Liquid water is supplied by *e.g.*, rain, mist or condensation. RH is a central concept in atmospheric corrosion and designates the ratio of the partial pressure of water vapor, $P_{H2O}$, to the saturation vapor pressure of water, $P^o_{H2O}$, at a given temperature (RH = $(P_{H2O}/P^o_{H2O}) \times 100$). The dew point corresponds to the temperature where air is saturated with water vapor, *i.e.*, RH = 100% [87,88]. While liquid water thus evaporates at RH < 100%, a clean surface is still covered by a thin *adsorbed* water layer under those conditions. According to Phipps et al. [459], the first reversibly adsorbed water monolayer forms at RH ~ 25% at ambient temperature while the thickness of the aqueous film at 95% RH is about 10 monolayers (Table 7). Although the layer of adsorbed water present on a clean surface at RH < 100% is thus very thin, it can still sustain corrosion [88,459]. However, corrosion is greatly accelerated by condensation, causing much thicker water layers to form. In a concentrated salt solution the equilibrium vapor pressure of water is decreased. This causes condensation to happen at RH < 100% when soluble salts are present, otherwise known as deliquescence. For example, NaCl(*s*) forms an aqueous solution at RH > 76% at room temperature.

There is a general, positive correlation between RH and the rate of metallic corrosion. Early on in 1924, Vernon [108] observed that corrosion of Fe in $SO_2$ polluted air was negligible below a certain threshold RH (Fig. 45a), only becoming significant above that level. Such a "critical RH", above which significant corrosion starts, can be found for all metal/environment combinations. For example, Whitby [170] reported that RH was strongly correlated to the mass gain of Mg (Fig. 45b). Clean metal surfaces exposed to clean air either tend not to corrode significantly at all (*e.g.*, Al and stainless steel) or to exhibit a critical RH just below 100% (Fe). In many cases, critical RHs in the range 50–70% are reported [460].

The occurrence of such low critical RH values imply that water-soluble substances have deposited on the surface (*e.g.*, NaCl or sea salt) or that water-soluble corrosion products have formed (*i.e.*, in the case of Vernon's experiment [108], products of the reaction of $SO_2$ and Fe). The "critical humidity" needed for significant corrosion to happen is usually slightly lower than the value needed for the pure salt to form an aqueous solution by deliquescence.

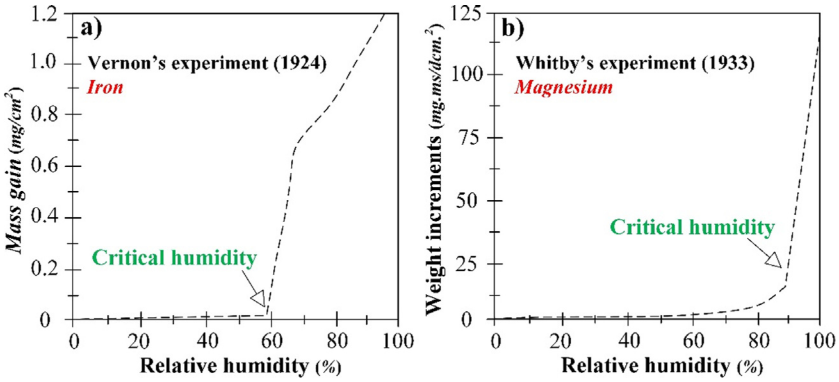

**Fig. 45.** The "critical humidity" in atmospheric corrosion | (a) Corrosion of iron after 55 days in air containing 0.01% $SO_2$ illustrating the presence of a critical RH (60% in this case) [108], and (b) corrosion of Mg after 77 days showing a critical RH of 90% [170]. Reproduced with kind permission from the Royal Society of Chemistry.

### *4.2.3. Substances influencing atmospheric corrosion*

Substances reach the metal surface either by dry or wet deposition. For particulates, dry deposition means impingement on the surface while for gaseous substances it signifies surface adsorption or dissolution of the gas in an aqueous surface film. Wet deposition means that the substance in question (acid, salt or gas) is deposited in the form of an aqueous solution, *i.e.*, dissolved in rain or mist (*c.f.*, acid rain) [88,460]. The ability of a substance to influence the atmospheric corrosion of a metal depends on its chemical properties in relation to the material. As mentioned above, the solubility in water is an important factor. Thus, the ability of NaCl to deliquesce at 76% RH is directly linked to its high solubility. Other important chemical properties that determine the corrosivity of a compound include the acidity, the redox properties and the ability to form chemical bonds with species in solution and with the oxide surface. For insoluble substances, electronic conductivity and the ability to catalyze chemical reactions are important [88,460]. The discussion below is limited to gases and soluble inorganic salts.

### *4.2.4. Inorganic salts*

Most sulfates, chlorides and nitrate salts are highly soluble in water and consequently cause water to condense at RH < 100%, forming a surface electrolyte on the metal surface. For example, at room temperature, $Na_2SO_4$ causes water to condense at RH > 93%, while $CaCl_2$ forms an aqueous solution already > 32% RH [461,462]. Even though the amount of condensate may be quite small, its high conductivity creates beneficial conditions for electrochemical corrosion.

The corrosivity of a salt is highly dependent on the chemistry of the anion. For example, $Cl^-$ and $SO_4^{2-}$ tend to stimulate corrosion of most metals because they form chemical bonds with many cations in aqueous solution as well as with the oxide or hydroxide film that covers the metal surface. In particular, $Cl^-$ is highly detrimental for the protectiveness of the passive/quasi-passive surface films formed on the metal surface (see Sections 4.3.1 and 4.3.6). In contrast, $NO_3^-$ is much less corrosive in most cases because the bonds formed to cations in solution and to the surface are weak. A variety of soluble cations are present on surfaces exposed to the atmosphere, *e.g.*, sea salt contains significant amounts of $Mg^{2+}$, $Ca^{2+}$, and $K^+$ together with $Na^+$. Atmospheric corrosion is also influenced by the aqueous chemistry of the cation, especially by its basicity. Thus, because NaOH is very soluble in water, the presence of a sodium salt (*e.g.*, NaCl) enables the development of very high pH values in the cathodic regions. In comparison, $Mg(OH)_2$ is relatively insoluble, preventing the development of cathodic alkalinity in the presence of a Mg salt (*e.g.*, $MgCl_2$) [88,460,463].

### *4.2.5. Gases*

Atmospheric corrosion is strongly influenced by gaseous compounds, including the major atmospheric constituents $O_2$ and $CO_2$ and several trace gases such as $SO_2$, $NO_2$, $HNO_2$, $HNO_3$, $H_2S$, HCl, $NH_3$, $O_3$, formic acid, and acetic acid [88,464,465]. In this review, we will mainly be concerned with the corrosion effects of $CO_2$ and $SO_2$ and to some extent $NO_2$ and $O_3$.

$CO_2$ is the main greenhouse gas. The average concentration of $CO_2$ has risen from 280 ppm in pre-industrial times to about 400 ppm at present because of emissions from combustion of fossil fuels and due to deforestation [466,467]. Generally, the influence of $CO_2$ on corrosion is connected to its acidity, the reactive dissolution of $CO_2$ in the electrolyte generating carbonic acid (Eqs. (36)–(39)), ($pk_{a1} = 6.35$ and $pk_{a2} = 10.33$) and decreasing pH [122,123]. $CO_2$ affects the Mg corrosion mechanism profoundly, see Section 4.3.2 (below).

$$CO_2(g) \rightarrow CO_2(aq) \tag{36}$$

$$CO_2(aq) + H_2O(l) \rightarrow H_2CO_3(aq) \tag{37}$$

**Table 8**
Representative peak concentrations of $NO_2$ and $O_3$ in the over the continents [474,475].

| Pollutant | Remote | Rural | Moderately polluted | Heavily polluted |
|---|---|---|---|---|
| $NO_2$ | 1 | 1–20 | 20–200 | 200–500 |
| $O_3$ | 50 | 20–80 | 100–200 | 200–500 |

[*] Concentrations are in part per billion by volume (ppbv).

$$H_2CO_3(aq) + OH^-(aq) \rightarrow HCO_3^-(aq) + H_2O(l) \tag{38}$$

$$HCO_3^-(aq) + OH^-(aq) \rightarrow CO_3^{2-}(aq) + H_2O(l) \tag{39}$$

$SO_2$ is one of the most important corrosive air pollutants (see Section 4.3.3). Atmospheric $SO_2$ is partly anthropogenic, mainly from the combustion of fossil fuels, and partly has natural sources such as volcanic eruptions [434,438]. Atmospheric $SO_2$ is oxidized to $SO_3$, which forms sulfuric acid ($H_2SO_4$) and sulfates. Sulfuric acid is a major cause of “acid rain”. $SO_2$ levels have decreased a lot in North America and Europe since the 1970s and the average concentrations are now usually on the $10^{-9}$ atm level or lower, even in urbanized areas. However, $SO_2$ concentrations are still rising in parts of Asia where peak concentrations in cities often reach $10^{-7}$ atm [468].

Ozone ($O_3$) and $NO_2$ are important trace oxidants in the atmosphere and tend to accelerate the corrosion of many metals (Table 8) [468,469]. $NO_2$ in the atmosphere is originated mainly via the oxidation of NO(*g*). Because the main source of NO is vehicular traffic, $NO_2$ levels tend to be high in areas with heavy traffic. $NO_x$ concentrations are slowly decreasing in North America and Europe while concentrations are on the increase elsewhere. A main source of $O_3$ is the photocatalytic reaction of NO and $NO_2$ with volatile organic compounds [468,470]. Hence, high ground level ozone levels occur in areas featuring a combination of intense UV radiation and high levels of organic pollutants and $NO_x$.

To influence corrosion, gaseous compounds must deposit on the metal surface, either by dissolving in a water film or by adsorbing on the surface. Both gas dissolution and surface adsorption are exothermic processes, meaning that the condensed (*i.e.*, dissolved or adsorbed) state is favored by lowering the temperature. The adsorption of a gas on the oxide-covered surface is exemplified by the adsorption of $SO_2$ on an MgO-covered Mg surface under dry conditions (Eq. (40)).

$$SO_2(g) \leftrightharpoons SO_2(\text{add on MgO}) \tag{40}$$

The adsorbed $SO_2$ is weakly bonded but may convert to form much more strongly bonded sulfite.

$$SO_2(\text{ad on MgO}) \rightarrow MgSO_3(\text{surface}) \tag{41}$$

In dry conditions, the deposition of gases on metals is normally slow and very limited in extent. The interaction between gases and metal surfaces is usually much stronger in humid conditions when a water film is present on the surface. The equilibrium solubility of gases in water is described by: $K_H(X)_K = [X(aq)]/P(X)(g)$, where $K_H$ is the inverse Henry’s law constant, [X (*aq*)] is the concentration of X (*M*) and P(X) (*g*) is the partial pressure of X (atm). Generally, the logarithm of the Henry's law constant is correlated to the boiling point of the pure gas, such that gases with low boiling point (*e.g.*, $O_2$) show lower Henry's law solubility than high boiling point gases (*e.g.*, $SO_2$) [468–470]. In addition to dissolving in water, many gases react to form new aqueous species. Thus, when $SO_2(g)$ dissolves in water there is protolysis, according to the following reactions [109,110,120,472,473]:

$$SO_2(g) \leftrightharpoons SO_2(aq) \tag{42}$$

$$SO^2(aq) + H_2O(l) \leftrightharpoons HSO_3^-(aq) + H^+(aq) \tag{43}$$

$$HSO_3^-(aq) \leftrightharpoons SO_3^{2-}(aq) + H^+(aq) \tag{44}$$

Because protolysis is favored by equilibrium thermodynamics, the total solubility of $SO_2$ in water ($[SO_2]tot = [SO_2(aq)] + [HSO_3^-\ (aq)] + [SO_3^{2-}\ (aq)]$) is much greater than the solubility of the $SO_2$ molecule. The combination of gas dissolution and a secondary reaction is termed *reactive dissolution.* It is especially important for strong acids such as HCl(*g*) and $HNO_3(g)$ but is also very important for acidic and basic gases in general [110,120]. $NO_2$ is quite different from $SO_2$ in its interaction with water because it does not form an acid directly upon dissolution, but only after disproportionation (a redox reaction) (Eq. (45)) [120,473]. Hence, $NO_2$ causes acidification indirectly, by forming nitric acid ($HNO_3$ and nitrous acid ($HNO_2$)).

$$2NO_2(g) + H_2O(l) \rightarrow 2H^+(aq) + NO_3^-(aq) + NO_2^-(aq) \tag{45}$$

It may be noted that protolysis reactions are generally extremely rapid while redox reactions for $NO_2$ are relatively slow. Hence, the reaction of $NO_2$ with the surface electrolyte is quite slow compared to the protolysis of an acid as in Eqs. (43) and (44). Together with a lower Henry’s law solubility, this causes the rate of deposition of $NO_2$ to be a lot less than for $SO_2$ on most surfaces exposed to the atmosphere [120,473–475]. Also, the acidification of the surface electrolyte by $NO_2$ is much less prominent than for $SO_2$. In this context, the reactive dissolution of acidic gases plays a crucial role in atmospheric corrosion. Firstly, the oxide/hydroxide surface layer covering most metals in air can react with the protons generated (Eq. (46)).

$$Mg(OH)_2(surface) + 2H^+(aq) \rightarrow Mg^+(aq) + 2H_2O(l) \tag{46}$$

Secondly, acid gases react with any alkali generated in electrochemical corrosion processes. As a result, oxide and hydroxide surfaces are often efficient getters for acidic gases under humid conditions. Note that Eq. (46) results in dissolution of the surface film, which may trigger corrosion (see below).

### 4.2.6. Temperature

Short-term variations in temperature directly influence RH, *e.g.*, resulting in dew formation, which has major consequences for corrosion. Hence, any attempt to investigate the effect of temperature on atmospheric corrosion must be performed under careful control of RH. Corrosion consists of a number of interconnected chemical and electrochemical reactions (see Section 3.1). All the reactions are thermally activated, obeying the Arrhenius relationship [472,476], (Eq. (47)).

$$D = Ae^{-Q/RT} \tag{47}$$

where $D$ is the reaction rate, $Q$ is the activation energy, $R$ is the general gas constant, and $T$ is temperature. The Arrhenius relationship thus predicts a positive correlation between temperature and rate for each of the reaction steps that make up the overall the corrosion process. It also applies to conduction in the electrolyte, nucleation of corrosion products, etc. If the overall corrosion rate is determined by a single rate-determining reaction step, corrosion rate will show the Arrhenius dependence of that reaction. However, this is often not the case. Thus, the rate-determining step may not be the same at different temperatures and, indeed, the mechanism of corrosion may change with temperature. Also, corrosion rate can be influenced by changes in the equilibrium constant of a fast reaction. Thus, as mentioned above, the solubility of gases in the surface electrolyte and the adsorption of gases on surfaces show an inverse dependence on temperature. In most cases, the rate of atmospheric corrosion shows a positive correlation with temperature. For example, Blücher et al. [477] reported a strong positive correlation between temperature and the rate of NaCl-induced corrosion of Al in humid air. The role of temperature in the corrosion of Mg and Mg-Al alloys is discussed in Section 4.3.5.

### 4.2.7. Ultraviolet (UV) radiation

The interaction of UV radiation with the metal surface can generate reactive species *e.g.*, atomic oxygen and hydroxy radicals [115,478]. Also, UV radiation can increase the electronic conductivity of semiconducting corrosion products and surface films, thereby enhancing cathodic activity. There are few investigations of UV radiation effects on atmospheric corrosion. Chen et al. [115] and Liang et al. [479] reported an accelerated corrosion of Ag by the synergetic effect of UV radiation and $O_3$. They attributed the rapid corrosion of Ag to the generation of reactive atomic oxygen by the photodissociation of $O_3$, causing rapid formation of $Ag_2O$. Thompson et al. [480] reported that UV radiation enhanced the atmospheric corrosion of Zn alloys. The effect of UV irradiation on the atmospheric corrosion of Mg and its alloys has not been investigated.

## 4.3. Atmospheric corrosion of Mg and Mg alloys

In addition to Mg, this review focuses on Mg-Al alloys, which are the dominant Mg alloy group. Similar to most metallic materials, much of the knowledge on the corrosion properties of Mg and Mg-Al is based on experiments where the metal is immersed in an aqueous electrolyte. However, nearly all applications of Mg-Al alloys (*i.e.*, automotive, building, and aerospace) involve exposure to the ambient atmosphere rather than submersion in liquid water, explaining the interest in the atmospheric corrosion behavior of Mg alloys. Similar to most metals, the atmospheric corrosion of Mg alloys is influenced by RH, temperature and exposure to chloride salts and to several gaseous compounds, including $CO_2$, $SO_2$, $NO_x$, and $O_3$ (see s 4.3.1–4.3.7).

Mg alloys tends to suffer electrochemical corrosion in the atmosphere and the atmospheric corrosion of Mg can be considered to be a special case of aqueous corrosion. Thus, in atmospheric corrosion the anodic dissolution of Mg is described by Eq. (7) (Section 3.1) while the cathodic current is mainly provided by HE (*e.g.*, Eq. (9), refer Section 3.1).

Investigations of the atmospheric corrosion of Mg in the field are few [90,92–96,98,454,455]. In an attempt to evaluate the corrosivity of the global vehicle environment (see Section 2.2), coupons made from the Mg-Al alloy AZ91D were attached to trailers operating in six countries (see the exposure set-up in Fig. 6c, above), together with other materials [100], see Table 9. The highest corrosion rates were recorded in locations with temperate climate and where de-icing salt is used during winter. The authors also considered that the time of wetness (TOW) was an important factor (TOW being defined as the time for which the RH exceeds 80% and T > 0 °C, supposedly corresponding to the duration of the electrochemical corrosion process). The table shows that alloy AZ91D exhibited significantly lower corrosion rates than carbon steel in all six regions included in the study. In the temperate regions, the corrosion rate of AZ91D tended to be somewhat higher than for zinc. In the relatively mild tropical conditions, the relative advantage of Zn was greater.

**Table 9**
Corrosion rate, in µm/year (mg/cm$^2$/day) of AZ91D, carbon steel and zinc exposed at six locations [100].

| Location | Alloy AZ91D | Carbon steel | Zinc (Zn) |
|---|---|---|---|
| France | 3.9 ($1.9 \times 10^{-3}$) | 20.7 ($9.86 \times 10^{-3}$) | 5.2 ($2.5 \times 10^{-3}$) |
| Dubai | 4.0 ($1.9 \times 10^{-3}$) | 6.4 ($3.0 \times 10^{-3}$) | 0.7 ($3.3 \times 10^{-4}$) |
| Thailand | 3.1 ($1.5 \times 10^{-3}$) | 11.1 ($5.29 \times 10^{-3}$) | 0.3 ($1.4 \times 10^{-4}$) |
| Canada | 8.5 ($4.1 \times 10^{-3}$) | 57.3 ($2.73 \times 10^{-2}$) | 4.8 ($2.3 \times 10^{-3}$) |
| Sweden | 14.7 ($7.00 \times 10^{-3}$) | 60.1 ($2.86 \times 10^{-2}$) | 3.6 ($1.7 \times 10^{-3}$) |
| England | 10.7 ($5.10 \times 10^{-3}$) | 66.8 ($3.18 \times 10^{-2}$) | 8.9 ($4.2 \times 10^{-3}$) |

### 4.3.1. The role of chloride

Chloride salts originating from the sea are ubiquitous in atmospheric aerosols, especially in marine environments. In addition, cars are exposed to NaCl on winter roads in many parts of the world where deicing salts are used. Exposure of Mg and its alloys to gaseous HCl results in the formation of $MgCl_2$ on the metal surface by reaction with the surface film (Eq. (48)).

$$2HCl(g) + Mg(OH)_2(s) \rightarrow MgCl_2.H_2O(s) + H_2O(g) \tag{48}$$

Chloride salts play two vital roles in the atmospheric corrosion of metals: (i) similar to other highly soluble salts, they cause condensation at RH < 100%, promoting the formation of the surface electrolyte (*e.g.*, NaCl(*aq*) $MgCl_2$(*aq*)) necessary for electrochemical corrosion and (ii) $Cl^-$ tends to cause local failure of passive and quasi-passive films on metals, giving rise to localized corrosion. The corrosion of a Mg surface contaminated with NaCl(*aq*) causes the anodic sites to accumulate $Cl^-$(*aq*) due to migration. The resulting $MgCl_2$(*aq*) anolyte is slightly acidic, which further enhances the dissolution process. In contrast, the cathodic sites experience a pH increase because of water reduction and the migration of $Na^+$ ions (and accordingly, the formation of a strongly alkaline NaOH(*aq*) catholyte), stabilizing a protective $Mg(OH)_2$ surface film in the cathodic areas. Thus, the pH and chloride concentration gradients set up on the corroding metal tend to establish a stable distribution of anodic and cathodic areas on the surface. It may be noted that there is a feedback between the setting up of an electrochemical corrosion cell and the ability of the surface to form an aqueous electrolyte. Thus, the RH needed to sustain an $MgCl_2$(*aq*) solution at room temperature is only about 34%, while NaOH is even more hygroscopic [461]. Hence, once started, the corrosion cell can in principle run under conditions that are much drier than those needed for NaCl(*aq*) to form (RH = 75%).

The chloride ion is a known corrosion accelerator for metals. In particular, it causes pitting corrosion and other types of localized corrosion on metals that form passive films, *e.g.*, Al. The mechanisms by which the passive films are disrupted by $Cl^-$ is a long-standing issue in corrosion science. In the case of Al, reviews by Frankel [481], Kruger [482], and Streblow [483] attribute the initiation of Al pitting by chloride to *two* main, alternative, mechanisms; (i) penetration of the passive film by chloride through, *e.g.*, oxygen vacancies and (ii) adsorption/ion displacement, resulting in passive film thinning. Similar to Al, Mg corrosion is strongly accelerated by chloride. Thus, in the presence of NaCl, Mg alloys suffer localized corrosion. Investigations of Mg-Al alloys exposed to NaCl(*aq*) solution (see *e.g.*, [179]) show that the quasi-passive films formed feature a bottom Al-enriched layer and that the entire film is penetrated by $Cl^-$, suggesting that the film breakdown is similar to the type (i) mechanism for Al. Details on the films formed on Mg-Al alloys and film penetration by chloride are given in Section 4.3.6.

### 4.3.2. The role of carbon dioxide ($CO_2$)

While $CO_2$ often has free access to metals corroding the atmosphere, occluded regions are also common on many structures, including areas in crevices, beneath deposits and under non-adherent paint layers and paint blisters. These areas will become $CO_2$-depleted because $CO_2$ tends to be consumed at the corroding surface. Notably, ambient concentrations of $CO_2$ have been reported to inhibit the atmospheric corrosion of Zn [484], Al [121,466,477], pure Mg, and Mg-Al alloys [32,122–124].

The inhibitive effect of $CO_2$ in the atmospheric corrosion of Zn in the presence of NaCl has been attributed to the formation of a somewhat protective zinc hydroxy-carbonate surface layer. While Zn oxide is reported to be an active substrate for $O_2$ reduction, the Zn hydroxy-carbonates do not conduct electrons and hence cannot act as cathodes [484]. In contrast, the strong inhibitive effect of $CO_2$ on Al corrosion in the presence of NaCl cannot be attributed to carbonate precipitates, no solid carbonate containing product having been detected [32]. Instead, the inhibitive effect of $CO_2$ has been tentatively attributed to the neutralization of the catholyte by carbonic acid (Eqs. (36)–(39), above), the cathodic sites being blocked by the resulting precipitation of Al hydroxide. Similar to Zn and Al, the corrosion rate of the Mg-Al alloy AM50 in humid air in the presence of NaCl, was reported to be 6–7 times higher in the absence of $CO_2$, compared to when 400 ppm $CO_2$ was present [122]. Also, the relatively benign behavior of Mg-Al alloys in atmospheric corrosion (Table 9) has been attributed partly to the inhibitive effect of $CO_2$ [122,124]. Thus, it is necessary to account for the influence of $CO_2$ when describing the corrosion of Mg and its alloys in the atmosphere.

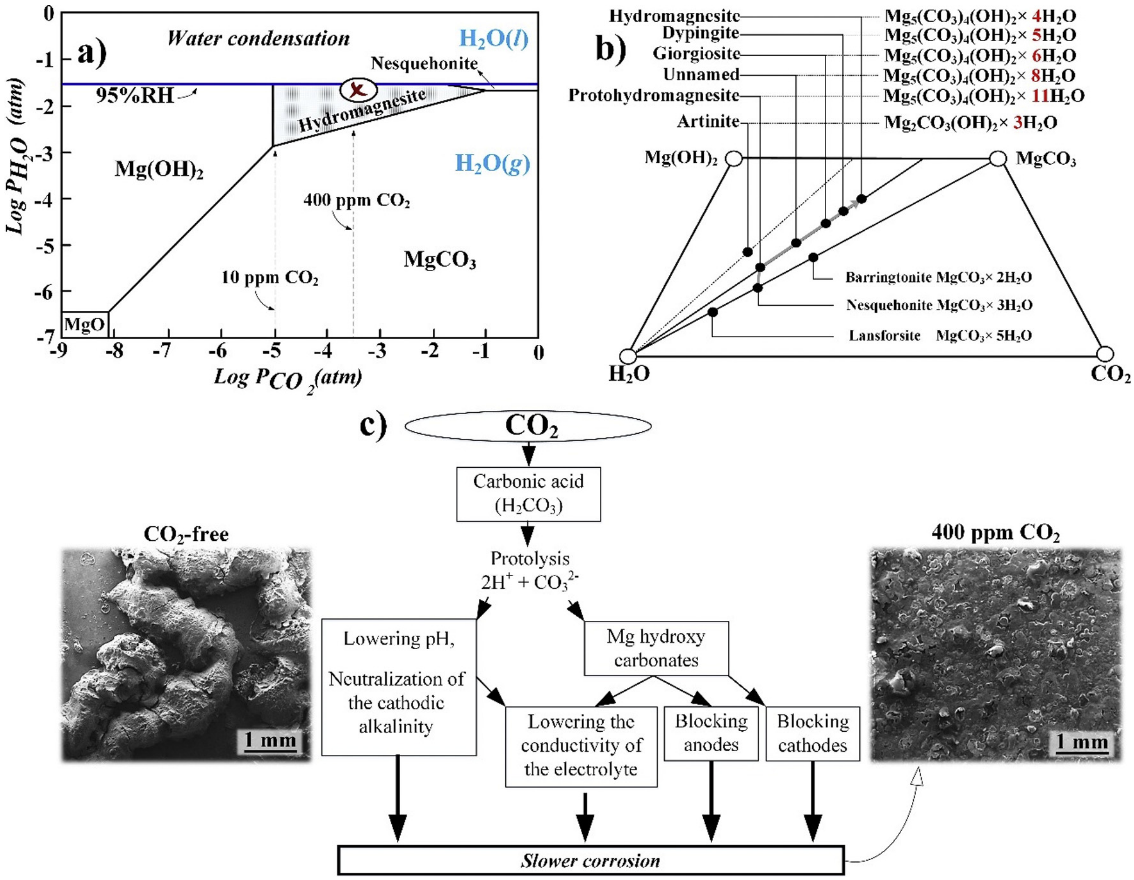

**Fig. 46.** The effect of $CO_2$ on Mg (alloys) corrosion. (a) A calculated diagram showing the $Mg^{2+}$ compounds favored by equilibrium thermodynamics (at 25 °C), as a function of the partial pressure of $H_2O$ and $CO_2$. The cross in (a), corresponds to air with ambient levels of water vapor and $CO_2$, (b) phase diagram for the $Mg(OH)_2$-$CO_2$-$H_2O$ system. In addition to the (thermodynamically stable) compounds in 4.2(a), a number of metastable compounds are also shown, and (c) sketch showing how $CO_2$ impacts Mg corrosion, together with two SEM images illustrating the effect of $CO_2$ on corrosion morphology, (b) is reproduced based on [486,487], published by the PCCP Owner Societies.

*4.3.2.1. Corrosion products.* $CO_2$ tends to neutralize high pH regions on the cathodic areas. In the absence of $CO_2$, the quasi-passive film formed on Mg consists of an MgO bottom layer and a top layer consisting of Mg hydroxide (brucite). Because water in contact with brucite has an equilibrium pH of 10.33 [122,485], the entire Mg surface reacts with $CO_2$ under humid conditions, even before corrosion has started. The reaction of Mg hydroxide with $CO_2$ results in the formation of Mg hydroxy carbonates. The predominance diagram (Fig. 46a) shows the thermodynamically stable phases at 25 °C as a function of the partial pressure of $CO_2$ and water. The diagram shows that $Mg_5(CO_3)_4(OH)_2{\cdot}4H_2O$: hydromagnesite is the stable phase in humid air with ambient concentrations of $CO_2$. In dry conditions, magnesite ($MgCO_3$) becomes thermodynamically favored. Interpreting corrosion product composition in terms of the thermodynamics of chemical equilibrium (Fig. 46a) is always somewhat problematic, primarily because *corrosion* implies that the system we are observing is *not at equilibrium*.

For example, the $Mg(OH)_2$ precipitates which are the primary product of electrochemical corrosion of Mg reacts relatively slowly with the ambient $CO_2$. Thus, a Mg surface corroding in pure $CO_2$-containing humid air will be covered by a mixture of $Mg(OH)_2$ and Mg hydroxy carbonates, in proportions that depend on the rates of corrosion and of brucite carbonization. The carbonization of the surface corresponds to a movement from left to right in Fig. 46a, the end point in air corresponding to the cross in the figure. MgO (lower left corner in Fig. 46a) is always a component in the corrosion product, appearing at the very bottom of the corrosion product layer.

Fig. 46b shows several compounds in the $Mg(OH)_2$ - $CO_2$ - $H_2O$ system. In addition to the thermodynamically stable phases ($Mg(OH)_2$, $MgCO_3$ and hydromagnesite) a number of metastable compounds are also shown. As expected from Fig. 46a, the corrosion products formed on Mg and its alloys in the atmosphere are often dominated by hydromagnesite. In addition, the metastable $Mg_5(CO_3)_4(OH)_2{\cdot}5H_2O$ (dypingite), and $Mg_5(CO_3)_4(OH)_2{\cdot}8H_2O$ (unnamed) are often detected both on lab- [122,149] and field-exposed [88,97] specimens. Mg hydroxy-carbonates, *e.g.*, hydromagnesite [122,149] can form both by precipitation from aqueous solution (Eq. (49)) and by direct reaction of $CO_2$ with $Mg(OH)_2$ (Eq. (50)).

$$5Mg^{2+}(aq) + 4CO_3^{2-}(aq) + 2OH^-(aq) + 4H_2O(l) \rightarrow Mg_5(CO_3)_4(OH)_2 \times 4H_2O(s) \qquad (49)$$

$$5\mathrm{Mg(OH)_2(s)} + 4\mathrm{CO_2(aq)} \rightarrow \mathrm{Mg_5(CO_3)_4(OH)_2} \times 4\mathrm{H_2O(s)} \tag{50}$$

It may be noted that the carbonization of the surface is accompanied by a general decrease in the pH of the surface film. Thus, the equilibrium pH of water in contact with brucite is 10.3 while the corresponding value for hydromagnesite is 8.7 [472,473].

Fig. 46a appears to be in contradiction to papers reporting that normal Mg carbonate hydrates ($Mg(CO_3){\cdot}xH_2O$ ($x = 3$ and 5)) and magnesite ($MgCO_3$) form as corrosion products on Mg in ambient air (*e.g.*, [198]). However, most of those claims are based on techniques (XPS and FTIR) that cannot easily distinguish those phases from the ubiquitous Mg hydroxy-carbonates. One claim to have identified the normal Mg carbonate hydrates in corrosion products by Liao et al. [95] is supported by unconvincing XRD evidence. In any case, if normal Mg carbonates are indeed formed on Mg alloys in the ambient atmosphere, their formation needs to be addressed on the basis of strong exponential evidence such as XRD and thermodynamics.

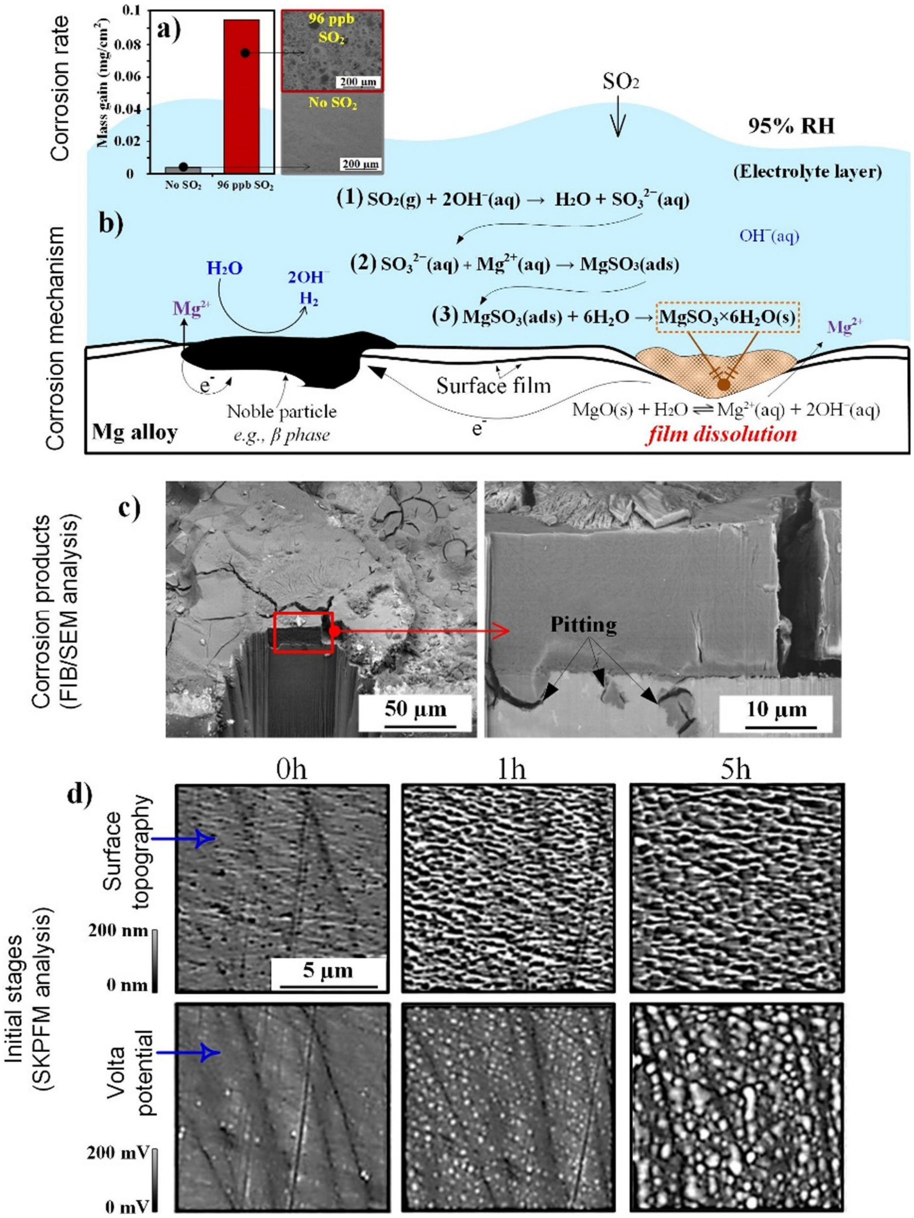

**Fig. 47.** The effect of $SO_2$ on Mg (alloys) corrosion. (a) Illustration of Mg corrosion in humid air with ppb levels of $SO_2$ [487], (b) the effect of traces of $SO_2$ on the corrosion of Mg alloy AZ91D (RH: 95%, time: 672 h), (c) FIB/SEM analysis showing the corrosion pits formed in Mg alloy AZ91D (48 ppb $SO_2$ after 672 h) [472], and (d) time-resolved *in situ* AFM/SKPFM micrographs of pure Mg during an $SO_2$-induced corrosion exposure (48 ppb $SO_2$ after 672 h) in a specially designed corrosion cell, showing the topography and Volta potential maps [120]. Reproduced with permission from the cited studies.

*4.3.2.2. The inhibitive effect of $CO_2$.* The central part of Fig. 46c summarizes the impact of $CO_2$ on the atmospheric corrosion of Mg and its alloys in the presence of NaCl. In short, the inhibitive effect of $CO_2$ (the SEM micrographs in Fig. 46c) is attributed to the formation of slightly soluble Mg hydroxy-carbonates, providing a somewhat protective, electronically insulating, layer on the surface. The layer is suggested to suppress corrosion by blocking the anodic and/or cathodic sites. For Mg-Al alloys, $CO_2$ may also protect against corrosion by stabilizing the alumina component in the film through suppressing the formation of high pH values on the surface.

*4.3.2.3. Impact of $CO_2$ on corrosion morphology.* The morphology of corrosion is also affected by $CO_2$ (compare the SEM images in Fig. 46c). Thus, while exposure of Mg to NaCl and humid air in the presence of $CO_2$ results in rather uniform corrosion, strongly localized corrosion results in the absence of $CO_2$. Thus, the corrosion pits formed in the absence of $CO_2$ (beneath the worm-like corrosion product aggregates in the left image) were ~4–6 times deeper than those formed in the presence of $CO_2$ (see image to the right) [122,149]. This has been explained by the neutralizing effect of carbonic acid.

High pH was suggested to lower the surface tension at the electrolyte/oxide interface, causing the droplets to spread over the surface and coalesce [488]. A more detailed discussion of the inhibitive effect of $CO_2$ towards the atmospheric corrosion of Mg and Mg-Al alloys follows in Section 4.3.7.

### *4.3.3. The role of sulfur dioxide ($SO_2$)*

As mentioned in Section 4.2, the corrosivity of traces of $SO_2$ in the atmosphere towards several metals (*e.g.*, Zn [109,112,470], Ni [126], Al [219,472], and Cu [439,465,471],) is well documented. Investigations of the corrosivity of $SO_2$ towards Mg alloys are scarce. A few field studies report on the corrosion behavior of Mg and its alloys in heavily $SO_2$ -polluted environment (*e.g.*, [92]).

Recently, a laboratory study [120] showed that the atmospheric corrosion of Mg is accelerated by traces of $SO_2$ (the mechanism is presented in Fig. 47a). Several papers on the corrosion behavior of Mg in aqueous sulfate ($Na_2SO_4$ and $MgSO_4$) solutions [489–491] all show that the aqueous corrosion of Mg is accelerated by sulfate.

The high pH of the surface electrolyte causes the Mg surface to be a very efficient getter for $SO_2$ under humid conditions [120]. Thus, the reactive dissolution of $SO_2$, forming hydrogen sulfite, $HSO_3^-$, and sulfite, $SO_3^{2-}$ (Eqs. (43) and (44)) acidifies the aqueous layer present on the Mg surface in humid air, causing the quasi-passive $MgO/Mg(OH)_2$ surface film to dissolve (see Eqs. (5) and (6)). Sulfite forms weak complexes with $Mg^{2+}(aq)$ [120,473], further promoting film dissolution. Mg sulfite is sparingly soluble and forms crystalline precipitates (Eq. (51)).

$$SO_3^{2-}(aq) + Mg^{+}(aq) + 6H_2O(ads) \rightarrow MgSO_3.6H_2O(s) \qquad (51)$$

The thinning of the surface film by dissolution triggers electrochemical corrosion involving cathodic reduction of water and anodic dissolution of Mg (Fig. 47b). In the presence of oxygen and/or other oxidizing agents, sulfite tends to oxidize to sulfate ($SO_4^{2-}$).

$$SO_3^{2-}(aq) + \frac{1}{2}O_2(g) \rightarrow SO_4^{2-}(aq) \qquad (52)$$

Indeed, sulfite oxidation is catalyzed by many transition metal ions and compounds [120]. Also, sulfite reacts rapidly with peroxide ($O_2^{2-}$), which is a by-product of the cathodic reduction of $O_2$. Hence, with most metals, the sulfur detected after exposure in air containing traces of $SO_2$ is overwhelmingly in sulfate form [120]. However, Mg and its alloys are exceptions in this respect, several field studies reporting $MgSO_3{\cdot}6H_2O$ to form in $SO_2$ -polluted environments [92,454]. A single report of solid Mg sulfate corrosion products from the field is by Li et al. [92] who detected both $MgSO_4{\cdot}6H_2O$ and $MgSO_3{\cdot}6H_2O$ on alloy AM60 in a heavily $SO_2$-polluted industrial/urban environment. The scarce evidence for Mg sulfate corrosion products may imply that the oxidation of S(IV) (sulfite, hydrogen sulfite and $SO_2$) to the hexavalent (sulfate) state is very much slower on Mg than on other metals. Another possible explanation is that sulfate, formed by oxidation of sulfite on the metal surface (Eqs. (43) and (44)), is reduced back to sulfite by the metal (Eq. (53)).

$$Mg(s) + SO_3^{2-}(aq) \rightarrow MgO(s) + SO_3^{2-}(aq) \qquad (53)$$

This suggestion finds support in a paper by Samaniego et al. [224], who reports that $SO_4^{2-}$ is reduced to $SO_2$ on the surface of Mg in solution at the open circuit potential (~−1.9 VSCE).

There is ample evidence for localized corrosion of Mg and its alloys in the presence of $SO_2$, both in the early stages of corrosion (see the SKPFM image in Fig. 47c) and for heavily corroded specimens, see the corrosion pits in FIB/SEM analysis in Fig. 47d. The localized corrosion implies that the $SO_2$-induced corrosion of Mg and its alloys is electrochemical in nature.

### *4.3.4. The role of nitrogen dioxide ($NO_2$) and ozone ($O_3$)*

While the corrosivity of traces of $NO_2$ in the atmosphere has been demonstrated for a number of materials [109,126,436], it is much less aggressive than $SO_2$. Small amounts of $Mg(NO_3)_2{\cdot}6H_2O$ have been detected in the corrosion products formed on Mg alloys in polluted industrial environments [90]. The nitrate was attributed to the deposition of nitric acid ($HNO_3$) partly in gaseous or aerosol form and partly through reactive dissolution of $NO_2$ (see Eq. (45)). The acid dissolves the surface film.

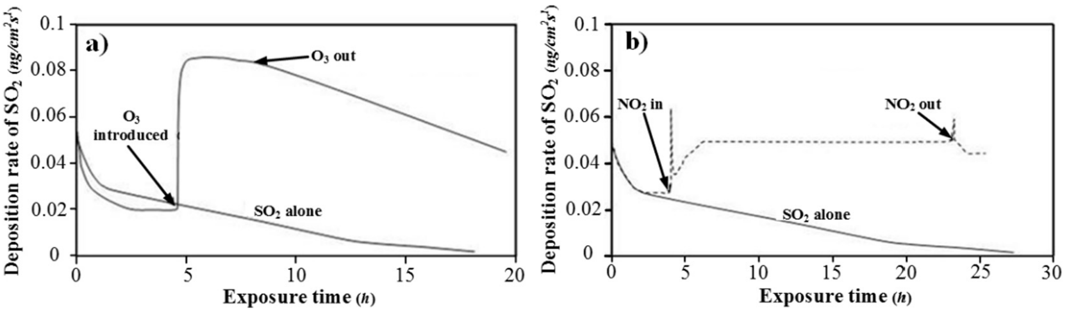

**Fig. 48.** Influence of the addition of 200 ppb $NO_2$ and $O_3$ on $SO_2$ deposition rate on AZ91 at 60% RH. The $SO_2$ concentration was 48 ppb. Reproduced based on [120], with a permission from The Electrochemical Society, licensed under CC-BY 4.0.

$$Mg(OH)_2(s) + 2H^+(aq) \rightarrow Mg^{2+}(aq) + 2H_2O(l) \tag{54}$$

The resulting thinning of the surface film then causes activation of electrochemical corrosion, similar to $SO_2$, see above. However, in addition, traces of $NO_2$ have been shown to increase the corrosivity of $SO_2$ towards several metals such as Zn [112], and Cu [471]. In several cases, the synergistic effect of $SO_2$ and $NO_2$ in atmospheric corrosion has been attributed to $NO_2$ or its reaction products catalyzing the oxidation of surface sulfite to sulfate [120,469].

A trace amount of ozone in air does not cause corrosion by itself, except for a few cases, *i.e.,* silver. In contrast, ozone is similar to $NO_2$ in exacerbating the corrosivity of $SO_2$ towards many materials. The effect of ozone has been attributed to direct oxidation of surface sulfite to sulfate by $O_3$.

It was recently shown that ppb levels of both $O_3$ and $NO_2$ accelerated the deposition of $SO_2$ deposition on Mg and Mg-Al alloys (Fig. 48). Also, the corrosion rate in the combined $SO_2 + O_3$ and $SO_2 + NO_2$ environments were much higher than for exposures with only $SO_2$.

Because the increased uptake of $SO_2$ was not accompanied by the formation of surface sulfate, the $SO_2/NO_2$ and the $SO_2/O_3$ synergistic effects in relation to Mg appear to be fundamentally different from those described above. Recently the synergistic effects were attributed to $O_3$ and $NO_2$ (or its reaction products) acting as cathodic depolarizers on Mg [120], based on the following reactions:

$$NO_2^- + H_2O + e^- \rightarrow NO(g) + 2OH^- \quad E^o = -0.46\ V \tag{55}$$

$$2NO_2 + 2OH^- \rightarrow NO_2^- + NO_3^- + H_2O \tag{56}$$

$$O_3 + H_2O + 2e^- \rightarrow O_2(g) + 2OH^- \quad E^o = 1.24V \tag{57}$$

The resulting increased cathodic activity would explain both the faster $SO_2$ deposition and the higher rate of corrosion.

### *4.3.5. The role of temperature*

As mentioned, the use of de-icing salt on roads means that vehicles are heavily exposed to NaCl during winter in large parts of the world. As a result, materials used in automotive applications experience the most challenging corrosion conditions at temperatures close to or below 0 °C. In contrast, most investigations of atmospheric corrosion are performed at room temperature or higher. Consequently, there is a lack of information concerning the atmospheric corrosion behavior of alloys and materials systems at low temperatures in the presence of NaCl. This is also the case for Mg, as there are few investigations focusing on the corrosion of Mg and its alloys at low temperature [119,166,167,231].

Recently, the NaCl-induced atmospheric corrosion of Mg and several Mg-Al alloys was investigated in the temperature range −4 °C to 22 °C [119]. While the alloys exhibited a strong positive correlation between temperature and corrosion rate, the atmospheric corrosion of pure Mg was independent of temperature, see the SEM micrographs and gravimetric results in Fig. 49. The corrosion product composition also depended on temperature. Analysis by XRD [119,166], FTIR [119], XPS and AES [166] showed that Mg hydroxy carbonates were the dominant corrosion products in the presence of $CO_2$ at 4 °C and higher, but these compounds did not form at −4 °C. The extent of the temperature-dependence of the corrosion of Mg-Al alloys was proportional to the Al content (Fig. 49). Thus, while in the case of alloy AM20 (2 wt.% Al) decreasing the temperature from 22 to −4 °C resulted in a 15% decrease in corrosion rate, the corresponding decrease was 92% for AZ91 (9 wt.% Al). The absence of a clear temperature dependence of the corrosion of pure Mg and the strong positive correlation between temperature and the corrosion rate of Al reported by Blücher et al. [477], imply that the temperature dependence of Mg-Al alloy corrosion is linked to the Al content.

### *4.3.6. Mg (alloy) atmospheric corrosion at the nanoscale*

During the last decades, several studies have been performed to understand the composition and microstructure of the surface films formed on Mg (alloys) [24–27,177–185]. Earlier (Section 3.1), we shortly discussed the process by which the

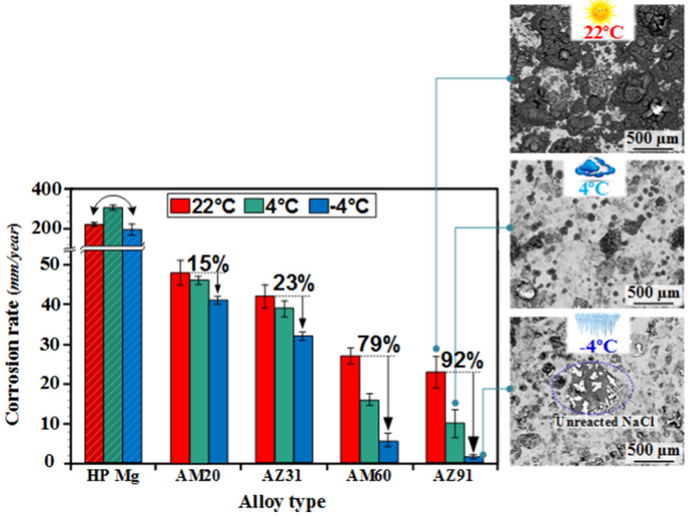

**Fig. 49.** The effect of temperature on Mg corrosion. Corrosion rate of HP Mg and four HPDC Mg–Al alloys (RH: 95%, $CO_2$: 400 ppm, NaCl: 70 µg/cm$^2$, time: 504 h). The decrease in the corrosion rate from 22 to −4 °C is given as a percentage. The SEM micrographs show the corrosion morphology of AZ91D at three temperatures [166,473]. Reproduced with permission from the cited studies. Reproduced with permission from Elsevier and The Electrochemical Society, licensed under CC-BY 4.0.

oxide and hydroxide films are formed on the metal surafce. Table 10 summarizes the results of selected studies that have provided detailed view of the quasi-passive films formed on Mg and Mg alloys, in both aqueous and atmospheric environments, since the early 1990s. Note that the table does not include all investigations with a focus on Mg (alloys) corrosion film (see *e.g.,* [182,185]) and that some aspects of surface film were discussed in Sections 2.3 and 3.1.

In regards to atmospheric conditions, *e.g.,* where $CO_2$ is present, there is little knowledge on the formation of the surface films (Table 10). Above, we showed that the reaction between $Mg(OH)_2(s)$ and $CO_2$ at ambient concentrations (400 ppm), forming Mg hydroxy carbonate, is allowed by equilibrium thermodynamics, Fig. 46a. Accordingly, a corrosion product film formed on Mg in clean humid air is expected to consist of a $Mg(OH)_2$ layer sandwiched between a top "carbon"-rich layer and a bottom MgO layer (Fig. 50a), which is consistent with experimental results of Feliu et al. [165], who used XPS to investigate the surface films formed on Mg and a Mg-Al alloy after exposing to 98% RH air at 50 °C for 28 days. A carbon-rich layer was detected in the upper part of the surface film, on top of the $MgO/Mg(OH)_2$ layer. Note that the surface films formed on Mg in liquid water have a similar layer sequence (see Section 2.3.7) except that the carbonate layer is absent.

*4.3.6.1. Mg-Al alloys.* In addition to the $MgO/Mg(OH)_2$/hydroxy carbonate film found on Mg, the surface layers formed on Mg-Al alloys in air tend also to include Al. Thus, an Al- enriched layer has been frequently detected at the oxide/ alloy surface interface on Mg-Al alloys subjected to aqueous (Fig. 11 and Sections 2.3.6 and 2.3.7) and atmospheric corrosion [166]. Recently, the surface film formed on the inter-dendritic regions in alloy AZ91D after atmospheric corrosion at 22 and −4 °C was carefully analyzed using site-specific HR-AES to analyze (Fig. 50b and c). As expected, that analysis (Fig. 50b) also showed a typical corrosion film with a bottom MgO section, a middle $Mg(OH)_2$ layer and a carbonate–rich top layer.

While the "bulk" of the film contained about 1 at.% of Al there is a much greater Al enrichment at the film/metal interface (Fig. 50c). Thus, the AES depth profiles show that the film formed at −4 °C exhibits a bottom Al-rich layer with a thickness of 7 nm and a maximum Al content of 10 at.%, while at 22 °C the corresponding values were 2 nm and 7.5 at.%, respectively. According to Fig. 50c, the Al enriched region is rich in oxygen, suggesting that Al is in oxidized form. This is in agreement with Shahabi-Navid et al. [194], who used a combination of sputtering and XPS analysis to show that the Al enrichment detected at the film/alloy interface after exposure of alloy AM50 in humid air consisted of $Al^{3+}$. It has been suggested that "alumina" in the surface film plays an important role for the atmospheric corrosion behavior of Mg-Al alloys [166,184], *i.e.,* explaining why high Al content alloys tend to corrode slower than Mg-Al alloys containing small amounts of Al, see Fig. 49 (above).

Interestingly, Fig. 50c shows that the entire film contains significant amounts of chloride. Indeed, at 22 °C the chloride concentration peaks at the Al-rich layer at the bottom of the film (shown by a star), indicating chloride penetration of the film. In contrast, chloride did not penetrate the film at −4 °C. On the basis of these observations, Esmaily et al. [166] proposed that chloride ions assist in the breakdown of a protective alumina-containing film formed on Mg-Al alloys under atmospheric conditions. The chloride-induced process would involve bond breaking within the film and is predicted to be thermally activated, in accordance with the strong temperature dependence of corrosion (see Fig. 49).

**Table 10**
Examples of investigations on the surface films formed on Mg and Mg alloy since 1993.

| Mat./Env./Time | Comments | Ref. |
|---|---|---|
| Mat.: Mg<br>Env.: $H_2O(g)$<br>Time: Up to 2 h | Formation of a defective MgO film.<br>H in the film.<br>The nucleation and growth mechanism depends on crystallographic orientation (open- and close- packed faces exhibited dissimilar ordering of the chemisorbed species into oxide nuclei). | Splinter et al. [24] |
| Mat.: Mg<br>Env.: Humid air and $H_2O$ | A dense MgO layer is formed when metal is exposed to air. In water, single MgO layer is transformed/dissolved into a newly precipitated amorphous platelets of $Mg(OH)_2$ (little evidence of the oxide layer). | Nordlien et al. [25] |
| Mat.: Mg<br>Env.: 35–60% RH at 20–30 °C | ***In pure air:*** A thin and amorphous oxide (MgO).<br>***In humid air:*** MgO is hydrated. A mixture of $MgO/Mg(OH)_2$.<br>A three-layered (Metal/*cellular*/*dense*/*platelet*) film at high humidities. | Nordlien et al. [26] |
| Mat.: Mg electrodes<br>Env.: 0.1 M NaOH (*aq*) at 80 °C<br>Time: 1–2 h | An outer porous $Mg(OH)_2$ layer the thickness of which increases with time, an underlying thin MgO layer.<br>A thin $MgO/Mg(OH)_2$ layer in some regions. | Santamaria et al. [202] |
| Mat.: Mg & AZ31<br>Env.: RH: 98% at 50 °C<br>Time: 1–30 days | ***Pure Mg***: $MgO/MgCO_3$.<br>Substitution of MgO by the C-rich product with exposure time.<br>***AZ31***: $MgO/Mg(OH)_2/MgCO_3$. | Feliu et al. [198] |
| Mat.: AZ31, AZ80 & AZ91D<br>Env.: 98% RH at 50 °C<br>Time: 1–30 days | ***Pure Mg***: Similar to those reported by Feliu et al. [143]<br>***Alloys***: AZ80 forms the highest amount of carbonates. Alloy microstructure has an impact on the surface film. | Feliu et al. [197] |
| Mat.: Pure Mg, Synthesized $Mg_{17}Al_{12}$ & $Al_3Mg_2$<br>Env.: Ultra-pure $H_2O$<br>Time: 0.5–7 min | ***Pure Mg***: a MgO layer covered by a porous $Mg(OH)_2$ film<br>***$Mg_{17}Al_{12}$***: A film with a composition of $AlMg_{2.5}(OH)_8$ ( ~ 10 nm thick).<br>***$Al_3Mg_2$***: A film with a composition of $AlMg_{1.4}O_{0.2}(OH)_5$. | Liu et al. [103] |
| Mat.: Pure Mg<br>Env.: Pure $H_2O$<br>Time: 48 h | A thin porous/nanocrystalline MgO-rich layer at bottom and an outer less-porous $Mg(OH)_2$-rich layer. | Taheri et al. [178] |
| Mat.: AM50<br>Env.: 1.6 *wt.%* NaCl (*aq*)<br>Time: 95 h | ***Inter-dendritic region***: Light corrosion attack.<br>The film is composed of a columnar mixture of amorphous $MgO/Mg(OH)_2$.<br>A thin Al-rich layer.<br>***α-Mg grain***: Heavy corrosion attack.<br>Predominantly crystalline $MgO/Mg(OH)_2$.<br>No Al-rich layer is observed. | Danaie et al. [179] |
| Mat.: Pure Mg<br>Env.: 0.01 M NaCl<br>Time: 24 h | A bi-layered film composed of a thin MgO following and a thick and more porous mixed MgO and $(Mg(OH)_2$ region adjacent to the film/electrolyte interface. | Taheri et al. [183] |
| Mat.: AZ31B & ZE10A<br>Env.: $H_2O$ and $D_2O$ 1 or 5 wt% NaCl<br>Time: 24 h | ***No NaCl***: MgO-base film on both alloys.<br>***With NaCl***: An inner MgO layer, intermediate laminar $Mg(OH)_2$ layer supported by an outer filamentous and porous $Mg(OH)_2$. Cl enriched at interfaces. | Brady et al. [213] |

However, the nature of the Al-rich layers in the surface films on Mg-Al alloys is still a contentious issue. Some workers claim that the Al-rich bottom layer is metallic. For example, Danaie et al. [179] investigated the Al-rich layer in the film formed on alloy AM50 during immersion in aerated NaCl solution. Based on low-loss EELS analysis they concluded that the Al layer had "metallic character". Also, the formation of an $Al^{3+}$-enriched layer on the alloy surface during corrosion and oxidation is unexpected because Mg has higher oxygen affinity than Al. Thus, $\Delta G^{\circ}{}_{formation}^{(298\ K)}$ is negative for the reaction (calculated from data in [492]) (Eq. (59)).

$$Al_2O_3(s) + 3Mg(s) \rightarrow 2Al(s) + 3MgO(s) \tag{58}$$

If the Al enrichment at the alloy/metal interface is indeed metallic, it may be explained by incongruent alloy dissolution [169]. To summarize, the formation and nature of the alumina-rich layer at the bottom of the film on Mg-Al alloys is still unresolved.

*4.3.6.2. Al content and the thickness of the carbonate-rich film.* The hydoxy-carbonate layer is believed to protect the metal substrate against corrosion [32]. Feliu et al. [197], who studied the surface films formed on AZ31, AZ80 and AZ91D, found a linear relation between the amount of carbonate-rich product formed on the surface and the subsequent corrosion behavior in

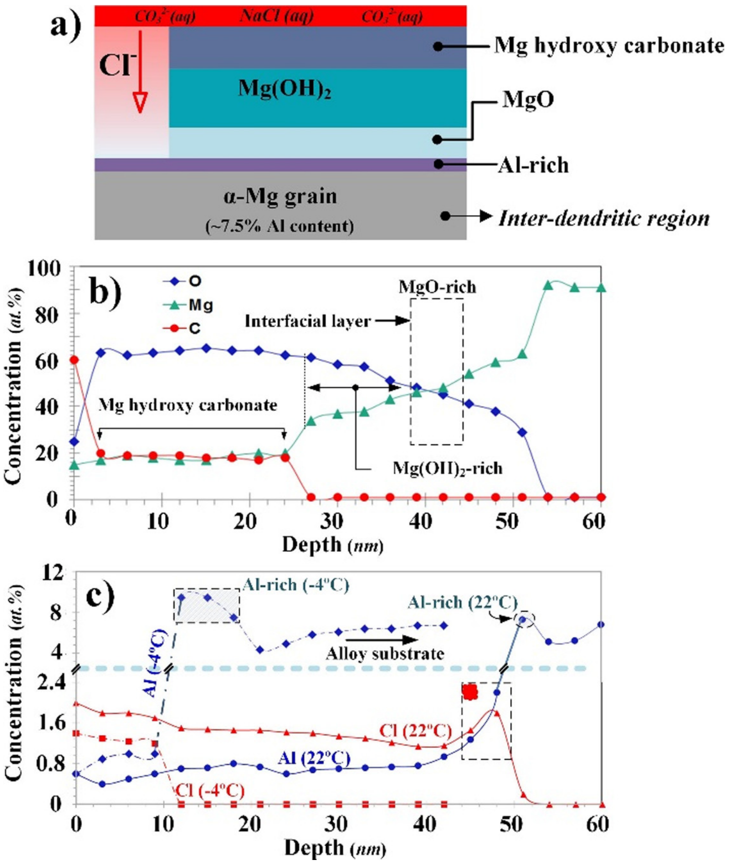

**Fig. 50.** The surface film formed on Mg-Al alloys. (a) Schematic of the multi-layered surface film. AES depth profiles (area of 2 × 2 μm$^2$) from inter-dendritic regions in AZ91D as a function of film thickness (10 μg/cm$^2$ NaCl 400 ppm $CO_2$, exposed fo 672 h); (b) specimen exposed at ambient temperature showing composition of O, Mg, C, and (c) specimens exposed at 22 and −4 °C showing the composition of Al and Cl. (b) and (c) are reproduced based on [166].

**Table 11**
AES data describing the relationship between the Al content and the thickness/fraction of the Mg hydroxy layer. Note to the growth of the C-rich layer with an increase in the Al content [493].

| Alloy | AM50 | AZ91D | AZ91D |
|---|---|---|---|
| Location | α-Mg | α-Mg | Inter-dendritic |
| Al content (at.%) | ~1.9 | ~3.8 | ~7 |
| Thickness (nm) | 9→ | 16→→ | 26 |
| Fraction (%) of “entire” film thickness | 10→ | 17→→→→→ | 50 |

humid environment, such that a thicker carbonate layer corresponded to slower corrosion. When analyzing the surface films formed on α-Mg grains with varying Al content (1.5, 3.8, and 7.5 at.%) in AZ91D and AM50, it was reported that the thickness of the Mg hydroxy-carbonate layer formed on Mg-Al alloys showed a positive correlation to the Al content of the metal substrate (see Table 11) [473]. A recent systematic investigation revealed the same trend for several Mg-Al alloys (Fig. 51) [493]. The explanation of the dependency of carbonate-rich layer thickness on Al content is discussed the following section.

### 4.3.7. Novel concepts in atmospheric corrosion of Mg alloys

*4.3.7.1. Layered double hydroxides (LDH).* It is suggested that the observed correlation between the Al content of Mg-Al alloys and the thickness of the carbonated layer formed during atmospheric corrosion (Fig. 51) is due to the formation of LDHs. Indeed, LDH formation can partly explain the beneficial role of Al in conjunction with $CO_2$, in the atmospheric corrosion of Mg alloys (Fig. 49).

Structurally, the LDHs are related to brucite, where $Mg^{2+}$ octahedra (6-fold coordinated to $OH^-$) share edges to form infinite sheets that are stacked on top of one other, with inter-sheet bonding provided by weak Van der Waals forces. Partial substitution of $Mg^{2+}$ by a trivalent ion, *e.g.*, $Al^{3+}$, results in the sheets becoming positively charged (Fig. 52a). The excess charge is compensated for by anions that occupy the interlayer region, together with water [494]. LDHs have the general

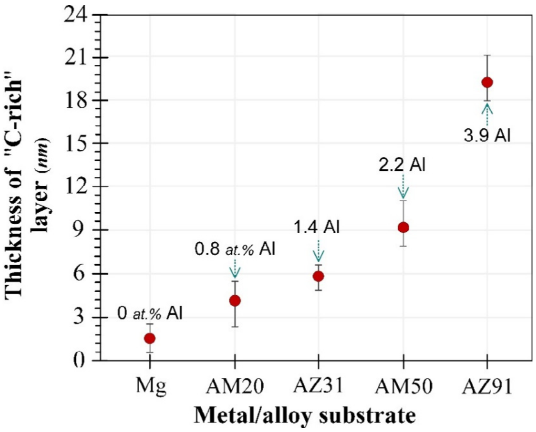

**Fig. 51.** The thickness of the C (carbonate)-rich layer on top of the surface film formed on the Mg-Al alloys studied as a function of Al content in the substrate. Note: The average Al content (at.%) of the grains was determined prior to exposure and are given inside the graph. Note: Each data point is an average value of three different measurements [466].

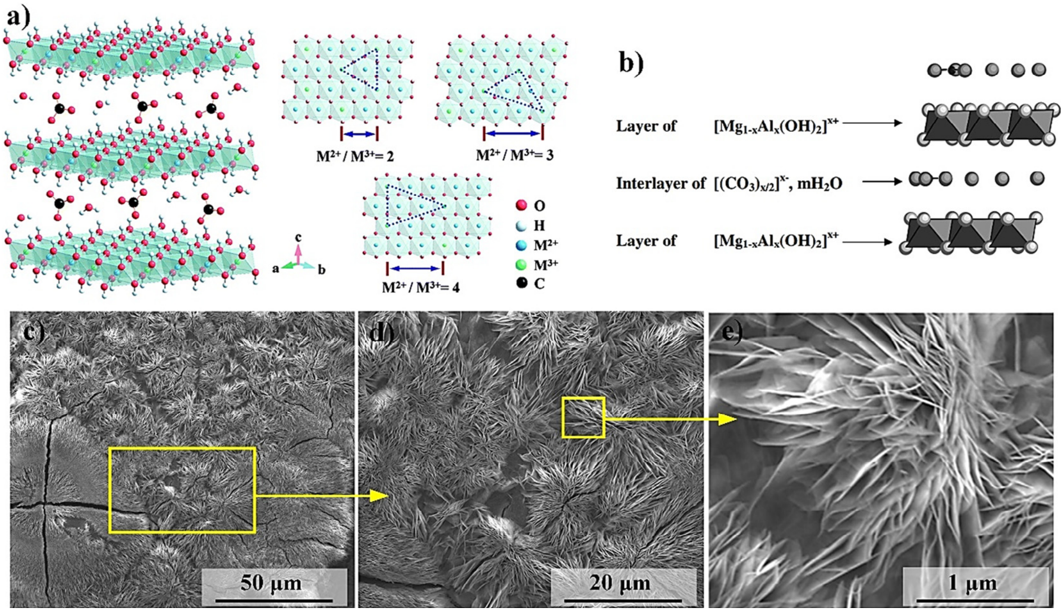

**Fig. 52.** Structure of carbonate-intercalated LDHs with different $M^{2+}/M^{3+}$ molar ratios showing the metal hydroxide octahedra stacked along the c-axis, and water and anions in the interlayer region [502], (b) structure of the Mg Al LDH (hydrotalcite) proposed by Mathieu et al. [496], and (c–e) the morphology of corrosion products formed on AZ91D (exposed to air with $CO_2$ and NaCl at 22 °C) [493]. In (c–e), the attention is drawn to the similarity between the morphology of the corrosion products formed during atmospheric corrosion and the LDHs (see [503]). Reproduced with permission from The Royal Society of Chemistry. Reprinted with permission from Elsevier. With permission of Springer.

formula $[M^{2+}_{1-x}M^{3+}_{x}(OH)_2]^{x+}\ A^{n-}_{x/n}xmH_2O$ [495]. In our case, $M^{2+}$corresponds to $Mg^{2+}$, $M^{3+}$ to $Al^{3+}$, and the inter-layer anion $A^{n-}$ is $OH^-$ and $CO_3^{2-}$.

Several workers have reported the formation of LDHs on Mg-Al alloys. Mathieu et al. [496] detected a surface film with the approximate composition $Mg_{0.85}Al_{0.15}(OH)_2(CO_3)_{0.075}xH_2O$ on Mg-Al alloys after immersing in $NaHCO_3^-(aq)$ solution (Fig. 52b). A similar surface film composition was reported by Baliga et al. [497] on an Mg-Al alloy after immersion in a 3% NaCl solution saturated with $Mg(OH)_2$. Recently, Lia and Hotta [95] identified the LDH $Mg_{0.833}Al_{0.167}(OH)_2(CO_3)_{0.083}$-$x{\cdot}0.75H_2O$, using XRD, as a corrosion product on several Mg-Al alloys after three years exposure in urban and marine environments. Also, the LDH meixnerite ($Mg_6Al_2(OH)_{18}\ x4H_2O = Mg_{0,75}Al_{0.25}(OH)_2(OH^-)_{0.25}x0.5H_2O$) was detected by XRD in a laboratory investigation of the atmospheric corrosion of Mg-Al alloys [122]. The cited evidence indicates that Mg-Al alloys subjected to atmospheric corrosion tend to form LDHs. Also, the reports suggest that long exposure times are needed to detect LDHs on Mg-Al alloys by XRD.

The Al-containing, carbonate-rich surface layer formed during atmospheric corrosion of Mg-Al alloys (see Figs. 49 and 51) is interpreted in terms of layered double hydroxides (LDHs). Because the LDHs rely on the availability of trivalent ions, the occurrence of LDHs in the surface film is expected to be proportional to the Al content of the metal substrate. The observed correlation between the thickness of the carbonated surface layer and the substrates Al content is attributed, partly to the higher availability of $Al^{3+}$, promoting LDH formation, and partly to the very fast reaction of LDHs with $CO_2$. The fast reaction with $CO_2$ is characteristic for all LDHs, being much faster than for brucite. Actually, the LDH meixnerite has been marketed as an absorbent for $CO_2$ [495]. Importantly, the LDHs have been reported to provide corrosion protection with several alloy systems [498–501]. The observed thickening of Mg hydroxy-carbonate layer with increasing the substrate Al content is attributed to the LDHs. Indeed, the tendency of the Mg-Al alloys to show improved corrosion properties with increasing Al content is partly attributed to the formation of a protective (carbonated) surface LDH layer. The absence of a corresponding positive effect of Al alloying in immersion corrosion experiments may be explained by the absence of LDHs due to dissolution of $Al^{3+}$ into the solution and by the weak influence of $CO_2$.

*4.3.7.2. Hydrogen uptake by Mg alloys.* Atmospheric corrosion of Mg and Mg alloys frequently leads to cracking, mechanical deformation and spallation. Investigating the atmospheric corrosion of several Mg-Al alloys, Liao and Hotta [96] reported the formation of macro-cracks in the alloy substrate (see *e.g.*, Fig. 53a and b, showing alloy AZ31 after 1 and 3 months exposure). In another case [174], FIB/SEM analysis demonstrated corrosion-induced micro-cracks in alloy AM50 after 168 h exposure to

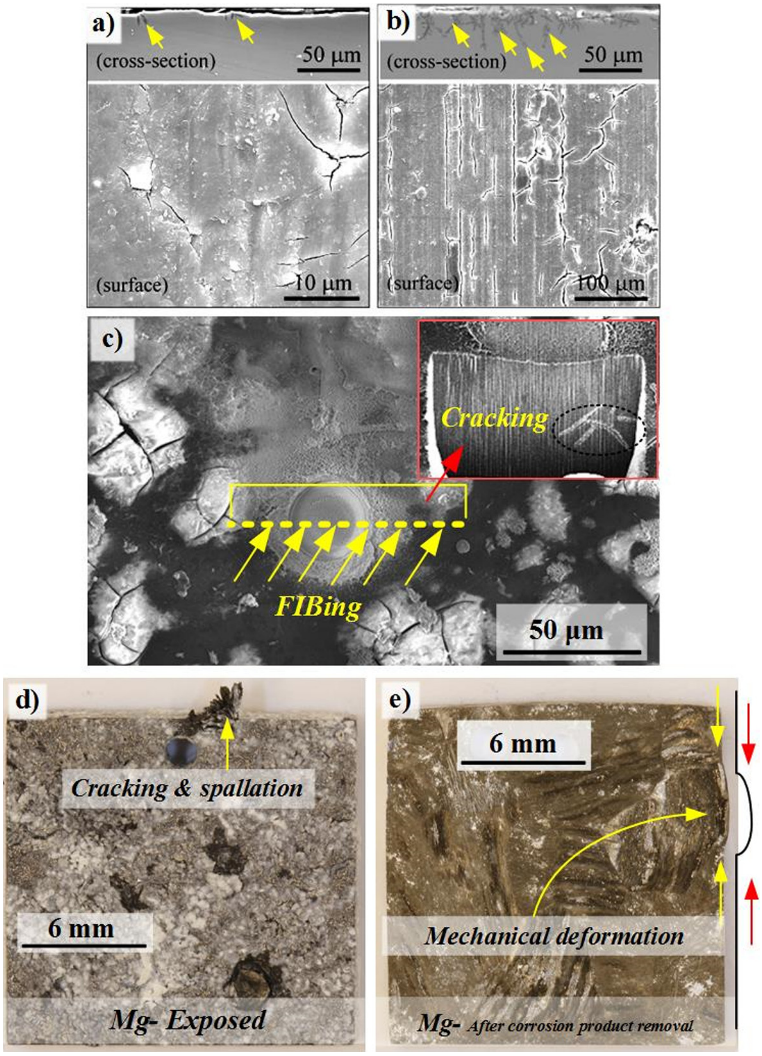

**Fig. 53.** Corrosion-induced phenomena in Mg and Mg-Al alloys. (a) and (b) Plan-view and cross-sections of AZ31 exposed to atmospheric corrosion [96], (c) a FIB/SEM analysis of the corroded surface of AM50 after 168 h, (d) and (e) photographs taken by a camera showing HP Mg surface after 672 h an atmospheric exposure, before and after pickling, reproduced based on [174]. The attention is drawn to: the formation of cracks in the alloy substrate in (e–c), spallation in (d), mechanical deformation in (e). Reproduced with permission from Elsevier.

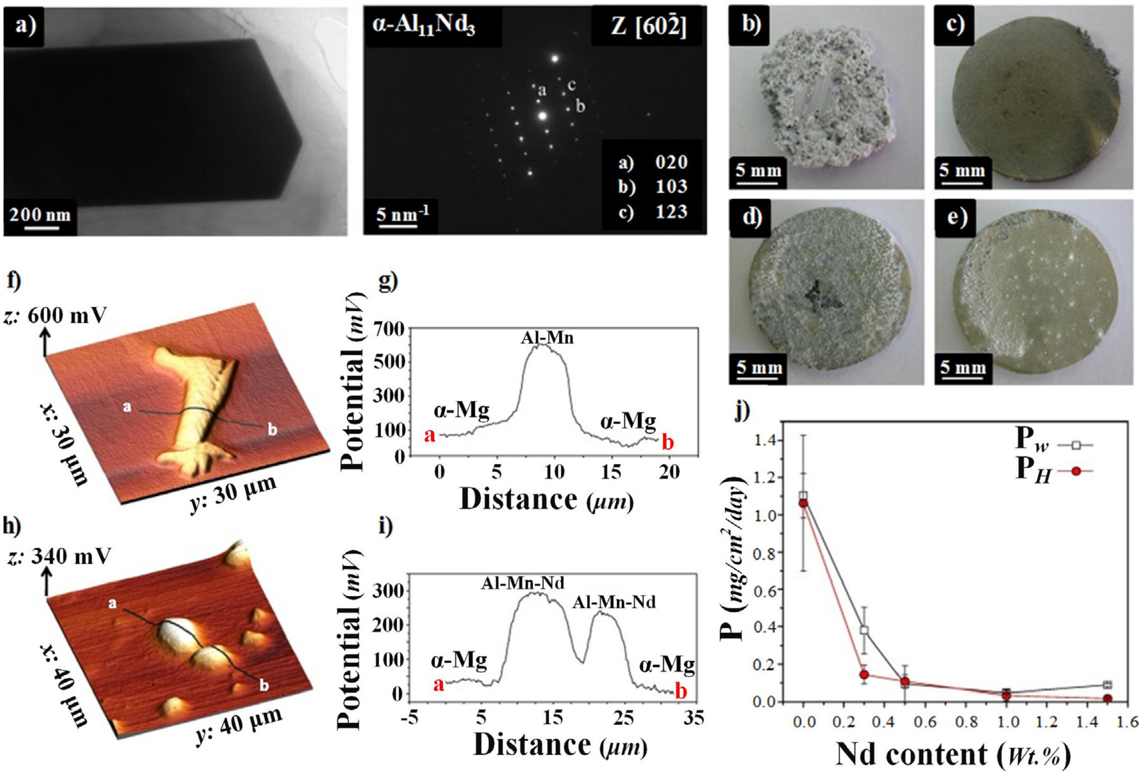

**Fig. 54.** Role of Nd addition on the corrosion of Mg-Al alloys. (a) Transmission electron micrograph (a) and electron diffraction pattern (b) of α–$Al_{11}Nd_3$ intermetallic particle; Surface appearance of (b) AM50, (c) AM50Nd, (d) AZ91, (e) AZ91Nd alloys; Surface potential maps and potential profiles of (f and g) Al-Mn, and (h and i) Nd-containing phases; corrosion rate evolution as a function of the Nd calculated from mass loss ($P_w$) and hydrogen collection ($P_H$) measurements after 8 days of immersion in NaCl solution. The presented results were reproduced based on [161,472], with a permission from Elsevier.

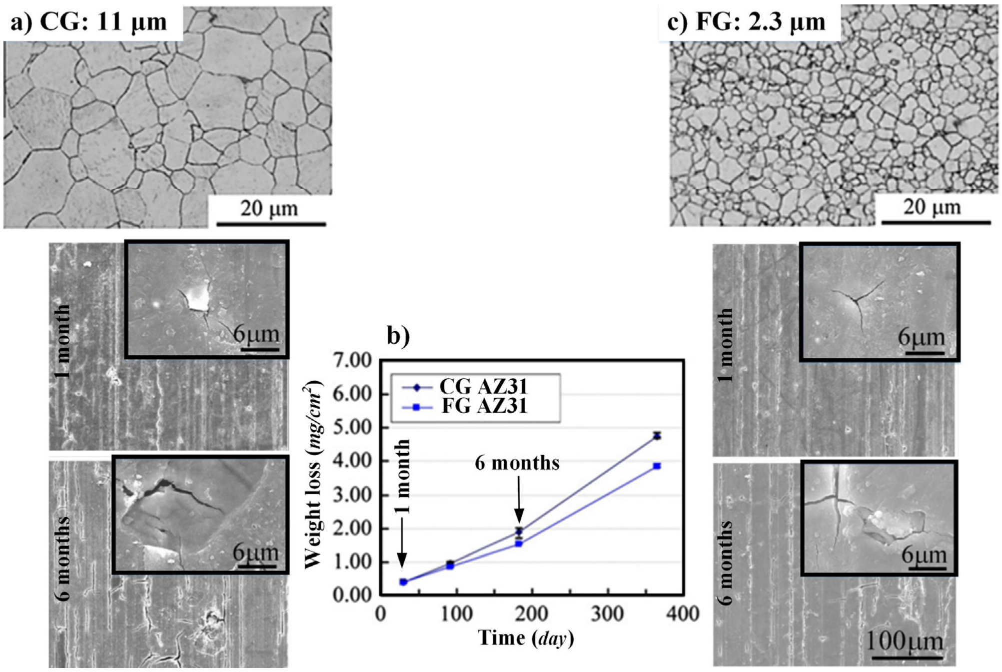

**Fig. 55.** Atmospheric corrosion behavior of AZ31 with two different microstructures; (a) coarse grained (CG) AZ31 before and after exposure in an urban environment, (b) weight loss measurements, and (c) fine-grained (FG) AZ31 before and after the exposure, Reproduced based on [95] with permission from Elsevier.

atmospheric corrosion, see Fig. 53c. Also, atmospheric corrosion of pure Mg was reported to result in cracking, spallation (Fig. 53d) and deformation of the metal substrate, see Fig. 53e. Several authors have suggested that these features are induced by the repeated wetting–drying cycles during the exposures [231,96]. However, because they also occur under constant RH conditions [119,174], much of the cracking and deformation is likely due to the corrosion process itself.

Thus, it is suggested that the cracking and deformation is caused by hydrogen uptake by the metal. In this scenario, the cracking and deformation observed during Mg corrosion is due to a combination of volume expansion and brittleness caused by dissolution of hydrogen in the metal. Indeed, H has been detected in surface films formed on Mg during aqueous corrosion using ToF-SIMS [180].

While hydrogen uptake indeed occurs in connection with the cathodic reduction of water, it is argued that it may also have an alternative explanation. It may be noted that HP Mg corrodes rapidly under atmospheric conditions (see Fig. 53e and the gravimetric data in Fig. 49). The material investigated had impurity levels well below the “tolerance limit”, implying that cathodically active precipitates are very scarce. In the absence of such precipitates, an electrochemical corrosion scenario would require the cathodic process to occur on top of the surface film. Because of the insulating nature of the MgO/$Mg(OH)_2$ film, such a process would have to overcome a substantial resistance towards electronic transport. Indeed, such a water reduction process is not expected to lead to hydrogen uptake by the metal in this case because the film separates the cathode from the metal.

As mentioned in Section 4.3.7, it was recently demonstrated that the layered surface film formed when Mg is exposed to water contained a brucite top layer and a 20–50 nm thick bottom part consisting of nanocrystalline MgO [178], see Fig. 10b in Section 2.3. Also, the MgO grains were described as being hydrated [178]. It is likely that the hydration of the MgO layer corresponds to the presence of Mg hydroxide in the MgO grain boundaries. Grain boundary hydroxylation is analogous to the hydroxylation of an MgO surface described in Section 3.1. Hence, the reaction of water with the MgO grain boundaries, forming hydroxide, is expected to be thermodynamically favored:

$$O^{2-}(GB) + H_2O \rightarrow 2OH^-(GB) \tag{59}$$

The reaction is tantamount to forming Mg hydroxide in the grain boundaries:

$$MgO(GB) + H_2O \rightarrow Mg(OH)_2(GB) \tag{60}$$

The water would be provided from the top brucite layer. If surface hydroxylation reaches the metal/film interface, direct “chemical” reaction with Mg is enabled:

$$Mg(s) + Mg(OH)_2(GB) \rightarrow 2MgO(s) + 2H \tag{61}$$

In this scenario then, hydroxylation of the MgO grain boundaries allows water to penetrate the film via grain boundary transport. Because the reaction requires direct contact between Mg hydroxide and metallic Mg, the released hydrogen tends to be picked up by the metal.

$$Mg(s) + Mg(OH)_2(GB) \rightarrow 2MgO(s) + 2H(alloy) \tag{62}$$

The dissolved hydrogen can later be released from the metal by forming $H_2(g)$ or Mg hydride, which results in cracking. The validity of the ideas presented here on water permeation through the surface film on Mg and subsequent hydrogen uptake should be explored by a combination of experimental work (*e.g.*, Nano-SIMS) and theory (DFT). It should also be added that the hypothesis presented here was inspired by recent elegant works of Lindgren and Panas [504–506], who proposed a similar scenario for describing the diffusion of water through the oxide layer formed on Zr (which also cracks by hydriding [506]). Using a combination of experiment and DFT, they showed that the grain boundaries of the electronically insulating, polycrystalline $ZrO_2$ layer tend to become hydroxylated, providing a route for water to penetrate the oxide and react directly with the metal substrate [504].

### *4.4. Protection against atmospheric corrosion*

Under real atmospheric conditions, the corrosion rate of Mg alloys usually varies between <1 μm/year ($5 \times 10^{-4}$ mg/cm$^2$/day) and 40 μm/year ($2 \times 10^{-2}$ mg/cm$^2$/day), depending on the alloy and the concentration of aggressive species such as $Cl^-$ and $SO_2$. In “dry” conditions, *i.e.*, <80% RH, typically found in the interior of vehicles or buildings, Mg alloys provide good service with corrosion rates well below 1 μm/year ($5 \times 10^{-4}$ mg/cm$^2$/day). However, in rural, industrial and marine atmospheres, Mg corrosion rates are much higher with values in the range between 2 μm/year ($1 \times 10^{-3}$ mg/cm$^2$/day) and 40 μm/year ($2 \times 10^{-2}$ mg/cm$^2$/day) [454]. To mitigate surface degradation of Mg alloys so as to widen their range of applications, it is common to act either on the component design, environment and/or the material itself. An important consideration when implementing these strategies is that they should not compromise other material properties that comply with design requirements, such as yield strength, fatigue life, and density.

Component design is a cost-effective and often successful approach for minimizing corrosion. For Mg alloys, special care should be taken to avoid design configurations involving galvanic connection of dissimilar metals and geometries prone to moisture accumulation. Good examples of design-related studies of Mg components from a corrosion point of view can be found in the literature [507–509]. An area of particularly high interest is the application of anticorrosion measures for multi-material solutions, which are almost unavoidable in the automotive sector. Some examples in this regard can also be found [510,511].

Environmental modification is rarely an option for corrosion control in open atmospheric systems. In closed service environments, however, good results can be achieved by keeping the RH and the concentration of pollutants to a minimum. The addition of inhibitors is also an option, although they should be compatible with other metals and environmentally friendly.

### *4.4.1. Protection strategies: Chemistry and microstructure*

The most frequent and reliable strategy for improving the corrosion resistance of Mg alloys is tailoring the surface properties of the material, either by changing its composition and microstructure or by applying a proper surface treatment. With respect to the bulk material, the latest advances focus on one of the following approaches.

*4.4.1.1. High purity alloys.* As detailed in Section 3.3, it has been known for over seventy years [278] that the corrosion rate of Mg can be accelerated by one to two orders of magnitude when Fe, Co, Cu, and Ni impurities are above their tolerance limits [512]. Commercial alloys comply with these limits, but further improvement is still possible by using UHP materials. Some studies in this regard have been made [61,513].

*4.4.1.2. Minor alloying elements.* Taking commercial Mg alloys as a starting point, it is possible to decrease significantly their corrosion rate by adding small quantities of elements such as Mn, Nd, Gd [42,514]. In general, the positive effect of the added element is attributed either to microstructure refinement and/or modification of the electrochemical activity of intermetallic particles [161].

Several examples of this approach were recently provided by Arrabal [161,448,456], who studied the effect of Nd and Gd on the microstructure and corrosion behavior of AM50 and AZ91D alloys exposed to humid and saline environments. By using SEM/EDX and SKPFM, it was demonstrated that both Nd and Gd additions (<1.5 wt.%) produced rE-intermetallics that were less noble than Al-Mn inclusions, thus reducing the effect of micro-galvanic couples and the corrosion rate, i.e., the addition of just 0.5 wt.% Nd yielded corrosion rate up to 96% lower than that of the unmodified alloy (Fig. 54). It is worth mentioning that this topic has received considerable interest in recent years as it does not require drastic changes in Mg technology (see also Section 3.3).

*4.4.1.3. Design of new alloys.* Although designing new alloys is more complex than minor alloying and requires a profound knowledge of physical metallurgy and thermodynamics, there are recent successful examples of new Mg alloys introduced in the market, such as the AJ62, MRI153M and Elektron®21. Based on the existing literature, alloying elements such as Li, Nd, Ca, Ti and Sr or their combinations are the most promising candidates in the near future of Mg alloys. For instance, an ultra-low density (1.4 g/cm$^3$) Mg-Li-based alloy that is strong, ductile and more corrosion resistant than many Mg-based alloys was recently developed [35] (see Section 3.3).

*4.4.1.4. Modifying the materials microstructure.* As shown in Fig. 55, substrate cracking is an issue in the atmospheric corrosion of Mg-Al alloys. Recent studies have shown that cracking caused by environmental degradation can be mitigated by a finer grain structure. Thus, Liao et al. [96] exposed two AZ31 materials with the same state of intermetallic particles, impurities, and texture, but different average grains sizes (11 and 2.3 μm) in the atmosphere for up to 24 months (Fig. 55). Liao et al. [96] observed that the fine-grained AZ31 corroded more slowly than the coarse-grained one and that the atmospheric corrosion-induced cracks in the alloy substrate were consistently more pronounced in the latter (compare Fig. 55a and c). They suggested that the superior corrosion resistance of the fine-grained alloy was connected to the smaller grain size.

While refining the alloy grain structure can reduce the extent of cracking, the improvement achieved is only marginal, see Fig. 55b. However, it was recently shown that the corrosion performance of Mg-Al alloys can be significantly improved through tailoring the alloy microstructure via casting technology *or* certain heat treatments.

Thus, Mg-Al alloys produced by rheocasting (RC), a semi-solid casting (SSC) technique, exhibited much better atmospheric corrosion performance in two different atmospheric environments than alloys with the same elemental composition that were produced using high pressure die-casting (HPDC) (Fig. 56). By characterizing the alloy microstructure before and after corrosion, it has been noted that the observed improvement in corrosion performance can be explained by higher concentration of Al within α-Mg grains, lower fraction of casting pores in the RC alloys, the size, fraction, and distribution of β phase particles [149,166,174,515]. In a similar study by Mingo et al. [164] on the alloy AZ91D, the benefits of RC processing where also highlighted.

Certain heat treatments [516,517,526], have demonstrated potential for modifying the microstructure and, therefore, improving the corrosion resistance of Mg alloys. A clear example of this was given by Arrabal et al. [518], where the AZ80 alloy showed a superior performance over the AZ91D in high humidity atmospheres. Both alloys have similar compositions but the recrystallization heat treatment applied on the AZ80 resulted in a biphasic microstructure consisting of Al-rich α-Mg grains and a fine lamellar α + β aggregate (see Fig. 56), formed by cellular transformation, which significantly delayed corrosion. However, it is important to consider that this approach also supposes a notable change in the mechanical properties and is not always positive from a corrosion point of view. Heat treatments are readily adaptable to industrial use, but most of the rheo- and thixo-routes are still at the development stage.

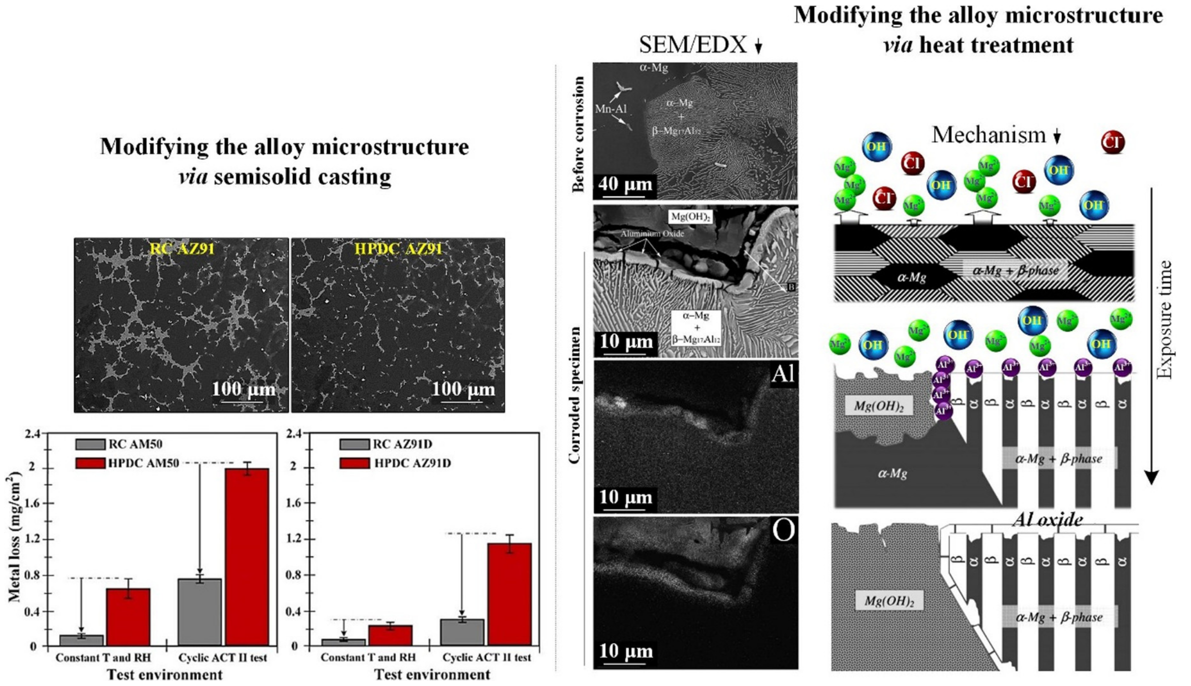

**Fig. 56.** Effect of microstructure on the atmospheric corrosion. (Left-hand side) The effect of microstructure on the metal loss of Mg alloys exposed at constant temperature and constant RH and in cyclic conditions for AM50 and AZ91D in the RC and HPDC states, reproduced based on [149,473]. (Right-hand side) The lamellar microstructure of a heat treated AZ80 with superior corrosion resistance, reproduced based on [519] with permission from Elsevier.

### *4.4.2. Protection strategies: Surface modification*

As already mentioned, surface modification is frequently used on Mg alloys, especially when mechanical properties of the alloy are to be maintained. Useful reviews on the subject can be found [520,102]. In most cases, prior to surface treatment and on an industrial scale, Mg parts first go through standard procedures such as machining, grinding, degreasing, and pre-treatment. Degreasing in an alkali solution is preferred over organic solvents and pre-treatment usually consists in acid pickling and alkaline cleaning with our without chelating agents [520,102]. As for the applied treatment, there is a myriad of methods, but conversion and anodizing treatments are most commonly applied (alone or in combination with organic coatings). Table 12 lists some examples of conversion and anodic films on Mg alloys (This list is not comprehensive. Many other coatings and references are available). As shown in this table, conversion coatings without top-coats usually show clear signs of corrosion just after 24 h of exposure to continuous salt spray, whereas unsealed anodic films can perform well up to 100–1000 h depending on its thickness, composition, and the alloy substrate.

Conversion treatments (Table 13) in acidic solutions based on Cr(VI) are typically used for passivation of Mg alloys [529]. These substances (chromium trioxide and dichromates) are included in the REACH regulation and suitable substitutes need to be developed urgently [530]. Non-chromate alternatives have already been introduced in the market; *e.g.*, Magpass-Coat, Gardobond® X4729, Bonderite® M-NT 5700 and Oxsilan® 0611 [531]. However, in aerospace and automotive applications there is still a need for Cr(VI)-free conversion coatings that can be applied at room temperature and can meet quality criteria (*e.g.*, corrosion resistance, electrical resistance, paint adhesion, fatigue) like those described in the AMS2473 standard. Phosphate-related conversion treatments with or without metallic compounds (*e.g.*, Co, Ni, Mn, Ca, and Zn) are the most popular, with a high number of patents/papers in recent years [102]. Recent trends in this field are the development of conversion treatments based on fluoro-zirconates/-titanates, layered double hydroxides (LDHs), silanes, Cr(III) solutions, rare earths (Ce and La), stannates, ionic liquids, vanadates, titanates and molten salts. Many of these Cr(VI)-free recipes aim at improving the active corrosion inhibition (self-healing) of the coating, which is a very well-known property of Cr(VI) compounds and particularly useful in case of defective or damaged coatings. Key features and anticorrosion performance of various conversion coatings have been discussed [529].

The first commercial anodizing treatments for Mg were patented in the 1950s (see Table 13). However, the electrolytes used in these processes (HAE, DOW-17) contain chromates and/or hydrofluoric acid. Thus, with the renewed interest for Mg alloys a radical change on this technology is taking place with newly patented processes (Anomag, Magoxid-Coat, Keronite, Tagnite, SweetMag, Bonderite). Anodizing has potential to produce thick uniform ceramic-like coatings (5–200 µm) with high level of protection against crucial parameters such as wear and corrosion, improved hardness, temperature and load capacity. In addition, as they are an excellent paint base, superior corrosion resistance and cosmetic finish can be obtained.

**Table 12**
List of some examples of conversion treatments on Mg alloys.

| Conversion treatments | Pretreatment | Treatment conditions | Thickness | Salt spray performance | Ref. |
|---|---|---|---|---|---|
| Dow 1 | – | RT<br>30–120 s | – | Less than 24 h 20% salt spray resistance | [521] |
| Dow 7 | RT<br>30%HF<br>1–5 min | 100 °C<br>30–40 min | – | Less than 24 h 20% salt spray resistance. | [521] |
| Phosphate | Conditioning | 40–45 °C<br>< 40 min | 6 μm | Similar to chromate conversion coating. Better adhesion | [522] |
| Phosphate | Solvent degreasing and alkaline cleaning | 40–70 °C<br>10 min | 7–10 μm | Similar to Dow 1 | [523] |
| Phosphate | Alkaline degreasing | 55 °C<br>7 min | 7–15 μm | 5 times better than Dow 1 | [524] |
| Cerium | Alkaline degreasing and acid pickling | RT<br>3–1440 min | 0.5 μm | Better than Dow 22 | [525] |
| Magpass-Coat | $H_3PO_4$ 75%<br>30 s | 25–35 °C<br>5 min | 0.3–1.0 μm | 5–10 h (according to DIN EN ISO 10 289) | [526] |
| Stannate | HF pickling | 82 °C<br>10 min | <1 μm | **AZ61**<br>Rating 10: 18 h<br>(according to CNS-8886) | [527] |
| Titanate | 1200 grit | 40 °C<br>3–6 min | – | AZ31<br>Corroded area fraction <5% after 24 h salt spray exposure | [528] |

There are two main types of anodizing processes, namely conventional anodizing and micro-arc oxidation (MAO), also called plasma electrolytic oxidation (PEO). Conventional anodizing of Mg alloys significantly differs from the process for Al alloys, because the typical self-organised porosity found on Al does not usually form on Mg. Commonly, MAO or PEO processes are employed, where anodic oxidation occurs above the dielectric breakdown voltage of the coating (100–600 V) and micro-discharges appear on the surface enhancing the rapid growth of the coating (1–4 μm/min). (Table 13). A systematic study by Arrabal et al. [540] depicted many of the characteristics of PEO coatings produced on a variety of commercial Mg alloys, including a detailed characterization of the barrier layer that forms at the substrate/coating interface (Fig. 57). This layer is largely responsible for the corrosion properties of PEO coatings.

Surface preparation prior to coating by abrasive-finishing can be eliminated by the use of the proper chemical surface pretreatment, reducing serious environmental hazards related to the explosive nature of Mg dust. Alkaline electrolytes with less than 20 g/l of solute are preferred (*e.g.,* silicate, phosphates, and aluminates) since they are environmental-friendly and easy to dispose. Latest trends in the field of anodizing of Mg, which is a highly active topic, include *in situ* incorporation of particles [541], inhibitors [542] and nano-containers [543], film growth in non-aqueous electrolytes [544], and strategies for more energy-efficient treatments [545].

## 5. Outlook

This review covered several aspects of this rapidly growing field, from surface films and aqueous corrosion to effect of alloying, atmospheric corrosion, MMCs and biodegradable materials. The review also covered both generic and applied aspects. We hope that it will give established researchers in Mg corrosion an opportunity to glean information about recent advances in neighboring areas and that “newcomers” will find it a useful guide to the intricacies of Mg corrosion. Indeed, the main point with this review is to help inspire new research that will develop and expand the science of Mg corrosion even further. To help provide such inspiration and to provoke new ideas for research in this exciting field, a selection of ideas for new research in Mg corrosion is presented below.

### *5.1. Corrosion mechanism*

Despite the considerable work performed over the past 5 years, there have been no definitive experiments that clearly identify the mechanism of Mg corrosion and anomalous HE. Many effects have been identified but none can explain all of the observations. Clarification has impacts on the design of new alloys, and on the behavior of Mg alloys when galvanically coupled to more noble metals in engineering applications. Therefore, more work aimed at identifying the mechanism is warranted. It is recommended that experiments be performed in the following areas:

**Table 13**
List of some examples of anodic treatments on Mg alloys.

| Anodizing treatments | Pretreatment | Treatment conditions | Thickness | Salt spray performance | Ref. |
|---|---|---|---|---|---|
| Dow 17 | Alkaline | 70–80 °C<br>AC 0.5–5 $A/dm^2$<br>Thin coating:<br>$V_{end}$ 60–75 V, 4–5 min<br>Thick coating:<br>$V_{end}$ 90–100 V, 25 min | Thin coatings<br>2.5–7.5 μm (thin coatings)<br>23–38 μm (thick coatings) | **AZ91D**<br>Rating 5–14 days<br>**ZE41A**<br>Rating 0–2 days<br>(ASTM D1654-Method B) | [532]<br>[533] |
| HAE | Alkaline | 27 °C<br>AC 1.5–2.5 $A/dm^2$<br>Thin coating:<br>$V_{end}$ 65–70 V, 7–10 min<br>Thick coating:<br>$V_{end}$ 80–90 V, 60–90 min | 5–10 μm (thin coatings)<br>25–80 μm (thick coatings) | **AZ91 HP**<br>25 μm (3–41 corrosion points/$dm^2$ after 24 and 100 h)<br>40 μm (0–18 corrosion points/$dm^2$ after 24 and 100 h)<br>Better than Dow 17 | [532]<br>[534] |
| Tagnite | Alkaline + Activation<br>0.5–1.2 M $NH_4F$ 70–80 °C,<br>30–40 min | 10–20 °C<br>$DC_{pulsed}$ 1–5 $A/dm^2$<br>$V_{end}$ 200–400 V | 5–10 μm (thin coatings)<br>20–25 μm (thick coatings) | **ZE41**<br>Rating 9: 24–200 h (ASTM D1654-Method B)<br>Far superior compared to HAE and Dow 17 | [532]<br>[535] |
| Magoxid-Coat | Alkaline + Activation<br>10%$H_2F_2$ RT, 30–60 s | RT<br>DC 1–2 $A/dm^2$<br>400 V<br>Thick coating:<br>$V_{end}$ 90–100 V, 25 min | 5 μm (thin coatings)<br>30 μm (thick coatings) | **AZ91HP**<br>80–100 h (evaluation according to DIN EN ISO 10 289) | [532]<br>[536] |
| Anomag | | RT<br>DC ~10 $mA/cm^2$<br>170–350 V | 3–8 μm<br>10–15 μm<br>20–25 μm | **AZ91**<br>3–8 μm<br>Rating 9: 150 h<br>10–15 μm<br>Rating 9: 400 h<br>20–25 μm<br>Rating 9: 1300 h | [532]<br>[537] |
| SweetMag | Cathodic activation | 10–30 °C<br>DC 2 $A/dm^2$<br>$V_{end} < 350$ V | <25 μm | – | [538] |
| *Keronite* | – | 20–50 °C<br>Bipolar signal | 25–30 μm | **AZ91D die cast**<br>Rating 9: 336 h<br>**AZ91D thixocast**<br>Rating 9: 1000 h<br>(ASTM D1654-Method B) | [539] |

- Advanced surface analysis. The nature of the corrosion film and the fate of impurity elements need to be addressed. Why does the corrosion film promote HE? Are impurity atoms released into solution non-Faradaically or do accumulate in or under the corrosion film?
- In situ analysis. What is the oxidation state of Mg ions and is there evidence for $Mg^+$? What other species are formed near the electrode surface? *In situ* analysis is complicated by the copious evolution of $H_2$ bubbles, which displaces solution and creates convection. Furthermore, the low Z number of Mg means that the electron binding energy is relatively small, which limits the penetration of fluorescing x-rays through matter.
- Other unexplored or novel methods. This problem has attracted new and interesting methods, such as PIXIE, atomic emission spectroelectrochemistry, and gravimetric analysis, and older methods that had not been applied previously, such as RBS, SVET, and SECM. It is expected that new or previously unused techniques will continue to be applied to this problem.

It is likely that real advances will require advanced atomistic modeling using techniques such as DFT and Monte Carlo simulation. Modeling efforts have already shed insight into the problem, but considerable work is required to advance the modeling beyond simplified situations and to capture the complexities of the phenomena.

### *5.2. Effect of alloying*

Based on the effects of alloying additions on the corrosion of Mg-alloys as summarized concisely herein, there are several key aspects that can guide the outlook for alloy development. Firstly, it can be recognized that – when combined with knowledge of solid solubility of elements in Mg – alloying to produce a thermodynamic passivity such as that observed with stain-

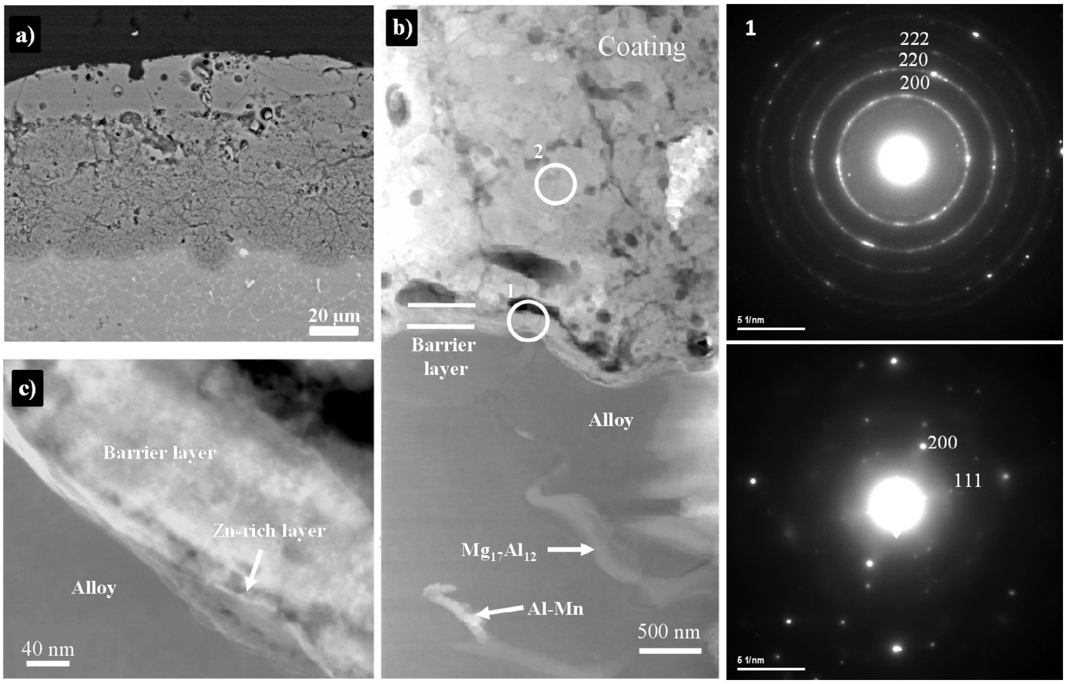

**Fig. 57.** PEO layer formed on AZ91D. Backscattered scanning electron (a) micrograph of a PEO coating formed on the AZ91D Mg alloy, (b and c) transmission electron micrographs and SAED patterns of (1) inner barrier layer and (2) intermediate layer of the coating formed on AZ91. Reproduced based on [540] with permission from Elsevier.

less steel is not possible or tenable [279]. Furthermore, heavy alloying of Mg with "heavier" elements will create an alloy density whereby Al-alloys or other alloys become more favourable. As such, so-called "kinetic" restriction of corrosion rates is a more logical, if not realistic, approach. To this end, a number of advances have been shown in recent years to have promise. These include;

- The retardation of the cathodic reaction upon Mg-alloys, which has been shown to be possible via the use of Group 14 and Group 15 alloying additions, namely As and Ge [294,295,309]. This approach is merely a kinetic restriction of one of the partial reactions that controls corrosion rate. It is noted that the use of either As or Ge remains to be exploited in the context of commercial alloys or higher order (*i.e.,* quaternary, quinternary, etc.) alloy systems.
- The kinetic restriction of the anodic reaction by the use of Li additions [308], in the single-phase region of the Mg-Li system (in range of ~33 at.% Li). Such a kinetic restriction was ascribed to the "dynamic" development of an insoluble surface film that relies upon some critical alloy dissolution to generate a surface enrichment of Li, which then reacts to form a surface film consisting primarily of sparingly soluble Li-carbonate.

The above list is obviously however, not exhaustive, and the approaches were considered (until their discovery) non intuitive. As such, there remains a prospect for a number of other seemingly non-intuitive approaches, which may include alloying elements capable of sequestering impurities in a superior manner, or second phases that serve as local reaction sites with low reaction kinetics. It is not unreasonable to state that alloy development for the sake of minimisation of corrosion in Mg-alloys is grossly under-researched. Whilst a large number of research papers study the corrosion of Mg-alloys (namely repeating analysis of commercial alloys), the number of works exploring new alloys with rational design remains restricted to works prior to the 1950s [21,30,278], and works since 2010. It is hoped that the comprehensive nature of the present review – which in its entirety also puts forth the challenges in understanding the precise electrochemical nature of Mg dissolution - will serve as a platform to researchers in this field.

### *5.3. Mg-based MMCs*

Mg-based metal matrix composites have always been excellent candidates for lightweight applications as they often show higher yield strength, damping capacity, wear, fatigue and creep resistances than their monolithic counterparts. With a judicious selection of matrix and reinforcement the end mechanical properties can be fine-tuned to suit specific requirements. So far, commercial grade alloys reinforced with micro-sized ceramic reinforcements and manufactured by standard routes have received most of the attention. Over the last few years, this trend is changing and research is being directed towards sub-micron sized reinforcements, modified alloy matrices and innovative processing routes. Some examples of this trend are Mg nano-composites without reduction of ductility, RE-modified Mg alloys with improved contact between matrix and carbon-based reinforcements and semisolid composites with better reinforcement distribution. Another relatively new topic in this field is the design of biodegradable Mg-based composites with bone-like apatite layers on their corroded surface.

From a corrosion point of view, it is generally observed that the incorporation of a reinforcement leads to higher corrosion rates, especially in the case of Mg alloys reinforced with carbon fibers and carbon nanotubes, due to galvanic corrosion. Other detrimental factors to consider are heterogeneities found at the matrix/reinforcement interface (*e.g.,* discontinuity of surface film, crevices, and additional interfacial phases) and modifications of the surrounding matrix (*e.g.,* microstructure, defects, and compositional segregation). Future research should focus on cheap and chemically compatible alloys and reinforcements, studies of corrosion under atmospheric and real-life service conditions and, more importantly, on anticorrosion treatments.

### 5.4. Mg biocorrosion

Due to the high complexity of the interactions between Mg corrosion and the biological surroundings, many open questions still exist, especially regarding detailed mechanistic understanding. There is still need to define protocols for laboratory experiments that to the best of our understanding mimic the *in vivo* exposure. In addition, a combination of experimental approached is required, ranging from conventional techniques to study corrosion (electrochemistry, immersion testing, and $H_2$ gas collection), surface analysis, and solution analysis for metal release, to exploratory approaches as well as to correlation of the *findings* with *in vivo* behavior. Finally, the research in this field being at the interface of materials science and medicine, collaboration between experts from the related fields is of utmost importance.

### 5.5. Atmospheric corrosion

In view of the crucial importance of atmospheric corrosion for Mg, surprisingly very little work has been devoted to the subject as compared to the aqueous corrosion. The importance of the subject is highlighted by the discrepancy between the results from immersion testing and the behavior observed when Mg is subjected to atmospheric corrosion, which is discussed in terms of a role played by $CO_2$ and Al in the corrosion process. The corrosion behavior of Mg in the atmosphere tends to be more benign compared to the outcome of many immersion tests. Also, the results from the two types of experiments can differ greatly in other important respects, *e.g.,* concerning the effect of alloying elements on corrosion properties. This shows that a detailed understanding of the atmospheric corrosion of Mg can only be achieved by performing experiments under atmospheric conditions. The inconsistencies mentioned are discussed in this review, and are partly attributed to the effect of atmospheric $CO_2$ (in conjunction with the alloy Al content) and the formation of slightly soluble and protective LDHs that do not form under immersion conditions. However, it is stressed that the understanding of this phenomenon is still very incomplete.

Among the many outstanding issues in this rapidly evolving field we would like to mention a few, starting with the highly detrimental, corrosion-induced cracking of the metal which is often observed. In this review it is suggested that the cracking is related to hydrogen uptake. If this is indeed the case, the mechanism of H uptake should be addressed. Is it connected to the electrochemical reduction of water at the cathodes or does it emanate from a "chemical" reaction? Also, the state of H in the metal should be addressed. Does it form a solid solution or $MgH_2$, do $H_2$ gas bubbles nucleate within the metal? The problem may be addressed by high resolution analytical tools, using *e.g.,* vibrational EELS and NanoSIMS, to detect hydrogen in the substrate. Another issue is the contorvecies surrounding the $Al^{3+}$ enriched layer, which has been observed at the metal/film interface on Mg-Al alloys. As alumina is far less soluble than MgO and $Mg(OH)_2$ in neutral solution, the alumina enrichment may improve corrosion properties in some cases, *i.e.,* affecting the anodic reaction. Indeed, chloride-induced film failure should also be looked at in this context. The nature of the enrichment and its formation may be addressed by a combination of high resolution microscopy methods and HR-AES.

Concerning the corrosion product composition, while recent papers do suggest that the LDHs play an important role in Mg-Al alloy corrosion, much more research is needed to test the viability of the idea. In view of the sensitivity of this kind of compounds the work would probably involve both XRD and FTIR. Another somewhat more academic issue is the possible role of $O_2$ in Mg atmospheric corrosion. There are some published results that hint that $O_2$ can play a role. This issue could be addressed by comparing the corrosion behavior in exposures in $N_2$ and in air

To conclude, it is emphasized that a deeper understanding of the details of Mg atmospheric corrosion is not just of scientific interest. Mechanistic knowledge of corrosion will also enable the design of industrial corrosion testing procedures that can predict the corrosion behavior of Mg in engineering applications. Such procedures will be essential for developing processing routes and coating systems so as to combat and control Mg corrosion.

### 5.6. Protection against atmospheric corrosion

In regards to the protection strategies, it is essential to note that component design/maintenance, environment and the material itself are the key aspects to take into consideration for any corrosion protection scheme. For Mg alloys, dissimilar metal configurations and geometries prone to moisture accumulation should always be avoided. Future research efforts should concentrate on clever design solutions and versatile anticorrosion treatments whenever multi-material assemblies are unavoidable. The effect of environment variables such as RH, temperature, chloride concentration, inhibitors, and contaminants (*e.g.,* $SO_2$) on the long-term corrosion resistance of Mg alloys should be further studied, if more realistic service-life predictions are to be achieved.

The most frequent and reliable strategy for improving the corrosion resistance of Mg alloys is tailoring the surface properties of the material by either changing its composition/microstructure or by surface modification. At present, high purity alloys, minor alloying additions, sophisticated processing control (*e.g.,* heat treatments and semisolid processes) and innovative conversion and anodizing treatments are the most interesting approaches for improved corrosion performance of Mg alloys. Examples of hot topics in the field are the development of coatings with incorporated active corrosion protection, newly discovered and highly efficient Mg inhibitors, anodizing above and below breakdown with *in situ* incorporation of suitable chemical species (*e.g.,* inhibitors, particles, and nanocontainers).

## Acknowledgement

M. Esmaily would like to sincerely thank ÅF AB and Helge AX:son Johnsons Stiftelse (Sweden) for kindly supporting the research in the field of Mg corrosion and funding the project. J.E. Svensson is thankful to the Swedish Foundation for Strategic Research (SSF) (Grant number: RMA08-0138). S. Fajardo expresses his gratitude to the Ministry of Economy, Industry and Competitiveness of Spain, the Spanish National Research Council (CSIC) and the European Regional Development Fund (ERDF) for the financial support under the Project MAT2015-74420-JIN. S. Virtanen acknowledges the German Research Foundation (DFG) for financial support (grant numbers VI 350/7-1 and VI 350/12-1). N. Birbilis received support from the Army Research Laboratory (USA) and Baosteel Corporation. He is grateful for a personal Chair wholly supported by Woodside. G.S. Frankel thanks DNVGL through a gift in support of the DNV Designated Chair in Corrosion. R. Arrabal is grateful to MINECO/FEDER (Spain, Project MAT2015-66334-C3-3-R). L.G. Johansson is grateful to the Swedish Research Council (Vr) (Grant number: 2015-04977) and also the Swedish Foundation for Strategic Research (SSF) (Grant number: RMA08-0138).

## References

[1] Tokarska KB, Gillett NP, Weaver AJ, Arora VK, Eby M. The climate response to five trillion tonnes of carbon. Nat Clim Chang 2016;6:851–6.
[2] Fyfe JC, Meehl GA, England MH, Mann ME, Santer BD, Flato GM, et al. Making sense of the early-2000s warming slowdown. Nat Clim Chang 2016;6:224–8.
[3] Meinshausen M, Meinshausen N, Hare W, Raper SCB, Frieler K, Knutti R, et al. Greenhouse-gas emission targets for limiting global warming to 2 °C. Nature 2009;458:1158–62.
[4] EP. Regulation (EC) no 443/2009 setting emission performance standards for new passenger cars as part of the Community's integrated approach to reduce CO2 emissions from light-duty vehicles. Off J Eur Communities; 2009. p. 15.
[5] Can be found in <https://ec.europa.eu/clima/consultations/articles/0030_en.htm>.
[6] Kainer KU. Magnesium – alloys and technology. Wiley; 2003.
[7] Global climate change impacts in the United States, annual report; 2009.
[8] Abbott TB. Mg: Industrial and research developments over the last 15 years. Corrosion 2015;71:120–7.
[9] International Air Transport Association. Guidance Material and Best Practices for Fuel and Environmental Management, 1st ed. Montreal (Geneva); 2004.
[10] Zenkert D, Kaufmann M. The cost of weight – and how that affects the design. Sweden: Swerea SICOMP; 2010.
[11] Avedesian MM, Baker H. ASM specialty handbook: magnesium and magnesium alloys. ASM Int Mater Park OH; 1999.
[12] Kainer KU. Magnesium alloys and their applications; 2006.
[13] Mordike BL, Ebert T. Magnesium properties - applications - potential. Mater Sci Eng A 2001;302:37–45.
[14] Birbilis N, Easton MA, Sudholz AD, Zhu SM, Gibson MA. On the corrosion of binary magnesium-rare earth alloys. Corros Sci 2009;51:683–9.
[15] Kammer C. Mg-Taschenbuch. Düsseldorf: Aluminium-Verlag; 2000.
[16] Polmear IJ. Light alloys - from traditional alloys to nanocrystals. Elsevier; 2006.
[17] Bussy A. Mémoire Sur le radical métallique de la magnésie. J de Chimie Médic, de Pharma, et de Toxicologie 1830;6:141.
[18] Beetz W. On the development of hydrogen from the anode. Phil Mag 1866;32:269.
[19] Huse EC. A new ligature? Chicago Med J Exam 1878;172:2.
[20] Lambotte A. Technique et indications de la prothèse perdue dans la traitement des fractures. Presse Med Belge 1909;17:321–3.
[21] Boyer JA. The corrosion of magnesium and of the magnesium aluminum alloys containing manganese Report 248. American Magnesium Corporation; 1927.
[22] McNulty RE, Hanawalt JD. Some corrosion characteristics of high purity magnesium alloys. Trans Electrochem Soc 1942;81:423–33.
[23] Petty RL, Davidson AW, Kleinberg J. The anodic oxidation of magnesium metal: evidence for the existence of unipositive Mg. J Am Chem Soc 1954;76:363–6.
[24] Splinter SJ, McIntyre NS, Len WN, Griffiths K, Palumbo G. An AES and XPS study of the initial oxidation of polycrystalline magnesium with water vapour at room temperature. Surf Sci 1993;292:130–44.
[25] Nordlien JH, Ono S, Masuko N, Nisancioglu K. Morphology and structure of oxide films formed on magnesium by exposure to air and water. J Electrochem Soc 1995;142:3320–2.
[26] Nordlien JH, Ono S, Masuko N, Nisancioglu K. Morphology and structure of oxide films formed on MgAl alloys by exposure to air and water. J Electrochem Soc 1996;143:2564–72.
[27] Nordlien JH, Nisancioglu K, Ono S, Masuko N. Morphology and structure of water-formed oxides on ternary MgAl alloys. J Electrochem Soc 1997;144:461–6.
[28] Can be found in <http://www.Mg-elektron.com/Mg-elektron-welcomes-new-standard-use-Mg-commercial-aircraft-seats>.
[29] Blawert C, Hort N, Kainer KU. Automotive applications of magnesium and its alloys. Trans Indian Inst Met 2004;57:397–408.
[30] Brooks E. Magnesium base alloys. US Patent 1957934 A; 1934.
[31] Vermilyea DA, Kirk CF. Studies of inhibition of magnesium corrosion. J Electrochem Soc 1969;116:1487–92.
[32] Lindström R, Svensson JE, Johansson LG. The influence of carbon dioxide on the atmospheric corrosion of some magnesium alloys in the presence of NaCl. J Electrochem Soc 2002;149:B103–7.

[33] Williams G, Mc Murray H Neil. Localized corrosion of magnesium in chloride-containing electrolyte studied by a scanning vibrating electrode technique. J Electrochem Soc 2008;155. C340-C9.

[34] Williams G, Birbilis N, Mcmurray HN. The source of hydrogen evolved from a magnesium anode. Electrochem Commun 2013;36:1–5.

[35] Xu W, Birbilis N, Sha G, Wang Y, Daniels JE, Xiao Y, et al. A high-specific-strength and corrosion-resistant magnesium alloy. Nat Mater 2015;14:1229–35.

[36] Esmaily M, Shahabi-Navid M, Mortazavi N, Svensson JE, Halvarsson M, Wessén M, et al. Microstructural characterization of the Mg-Al alloy AM50 produced by a newly developed rheo-casting process. Mater Charact 2014;95:50–64.

[37] Schumann S, Friedrich H. Engineering requirements, strategies and examples. In: Friedrich HE, Mordike BL, editors. Magnesium technology, applications. Berlin: Springer-Verlag; 2006.

[38] Du Y, Wang J, Zhao J, Schuster JC, Weitzer F, Schmid-Fetzer R, et al. Reassessment of the Al-Mn system and a thermodynamic description of the Al-Mg-Mn system. Int J Mater Res 2007;98:855–71.

[39] Liu JC, Hu J, Nie XY, Li HX, Du Q, Zhang JS, et al. The interface bonding mechanism and related mechanical properties of Mg/Al compound materials fabricated by insert molding. Mater Sci Eng A 2015;635:70–6.

[40] Thomas S, Medhekar NV, Frankel GS, Birbilis N. Corrosion mechanism and hydrogen evolution on Mg. Curr Opin Solid State Mater Sci 2015;19:85–94.

[41] Atrens A, Song GL, Liu M, Shi Z, Cao F, Dargusch MS. Review of recent developments in the field of magnesium corrosion. Adva Eng Mater 2015;17:400–53.

[42] Gusieva K, Davies CHJ, Scully JR, Birbilis N. Corrosion of magnesium alloys: the role of alloying. Int Mater Rev 2015;60:169–94.

[43] Kirkland NT, Birbilis N, Staiger MP. Assessing the corrosion of biodegradable magnesium implants: a critical review of current methodologies and their limitations. Acta Biomater 2012;8:925–36.

[44] Agarwal S, Curtin J, Duffy B, Jaiswal S. Biodegradable magnesium alloys for orthopaedic applications: a review on corrosion, biocompatibility and surface modifications. Mater Sci Eng C 2016;68:948–63.

[45] Winzer N, Atrens A, Song GL, Ghali E, Dietzel W, Kainer KU, et al. A critical review of the stress corrosion cracking (SCC) of magnesium alloys. Adv Eng Mater 2005;7:659–93.

[46] Winzer N, Atrens A, Dietzel W, Song GL, Kainer KU. Stress corrosion cracking in magnesium alloys: characterization and prevention. J Mater Sci 2007;59:49–53.

[47] Dauphin-Ducharme P, Mauzeroll J. Surface analytical methods applied to magnesium corrosion. Anal Chem 2015;87:7499–509.

[48] Lebouil S, Duboin A, Monti F, Tabeling P, Volovitch P, Ogle K. A novel approach to on-line measurement of gas evolution kinetics: application to the negative difference effect of magnesium in chloride solution. Electrochim Acta 2014;124:176–82.

[49] Curioni M. The behaviour of magnesium during free corrosion and potentiodynamic polarization investigated by real-time hydrogen measurement and optical imaging. Electrochim Acta 2014;120:284–92.

[50] Fajardo S, Frankel GS. Gravimetric method for hydrogen evolution measurements on dissolving magnesium. J Electrochem Soc 2015;162:C693–701.

[51] Bland LG, King AD, Birbilis N, Scully JR. Assessing the corrosion of commercially pure magnesium and commercial AZ31B by electrochemical impedance, mass-loss, hydrogen collection, and inductively coupled plasma optical emission spectrometry solution analysis. Corrosion 2015;71:128–45.

[52] Curioni M, Scenini F, Monetta T, Bellucci F. Correlation between electrochemical impedance measurements and corrosion rate of magnesium investigated by real-time hydrogen measurement and optical imaging. Electrochim Acta 2015;166:372–84.

[53] Frankel GS. Electrochemical techniques in corrosion: status, limitations, and needs. J Test Eval 2014;42:517–40.

[54] King AD, Birbilis N, Scully JR. Accurate electrochemical measurement of magnesium corrosion rates; a combined impedance, mass-loss and hydrogen collection study. Electrochim Acta 2014;121:394–406.

[55] Stern M, Geary AL. A theoretical analysis of the shape of polarization curves. J Electrochem Soc 1957;104:56–63.

[56] Fajardo S, Frankel GS. Effect of impurities on the enhanced catalytic activity for hydrogen evolution in high purity magnesium. Electrochim Acta 2015;165:255–67.

[57] Elsentriecy HH, Azumi K, Konno H. Effects of pH and temperature on the deposition properties of stannate chemical conversion coatings formed by the potentiostatic technique on AZ91D magnesium alloy. Electrochim Acta 2008;53:4267–75.

[58] Elsentriecy HH, Azumi K, Konno H. Improvement in stannate chemical conversion coatings on AZ91D magnesium alloy using the potentiostatic technique. Electrochim Acta 2007;53:1006–12.

[59] Cain T, Madden SB, Birbilis N, Scully JR. Evidence of the enrichment of transition metal elements on corroding magnesium surfaces using rutherford backscattering spectrometry. J Electrochem Soc 2015;162:C228–37.

[60] Birbilis N, King AD, Thomas S, Frankel GS, Scully JR. Evidence for enhanced catalytic activity of magnesium arising from anodic dissolution. Electrochim Acta 2014;132:277–83.

[61] Fajardo S, Glover CF, Williams G, Frankel GS. The source of anodic hydrogen evolution on ultra high purity Mg. Electrochim Acta 2016;212:510–21.

[62] Frankel GS, Samaniego A, Birbilis N. Evolution of hydrogen at dissolving magnesium surfaces. Corros Sci 2013;70:104–11.

[63] Samaniego A, Birbilis N, Xia X, Frankel GS. Hydrogen evolution during anodic polarization of magnesium alloyed with Li, Ca, or Fe. Corrosion 2015;71:224–33.

[64] Scully JR. Polarization resistance method for determination of instantaneous corrosion rates. Corrosion 2000;56:199–218.

[65] Shkirskiy V, King AD, Gharbi O, Volovitch P, Scully JR, Ogle K, et al. Revisiting the electrochemical impedance spectroscopy of magnesium with online inductively coupled plasma atomic emission spectroscopy. Chem Phys Chem 2015;16:536–9.

[66] Isaacs HS. The effect of height on the current distribution measured with a vibrating electrode probe. J Electrochem Soc 1991;138:722–8.

[67] McMurray HN, Williams D, Worsley DA. Artifacts induced by large-amplitude probe vibrations in localized corrosion measured by SVET. J Electrochem Soc 2003;150:B567–73.

[68] Williams G, Llwyd Dafydd H, Grace R. The localised corrosion of magnesium alloy AZ31 in chloride containing electrolyte studied by a scanning vibrating electrode technique. Electrochim Acta 2013;109:489–501.

[69] Thomas S, Izquierdo J, Birbilis N, Souto RM. Possibilities and limitations of scanning electrochemical microscopy of Mg and Mg alloys. Corrosion 2015;71:171–83.

[70] Jamali SS, Moulton SE, Tallman DE, Forsyth M, Weber J, Wallace GG. Evaluating the corrosion behaviour of magnesium alloy in simulated biological fluid by using SECM to detect hydrogen evolution. Electrochim Acta 2015;152:294–301.

[71] Liu W, Cao F, Xia Y, Chang L, Zhang J. Localized corrosion of magnesium alloys in NaCl solutions explored by scanning electrochemical microscopy in feedback mode. Electrochim Acta 2014;132:377–88.

[72] Salleh SH, Thomas S, Yuwono JA, Venkatesan K, Birbilis N. Enhanced hydrogen evolution on $Mg(OH)_2$ covered magnesium surfaces. Electrochim Acta 2015;161:144–52.

[73] Tefashe UM, Snowden ME, Ducharme PD, Danaie M, Botton GA, Mauzeroll J. Local flux of hydrogen from magnesium alloy corrosion investigated by scanning electrochemical microscopy. J Electroanal Chem 2014;720–721:121–7.

[74] Dauphin-Ducharme P, Asmussen RM, Tefashe UM, Danaie M, Binns WJ, Jakupi P, et al. Local hydrogen fluxes correlated to microstructural features of a corroding sand cast AM50 magnesium alloy. J Electrochem Soc 2014;161:C557–64.

[75] Thomas S, Gharbi O, Salleh SH, Volovitch P, Ogle K, Birbilis N. On the effect of Fe concentration on magnesium dissolution and activation studied using atomic emission spectroelectrochemistry and scanning electrochemical microscopy. Electrochim Acta 2016;210:271–84.

[76] Ogle K, Weber S. Anodic dissolution of 304 stainless steel using atomic emission spectroelectrochemistry. J Electrochem Soc 2000;147:1770–80.

[77] Ogle K, Baeyens J, Swiatowska J, Volovitch P. Atomic emission spectroelectrochemistry applied to dealloying phenomena: I. The formation and dissolution of residual copper films on stainless steel. Electrochim Acta 2009;54:5163–70.

[78] Ogle K, Mokaddem M, Volovitch P. Atomic emission spectroelectrochemistry applied to dealloying phenomena II. Selective dissolution of iron and chromium during active-passive cycles of an austenitic stainless steel. Electrochim Acta 2010;55:913–21.

[79] Jiang L, Volovitch P, Sundermeier U, Wolpers M, Ogle K. Dissolution and passive film formation of Sn and Sn coated steel using atomic emission spectroelectrochemistry. Electrochim Acta 2011;58:322–9.

[80] Shkirskiy V, Ogle K. A novel coupling of electrochemical impedance spectroscopy with atomic emission spectroelectrochemistry: application to the open circuit dissolution of zinc. Electrochim Acta 2015;168:167–72.

[81] Świątowska J, Volovitch P, Ogle K. The anodic dissolution of Mg in NaCl and $Na_2SO_4$ electrolytes by atomic emission spectroelectrochemistry. Corros Sci 2010;52:2372–8.

[82] ASTM G1-03(2011). Standard practice for preparing, cleaning, and evaluating corrosion test specimens. ASTM International: West Conshohocken; 2011.

[83] Song GL, Atrens A, StJohn D. A hydrogen evolution method for the estimation of the corrosion rate of magnesium alloys. In: Magnesium technology. John Wiley & Sons, Inc; 2001. p. 254–62.

[84] Rybalka KV. Determination of metal corrosion rate using the pH-metry by the method of compensating additives. Russ J Electrochem 2014;50:500–2.

[85] Schweitzer PA. Atmospheric corrosion, atmospheric degradation and corrosion control. CRC Press; 1999.

[86] Graedel TE. Corrosion-related aspects of the chemistry and frequency of occurrence of precipitation. J Electrochem Soc 1986;133:2476–82.

[87] Holm R, Mattsson E. Atmospheric corrosion tests of copper and copper alloys in Sweden - 16-year results. In: Atmospheric corrosion of metals, ASTM STP 767. American Society for Testing and Materials; 1982. p. 85–105.

[88] Rozenfeld IL. Atmospheric corrosion of metals. Houston: National Association of Corrosion Engineers; 1972.

[89] Sanders CE, Verreault D, Frankel GS, Allen HC. The role of sulfur in the atmospheric corrosion of silver. J Electrochem Soc 2015;162:C630–7.

[90] Yang LJ, Li YF, Wei YH, Hou LF, Li YG, Tian Y. Atmospheric corrosion of field-exposed AZ91D magnesium alloys in a polluted environment. Corros Sci 2010;52:2188–96.

[91] Wang BB, Wang ZY, Han W, Ke W. Atmospheric corrosion of aluminium alloy 2024–T3 exposed to salt lake environment in Western China. Corros Sci 2012;59:63–70.

[92] Li YG, Wei YH, Hou LF, Han PJ. Atmospheric corrosion of AM60 magnesium alloys in an industrial city environment. Corros Sci 2013;69:67–76.

[93] Cui Z, Li X, Xiao K, Dong C. Atmospheric corrosion of field-exposed AZ31 magnesium in a tropical marine environment. Corros Sci 2013;76:243–56.

[94] Liao J, Hotta M. Atmospheric corrosion behavior of field-exposed magnesium alloys: influences of chemical composition and microstructure. Corros Sci 2015;100:353–64.

[95] Liao J, Hotta M. Corrosion products of field-exposed Mg-Al series magnesium alloys. Corros Sci 2016;112:276–88.

[96] Liao J, Hotta M, Motoda SI, Shinohara T. Atmospheric corrosion of two field-exposed AZ31B magnesium alloys with different grain size. Corros Sci 2013;71:53–61.

[97] Jönsson M, Persson D, Leygraf C. Atmospheric corrosion of field-exposed magnesium alloy AZ91D. Corros Sci 2008;50:1406–13.

[98] Jönsson M, Persson D. Accelerated corrosion tests for magnesium alloys: do they really simulate field conditions? In: 65th Annual world magnesium conference: Poland.

[99] Leygraf C, Graedel T. Atmospheric corrosion. Wiley-VCH: Electrochemical Society Series; 2000.

[100] Rendahl B, LeBozec N. Assessment of corrosivity of global vehicle environment. Sweden: Research Report Swerea KIMAB Stockholm; 2009.

[101] Schindelholz E, Kelly RG, Cole IS, Ganther WD, Muster TH. Comparability and accuracy of time of wetness sensing methods relevant for atmospheric corrosion. Corros Sci 2013;67:233–41.

[102] Song GL. Corrosion prevention of magnesium alloys. Woodhead Publishing in Materials; 2014.

[103] Liu M, Uggowitzer PJ, Nagasekhar AV, Schmutz P, Easton M, Song GL, et al. Calculated phase diagrams and the corrosion of die-cast Mg–Al alloys. Corros Sci 2009;51:602–19.

[104] Zhao MC, Schmutz P, Brunner S, Liu M, Song GL, Atrens A. An exploratory study of the corrosion of magnesium alloys during interrupted salt spray testing. Corros Sci 2009;51:1277–92.

[105] Corrosion testing standard. VCS 1027, 1449. Accelerated corrosion test, version II-ACT II, Volvo Car Corporation; 2014.

[106] Corrosion testing standard. VDA 233-102, Cyclic corrosion testing of materials and components in automotive construction, VDA; 2013.

[107] Ström M. 5th Int. Seminar in the Field of Automotive Corrosion: Findings and conclusions from three decades of automotive corrosion testing;2013 .

[108] Vernon WHJ. A laboratory study of the atmospheric corrosion of metals. Part II.—Iron: the primary oxide film. Part III.—the secondary product or rust (influence of sulphur dioxide, carbon dioxide, and suspended particles on the rusting of iron. Trans Faraday Soc 1935;31:1668–700.

[109] Svensson JE, Johansson LG. A laboratory study of the initial stages of the atmospheric corrosion of zinc in the presence of NaCl; Influence of $SO_2$ and $NO_2$. Corros Sci 1993;34:721–40.

[110] Niklasson A, Johansson LG, Svensson JE. The influence of relative humidity and temperature on the acetic acid vapour-induced atmospheric corrosion of lead. Corros Sci 2008;50:3031–7.

[111] Strandberg H, Johansson LG. Role of $O_3$ in the atmospheric corrosion of copper in the presence of $SO_2$. J Electrochem Soc 1997;144:2334–42.

[112] Svensson JE, Johansson LG. A laboratory study of the effect of ozone, nitrogen dioxide, and sulfur dioxide on the atmospheric corrosion of zinc. J Electrochem Soc 1993;140:2210–6.

[113] Tada E, Frankel GS. Effects of particulate silica coatings on localized corrosion behavior of AISI 304SS under atmospheric corrosion conditions. J Electrochem Soc 2007;154:C318–25.

[114] Lin H, Frankel GS. Atmospheric corrosion of Cu during constant deposition of NaCl. J Electrochem Soc 2013;160:C336–44.

[115] Chen ZY, Liang D, Ma G, Frankel GS, Allen HC, Kelly RG. Influence of UV irradiation and ozone on atmospheric corrosion of bare silver. Corros Eng Sci Techn 2010;45:169–80.

[116] Hallama KR, Minshall PC, Hearda PJ, Flewitt PEJ. Corrosion of the alloys Magnox AL80, Magnox ZR55 and pure magnesium in air containing water vapour. Corros Sci 2016;112:347–63.

[117] Jia R, Yan C, Wang F. Influence of Al content on the atmospheric corrosion behaviour of Mg-aluminum alloys. J Mater Sci Tech 2009;25:225–9.

[118] Christofer L, Wallinder IO, Tidblad J, Graedel T. Atmospheric corrosion. John Wiley & Sons; 2016.

[119] Esmaily M, Shahabi-Navid M, Svensson JE, Halvarsson M, Nyborg L, Cao Y, et al. Influence of temperature on the atmospheric corrosion of the magnesium alloy AM50. Corros Sci 2015;90:420–33.

[120] Esmaily M, Blücher DB, Lindström RW, Svensson JE, Johansson LG. The influence of $SO_2$ on the corrosion of magnesium and Mg-Al alloys. J Electrochem Soc 2015;162:C260–9.

[121] Esmaily M, Blücher DB, Svensson JE, Halvarsson M, Johansson LG, Shahabi-Navid M. Achieving superior corrosion resistance in friction stir processed AA6005-T6 aluminum alloy joints. ECS Trans 2015;64:29–43.

[122] Shahabi-Navid M, Esmaily M, Svensson JE, Halvarsson M, Nyborg L, Cao Y, et al. NaCl-induced atmospheric corrosion of the MgAl alloy AM50-the influence of $CO_2$. J Electrochem Soc 2014;161:C277–87.

[123] Esmaily M, Mortazavi N, Svensson JE, Johansson LG, Halvarsson M. On the capability of in situ exposure in an environmental scanning electron microscope for investigating the atmospheric corrosion of Mg. Ultramicro 2015;153:45–54.

[124] Esmaily M, Mortazavi N, Osikowicz W, Hindsefelt H, Svensson JE, Halvarsson M, et al. Corrosion behaviour of friction stir-welded AA6005-T6 using a bobbin tool. Corros Sci 2016;111:98–109.

[125] Strekalov PV. Atmospheric corrosion of metals in the tropics and subtropics.II. The corrosion resistance of various metals and alloys. Prot Met 1993;29:673–706.

[126] Zakipour S, Tidblad J, Leygraf C. Atmospheric corrosion effects of $SO_2$, $NO_2$, and $O_3$. A comparison of laboratory and field exposed nickel. J Electrochem Soc 1997;144:3513–7.

[127] Albright DL. Rrelationship of microstructure and corrosion performance in cast magnesium alloys. JOM 1987;39:32.
[128] Makar GL, Kruger J, Sieradzki K. Repassivation of rapidly solidified Mg-aluminum alloys. J Electrochem Soc 1992;139:47–53.
[129] Underwood EE. Quantitative stereology. Reading: Addison-Wesley; 1970.
[130] Practical guide to image analysis. ASM International, Materials Park; 2000.
[131] Wojnar L. Image analysis. Applications in materials engineering. Boca Raton: CRC Press; 1998.
[132] Pyrz R. Quantitative description of the microstructure of composites. Part I: morphology of unidirectional composite systems. Compos Sci Technol 1994;50:197–208.
[133] Tzamtzis S, Barekar NS, Babu H, Patel J, Dhindaw BK, Fan Z. Processing of advanced Al/SiC particulate metal matrix composites under intensive shearing - a novel rheo-process. Compos Part A Appl Sci Manuf 2009;40:144–51.
[134] Rogers A. Statistical analysis of spatial dispersions: the quadrat method. London: Pion; 1974.
[135] Esmaily M, Mortazavi N, Svensson JE, Halvarsson M, Cao Y, Wessén M, et al. A new semi-solid casting technique for fabricating SiC-reinforced Mg alloys matrix composites. Compos Part B: Eng 2016;94:176–89.
[136] Alkemper J, Voorhees PW. Quantitative serial sectioning analysis. J Microsc 2001;388:201–7.
[137] Prakash DG, Regener D, Vorster WJJ. Effect of long term annealing on the microstructure of hpdc AZ91 magnesium alloy: a quantitative analysis by image processing. Comp Mater Sci 2008;43:759–66.
[138] Tewari A, Gokhale AM. Nearest-neighbor distributions in thin films, sheets, and plates. Acta Mater 2006;54:1957–63.
[139] Xia X, Nie JF, Davies CHJ, Tang WN, Xu SW, Birbilis N. An artificial neural network for predicting corrosion rate and hardness of magnesium alloys. Mater Des 2016;90:1034–43.
[140] Kirkland NT, Staiger MP, Nisbet D, Davies CHJ, Birbilis N. Performance-driven design of Biocompatible Magnesium alloys. JOM 2011;63:28–34.
[141] Birbilis N, Cavanaugh MK, Sudholz AD, Zhu SM, Easton MA, Gibson MA. A combined neural network and mechanistic approach for the prediction of corrosion rate and yield strength of Mg-rare earth alloys. Corros Sci 2011;53:168–76.
[142] Willumeit R, Feyerabend F, Huber N. Magnesium degradation as determined by artificial neural networks. Acta Biomater 2013;9:8722–9.
[143] Kappatos V, Chamos AN, Pantelakis SG. Assessment of the effect of existing corrosion on the tensile behaviour of magnesium alloy AZ31 using neural networks. Mater Des 2010;31:336–42.
[144] Mortazavi N, Esmaily M, Halvarsson M. The capability of Transmission Kikuchi Diffraction technique for characterizing nano-grained oxide scales formed on a FeCrAl stainless steel. Mater Lett 2015;147:42–5.
[145] Orlov D, Ralston KD, Birbilis N, Estrin Y. Enhanced corrosion resistance of Mg alloy ZK60 after processing by integrated extrusion and equal channel angular pressing. Acta Mater 2011;59:6176–86.
[146] Kima HS, Kimb GH, Kimc H, Kimd WJ. Enhanced corrosion resistance of high strength Mg–3Al–1Zn alloy sheets with ultrafine grains in a phosphate-buffered saline solution. Corros Sci 2013;74:139–48.
[147] Pu Z, Song GL, Yang S, Outeiro JC, Dillon Jr OW, Puleo DA, et al. Grain refined and basal textured surface produced by burnishing for improved corrosion performance of AZ31B magnesium alloy. Corros Sci 2012;57:192–201.
[148] Bland LG, Rincon Troconis BC, Santucci Jr RJ, Fitz-Gerald JM, Scully JR. Metallurgical and electrochemical characterization of the corrosion of a Mg-Al-Zn Alloy AZ31B-H24 tungsten inert gas weld: galvanic corrosion between weld zones. Corrosion 2016;72:1226–42.
[149] Esmaily M, Mortazavi N, Svensson JE, Halvarsson M, Blücher DB, Jarfors AEW, et al. Atmospheric corrosion of magnesium alloy AZ91D fabricated by a semi-solid casting technique - The influence of microstructure. J Electrochem Soc 2015;162:C311–21.
[150] Thompson SP. The life of William Thomson, Baron Kelvin of Largs. London: Macmillan; 1910.
[151] Stratmann M. The investigation of the corrosion properties of metals, covered with adsorbed electrolyte layers—a new experimental technique. Corros Sci 1987;27:869–72.
[152] Yee S, Oriani RA, Stratmann M. Application of a Kelvin microprobe to the corrosion of metals in humid atmospheres. J Electrochem Soc 1991;138:55–61.
[153] Rohwerder M, Turcu F. High-resolution Kelvin probe microscopy in corrosion science: scanning Kelvin probe force microscopy (SKPFM) versus classical scanning Kelvin probe (SKP). Electrochim Acta 2007;53:290–9.
[154] Hurley MF, Efaw CM, Davis PH, Croteau JR, Graugnard E, Birbilis N. Volta Potentials measured by scanning Kelvin probe force microscopy as relevant to corrosion of magnesium alloys. Corrosion 2015;71:160–70.
[155] Guillaumin V, Schmutz P, Frankel GS. Characterization of corrosion interfaces by the scanning kelvin probe force microscopy technique. J Electrochem Soc 2001;148:B163–73.
[156] Schmutz P, Frankel GS. Characterization of AA2024-T3 by scanning kelvin probe force microscopy. J Electrochem Soc 1998;145:2285–95.
[157] Örnek C, Engelberg DL. SKPFM measured Volta potential correlated with strain localisation in microstructure to understand corrosion susceptibility of cold-rolled grade 2205 duplex stainless steel. Corros Sci 2015;99:164–71.
[158] Pan T. Corrosion behavior of a duplex stainless steel under cyclic loading: a scanning Kelvin probe force microscopy (SKPFM) based microscopic study. J Appl Electrochem 2012;42:1049–56.
[159] Jönsson M, Thierry D, LeBozec N. The influence of microstructure on the corrosion behaviour of AZ91D studied by scanning Kelvin probe force microscopy and scanning Kelvin probe. Corros Sci 2006;48:1193–208.
[160] Dauphin-Ducharme P, Binns WJ, Snowden ME, Shoesmith DW, Mauzeroll J. Determination of the local corrosion rate of magnesium alloys using a shear force mounted scanning microcapillary method. Faraday Discuss 2015;180:331–45.
[161] Arrabal R, Mingo B, Pardo A, Matykina E, Mohedano M, Merino MC, et al. Role of alloyed Nd in the microstructure and atmospheric corrosion of as-cast magnesium alloy AZ91. Corros Sci 2015;97:38–48.
[162] Williams G, Grace R. Chloride-induced filiform corrosion of organic-coated magnesium. Electrochim Acta 2011;56:1894–903.
[163] Baek S, Kim HJ, Jeong HY, Sohn S, Shin H, Choi K, et al. Effect of alloyed Ca on the microstructure and corrosion properties of extruded AZ61 magnesium alloy. Corros Sci 2016;112:44–53.
[164] Mingo B, Arrabal R, Mohedano M, Pardo M, Matykina E, Rivas A. Enhanced corrosion resistance of AZ91 alloy produced by semisolid metal processing. J Electrochem Soc 2015;162:C180–8.
[165] Feliu Jr S, Maffiotte C, Galván JC, Pardo A, Merino MC, Arrabal R. The application of X-ray photoelectron spectroscopy in understanding corrosion mechanisms of magnesium and Mg-Al alloys. Open Surf Sci J 2011;3:1–14.
[166] Esmaily M, Blücher DB, Svensson JE, Halvarsson M, Johansson LG. New insights into the corrosion of magnesium alloys - the role of aluminum. Scripta Mater 2016;115:91–5.
[167] Esmaily M, Malmberg P, Shahabi-Navid M, Svensson JE, Johansson LG. A ToF-SIMS investigation of the corrosion behavior of magnesium alloy AM50 in atmospheric environments. Appl Surf Sci 2016;360:98–106.
[168] Bakhsheshi-Rad HR, Idris MH, Abdul-Kadir MR. Synthesis and in vitro degradation evaluation of the nano-HA/$MgF_2$ and DCPD/$MgF_2$ composite coating on biodegradable Mg–Ca–Zn alloy. Surf Coat Technol 2013;222:79–89.
[169] Birbilis N, Cain T, Laird JS, Xia X, Scully JR, Hughes AE. Nuclear microprobe analysis for determination of element enrichment following magnesium dissolution. ECS Electrochem Lett 2015;4:C34–7.
[170] Whitby L. The atmospheric corrosion of Mg. Trans Farad Soc 1933;29:0844–52.
[171] Waseda Y, Matsubara E, Shinoda K. X-ray diffraction crystallography. Springer Publication; 2011.
[172] Zolotoyabko E. Basic concepts of X-ray diffraction. Wiley 2014.
[173] Pawley J. Handbook of biological confocal microscopy. Springer; 2012.
[174] Esmaily M, Ström M, Svensson JE, Halvarsson M, Johansson LG. Corrosion behavior of alloy AM50 in semisolid cast and high-pressure die cast states in cyclic conditions. Corrosion 2015;71:737–48.

[175] Giannuzzi LA. Introduction to focused ion beams instrumentation, theory, techniques and practice. Springer; 2005.
[176] Burnett TL, Kelley R, Winiarski B, Contreras L, Daly M, Gholinia A, et al. Large volume serial section tomography by Xe Plasma FIB dual beam microscopy. Ultramicroscopy 2016;161:119–29.
[177] Taheri M, Kish JR, Birbilis N, Danaie M, McNally MA, McDermid JR. Towards a physical description for the origin of enhanced catalytic activity of corroding magnesium surfaces. Electrochim Acta 2016;116:396–403.
[178] Taheri M, Phillips RC, Kish JR, Botton GA. Analysis of the surface film formed on Mg by exposure to water using a FIB cross-section and STEM–EDS. Corros Sci 2012;59:222–8.
[179] Danaie M, Asmussen RM, Jakupi P, Shoesmith DW, Botton GA. The role of aluminum distribution on the local corrosion resistance of the microstructure in a sand-cast AM50 alloy. Corros Sci 2013;77:151–63.
[180] Unocic KA, Elsentriecy HH, Brady MP, Meyer III HM, Song GL, Fayek M, et al. Transmission electron microscopy study of aqueous film formation and evolution on Mg alloys. J Electrochem Soc 2014;161:C302–11.
[181] Taheri M, Kish JR. Nature of surface film formed on magnesium exposed to 1 M NaOH. J Electrochem Soc 2013;160:C36–41.
[182] Phillips RC, Kish JR. Nature of surface film on matrix phase of magnesium alloy AZ80 formed in water. Corrosion 2013;69:813–20.
[183] Taheri M, Danaie M, Kish JR. TEM examination of the film formed on corroding magnesium prior to breakdown. J Electrochem Soc 2014;161:C89–94.
[184] Asmussen RM, Jakupi P, Danaie M, Botton GA, Shoesmith DW. Tracking the corrosion of magnesium sand cast AM50 alloy in chloride environments. Corros Sci 2013;75:114–22.
[185] Chu PW, Marquis EA. Linking the microstructure of a heat-treated WE43 magnesium alloy with its corrosion behavior. Corros Sci 2015;101:94–104.
[186] Williams DB, Barry CC. Transmission electron microscopy. A textbook for materials science. Springer; 2009.
[187] Kang H, Choi HJ, Kang SW, Shin SE, Choi GS, Bae DH. Multi-functional magnesium alloys containing interstitial oxygen atoms. Sci Rep 2016. 23184.
[188] Zhang X, Wu G, Peng X, Li L, Feng H, Gao B, et al. Mitigation of corrosion on magnesium alloy by predesigned surface corrosion. Sci Rep 2015;5:17399.
[189] Lagos MJ, Trügler A, Hohenester U, Batson PE. Mapping vibrational surface and bulk modes in a single nanocube. Nature 2017;543:529–32.
[190] Warner TJ, Thorne NA, Nussbaum G, Stobbs WM. A cross-sectional TEM study of corrosion initiation in rapidly solidified Mg-based ribbons. Surf Interf Anal 1992;19:386–92.
[191] Zhou X, Luo C, Hashimoto T, Hughes AE, Thompson GE. Study of localized corrosion in AA2024-T3 aluminium alloy using electron tomography. Corros Sci 2012;58:299–306.
[192] Hashimoto T, Thompson GE, Zhou X, Withers PJ. 3D imaging by serial block face scanning electron microscopy for materials science using ultramicrotomy. Ultramicroscopy 2016;163:6–18.
[193] Krebs HM, Chirazi A, Lechner L, Withers PJ. Time-lapse correlative 3D imaging applied to the corrosion study of AZ31 Mg alloy in a saline environment (conference paper). FIMPART Hyderabad India 2015;1.
[194] Shahabi-Navid M. Atmospheric corrosion of Mg and MgAl alloys–characterization and mechanisms. Gothenburg (Sweden): Chalmers University of Technology; 2015.
[195] Heide P. X-ray photoelectron spectroscopy: an introduction to principles and practices. Wiley; 2011.
[196] Hofmann S. Auger- and X-ray photoelectron spectroscopy in materials science. Springer; 2013.
[197] Feliu Jr S, Pardo A, Merino MC, Coy AE, Viejo F, Arrabal R. Correlation between the surface chemistry and the atmospheric corrosion of AZ31, AZ80 and AZ91D magnesium alloys. Appl Surf Sci 2009;255:4102–8.
[198] Feliu Jr S, Merino MC, Arrabal R, Coy AE, Matykina E. XPS study of the effect of aluminium on the atmospheric corrosion of the AZ31 magnesium alloy. Surf Interf Anal 2009;41:143–50.
[199] Ballerini G, Bardi U, Bignucolo R, Ceraolo G. About some corrosion mechanisms of AZ91D magnesium alloy. Corros Sci 2005;47:2173–84.
[200] Hallam KR, Minshall PC, Heard PJ, Flewitt PEJ. Corrosion of the alloys Magnox AL80, Magnox ZR55 and pure magnesium in air containing water vapour. Corros Sci 2016;112:347–63.
[201] Wang L, Shinohara T, Zhang BP. XPS study of the surface chemistry on AZ31 and AZ91 magnesium alloys in dilute NaCl solution. Appl Surf Sci 2010;256:5807–12.
[202] Santamaria M, Di Quarto F, Zanna S, Marcus P. Initial surface film on magnesium metal: a characterization by X-ray photoelectron spectroscopy (XPS) and photocurrent spectroscopy (PCS). Electrochim Acta 2007;53:1314–24.
[203] Cui X, Li Q, Li Y, Wang F, Jin G, Ding M. Microstructure and corrosion resistance of phytic acid conversion coatings for magnesium alloy. Appl Surf Sci 2008;255:2098–103.
[204] Montemor MF, Simões AM, Carmezim MJ. Characterization of rare-earth conversion films formed on the AZ31 magnesium alloy and its relation with corrosion protection. Appl Surf Sci 2007;253:6922–31.
[205] Wang X, Zeng X, Wu G, Yao S, Lai Y. Effects of tantalum ion implantation on the corrosion behavior of AZ31 magnesium alloys. J Alloys Compd 2007;437:87–92.
[206] Montemor MF, Simões AM, Ferreira MGS, Carmezim MJ. Composition and corrosion resistance of cerium conversion films on the AZ31 magnesium alloy and its relation to the salt anion. Appl Surf Sci 2008;254:1806–14.
[207] Saniger JM, Cota L. An auger electron spectroscopy study of the fluorination of Al-7075 alloy. Corros Sci 1990;30:107–12.
[208] Arnott DR, Ryan NE, Hinton BRW, Sexton BA, Hughes AE. Auger and XPS studies of cerium corrosion inhibition on 7075 aluminum alloy. Appl Surf Sci 1985;22–23:236–51.
[209] Hughes AE, Gorman JD, Paterson PKJ. The characterisation of Ce-Mo-based conversion coatings on Al-alloys: part I. Corros Sci 1996;38:1957–76.
[210] Zheng YF, Gu XN, Witte F. Biodegradable metals. Mater Sci Eng, R 2014;77:1–34.
[211] Mahoney CM. Cluster secondary ion mass spectrometry: principles and applications. Wiley; 2013.
[212] Fearn S. An Introduction to time-of-flight secondary ion mass spectrometry (ToF-SIMS) and its application to materials science. Morgan & Claypool; 2015.
[213] Brady MP, Fayek M, Meyer III HM, Leonard DN, Elsentriecy HH, Unocic KA, et al. Tracer study of oxygen and hydrogen uptake by magnesium alloys in air with water vapor. Scripta Mater 2015;106:38–41.
[214] Seyeux A, Frankel GS, Missert N, Unocic KA, Klein LH, Galtayries A, et al. ToF-SIMS imaging study of the early stages of corrosion in Al-Cu thin films. J Electrochem Soc 2011;158:C165–71.
[215] Chang CC, Wang CC, Wu CH, Liu SC, Mai FD. ToF-SIMS and EIS to evaluate green pretreatment reagent: corrosion protection of aluminum alloy by silica/zirconium/cerium hybrid coating. Appl Surf Sci 2008;255:1531–3.
[216] Seyeux A, Liu M, Schmutz P, Song GL, Atrens A, Marcus P. ToF-SIMS depth profile of the surface film on pure magnesium formed by immersion in pure water and the identification of magnesium hydride. Corros Sci 2009;51:1883–6.
[217] Griffiths R, Haseth JD. Fourier Transform Infrared Spectrometry. Wiley; 2007.
[218] Gaffney Jeffrey S, Marley Nancy A, Jones Darin E. Fourier transform infrared (FTIR) spectroscopy. John Wiley & Sons; 2003.
[219] Blücher DB, Svensson JE, Johansson LG. Influence of ppb levels of $SO_2$ on the atmospheric corrosion of aluminum in the presence of NaCl. J Electrochem Soc 2005;152:B397–404.
[220] Ferraro JR, Nakamoto K, Brown CW. Introductory Raman spectroscopy. Elsevier; 2003.
[221] Kouisni L, Azzi M, Zertoubi M, Dalard F, Maximovitch S. Phosphate coatings on magnesium alloy AM60 part 1: study of the formation and the growth of zinc phosphate films. Surf Coat Technol 2004;185:58–67.
[222] Zhang J, Dai C, Wei J, Wen Z, Zhang S, Chen C. Degradable behavior and bioactivity of micro-arc oxidized AZ91D magnesium alloy with calcium phosphate/chitosan composite coating in m-SBF. Colloids Surf., B 2013;111:179–87.
[223] Zuleta AA, Correa E, Villada C, Sepúlveda M, Castaño JG, Echeverría F. Comparative study of different environmentally friendly (Chromium-free) methods for surface modification of pure magnesium. Surf Coat Technol 2011;205:5254–9.

[224] Samaniego A, Hurley BL, Frankel GS. On the evidence for univalent Mg. J Electroanal Chem 2015;737:123–8.
[225] Fritz JS, Gjerde DT. Ion chromatography. Wiley; 2009.
[226] Nash BK, Kelly RG. Application of ion chromatography to corrosion studies. J Chromatogr A 1992;602:135–40.
[227] Jönsson M, Persson D, Thierry D. Corrosion product formation during NaCl induced atmospheric corrosion of magnesium alloy AZ91D. Corros Sci 2007;49:1540–58.
[228] Stokes D. Principles and practice of variable pressure: environmental scanning electron microscopy (VP-ESEM). Wiley; 2011.
[229] Mortazavi N, Intiso L, Israelsson N, Johansson LG, Halvarsson M. In situ investigation of the initial stages of KCl-induced corrosion of a chromia-forming steel at 450 °C using an environmental scanning electron microscope. Corrosion 2016;72:23–32.
[230] Mortazavi N, Intiso L, Israelsson N, Johansson LG, Halvarsson M. In situ ESEM investigation of KCl-induced corrosion of a FeCrAl and a model FeNiCrAl alloy in lab air at 450 °C. J Electrochem Soc 2015;162:C744–53.
[231] Chen J, Wang JQ, Han EH, Ke W. Effect of temperature on initial corrosion of AZ91 magnesium alloy under cyclic wet-dry conditions. Corros Eng Sci Technol 2011;46:267–77.
[232] Turnbull A. Corrosion pitting and environmentally assisted small crack growth. Proc Math Phys Eng Sci 2014;470(2169):20140254.
[233] Burnett TL, McDonald SA, Gholinia A, Geurts R, Janus M, Slater T, et al. Correlative tomography. Sci Rep 2014;4:4711.
[234] Connolly BJ, Horner DA, Fox SJ, Davenport AJ, Padovani C, Zhou S, et al. X-ray microtomography studies of localised corrosion and transitions to stress corrosion cracking. Mater Sci Technol 2006;22:1076–85.
[235] Davenport AJ, Padovani C, Connolly BJ, Stevens NP, Beale TA, Groso A, et al. Synchrotron X-ray microtomography study of the role of Y in corrosion of magnesium alloy WE43. Electrochem Solid State Lett 2007;10:C5–8.
[236] Hörnqvist M, Mortazavi N, Halvarsson M, Ruggiero A, Iannitti G, Bonora N. Deformation and texture evolution of OFHC copper during dynamic tensile extrusion. Acta Mater 2015;89:163–80.
[237] Chyrkin A, Mortazavi N, Halvarsson M, Grüner D, Quadakkers WJ. Effect of thermal cycling on protective properties of alumina scale grown on thin Haynes 214 foil. Corros Sci 2015;98:688–98.
[238] Lozano-Perez S, Kilburn MR, Yamad T, Terachi T, English CA, Grovenor CRN. High-resolution imaging of complex crack chemistry in reactor steels by NanoSIMS. J Nucl Mater 2008;374:61–8.
[239] Thomas LE, Bruemmer SM. High-resolution characterization of intergranular attack and stress corrosion cracking of alloy 600 in high-temperature primary water. Corrosion 2000;56:572–87.
[240] Nastasi M, Mayer JW, Wang Y. Ion beam analysis: fundamentals and applications. CRC Press; 2014.
[241] Mandò PA. PIXE (particle-induced X-ray emission). Wiley; 2006.
[242] Cabrera N, Mott NF. Theory of the oxidation of metals. Rep Progr Phys 1948;12:163–84.
[243] Do T, Splinter SJ, Chen C, McIntyre NS. The oxidation kinetics of magnesium and Al surfaces studied by AES and XPS. Surf Sci 1997;387:192–8.
[244] Mathaudhu SN, Luo AA, Neelameggham NR, Nyberg EA, Sillekens WH. Essential readings in magnesium technology. Wiley; 2014.
[245] Xu CH, Gao W. Pilling-Bedworth ratio for oxidation of alloys. Mater Res Innov 2000;3:231–5.
[246] Splinter SJ, Mcintyre NS. The initial interaction of water-vapor with Mg-Al alloy surfaces at room-temperature. Surf Sci 1994;314:157–71.
[247] Wlodarczyk R, Sierka M, Kwapien K, Sauer J, Carrasco E, Aumer A, et al. Structures of the ordered water monolayer on MgO(001). J Phys Chem C 2011;115:6764–74.
[248] Ončák M, Włodarczyk R, Sauer J. Water on the MgO(0 0 1) surface: surface reconstruction and ion solvation. J Phys Chem Lett 2015;6:2310–4.
[249] Ončák M, Włodarczyk R, Sauer J. Hydration structures of MgO, CaO, and SrO(0 0 1) surfaces. J Phys Chem C 2016;120:24762–9.
[250] Refson K, Wogelius RA, Fraser DG, Payne MC, Lee HM, Milman V. Water chemisorption and reconstruction of the MgO surface. Phys Rev B 1995;52:10823–6.
[251] Martell AE, Smith RM. Critical stability constants. New York; London: Plenum Press; 1974.
[252] Cain T, Bland LG, Birbilis N, Scully JR. A compilation of corrosion potentials for magnesium alloys. Corrosion 2014;70:1043–51.
[253] Atrens A, Dietzel W. The negative difference effect and unipositive Mg. Adv Eng Mater 2007;9:292–7.
[254] Turrentine JW. Reversed electrolysis. J Phys Chem 1907;12:448–67.
[255] Song GL, Atrens A. Corrosion mechanisms of magnesium alloys. Adv Eng Mater 1999;1:11–33.
[256] Song GL, Atrens A. Recent insights into the mechanism of magnesium corrosion and research suggestions. Adv Eng Mater 2007;9:177–83.
[257] Atrens A, Liu M, Zainal Abidin NI. Corrosion mechanism applicable to biodegradable magnesium implants. Mater Sci Eng B: Solid-State Mater Adv Technol 2011;176:1609–36.
[258] Shi Z, Jia JX, Atrens A. Galvanostatic anodic polarisation curves and galvanic corrosion of high purity magnesium in 3.5% NaCl saturated with Mg $(OH)_2$. Corros Sci 2012;60:296–308.
[259] Song GL, Atrens A. Understanding magnesium corrosion-a framework for improved alloy performance. Adv Eng Mater 2003;5:837–58.
[260] Shi Z, Cao F, Song GL, Atrens A. Low apparent valence of magnesium during corrosion. Corros Sci 2014;88:434–43.
[261] Kirkland NT, Williams G, Birbilis N. Observations of the galvanostatic dissolution of pure Mg. Corros Sci 2012;65:5–9.
[262] Bender S, Goellner J, Heyn A, Schmigalla S. A new theory for the negative difference effect in magnesium corrosion. Mater Corros 2013;63:707–12.
[263] Rossrucker L, Samaniego A, Grote J-P, Mingers AM, Laska CA, Birbilis N, et al. The pH dependence of magnesium dissolution and hydrogen evolution during anodic polarization. J Electrochem Soc 2015;162:C333–9.
[264] Rossrucker L, Mayrhofer KJJ, Frankel GS, Birbilis N. Investigating the real time dissolution of magnesium using online analysis by ICP-MS. J Electrochem Soc 2014;161:C115–9.
[265] Lebouil S, Gharbi O, Volovitch P, Ogle K. Mg dissolution in phosphate and chloride electrolytes: insight into the mechanism of the negative difference effect. Corrosion 2015;71:234–41.
[266] Williams G, Birbilis N, McMurray HN. Controlling factors in localised corrosion morphologies observed for magnesium immersed in chloride containing electrolyte. Faraday Discuss 2015;180:313–30.
[267] Lysne D, Thomas S, Hurley MF, Birbilis N. On the Fe enrichment during anodic polarization of magnesium and its impact on hydrogen evolution. J Electrochem Soc 2015;162:C396–402.
[268] Fajardo S, Glover CF, Williams G, Frankel GS. The evolution of anodic hydrogen on high purity magnesium in acidic buffer solution. Corrosion 2017;73:482–93.
[269] Hoche D, Blawert C, Lamaka SV, Scharnagl N, Mendis C, Zheludkevich ML. The effect of iron re-deposition on the corrosion of impurity-containing magnesium. Phys Chem Chem Phys 2016;18:1279–91.
[270] Buchheit RG, Grant RP, Hlava PF, Mckenzie B, Zender GL. Local Dissolution Phenomena Associated with S Phase (Al2CuMg) Particles in Aluminum Alloy 2024–T3. J Electrochem Soc 1997;144:2621–8.
[271] Lamaka SV, Höche D, Petrauskas RP, Blawert C, Zheludkevich ML. A new concept for corrosion inhibition of magnesium: suppression of iron re-deposition. Electrochem Comm 2016;62:5–8.
[272] Yuwono JA, Birbilis N, Williams KS, Medhekar NV. Electrochemical stability of magnesium surfaces in an aqueous environment. J Phys Chem C 2016;120:26922–33.
[273] Williams KS, Labukas JP, Rodriguez-Santiago V, Andzelm JW. First principles modeling of water dissociation on Mg(0 0 0 1) and development of a magnesium surface pourbaix diagram. Corrosion 2015;71:209–23.
[274] Bockris JOM, Reddy AKN. Modern electrochemistry. New York: Kluwer Academic/Plenum Publishing; 2000.
[275] Frankel GS, Fajardo S, Lynch BM. Introductory lecture on corrosion chemistry: a focus on anodic hydrogen evolution on Al and Mg. Faraday Discuss 2015;180:11–33.

[276] Taylor CD. A first-principles surface reaction kinetic model for hydrogen evolution under cathodic and anodic conditions on Mg. J Electrochem Soc 2016;163. C602-C8.
[277] Hanawalt JD, Nelson CE, Peloubet JA. Corrosion studies of magnesium and its alloys. Trans AIME 1942;147:273–99.
[278] Samaniego A, Gusieva K, Llorente I, Feliu Jr S, Birbilis N. Exploring the possibility of protective surface oxides upon Mg alloy AZ31 via lutetium additions. Corros Sci 2014;89:101–10.
[279] Ghali E, Winston Revie R. Corrosion resistance of aluminum and magnesium alloys: understanding, performance, and testing. Wiley 2010.
[280] Okamoto H. Phase diagram for binary alloys. Materials Park (OH): ASM International; 2000.
[281] Massalski TB. Binary phase diagrams. Materials Park (OH): ASM International; 1990.
[282] Nayeb-Hashemi AA, Clark JB, Pelton AD. The Li-Mg (Lithium-Mg) system. Bull Alloy Phase Diagram 1985;5:365–74.
[283] Makar GL, Kruger J. Corrosion of Mg. Inter Mater Rev 1993;38:138–53.
[284] Liu M, Schmutz P, Uggowitzer PJ, Song G, Atrens A. The influence of yttrium (Y) on the corrosion of Mg–Y binary alloys. Corros Sci 2010;52:3687–701.
[285] Sudholz AD, Gusieva K, Chen XB, Muddle BC, Gibson MA, Birbilis N. Electrochemical behaviour and corrosion of Mg–Y alloys. Corros Sci 2011;53:2277–82.
[286] Liu M, Uggowitzer PJ, Schmutz P, Atrens A. Calculated phase diagrams, iron tolerance limits, and corrosion of Mg-Al alloys. JOM 2008;60:39–44.
[287] Gandel DS, Easton MA, Gibson MA, Birbilis N. CALPHAD simulation of the Mg–(Mn, Zr)–Fe system and experimental comparison with as-cast alloy microstructures as relevant to impurity driven corrosion of Mg-alloys. Mater Chem Phys 2014;143:1082–91.
[288] Simanjuntak S, Cavanaugh MK, Gandel DS, Easton MA, Gibson MA, Birbilis N. The influence of iron, manganese, and zirconium on the corrosion of magnesium: an artificial neural network approach. Corrosion 2015;71:199–208.
[289] Shaw BA. Corrosion resistance of magnesium alloys. ASM Int 2003;13A:692–6.
[290] Hillis JE, Reichek KN. Paper 870288. Society of Automotive Engineers; 1986.
[291] Xia X, Nie JF, Davies CHJ, Tang WN, Xu SW, Birbilis N. The influence of low levels of Zn, Ca, Gd, Sr and Zr on the corrosion of magnesium for wrought applications. Corrosion 2015;71:1370–86.
[292] Lunder O, Lein JE, Aune TK, Nisancioglu K. The role of $Mg_{17}Al_{12}$ phase in the corrosion of Mg alloy AZ91. Corrosion 1989;45:741–8.
[293] Williams G, Gusieva K, Birbilis N. Localized corrosion of binary Mg-Nd alloys in chloride-containing electrolyte using a scanning vibrating electrode technique. Corrosion 2012;68:489–98.
[294] Birbilis N, Williams G, Gusieva K, Samaniego A, Gibson MA, McMurray HN. Poisoning the corrosion of magnesium. Electrochem Commun 2013;34:295–8.
[295] Liu RL, Hurley MF, Kvryan A, Williams G, Scully JR, Birbilis N. Controlling the corrosion and cathodic activation of magnesium via microalloying additions of Ge. Sci Rep 2016;6.
[296] Kirkland NT, Birbilis N, Walker J, Woodfield T, Dias GJ, Staiger MP. In-vitro dissolution of magnesium–calcium binary alloys: clarifying the unique role of calcium additions in bioresorbable magnesium implant alloys. J Biomed Mater Res B: Appl Biomater 2010;95B:91–100.
[297] Gandel DS, Easton MA, Gibson MA, Birbilis N. Influence of Mn and Zr on the corrosion of Al-free Mg alloys: part 2—impact of Mn and Zr on Mg alloy electrochemistry and corrosion. Corrosion 2013;69:744–51.
[298] Zhang YN, Kevorkov D, Bridier F, Medraj M. Experimental study of the Ca–Mg–Zn system using diffusion couples and key alloys. Sci Technol Adv Mater 2011;12:025003.
[299] Gu X, Shiflet GJ, Guo FQ, Poon SJ. Mg–Ca–Zn bulk metallic glasses with high strength and significant ductility. J Mater Res 2005;20:1935–8.
[300] Zberg B, Uggowitzer PJ, Loffler JF. MgZnCa glasses without clinically observable hydrogen evolution for biodegradable implants. Nat Mater 2009;8:887–91.
[301] Laws KJ, Saxey DW, McKenzie WR, Marceau RKW, Gun B, Ringer SP, et al. Analysis of dynamic segregation and crystallisation in Mg65Cu25Y10 bulk metallic glass using atom probe tomography. Mater Sci Eng, A 2012;556:558–66.
[302] Ma H, Zheng Q, Xu J, Li Y, Ma E. Doubling the critical size for bulk metallic glass formation in the Mg–Cu–Y ternary system. J Mater Res 2005;20:2252–5.
[303] Zhou X, Ralston KD, Laws KJ, Cao JD, Gupta RK, Ferry M, et al. Effect of the degree of crystallinity on the electrochemical behavior of $Mg_{65}Cu_{25}Y_{10}$ and $Mg_{70}Zn_{25}Ca_5$ bulk metallic glasses. Corrosion 2013;69:781–92.
[304] Südholz AD, Kirkland NT, Buchheit RG, Birbilis N. Electrochemical properties of intermetallic phases and common impurity elements in magnesium alloys. Electrochem Solid St 2011;14:C5–7.
[305] Kirkland NT, Lespagnol J, Birbilis N, Staiger MP. A survey of bio-corrosion rates of magnesium alloys. Corros Sci 2010;52:287–91.
[306] Xia X, Davies CHJ, Nie JF, Birbilis N. Influence of composition and processing on the corrosion of magnesium alloys containing binary and ternary additions of zinc and strontium. Corrosion 2014;71:38–49.
[307] Gandel DS, Easton MA, Gibson MA, Abbott T, Birbilis N. The influence of zirconium additions on the corrosion of magnesium. Corros Sci 2014;81:27–35.
[308] Hou L, Raveggi M, Chen X-B, Xu W, Laws KJ, Wei Y, et al. Investigating the passivity and dissolution of a corrosion resistant Mg-33at.%Li alloy in aqueous chloride using online ICP-MS. J Electrochem Soc 2016;163. C324-C9.
[309] Williams G, Dafydd HA-L, McMurray HN, Birbilis N. The influence of arsenic alloying on the localised corrosion behaviour of magnesium. Electrochim Acta 2016;219:401–11.
[310] Ralston KD, Williams G, Birbilis N. Effect of pH on the grain size dependence of magnesium corrosion. Corrosion 2012;68:507–17.
[311] Hihara LH, Latanision RM. Corrosion of metal matrix composites. Int Mater Rev 1994;39:245–64.
[312] Dieringa H, Hort N, Kainer KU. Magnesium based MMCs reinforced with C-fibers. Adv Techn Mater Process 2004;6:136–41.
[313] Turnbull A. Review of corrosion studies on aluminium metal matrix composites. Br Corros J 1992;27:27–35.
[314] Trzaskoma PP. Corrosion behavior of a graphite fiber/magnesium metal matrix composite in aqueous chloride solution. Corrosion 1986;42:609–13.
[315] Hall IW. Corrosion of carbon/magnesium metal matrix composites. Scripta Metall 1987;21:1717–21.
[316] Hihara LH, Kondepudi PK. The galvanic corrosion of SiC monofilament/ZE41 Mg metal-matrix composite in 0.5 M $NaNO_3$. Corros Sci 1993;34:1761–72.
[317] Gupta M, Sharon NML. Magnesium, magnesium alloys, and magnesium composities. John Wiley and Sons; 2011.
[318] Ye HZ, Liu XY. Review of recent studies in magnesium matrix composites. J Mater Sci 2004;39:6153–71.
[319] Gupta M, Wong WLE. Mg-based nanocomposites: lightweight materials of the future. Mater Charact 2015;105:30–4.
[320] Razavi M, Fathi MH, Meratian M. Fabrication and characterization of magnesium–fluorapatite nanocomposite for biomedical applications. Mater Charact 2010;61:1363–70.
[321] Gupta RK, Sukiman NL, Fleming KM, Gibson MA, Birbilis N. Electrochemical behavior and localized corrosion associated with $Mg_2Si$ Particles in Al and Mg alloys. ECS Electrochem Lett 2012;1:C1–3.
[322] Esmaily M, Mortazavi N, Svensson JE, Halvarsson M, Jarfors AEW, Wessén M, et al. On the microstructure and corrosion behavior of AZ91/SiC composites produced by rheocasting. Mater Chem Phys 2016;180:29–37.
[323] Chawla N, Cha KK. Metal matrix composites. Springer; 2006.
[324] Huang Y, Liu D, Anguilano L, You C, Chen M. Fabrication and characterization of a biodegradable Mg–2Zn–0.5Ca/1β-TCP composite. Mater Sci Eng C 2015;54:120–32.
[325] Wu YH, Li N, Cheng Y, Zheng YF, Han Y. In vitro study on biodegradable AZ31 magnesium alloy fibers reinforced PLGA composite. J Mater Sci Technol 2013;29:545–50.
[326] Khalajabadi SZ, Abdul Kadir MR, Izman S, Ebrahimi-Kahrizsangi R. Fabrication, bio-corrosion behavior and mechanical properties of a Mg/HA/MgO nanocomposite for biomedical applications. Mater Des 2015;88:1223–33.

[327] Clyne T, Withers P. An introduction to metal matrix composites, Cambridge solid state science series; 1993.
[328] Voyiadjis G. Advances in damage mechanics: metals and metal matrix composites. Elsevier; 1999.
[329] Davim JP. Metal matrix composites. Nova Science Publishers; 2012.
[330] Kainer KU. Basics of metal matrix composites. Custom-made materials for automotive and aerospace engineering. Wiley-VCH Verlag GmbH & Co; 2006.
[331] Mazumdar KS. Composites manufacturing. RC Press; 2010.
[332] Hort N, Dieringa H, Kumar ST, Kainer KU. Magnesium matrix composites. In: Friedrich HE, Mordike BL, editors. Magnesium technology metallurgy, design data, applications. Berlin (Heidelberg): Springer-Verlag; 2006.
[333] Schiffl A, Easton M. Influence of SiC particles on the grain refinement of an Mg-Al alloy. Mater Sci Forum 2009;618–619:445–8.
[334] Feldhoff A, Pippel E, Woltersdorf J. Carbon-fibre reinforced magnesium alloys: nanostructure and chemistry of interlayers and their effect on mechanical properties. J Micros 1999;196:185–93.
[335] Flower HM, Morris AJ. Magnox oxidation in carbon dioxide. In: Baker C, editor. Magnesium technology. London (UK): The Institute of Metals; 1987. p. 128–32.
[336] Viala JC, Claveyrolas G, Bosselet F, Bouix J. The chemical behaviour of carbon fibres in magnesium base Mg-Al alloys. J Mater Sci 2000;35:1813–25.
[337] Mingo B, Arrabal R, Mohedano M, Pardo A, Matykina E. Corrosion and wear of PEO coated AZ91/SiC composites. Surf Coat Technol 2017;309:1023–32.
[338] Hihara LH, Kondepudi PK. Galvanic corrosion between SiC monofilament and magnesium in NaCl, $Na_2SO_4$ and $NaNO_3$ solutions for application to metal-matrix composites. Corros Sci 1994;36:1585–95.
[339] Nunez-Lopez CA, Skeldon P, Thompson GE, Lyon P, Karimzadeh H, Wilks TE. The corrosion behaviour of magnesium alloy ZC71/SiCp metal matrix composite. Corros Sci 1995;37:689–708.
[340] Nunez-Lopez CA, Habazaki H, Skeldon P, Thompson GE, Karimzadeh H, Lyon P, et al. An investigation of microgalvanic corrosion using a model magnesium-silicon carbide metal matrix composite. Corros Sci 1996;38:1721–9.
[341] Chan WM, Cheng FT, Leung LK, Horylev RJ, Yue TM. Corrosion behaviour of magnesium alloy AZ91 and its MMC in NaCl solution. Corros Rev 1998;16:43–52.
[342] Yue TM, Wang AH, Man HC. Improvement in the corrosion resistance of magnesium ZK60/SiC composite by excimer laser surface treatment. Scripta Mater 1998;38:191–8.
[343] Yue TM, Wang AH, Man HC. Corrosion resistance enhancement of magnesium ZK60/SiC composite by Nd:YAG laser cladding. Scripta Mater 1999;40:303–11.
[344] Yue TM, Hu QW, Mei Z, Man HC. Laser cladding of stainless steel on magnesium ZK60/SiC composite. Mater Lett 2001;47:165–70.
[345] Wang AH, Yue TM. YAG laser cladding of an Al-Si alloy onto an Mg/SiC composite for the improvement of corrosion resistance. Compos Sci Technol 2001;61:1549–54.
[346] Mei Z, Guo LF, Yue TM. The effect of laser cladding on the corrosion resistance of magnesium ZK60/SiC composite. J Mater Process Technol 2005;161:462–6.
[347] Zucchi F, Trabanelli G, Grassi V, Frignani A. Corrosion behavior in sodium sulfate and sodium chloride solutions of SiCp reinforced magnesium alloy metal matrix composites. Corrosion 2004;60:362–8.
[348] Suqiu J, Shusheng J, Guangping S, Jun Y. The corrosion behaviour of magnesium alloy AZ91D/TiCp metal matrix composite. Mater Sci Forum 2005;488–489:705–8.
[349] Wang YQ, Zheng MY, Wu K. Microarc oxidation coating formed on SiCw/AZ91 magnesium matrix composite and its corrosion resistance. Mater Lett 2005;59:1727–31.
[350] Tiwari S, Balasubramaniam R, Gupta M. Corrosion behavior of SiC reinforced magnesium composites. Corros Sci 2007;49:711–25.
[351] Bakkar A, Neubert V. Corrosion characterisation of alumina-Mg metal matrix composites. Corros Sci 2007;49:1110–30.
[352] Endo M, Hayashi T, Itoh I, Kim YA, Shimamoto D, Muramatsu H, et al. An anticorrosive magnesium/carbon nanotube composite. Appl Phys Lett 2008;92.
[353] Budruk Abhijeet S, Balasubramaniam R, Gupta M. Corrosion behaviour of Mg–Cu and Mg–Mo composites in 3.5% NaCl. Corros Sci 2008;50:2423–8.
[354] Bakkar A, Neubert V. Corrosion behaviour of carbon fibres/Mg metal matrix composite and electrochemical response of its constituents. Electrochim Acta 2009;54:1597–606.
[355] Xue W, Jin Q, Zhu Q, Hua M, Ma Y. Anti-corrosion microarc oxidation coatings on SiCP/AZ31 magnesium matrix composite. J Alloys Compd 2009;482:208–12.
[356] Arrabal R, Matykina E, Skeldon P, Thompson GE. Coating formation by plasma electrolytic oxidation on ZC71/SiC/12p-T6 magnesium metal matrix composite. Appl Surf Sci 2009;255:5071–8.
[357] Pardo A, Merino S, Merino MC, Barroso I, Mohedano M, Arrabal R, et al. Corrosion behaviour of silicon–carbide-particle reinforced AZ92 magnesium alloy. Corros Sci 2009;51:841–9.
[358] Aung NN, Zhou W, Goh CS, Nai SML, Wei J. Effect of carbon nanotubes on corrosion of Mg–CNT composites. Corros Sci 2010;52:1551–3.
[359] Fukuda H, Szpunar JA, Kondoh K, Chromik R. The influence of carbon nanotubes on the corrosion behaviour of AZ31B magnesium alloy. Corros Sci 2010;52:3917–23.
[360] Falcon LA, Bedolla BE, Lemus J, Leon C, Rosales I, Gonzalez-Rodriguez JG. Corrosion behavior of Mg-Al/TiC composites in NaCl solution. Int J Corros 2011;2011:7.
[361] Turhan MC, Li Q, Jha H, Singer RF, Virtanen S. Corrosion behaviour of multiwall carbon nanotube/Mg composites in 3.5% NaCl. Electrochim Acta 2011;56:7141–8.
[362] Hamid ZA, El-khair MTA, Hassan HB. Synthesis and protection of AM50 magnesium alloy and its composites using environmentally pretreatment electrolyte. Surf Coat Technol 2011;206:1041–50.
[363] Li Q, Turhan MC, Rottmair CA, Singer RF, Virtanen S. Influence of MWCNT dispersion on corrosion behaviour of their magnesium composites. Mater Corros 2012;63:384–7.
[364] Funatsu K, Fukuda H, Takei R, Umeda J, Kondoh K. Quantitative evaluation of initial galvanic corrosion behavior of CNTs reinforced Mg–Al alloy. Adv Powder Technol 2013;24:833–7.
[365] Zhang X, Niu X, Hu H. Effect of fiber volume fractions on corrosion resistance of magnesium AM60 alloy-based composites in NaCl solutions. In: Magnes Technol 2013. John Wiley & Sons, Inc.; 2013. p. 293–7.
[366] Mindivan H, Efe A, Kosatepe AH, Kayali ES. Fabrication and characterization of carbon nanotube reinforced magnesium matrix composites. Appl Surf Sci 2014;318:234–43.
[367] Gobara M, Shamekh M, Akid R. Improving the corrosion resistance of AZ91D magnesium alloy through reinforcement with titanium carbides and borides. J Magnes Alloys 2015;3:112–20.
[368] Zhang C, Zhang T, Wang Y, Wei F, Shao Y, Meng G, et al. Effect of SiC particulates on the corrosion behavior of extruded AZ91/SiCp composites during the early stage of exposure. J Electrochem Soc 2015;162:C754–66.
[369] Mondal AK, Blawert C, Kumar S. Corrosion behaviour of creep-resistant AE42 magnesium alloy-based hybrid composites developed for powertrain applications. Mater Corros 2015;66:1150–8.
[370] Kamieniak K, Malik MA. The influence of reinforcement purity on corrosion resistance of AM50/SiC composites. Solid State Phenom 2015;227:43–6.
[371] Hihara LH, Latansion RM. Localized corrosion induced in graphite/aluminum metal-matrix composites by residual microstructural chloride. Corrosion 1991;47:335–40.
[372] Hihara LH. Corrosion of metal matrix composites A2 - Cottis, Bob. In: Graham M, Lindsay R, Lyon S, Richardson T, Scantlebury D, Stott H, editors. Shreir's corrosion. Oxford: Elsevier; 2010. p. 2250–69.

[373] Huang Y, Kainer KU, Hort N. Mechanism of grain refinement of Mg–Al alloys by SiC inoculation. Scripta Mater 2011;64:793–6.
[374] Arrabal R, Pardo A, Merino MC, Mohedano M, Casajús P, Matykina E, et al. Corrosion behaviour of a magnesium matrix composite with a silicate plasma electrolytic oxidation coating. Corros Sci 2010;52:3738–49.
[375] Heublein B, Rohde R, Kaese V, Niemeyer M, Hartung W, Haverich A. Biocorrosion of magnesium alloys: A new principle in cardiovascular implant technology? Heart 2003;89:651–6.
[376] Staiger MP, Pietak AM, Huadmai J, Dias G. Magnesium and its alloys as orthopedic biomaterials: A review. Biomaterials 2006;27:1728–34.
[377] Williams D. New interests in Mg. Med Device Technol 2006;17:9–10.
[378] Shaw BA, Sikora E, Virtanen S. Fix, heal, and disappear: a new approach to using metals in the human body. Electrochem Soc Interf 2008;17:45–9.
[379] Witte F, Hort N, Vogt C, Cohen S, Kainer KU, Willumeit R, et al. Degradable biomaterials based on magnesium corrosion. Curr Opin Solid St Mater Sci 2008;12:63–72.
[380] Virtanen S. Biodegradable Mg and Mg alloys: corrosion and biocompatibility. Mater Sci Eng B 2011;176:1600–8.
[381] Walker J, Shadanbaz S, Woodfield TBF, Staiger MP, Dias GJ. Magnesium biomaterials for orthopedic application: a review from a biological perspective. J Biomed Mater Res B 2014;102:1316–31.
[382] Witte F. The history of biodegradable magnesium implants: a review. Acta Biomater 2010;6:1680–92.
[383] Zheng YF, Gu XN, Witte F. Biodegradable metals. Mater Sci Eng R 2014;77:1–34.
[384] Navarro M, Michiardi A, Castano O, Planell JA. Biomaterials in orthopaedics. J R Soc Interface 2008;5:1137–58.
[385] Cecchinato F, Agha NA, Martinez-Sanchez AH, Luthringer BJC, Feyerabend F, Jimbo R, et al. Influence of magnesium alloy degradation on undifferentiated human cells. PloS one 2015;10(11):e0142117.
[386] Gu XN, Zheng YF, Chen LJ. Influence of artificial biological fluid composition on the biocorrosion of potential orthopedic Mg–Ca, AZ31, AZ91 alloys. Biomed Mater 2009;4:065011.
[387] Xin Y, Chu PK. Influence of Tris in simulated body fluid on degradation behavior of pure Mg. Mater Chem Phys 2010;124:33–5.
[388] Xin Y, Hu T, Chu PK. Influence of test solutions on in vitro studies of biomedical magnesium alloys. J Electrochem Soc 2010;157. C238-C43.
[389] Seuss F, Seuss S, Turhan MC, Fabry B, Virtanen S. Corrosion of magnesium alloy AZ91D in the presence of living cells. J Biomed Mater Res B 2011;99 B:276–81.
[390] Virtanen S, Milošev I, Gomez-Barrena E, Trebše R, Salo J, Konttinen YT. Special modes of corrosion under physiological and simulated physiological conditions. Acta Biomater 2008;4:468–76.
[391] Agha NA, Feyerabend F, Mihailova B, Heidrich S, Bismayer U, Willumeit-Römer R. Magnesium degradation influenced by buffering salts in concentrations typical of in vitro and in vivo models. Mater Sci Eng C 2016;58:817–25.
[392] Walker J, Shadanbaz S, Kirkland NT, Stace E, Woodfield T, Staiger MP, et al. Magnesium alloys: Predicting in vivo corrosion with in vitro immersion testing. J Biomed Mater Res B 2012;100 B:1134–41.
[393] Kirkland NT, Waterman J, Birbilis N, Dias G, Woodfield TBF, Hartshorn RM, et al. Buffer-regulated biocorrosion of pure magnesium. J Mater Sci Mater Med 2012;23:283–91.
[394] Wagener V, Virtanen S. Protective layer formation on magnesium in cell culture medium. Mater Sci Eng C 2016;63:341–51.
[395] Yamamoto A, Hiromoto S. Effect of inorganic salts, amino acids and proteins on the degradation of pure magnesium in vitro. Mater Sci Eng C 2009;29:1559–68.
[396] Zeng R-C, Li X-T, Li S-Q, Zhang F, Han E-H. In vitro degradation of pure magnesium in response to glucose. Sci Rep 2015;5:13026.
[397] Wagener V, Faltz AS, Killian MS, Schmuki P, Virtanen S. Protein interactions with corroding metal surfaces: Comparison of Mg and Fe. Faraday Discuss 2015;180:347–60.
[398] Wang J, Giridharan V, Shanov V, Xu Z, Collins B, White L, et al. Flow-induced corrosion behavior of absorbable Mg-based stents. Acta Biomater 2014;10:5213–23.
[399] Silva-Bermudez P, Rodil SE. An overview of protein adsorption on metal oxide coatings for biomedical implants. Surf Coat Tech 2013;233:147–58.
[400] Hedberg Y, Wang X, Hedberg J, Lundin M, Blomberg E, Odnevall Wallinder I. Surface-protein interactions on different stainless steel grades: effects of protein adsorption, surface changes and metal release. J Mater Sci Mater Med 2013;24:1015–33.
[401] Hedberg Y, Karlsson M-E, Blomberg E, Odnevall Wallinder I, Hedberg J. Correlation between surface physicochemical properties and the release of iron from stainless steel AISI 304 in biological media. Colloid Surface B 2014;122:216–22.
[402] Lorenz C, Brunner JG, Kollmannsberger P, Jaafar L, Fabry B, Virtanen S. Effect of surface pre-treatments on biocompatibility of Mg. Acta Biomater 2009;5:2783–9.
[403] Keim S, Brunner JG, Fabry B, Virtanen S. Control of magnesium corrosion and biocompatibility with biomimetic coatings. J Biomed Mater Res B 2011;96 B:84–90.
[404] Wagener V, Schilling A, Mainka A, Hennig D, Gerum R, Kelch ML, et al. Cell adhesion on surface-functionalized magnesium. ACS Appl Mater Inter 2016;8:11998–2006.
[405] Brooks EK, Tobias ME, Yang S, Bone LB, Ehrensberger MT. Influence of MC3T3-E1 preosteoblast culture on the corrosion of a T6-treated AZ91 alloy. J Biomed Mater Res B 2016;104:253–62.
[406] Hiromoto S, Hanawa T. PH near cells on stainless steel and titanium. Electrochem Solid St 2004;7:B9–B11.
[407] Ahmad NA, Willumeit-Römer R, Laipple D, Luthringer B, Feyerabend F. The degradation interface of magnesium based alloys in direct contact with human primary osteoblast cells. Plos ONE 2016;11:e0157874.
[408] Zhang J, Hiromoto S, Yamazaki T, Niu J, Huang H, Jia G, et al. Effect of macrophages on in vitro corrosion behavior of magnesium alloy. J Biomed Mater Res A 2016;104:2476–87.
[409] Sanchez AHM, Luthringer BJC, Feyerabend F, Willumeit R. Mg and Mg alloys: how comparable are in vitro and in vivo corrosion rates? A review. Acta Biomater 2015;13:16–31.
[410] Hiromoto S, Inoue M, Taguchi T, Yamane M, Ohtsu N. In vitro and in vivo biocompatibility and corrosion behaviour of a bioabsorbable magnesium alloy coated with octacalcium phosphate and hydroxyapatite. Acta Biomater 2015;11:520–30.
[411] Zhao N, Zhu D. Endothelial responses of magnesium and other alloying elements in Mg-based stent materials. Metallomics 2015;7:118–28.
[412] Luthringer BJC, Willumeit-Römer R. Effects of magnesium degradation products on mesenchymal stem cell fate and osteoblastogenesis. Gene 2016;575:9–20.
[413] Feyerabend F, Fischer J, Holtz J, Witte F, Willumeit R, Drücker H, et al. Evaluation of short-term effects of rare earth and other elements used in magnesium alloys on primary cells and cell lines. Acta Biomater 2010;6:1834–42.
[414] Grillo CA, Alvarez F, de Mele MAFL. Cellular response to rare earth mixtures (La and Gd) as components of degradable magnesium alloys for medical applications. Colloid Surface B 2014;117:312–21.
[415] Zhao D, Wang T, Kuhlmann J, Dong Z, Chen S, Joshi M, et al. In vivo monitoring the biodegradation of magnesium alloys with an electrochemical $H_2$ sensor. Acta Biomater 2016;36:361–8.
[416] Mackenzie CG, Mackenzie JB, Beck P. The effect of pH on growth, protein synthesis, and lipid-rich particles of cultured mammalian cells. J Biophys Biochem Cytology 1961;9:141.
[417] Mareci D, Bolat G, Izquierdo J, Crimu C, Munteanu C, Antoniac I, et al. Electrochemical characteristics of bioresorbable binary MgCa alloys in Ringer's solution: revealing the impact of local pH distributions during in-vitro dissolution. Mater Sci Eng C 2016;60:402–10.
[418] Robinson DA, Griffith RW, Shechtman D, Evans RB, Conzemius MG. In vitro antibacterial properties of magnesium metal against *Escherichia coli*, Pseudomonas aeruginosa and Staphylococcus aureus. Acta Biomater 2010;6:1869–77.
[419] Grillo CA, Alvarez F, Fernández Lorenzo de Mele MA. Degradation of bioabsorbable Mg-based alloys: assessment of the effects of insoluble corrosion products and joint effects of alloying components on mammalian cells. Mater Sci Eng C 2016;58:372–80.

[420] Chen Y, Xu Z, Smith C, Sankar J. Recent advances on the development of magnesium alloys for biodegradable implants. Acta Biomater 2014;10:4561–73.
[421] Zhang L-N, Hou Z-T, Ye X, Xu Z-B, Bai X-L, Shang P. The effect of selected alloying element additions on properties of Mg-based alloy as bioimplants: a literature review. Front Mater Sci 2013;7:227–36.
[422] Hofstetter J, Martinelli E, Weinberg AM, Becker M, Mingler B, Uggowitzer PJ, et al. Assessing the degradation performance of ultrahigh-purity magnesium in vitro and in vivo. Corros Sci 2015;91:29–36.
[423] Hofstetter J, Becker M, Martinelli E, Weinberg AM, Mingler B, Kilian H, et al. High-strength low-alloy (HSLA) Mg–Zn–Ca alloys with excellent biodegradation performance. JOM 2014;66:566–72.
[424] Ralston KD, Birbilis N. Effect of grain size on corrosion: a review. Corrosion 2010;66:075005–75013.
[425] Mostaed E, Vedani M, Hashempour M, Bestetti M. Influence of ECAP process on mechanical and corrosion properties of pure Mg and ZK60 magnesium alloy for biodegradable stent applications. Biomatter 2014;4:e28283.
[426] Jiang J, Zhang F, Ma A, Song D, Chen J, Liu H, et al. Biodegradable behaviors of ultrafine-grained ZE41A magnesium alloy in DMEM solution. Metals 2016;6:3–7.
[427] Ratna Sunil B, Sampath Kumar TS, Chakkingal U, Nandakumar V, Doble M, Devi Prasad V, et al. In vitro and in vivo studies of biodegradable fine grained AZ31 magnesium alloy produced by equal channel angular pressing. Mater Sci Eng C 2016;59:356–67.
[428] Miskovic DM, Pohl K, Birbilis N, Laws KJ, Ferry M. Examining the elemental contribution towards the biodegradation of Mg-Zn-Ca ternary metallic glasses. J Mater Chem B 2016;4:2679–90.
[429] Hornberger H, Virtanen S, Boccaccini AR. Biomedical coatings on magnesium alloys - a review. Acta Biomater 2012;8:2442–55.
[430] Shadanbaz S, Dias GJ. Calcium phosphate coatings on magnesium alloys for biomedical applications: a review. Acta Biomater 2012;8:20–30.
[431] Wu G, Ibrahim JM, Chu PK. Surface design of biodegradable magnesium alloys — a review. Surf Coat Tech 2013;233:2–12.
[432] Agarwal S, Curtin J, Duffy B, Jaiswal S. Biodegradable magnesium alloys for orthopaedic applications: A review on corrosion, biocompatibility and surface modifications. Mater Sci Eng C 2016;68:948–63.
[433] Yang Y, Michalczyk C, Singer F, Virtanen S, Boccaccini AR. In vitro study of polycaprolactone/bioactive glass composite coatings on corrosion and bioactivity of pure Mg. Appl Surf Sci 2015;355:832–41.
[434] Townsend HE. Outdoor atmospheric corrosion. ASTM International: American Society for Testing and Materials; 2002.
[435] Eriksson P, Johansson LG, Gullman J. A laboratory study of corrosion reactions on statue bronze. Corros Sci 1993;34:1083–97.
[436] Strandberg H, Johansson LG, Lindqvist O. The atmospheric corrosion of statue bronzes exposed to $SO_2$ and $NO_2$. Mater Corr 1997;48:721–30.
[437] Niklasson A, Langer S, Arrhenius K, Rosell L, Bergsten CJ, Johansson LG, et al. Air pollutant concentrations and atmospheric corrosion of organ pipes in european church environments. Stud Conserv 2008;53:24–40.
[438] Tidblad J. Atmospheric corrosion of metals in 2010–2039 and 2070–2099. Atmos Env 2012;55:1–6.
[439] Strandberg H, Johansson LG. Some aspects of the atmospheric corrosion of copper in the presence of sodium chloride. J Electrochem Soc 1998;145:1093–100.
[440] Lindstrom R, Johansson LG, Svensson JE. The influence of $NaNO_3$ on the atmospheric corrosion of zinc. J Electrochem Soc 2003;150:B583–8.
[441] Inoue H, Sugahara K, Yamamoto A, Tsubakin H. Corrosion rate of magnesium and its alloys in buffered chloride solutions. Corros Sci 2002;44:603–10.
[442] Baril G, Blanc C, Pébère N. AC impedance spectroscopy in characterizing time-dependent corrosion of AZ91 and AM50 magnesium alloys characterization with respect to their microstructures. J Electrochem Soc 2001;148:B489–96.
[443] Pardo A, Merino MC, Coy AE, Arrabal R, Viejo F, Matykina E. Corrosion behaviour of magnesium/aluminium alloys in 3.5 wt.% NaCl. Corros Sci 2008;50:823–34.
[444] Wang L, Shinohara T, Zhang B. Corrosion behavior of Mg, AZ31, and AZ91 alloys in dilute NaCl solutions. J Solid State Electr 2010;14:1897–907.
[445] Cheng YL, Qin T, Wang H, Zhang Z. Comparison of corrosion behaviors of AZ31, AZ91, AM60 and ZK60 magnesium alloys. Trans Nonferrous Met Soc China 2009;19:517–24.
[446] Abidin NZ, Atrens AD, Martina D, Atrens A. Corrosion of high purity Mg, Mg2Zn0.2Mn, ZE41 and AZ91 in Hank's solution at 37 °C. Corros Sci 2011;53:3542–56.
[447] Song GL, Atrens A, Wu X, Zhang B. Corrosion behaviour of AZ21, AZ501 and AZ91 in sodium chloride. Corros Sci 1998;40:1769–91.
[448] Arrabal R, Pardo A, Merino MC, Mohedano M, Casajús P, Paucar K, et al. Effect of Nd on the corrosion behaviour of AM50 and AZ91D magnesium alloys in 3.5 wt.% NaCl solution. Corros Sci 2012;55:301–12.
[449] Abady GM, Hilal NH, El-Rabiee M, Badawy WA. Effect of Al content on the corrosion behavior of Mg–Al alloys in aqueous solutions of different pH. Electrochim Acta 2010;55:6651–8.
[450] Udhayan R, Bhatt DP. On the corrosion behaviour of magnesium and its alloys using electrochemical techniques. J Power Sources 1996;63:103–7.
[451] Singh IB, Singh M, Das S. A comparative corrosion behavior of Mg, AZ31 and AZ91 alloys in 3.5% NaCl solution. J Magnes Alloys 2015;3:142–8.
[452] El Shaye H, El Sawy EN. Corrosion behaviour of pure Mg, AS31 and AZ91 in buffered and unbuffered sulphate and chloride solutions. Corros Eng Sci Technol 2011;46:481–92.
[453] Shi Z, Song GL, Atrens A. Influence of the b phase on the corrosion performance of anodised coatings on Mg–aluminium alloys. Corros Sci 2005;47:2760–77.
[454] Godard HP, Jepson WP, Bothwell MR, Kane L. The corrosion of light metals. New York: John Wiley and Sons; 1967.
[455] Hui HD, Strekalov PV, Mikhailovskii YN, Bin DT, Mmikhailov AA. Composition and microstructure of corrosion products of aluminum and MA2-1 magnesium alloy in the wet tropical climate of Vietnam. Prot Met 1994;30:506–8.
[456] Arrabal R, Matykina E, Pardo A, Merino MC, Paucar K, Mohedano M, et al. Corrosion behaviour of AZ91D and AM50 Mg alloys with Nd and Gd additions in humid environments. Corros Sci 2012;55:351–62.
[457] Wright JM, Colling A, Bea G. Seawater: its composition, properties and behaviour. Open University; 1995.
[458] Santos PSM, Otero M, Santos EBH, Duarte AC. Chemical composition of rainwater at a coastal town on the southwest of Europe: what changes in 20 years? Sci Total Environ 2011;409:3548–53.
[459] Phipps PBP, Rice DW. Role of water in atmospheric corrosion. In: ACS symposium series, vol. 89; 1979. p. 235–41.
[460] Kirk WW. Atmospheric corrosion. ASTM International: American Society for Testing and Materials; 1995.
[461] Davila AF, Duport LG, Melchiorri R, Janchen J, Valea S, de los Rios A, et al. Hygroscopic salts and the potential for life on mars. Astrobiology 2010;10:617–28.
[462] Wadsö L, Anderberg A, Slund I, Söderman O. An improved method to validate the relative humidity generation in sorption balances. Eur J Pharm Biopharm 2009;72:99–104.
[463] Lindstrom R, Svensson JE, Johansson LG. The influence of salt deposits on the atmospheric corrosion of zinc. the important role of the sodium ion. J Electrochem Soc 2002;149:B57–64.
[464] Johansson LG, Vannerberg NG. The atmospheric corrosion of unprotected carbon steel – a comparison between field study and laboratory test. Mater Corr 1981;32:265–8.
[465] Strandberg H, Langer V, Johansson LG. Structure of $Cu_{2.5}(OH)3SO_{4.2}H_2O$ - a novel corrosion product of copper. Acta Chemica Scand 1995;49:5–10.
[466] Blucher DB, Lindstrom R, Svensson JE, Johansson LG. The effect of $CO_2$ on the NaCl-induced atmospheric corrosion of aluminum. J Electrochem Soc 2001;148:B127–31.
[467] Lindstrom R, Johansson LG, Svensson JE. The influence of NaCl and $CO_2$ on the atmospheric corrosion of magnesium alloy AZ91. Mater Corr 2003;54:587–94.
[468] Hasenberg L. Sulfur dioxide. USA: Corrosion Handbook; 1991;
Svensson JE, Johansson LG. Sulfidation of zinc by traces of hydrogen-sulfide in air. J Electrochem Soc 1995;142:1484–9.

[469] Svensson JE, Johansson LG. The synergistic effect of hydrogen sulfide and nitrogen dioxide on the atmospheric corrosion of zinc. J Electrochem Soc 1996;143:51–8.
[470] Svensson JE, Johansson LG. The temperature-dependence of the $SO_2$-induced atmospheric corrosion of zinc. A laboratory study. Corros Sci 1996;38:2225–33.
[471] Strandberg H, Johansson LG. The formation of black patina on copper in humid air containing traces of $SO_2$. J Electrochem Soc 1997;144:81–9.
[472] Blücher DB. Carbon dioxide: the unknown factor in the atmospheric corrosion of light metals. a laboratory study [Ph.D. dissertation]. Gothenburg (Sweden): Chalmers University of Technology; 2005.
[473] Esmaily M. The role of microstructure in the atmospheric corrosion of selected light alloys and composites [PhD Thesis]. Sweden: Department of Chemistry and Chemical Engineering Chalmers University of Technology Gothenburg; 2015.
[474] Graedel TE. Copper patinas formed in the atmosphere - II. A qualitative assessment of mechanisms. Corros Sci 1987;27:721–40.
[475] Finlayson-Pitts BJ, Pitts JN. Atmospheric chemistry fundamentals and experimental techniques. New York: John Wiley and Sons; 1986.
[476] Zarrouk A, Warad I, Hammouti B, Dafali A, Al-Deyab SS, Benchat N. The effect of temperature on the corrosion of Cu/$HNO_3$ in the presence of organic inhibitor: part-2. Int J Electrochem Sci 2010;5:1516–26.
[477] Blücher DB, Svensson JE, Johansson LG. The NaCl-induced atmospheric corrosion of aluminum-The influence of carbon dioxide and temperature. J Electrochem Soc 2003;150:B93–8.
[478] Vázquez M, Hanslmeier A. Ultraviolet radiation in the solar system. Springer; 2016.
[479] Liang D, Allen HC, Frankel GS, Chen ZY, Kelly RG, Wu Y, et al. Effects of sodium chloride particles, Ozone, UV, and relative humidity on atmospheric corrosion of silver. J Electrochem Soc 2010;157:C146–56.
[480] Thompson EA, Burleigh TD. Accelerated corrosion of zinc alloys exposed to ultraviolet light. Corros Eng Sci Techn 2007;2:237–41.
[481] Frankel GS. Pitting corrosion of metals: a review of the critical factors. J Electrochem Soc 1998;145:2186–98.
[482] Kruger J. Passivity of metals - a materials science perspective. Int Mater Rev 1988;33:113–30.
[483] Strehblow HH. Mechanisms of pitting corrosion in corrosion mechanisms in theory and practice. Basel (New York): Marcel Dekker; 2002.
[484] Falk T, Svensson JE, Johansson LG. The role of carbon dioxide in the atmospheric corrosion of zinc. J Electrochem Soc 1998;145:39–44.
[485] Lindstrom R, Johansson LG, Thompson GE, Skeldon P, Svensson JE. Corrosion of magnesium in humid air. Corros Sci 2004;46:1141–58.
[486] Werner M, Hariharan S, Mazzotti M. Flue gas $CO_2$ mineralization using thermally activated serpentine: from single- to double-step carbonation. Phys Chem Chem Phys 2014;16:24978–93.
[487] White WB. Thermodynamic equilibrium, kinetics, activation barriers, and reaction mechanisms for chemical reactions in Karst Terrains. Environ Geol 1997;30:46–58.
[488] Chen ZY, Persson D, Nazarov A, Zakipoura S, Thierry D, Leygraf C. In situ studies of the effect of $CO_2$ on the initial NaCl-induced atmospheric corrosion of copper. J Electrochem Soc 2005;152:B342–51.
[489] Chen J. AC impedance spectroscopy study of the corrosion behavior of an AZ91 magnesium alloy in 0.1 mol/L sodium sulfate solution. Electrochim Acta 2007;52:3299–309.
[490] Yang L, Wei Y, Hou L, Zhang D. Corrosion behaviour of die-cast AZ91D magnesium alloy in aqueous sulphate solutions. Corros Sci 2010;52:345–51.
[491] Yun I. Corrosion behaviour of die-cast AZ91D magnesium alloys in sodium sulphate solutions with different pH values. Trans Nanferrous Met Soc China 2011;21:912–20.
[492] Barin I. Thermochemical data of pure substances. 3rd ed. VCH Verlagsgesellschaft mbH; 2008.
[493] Esmaily M, Svensson JE, Johansson LG. Corrosion of Mg-aluminum (Mg-Al) alloys – an interplay between Al content and CO2. Magnes Technol 2017;397–403 [The Minerals, Metals & Materials].
[494] Evans DG. Structural aspects of layered double hydroxides Layered double hydroxides. Springer; 2015.
[495] Duan X, Evans DG. Layered double hydroxides, structure and bonding. Berlin (Heidelberg): Springer-Verlag; 2006.
[496] Mathieu S, Rapin C, Steinmetz J, Steinmetz P. A corrosion study of the main constituent phases of AZ91 magnesium alloys. Corros Sci 2003;45:2741–55.
[497] Baliga CB, Tsakiropoulos P. Development of corrosion resistant magnesium alloys. Part 2. Structure of corrosion products on rapidly solidified Mg–16Al alloys. Mater Sci Technol 1993;9:513–21.
[498] Leggat RB, Zhang W, Buchheit RG, Taylor SR. Performance of hydrotalcite conversion treatments on AA2024-T3 when used in a coating system. Corrosion 2002;58:322–8.
[499] Zheludkevich ML, Poznyak SK, Rodrigues LM, Raps D, Hack T, Dick LF, et al. Active protection coatings with layered double hydroxide nanocontainers of corrosion inhibitor. Corros Sci 2010;52:602–11.
[500] Zhang F, Sun M, Xu S, Zhao L, Zhang B. Fabrication of oriented layered double hydroxide films by spin coating and their use in corrosion protection. Chem Eng J 2008;141:362–7.
[501] Hang TTX, Truc TA, Duong NT, Pébère N, Olivier MG. Layered double hydroxides as containers of inhibitors in organic coatings for corrosion protection of carbon steel. Prog Org Coat 2012;74:343–8.
[502] Fan G, Li F, Evans DG, Duan X. Catalytic applications of layered double hydroxides: recent advances and perspectives. Chem Soc Rev 2014;43:7040–66.
[503] Liu Z, Ma R, Osada M, Iyi N, Ebina Y, Takada K, et al. Synthesis, anion exchange, and delamination of Co-Al layered double hydroxide: assembly of the exfoliated nanosheet/polyanion composite films and magneto-optical studies. J Am Chem Soc 2006;128:4872–80.
[504] Lindgren M, Panas I. Impact of additives on zirconium oxidation by water: mechanistic insights from first principles. RSC Adv 2013;3:21613–9.
[505] Lindgren M, Panas I. Confinement dependence of electro-catalysts for hydrogen evolution from water splitting. Beilstein J Nanotechnol 2014;5:195–201.
[506] Lindgren M, Panas I. Oxygen vacancy formation, mobility, and hydrogen pick-up during oxidation of zirconium by water. Oxid Met 2017;87:355–65.
[507] LeBozec N, Thierry D. Influence of test parameters in an automotive cyclic test on the corrosion and mechanical performance of joined materials. Mater Corros 2015;66:1051–9.
[508] Chen YF, Liu M, Zeng XQ, Ding WJ. Investigation of effect of geometry design on the galvanic corrosion of magnesium component. Mater Corros 2015;66:949–62.
[509] Jia JX, Song GL, Atrens A. Influence of geometry on galvanic corrosion of AZ91D coupled to steel. Corros Sci 2006;48:2133–53.
[510] Baron-Wiecheć A, Curioni M, Arrabal R, Matykina E, Skeldon P, Thompson GE. Plasma electrolytic oxidation of coupled light metals. Trans IMF 2013;91:107–12.
[511] Kish JR, Cano Z, Kobylecky A, McDermid J, Skszek T. Comparative corrosion assessment of coated alloys for multi-material lightweight vehicle architectures. SAE International; 2015.
[512] Hillis JE, Murray RW. Finishing alternatives for high purity magnesium alloys. In: 14th International die casting congress and exposition. Toronto 1987. p. Paper No. G-T 87–003.
[513] Cao F, Shi Z, Hofstetter J, Uggowitzer PJ, Song GL, Liu M, et al. Corrosion of ultra-high-purity magnesium in 3.5% NaCl solution saturated with $Mg(OH)_2$. Corros Sci 2013;75:78–99.
[514] Südholz AD, Birbilis N, Bettles CJ, Gibson MA. Corrosion behaviour of Mg-alloy AZ91E with atypical alloying additions. J Alloys Compd 2009;471:109–15.
[515] Esmaily M, Mortazavi N, Shahabi-Navid M, Svensson JE, Halvarsson M, Nyborg L, et al. Effect of rheocasting on corrosion of AM50 magnesium alloy. J Electrochem Soc 2015;162:C85–95.
[516] Aung NN, Zhou W. Effect of heat treatment on corrosion and electrochemical behaviour of AZ91D magnesium alloy. J Appl Electrochem 2002;32:1397–401.

[517] Li J, Jiang Q, Sun H, Li Y. Effect of heat treatment on corrosion behavior of AZ63 magnesium alloy in 3.5 wt.% sodium chloride solution. Corros Sci 2016;111:288–301.

[518] Arrabal R, Pardo A, Merino MC, Merino S, Mohedano M, Casajús P. Corrosion behaviour of Mg/Al alloys in high humidity atmospheres. Mater Corros 2011;62:326–34.

[519] Pardo A, Merino MC, Coy AE, Viejo F, Arrabal R, Feliú Jr S. Influence of microstructure and composition on the corrosion behaviour of Mg/Al alloys in chloride media. Electrochim Acta 2008;53:7890–902.

[520] Gray JE, Luan B. Protective coatings on magnesium and its alloys – a critical review. J Alloys Compd 2002;336:88–113.

[521] ASTM D1732–03(2013). Standard practices for preparation of magnesium alloy surfaces for painting, ASTM International; 2013.

[522] Niu LY, Jiang ZH, Li GY, Gu CD, Lian JS. A study and application of zinc phosphate coating on AZ91D magnesium alloy. Surf Coat Technol 2006;200:3021–6.

[523] Zhao M, Wu S, Luo J, Fukuda Y, Nakae H. A chromium-free conversion coating of magnesium alloy by a phosphate–permanganate solution. Surf Coat Technol 2006;200:5407–12.

[524] Zhao M, Wu S, An P, Luo J, Fukuda Y, Nakae H. Microstructure and corrosion resistance of a chromium-free multi-elements complex coating on AZ91D magnesium alloy. Mater Chem Phys 2006;99:54–60.

[525] Ardelean H, Frateur I, Marcus P. Corrosion protection of magnesium alloys by cerium, zirconium and niobium-based conversion coatings. Corros Sci 2008;50:1907–18.

[526] AIMT. MAGPASS-COAT® Chrome-free passivation of Mg-based materials; 2016.

[527] Lin CS, Lin HC, Lin KM, Lai WC. Formation and properties of stannate conversion coatings on AZ61 magnesium alloys. Corros Sci 2006;48:93–109.

[528] Yang YC, Tsai CY, Huang YH, Lin CS. Formation mechanism and properties of titanate conversion coating on AZ31 magnesium alloy. J Electrochem Soc 2012;159:C226–32.

[529] Chen XB, Easton MA, Birbilis N, Yang HY, Abbott TB. 10 - Corrosion-resistant coatings for magnesium (Mg) alloys A2 – Song GL. Corrosion prevention of magnesium alloys. Woodhead Publishing; 2013. p. 282–312.

[530] REACH. Regulation (EC) No 1907/2006 of 18 December 2006 concerning the Registration, Evaluation, Authorisation and Restriction of Chemicals (REACH) and establishing a European Chemicals Agency.

[531] AMS2473H standard. Chemical film treatment for aluminum alloys, general purpose coating. SAE International; 2013.

[532] Kurze P. Corrosion and surface protections. In: Friedrich HE, Mordike BL, editors. Magnesium technology metallurgy, design data, applications. Berlin (Heidelberg): Springer-Verlag; 2006.

[533] DOW MAGNESIUM, Operations in Magnesium Finishing, The Dow Chemical Company, 1990.

[534] Evangelides HA. Method of electrolytically coating magnesium and electrolyte therefor. US 2723952 A; 1955.

[535] Bartak DE, Lemieux BE, Woolsey ER. Hard anodic coating for magnesium alloys. US 5470664 A;1995.

[536] Schmeling EL, Roschenbleck B, Weidemann MH. Method of producing protective coatings that are resistant to corrosion and wear on magnesium and magnesium alloys. US 4978432A; 1990.

[537] Barton TF. Anodization of magnesium and magnesium based alloys. US 5792335A; 1998.

[538] Pozzoli AS, Strazzi E. Multivalent electrolytic process for the surface treatment of non ferrous metallic material. EP 1793019 A2; 2007.

[539] Samsonov VI, Shatrov AS. Process and device for forming ceramic coatings on metals and alloys, and coatings produced by this process. EP 1488024 A2; 2004.

[540] Arrabal R, Matykina E, Hashimoto T, Skeldon P, Thompson GE. Characterization of AC PEO coatings on magnesium alloys. Surf Coat Technol 2009;203:2207–20.

[541] Lu X, Mohedano M, Blawert C, Matykina E, Arrabal R, Kainer KU, et al. Plasma electrolytic oxidation coatings with particle additions – a review. Surf Coat Technol 2016;307:1165–82.

[542] Gnedenkov AS, Sinebryukhov SL, Mashtalyar DV, Gnedenkov SV. Localized corrosion of the magnesium alloys with inhibitor-containing coatings: SVET and SIET studies. Corros Sci 2016;102:269–78.

[543] Sun M, Yerokhin A, Bychkova MY, Shtansky DV, Levashov EA, Matthews A. Self-healing plasma electrolytic oxidation coatings doped with benzotriazole loaded halloysite nanotubes on AM50 magnesium alloy. Corros Sci 2016;111:753–69.

[544] Němcová A, Galal O, Skeldon P, Kuběna I, Šmíd M, Briand, et al. Film growth and alloy enrichment during anodizing AZ31 magnesium alloy in fluoride/glycerol electrolytes of a range of water contents. Electrochim Acta 2016;219:28–37.

[545] Schneider M, Kremmer K, Höhn S. Corrosion protection of thickness reduced plasma electrolytic layers on AZ31. Mater Corros 2016;67:921–8.

## Glossary

*ACT:* Accelerated corrosion testing
*AES:* Auger electron spectroscopy
*AESEC:* Atomic emission spectroelectrochemistry
*AFM:* Atomic force microscopy
*ANN:* Artificial neural network
$\boldsymbol{b}_{\mathbf{a}}$: Anodic Tafel slope
*BB:* Bragg-Brentano
*BBC:* Body centered cubic
$\boldsymbol{b}_{\mathbf{c}}$: Cathodic Tafel slope
*BG:* Bioactive glass
*BIB:* Broad ion beam
*CALPHAD:* Calculation of phase diagrams
*CBED:* Convergent-beam electron diffraction
*CCT:* Cyclic corrosion testing
*CNT:* Carbon nanotubes
*CP:* Commercial purity
*CT:* X-ray computed tomography
*DFT:* Density functional theory
*DMEM:* Dulbecco's modified eagle medium
*EBSD:* Electron backscatter diffraction
$E_{\mathbf{corr}}$: Corrosion potential
*EDS:* Energy-dispersive X-ray spectroscopy
*EFTEM:* Energy filtered transmission electron microscopy
*EIS:* Electrochemical impedance spectroscopy
$E_{\mathbf{rev}}$: Reversible potential
$E_{\mathbf{rev,H}}$: Reversible potential for hydrogen evolution
*ESEM:* Environmental scanning electron microscopy

*FIB:* Focused ion beam
*FTIR:* Fourier transform infrared spectroscopy
*FTIRAS:* Fourier transform infrared reflection absorption spectroscopy
*GB:* Grain boundary
*GI:* Grazing incidence
*HCP:* Hexagonal close-packed
*HE:* Hydrogen evolution
*HER:* Hydrogen evolution reaction
*HP:* High purity
*HRTEM:* High resolution transmission electron microscopy
*HV:* High vacuum
$i_\mathbf{0}$: Exchange current density
$i_\mathbf{0,H}$: Exchange current density for hydrogen evolution
$i_\mathbf{anod}$: Anodic current density
*IC:* Ion chromatography
$i_\mathbf{cath}$: Cathodic current density
$i_\mathbf{corr}$: Corrosion current density
*ICP:* Inductively coupled plasma optical emission spectrometry
*IM:* Interference microscopy
*IPF:* Inverse pole figure
*IR:* Infrared
*LDH:* Layered double hydroxides
*LPR:* Linear polarization resistance
*MAO:* Micro-arc oxidation
*MMC:* Metal matrix composite
*MS:* Mass spectrometry
*NDE:* Negative difference effect
*NND:* Nearest neighbor distance
*OCP:* Open circuit potential
*OES:* Optical emission spectrometry
*OM:* Optical microscope
*ORR:* Oxygen reduction reaction
*PCL:* Polycaprolactone
*PDP:* Potentiodynamic polarization
*PEO:* Plasma electrolytic oxidation
*PIXE:* Particle-induced X-ray emission
*RBS:* Rutherford backscattering spectrometry
*RC:* Rheocasting
$R_\mathbf{ct}$: Charge transfer resistance
*RH:* Relative humidity
$R_\mathbf{p}$: Polarization resistance
*SBF:* Simulated body fluid
*SCC:* Stress corrosion cracking
*SCE:* Saturated calomel electrode
*SECM:* Scanning electrochemical microscopy
*SEM:* Scanning electron microscopy
*SIMS:* Secondary ion mass spectrometry
*SKP:* Scanning Kelvin probe
*SKPFM:* Scanning Kelvin probe force microscopy
*SL:* Semisolid-liquid
*SS:* Semisolid-semisolid
*SSC:* Semi-solid casting
*STEM:* Scanning transmission electron microscopy
*SVET:* Scanning vibrating electrode technique
*TEM:* Transmission electron microscopy
*TKD:* Transmission Kikuchi diffraction
*TOF:* Time of flight
*TOW:* Time of wetness
*UHP:* Ultra high purity
*UHV:* Ultra high vacuum
*UV:* Ultraviolet radiation
*WDS:* Wavelength dispersive X-ray spectroscopy
*WL:* Weight loss
*XPS:* X-Ray photoelectron spectroscopy
*XRD:* X-ray diffraction